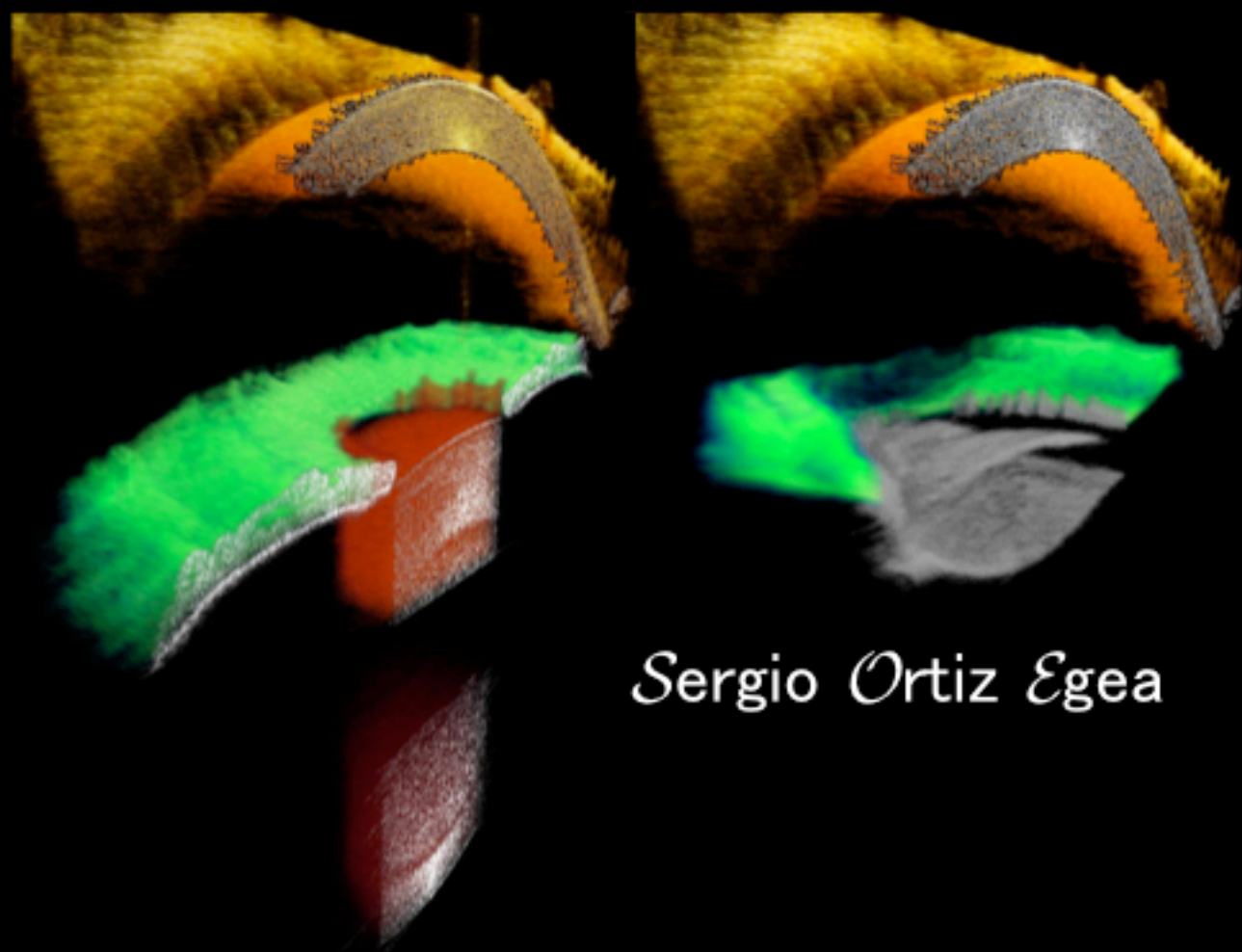


QUANTITATIVE ANTERIOR SEGMENT OPTICAL COHERENCE TOMOGRAPHY



Sergio Ortiz Egea

*Supervisor: Susana Marcos
Instituto de Óptica, CSIC
Doctoral Thesis, 2012*



Universidad de Valladolid

**INSTITUTO DE OFTALMOBIOLOGÍA
APLICADA**

TESIS DOCTORAL:

**QUANTITATIVE ANTERIOR SEGMENT
OPTICAL COHERENCE TOMOGRAPHY**

Presentada por SERGIO ORTIZ EGEA para optar al
grado de Doctor por la Universidad de Valladolid

Dirigida por:

SUSANA MARCOS CELESTINO

A mis padres, a mi hermana y a Vanessa

“Success is the ability to go from one failure
to another with no loss of enthusiasm.”

Winston Churchill (British Orator, Author and
Prime Minister during World War II. 1874-1965)



Instituto de óptica “Daza de
Valdes”

Madrid, 2012

Contents

Page

Table of contents	iii
Chapter1. Introduction	1
1.1 Motivation.....	2
1.2 Background of Optical Coherence Tomography	3
1.2.1 Definition	3
1.2.2 Partial Coherence Interferometry.....	3
1.3 Overview of different OCT modalities.....	6
1.3.1 Time Domain OCT Optical Coherence Tomography	6
1.3.2 Fourier-Domain Optical Coherence Tomography10	
1.3.3 Comparative of performance of different OCT modalities.....	13
1.4 Anterior segment optics and anatomy	14
1.4.1 Tear film.....	14
1.4.2 Cornea	15
1.4.3 Iris	18
1.4.4 Lens.....	19
1.4.5. Anterior Segment conditions studied in this thesis	23
1.5. State of the art of anterior segment imaging.....	25
1.5.1 Biometry	25
1.5.2 Anterior segment characterization	26
1.5.3 Corneal Measurements.....	27
1.5.4 Imaging Systems	29
1.6 State-of-the art of the OCT Technique	31
1.7 Open questions addressed in this thesis.....	34

1.8 Goals of this thesis	35
1.9 Hypothesis	36
1.10 Thesis Structure	36
Chapter2. Custom-Developed Optical Coherence Tomography Systems	39
2.1. Time Domain OCT	40
2.1.1 Optical Lay-out	41
2.1.2 Electronic lay-out.....	42
2.1.3 Software	44
2.2. Spectral Domain OCT	48
2.2.1 Optical lay-out	48
Chapter 3. Three-dimensional Ray tracing on Delaunay-based reconstructed surfaces	51
3.1 Introduction.....	52
3.2 Delaunay decomposition	52
3.2.1 Description of the algorithm	53
3.3. Numerical examples	58
3.3.1. Analytical surface with a regular and random grid	58
3.3.2. Noisy surface with a regular grid.....	59
3.3.3 Free-form surface (corneal topography)	61
3.4 Conclusions.....	66
Chapter 4. Optical Coherence Tomography for quantitative surface topography	69
4.1 Introduction.....	70
4.2 Methods	71

TABLE OF CONTENTS

4.2.1. Modeling of the fan distortion	71
4.2.2. Estimation of the residual fan distortion	73
4.2.3. Fan distortion correction	77
4.2.4. Validation on surfaces of known geometry	78
4.3. Results.....	78
4.3.1. Simulation of fan distortion	78
4.3.2 Residual fan distortion in the experimental system	80
4.3.3 Correction of fan distortion of OCT images	80
4.4 Conclusions.....	81
Chapter 5. Optical distortion correction in Optical Coherence Tomography for quantitative anterior segment three-dimensional Imaging	83
5.1. Introduction.....	84
5.2 Methods	86
5.2.1 Theoretical considerations	86
5.2.2. Experimental setups and protocols	91
5.2.3 Signal processing	93
5.3 Results.....	96
5.3.1. Computer simulations	96
5.3.2 Experimental data	98
5.4. Conclusions	103

Chapter 6. 3D Image processing tools for anterior segment clinical applications **105**

6.1. Introduction..... 106

6.2. Pre-Processing in Fourier Domain OCT..... 107

6.3. Denoising..... 107

6.4. Statistical thresholding..... 110

6.5. Volume Clustering..... 112

6.6. Multilayer segmentation 113

6.7 Further surface denoising..... 118

6.8 Pupil center reference 120

6.9. Merging 3-D volumes..... 121

6.10. Geometrical distances calculation 123

6.11. Surface fitting by quadrics, conicoids and topographic maps..... 124

Chapter 7. Topography from spectral domain optical coherence tomography for in vivo and in vitro surfaces **127**

7.1 Introduction..... 128

7.2. Methods 129

7.2.1 Image processing, automatic segmentation and surface fitting 129

7.2.2. Fan distortion measurement and correction: general considerations..... 132

7.2.3 Experiments on artificial lens surfaces (spherical and aspheric)..... 135

TABLE OF CONTENTS

7.2.4 Experiments on human corneas in vivo	136
7.3. Results.....	138
7.3.1 Fan distortion	138
7.3.2 Topographic measurements on artificial lens surface (spherical and aspheric).....	138
7.3.3 Topographic measurements on human corneas in vivo	141
7.4. Discussion.....	144
7.5. Conclusions.....	146
Chapter 8. Quantitative OCT-based corneal topography in keratoconus with intracorneal ring segments	149
8.1. Introduction	150
8.2. Material and Methods	152
8.2.1. Patient and ICRS surgery	152
8.2.2. Experimental acquisition protocols.....	152
8.2.3. 3D image analysis: denoising, segmentation and surface fitting	152
8.2.4. ICRS implantation evaluation.....	156
8.3. Results.....	156
8.3.1. Posterior corneal surface change after ICRS distortion correction	156
8.3.2. Corneal shape: radii of curvature and asphericities	156
8.3.3 Full corneal topography	157
8.3.4. Corneal pachymetry	158
8.3.5. ICRS location	159
8.4. Discussion.....	160
8.5. Conclusions.....	161

Chapter 9. In vivo human crystalline lens topography	163
9.1. Introduction	164
9.2. Material and Methods	166
9.2.1. Validation experiments on samples <i>in vitro</i>	166
9.2.2. Experimental protocols for anterior segment image acquisition <i>in vivo</i>	167
9.2.3. 3-D Image analysis: denoising, segmentation, merging, distortion correction and surface fitting.....	168
9.3. Results.....	171
9.3.1. <i>In vitro</i> samples.....	171
9.3.2. Corneal shape parameters	173
9.3.2. Effects of optical distortion on crystalline lens shape	174
9.3.3. Crystalline lens shape	175
9.3.4. Crystalline lens topography	177
9.3.5. Crystalline lens thickness.....	177
9.4. Discussion.....	178
9.5. Conclusions.....	182
Chapter 10. Anterior segment biometry: an application in cataract surgery	183
10.1. Introduction	184
10.2. Methods	186
10.2.1. Validation experiments on in Vitro samples...	186
10.2.2. Experiments on cataract surgery patient	187
10.2.3. 3-D Image analysis	188
10.3. Results.....	190
10.3.1. OCT-based lens tilt measurement: validation on an in vitro physical model eye	190
10.3.2. In vivo 3D anterior biometry: cornea and crystalline lens/IOL.....	191
10.4 Discussion.....	192

TABLE OF CONTENTS

10.5 Conclusions.....	194
Chapter 11. Conclusions	195
Bibliography	205
Publications	239

Chapter 1

Introduction

The optical quality of the human eye is mainly determined by the geometrical and optical properties of two elements, cornea and crystalline lens. The cornea accounts for two-thirds of the optical refractive power, while the crystalline lens provides approximately one third of the total static refractive power of the eye, and it is the responsible for accommodation. Accurate description of the geometry of the eye's optical components is particularly critical for understanding their contribution to optical aberrations.

The geometrical properties of the cornea have been previously studied due to its accessibility. Until recently, knowledge of the geometry of the lens was limited to *in vitro* studies, while *in vivo* data were referred in most cases to axial properties, such as the thickness or central radius of curvature. Videokeratography, or interferometric techniques have been used to characterize the anterior cornea, while optical (Purkinje and Scheimpflug) and non-optical (Ultrasound biomicroscopy and Magnetic Resonance Imaging (MRI)) techniques have been used to characterize several aspects of the crystalline lens.

Optical Coherence Tomography (OCT) is one of the most versatile and promising imaging techniques of the anterior segment of the eye, due to its high resolution, and the possibility of imaging the anterior and posterior cornea, the iris and the crystalline lens over a large cross-sectional area. The images provided by OCT show high contrast and high axial resolution. However, the data obtained are not quantitative since the OCT is affected by two sources of distortion: Fan and refraction distortion.

This thesis solves key problems of calibration, image analysis and quantification of OCT anterior segment imaging, providing for the first time fully quantitative OCT based corneal topography, crystalline lens surfaces topography and three-dimensional anterior segment biometry. The developed methodology is applied to normal subjects and to keratoconic corneas before and after implantation of Intracorneal Rings Segments (ICRS).

In this chapter we present background and state of the art of ocular anterior segment OCT technology, an anatomical review of the

structures of the anterior segment, a brief description of the applications of the developed technology for quantitative imaging in patients (keratoconus and its treatment by intrastromal ring segments, and intraocular Lens (IOL) implantation).

1.1 Motivation

This thesis addresses the study of the geometry of the eye, in particular the anterior segment, by developing devices and methods to provide quantitative data on the geometry and biometry of the cornea and lens. Accurate measurement of cornea and lens geometry and biometry is crucial in the understanding of ocular optical quality and to provide better diagnostics and treatment.

Anterior segment characterization is limited only to various commercial instruments, which provide images of anterior and posterior corneal surfaces and quantitative geometrical information of the cornea. However, there are not commercially available instruments that provide crystalline lens information. Scheimpflug imaging, which allows acquisition of cross-sectional images of the cornea and lens with the proper correction and validation, is able to provide quantitative geometrical features and topographic maps of the cornea, as well as radius of curvature and asphericity of the lens surfaces. The shape, location and phakometry of the crystalline lens have been reported *in vivo* and *in vitro* using different imaging techniques. Radii of curvature, tilt and decentration of the lens have been measured using Purkinje and Scheimpflug imaging. In addition to optical techniques, the anterior chamber of the eye can be imaged through non-optical imaging techniques such as ultrasound and Magnetic Resonance Imaging. These non-optical techniques allow visualization of the entire crystalline lens and its neighboring ocular structures. However, these are either invasive or time-consuming imaging methods, with significantly lower resolution than optical techniques, which impose major problems (low acquisition speed, motion artifacts or low sampling density), which prevent quantifying the crystalline lens geometry with high accuracy.

Even though Optical Coherence Tomography (OCT) is a versatile imaging technique of the anterior segment of the eye, since it provides high resolution and high contrasted large cross sectional images, the data collected by OCT are not quantitative since the system is subject to two types of distortions: fan and optical (refraction). Fan distortion is inherent to the architecture of the sample arm of the OCT and it is highly dependent of the separation of the rastering mirrors and of the location and focal of the lens. Optical distortion is produced when a structure is imaged through other refractive surfaces. Those distortions

cause inaccuracies in the reconstruction of the geometrical aspects of surfaces which need to be compensated to obtain quantitative data.

Quantitative biometry is essential in many areas of physiological optics (i.e. customized eye modeling understanding of the structural changes in the crystalline lens during accommodation and aging, crystalline lens gradient index of refraction reconstruction, etc...) and ophthalmology (i.e. changes in the anterior and posterior corneal topography after refractive surgery or after Intracorneal Rings segments for keratonus treatment and pre-operative biometry in the evaluation of cataract surgery).

1.2 Background of Optical Coherence Tomography

1.2.1. Definition

Optical coherence tomography (OCT) is a non-invasive, non contact imaging technique for high resolution, cross-sectional imaging of quasi-transparent media. OCT uses low-coherence interferometry to produce images from the light backscattered from tissue structures. An OCT image can be described as a collection of partial coherence interferograms (PCI), achieved using a scanning device to sweep the sample

1.2.2 Partial Coherence Interferometry

Partial coherence interferometry (PCI) was first used in a 1-D optical technique called Optical Coherence Domain Reflectometry (OCDR). It was first reported in an application for inspection of fiber optic cables or network components [Younquist et al, 1987, Takada et al, 1987]. The same concept of PCI was later demonstrated to measure the axial length of the eye by Fercher and co-workers in 1988 [Fercher et al, 1988].

The basic principles of operation of PCI rely on the interferometric properties of broadband light sources to find the optical distances. An optical probe directs a low-coherence light beam to a sample surface, which sends reflected light signals back to the interferometer. The back reflected light coming from each arm (sample and reference) produces an interference signal that is recorded as a depth profile (A-Scan).

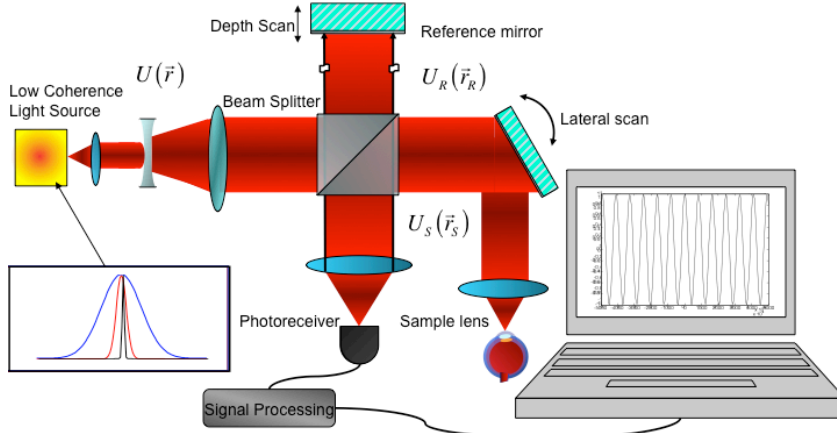


Figure 1.1. Schematic diagram of a partial coherence interferometer implemented in a Michelson configuration in air.

The most popular OCT interferometer implementation is based on a Michelson interferometer configuration, with a light source, a beam splitter, a reference mirror and a detection unit, composed of a detector unit (photoreceiver), a signal processing unit and computer, as main elements. A stationary field U produced by the low coherence source, is split in two arms, with two amplitudes, U_R and U_S .

The back reflected light from the sample is recombined with light from the reference arm by the beam splitter and it is led to a photoreceiver. The intensity at the detector plane can be described by Equation 1.1 as a combination of direct current (DC) term denoted by I_{DC} (intensities from reference I_R and sample arm I_S) plus an alternate current (AC) denoted by I_{AC} . The DC term results from the average temporal amplitude from the sample and reference arm, while the AC part expresses the difference in optical path of the two arms.

$$I(\tau) = I_{DC} + I_{AC} = I_R + I_S + 2\Re \left\langle U_R(\vec{r}_R) U_S^*(\vec{r}_S) \right\rangle \quad Eq.1.1$$

$$\text{where } \tau = |\vec{r}_R - \vec{r}_S|/c$$

where τ is the time difference produced by the spatial shift between arms, calculated as the spatial difference divided by the light speed c . Performing some algebra the AC part of the intensity can be expressed using the complex degree of coherence definition $\mu_{RS}(\tau)$ provided by Equation 1.2.

$$\mu_{RS}(\tau) = \frac{\langle U_R(\vec{r}_R) U_S^*(\vec{r}_S) \rangle}{\sqrt{I_R I_S}} \quad Eq.1.2$$

Physically speaking the I_{AC} term can be seen as a narrow band signal (Equation 1.3), since it is the product of the band-limited signal $|\mu_{RS}(\tau)|$ and a carrier $\cos(2\pi\nu_0\tau - \delta)$, where, ν_0 is the central frequency of the light spectrum and δ is the phase difference.

$$I_{AC} = 2\sqrt{I_R I_S} |\mu_{RS}(\tau)| \cos(2\pi\nu_0\tau - \delta) \quad Eq.1.3$$

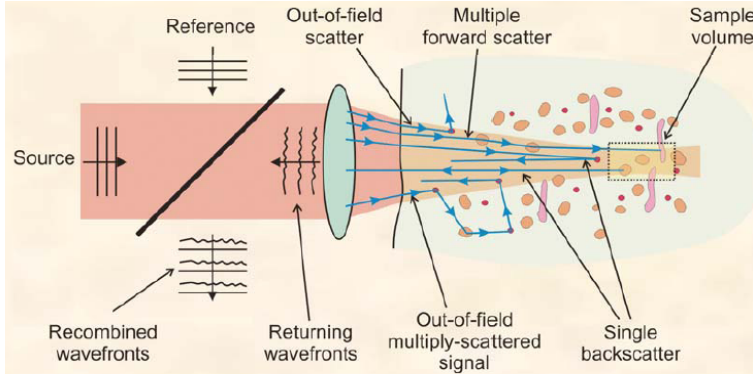


Figure 1.2. Interferometer and backscattered radiation (Single and multiple back reflected light).

When the sample arms of a PCI device illuminates a medium composed by a population of scatterers (Figure 1.2), the light strikes on a scatterer generating a scattering wave [Bohren et al, 1983, and Tsang, 2000], where part of the radiation is backreflected towards the collecting lens. Depending on the scattering properties of the sample tissue, single or multiple scattering can occur. The amount of light that reaches the detector depends on the nature (volumetric or surface) of scattering, on the reflectivity, size, position shape and concentration of the backscatter elements, on the irradiance level of the light at every point, and on the power spectrum of the light source used for illuminating the sample. Therefore, the AC intensity can be described as the sum of two components (Equation 1.5): The first term corresponds to a sinusoidal function with a frequency proportional to the path-length difference between the reflector and reference arm, and its amplitude is proportional to the modulus of the complex degree of coherence for every scatter. The second term is related to the so-called structure factor, which accounts for the scattering properties of the material. For random scattering the interference is destructive and the effect is

negligible. For tissue, this contribution is generally not negligible and it reduces the amount of back-reflected light.

$$I_{AC}(\tau) = 2 \sum_n \sqrt{I_R I_S^{(n)}} |\mu_{RS}^{(n)}(\tau)| \cos(2\pi\nu_0\tau_n - \delta_n) + 2 \sum_n \sum_{n \neq m} \Re \left[U_S^{(n)}(\vec{r}_S^{(n)}) U_S^{(m)*}(\vec{r}_S^{(m)}) \right] \quad Eq.1.4$$

1.3. Overview of different OCT modalities

OCT technology can be classified according to its detection process: directly from the detection unit in the case of the Time Domain, and through the Fourier transform in the case of spectral or swept source OCTs. The most important OCT modalities include: Time-Domain OCT (TD-OCT), Spectral-Domain OCT (SD-OCT) and Swept source (SS-OCT). Time-Domain OCT technology is more intuitive to understand, and most early research and commercial instrumentation were based on this technology. Fourier-Domain OCT, SD-OCT and SS-OCT are rapidly replacing the Time-Domain technology in most applications because it offers significant advantages in sensitivity and imaging speed

1.3.1 Time Domain OCT (TD-OCT)

In TD-OCT the location of scatters in a sample is observed by generation of interferometric fringes at the detector as the reference reflector position is axially translated (Figure 1.3). The back reflected signal is provided by a number of scattering centers that are embedded in a homogeneous medium. TD-OCT is generally implemented as Michelson interferometer with a broadband light source (femtosecond laser, super luminescence diode [SLD]) in the illumination channel. Light is divided in two channels by a beam splitter defining two arms, the reference and the sample arm. The reference arm is composed of an axial scanning mirror, while the sample arm is configured with a transverse scanning system for sweeping the sample and an optical system for focusing the light on the sample. The backreflected light from both arms is recombined by the beam splitter and directed to a single detector. The resultant interference is electronically filtered and stored in the computer.

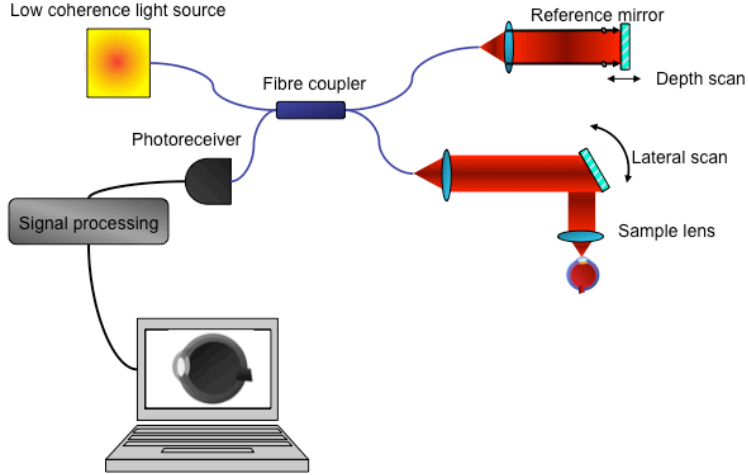


Fig 1.3. Schematic diagram of a TD-OCT based on a fiber optic Michelson interferometer.

As it has been introduced before, the envelope of the interferometric fringes changes as the path length difference is varied. The peak of the envelope signal is located at the path length-matching place. Assuming that the spectral component of the light can be modeled as a Gaussian function, the complex degree of coherence can be expressed in terms of the Optical Path Difference (OPD) as (Equation 1.5):

$$\mu_{RS}(OPD) = \exp\left[-\left(\frac{\pi \cdot \Delta\nu}{2c \ln 2} OPD\right)^2\right] \exp\left[-j2\pi\nu_0 \frac{OPD}{c}\right] \quad Eq.1.5$$

where $\Delta\nu$ represents the spectral width of the source in the optical frequency domain, and ν_0 is the central optical frequency of the source. The Gaussian envelope, i.e. the modulus of the complex degree of coherence, is modulated in amplitude by an optical carrier. The peak of this envelope locates a backscatter center. The amplitude of the peak will depend on the nature (volumetric or surface), the reflectivity, the size, the position and shape of the backscatter element, as well as, on the irradiance level of the light at this point and on the wavelength. The interference of both partially coherent light beams can be expressed in terms of an interference term for every position of the scanner (θ, φ) .

Replacing the complex degree of coherence in the AC intensity of Equation 1.4 and neglecting the structure factor the Equation 1.5 takes the following form (Equation 1.6):

$$I_{AC}(\theta, \varphi, OPD) = \sum_n 2\sqrt{I_R I_S^{(n)}} \exp\left[-\left(\frac{\pi \cdot \Delta v}{2c \ln 2} OPD_n\right)^2\right] \cdot \exp\left[-j2\pi\nu_0 \frac{OPD_n}{c}\right] \quad Eq.1.6$$

The influence of the bandwidth is illustrated in Figure 1.4, for two Gaussian spectra (5 nm, and 20 nm bandwidth) showing how the location where a scattering event occurs is determined.

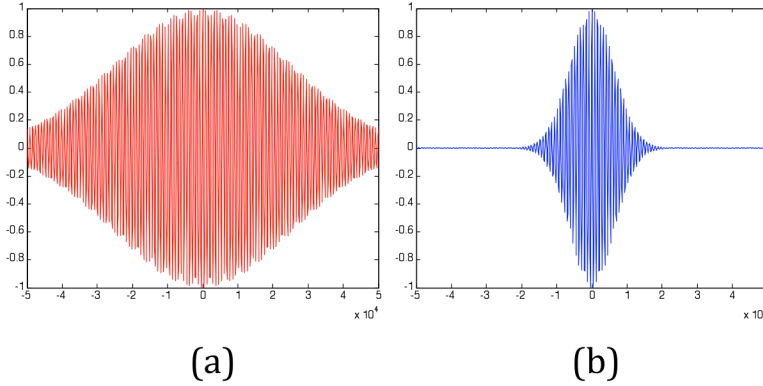


Figure 1.4. Influence of the bandwidth of the spectrum in the determination of the sample position. The AC component obtained for a Gaussian spectrum with a 5-nm bandwidth (a) a 20-nm bandwidth (b).

This Equation is valid for a quasi-static mirror that travels along the axial axis. The detectors used in TD-OCT are photodiodes, i.e. broadband sensors with noise distributed along all their bandwidth [Frieden, 1985]. The sources of noise are: shot, thermal (or Johnson) noise and excess noise depending on the sensor type (photodiode or avalanche photodiode) [Agrawal, 2002, Osche, 2002, and Ramawami, 2002]. Essentially, the dependence of the noise is linear with respect to the irradiance impinging on the detector, with the frequency of the noise inversely related to noise power. As the signal provided by the scatterers is very weak, the time domain OCT typically uses the heterodyne optical detection. This technique is very common in coherent optical communications [Agrawal, 2002] to remove the noise and to amplify weak optical signals. It consists of the combination of a weak signal with a frequency ν_0 with a strong local oscillator with a different optical frequency ν_1 to obtain a beat or intermediate frequency $\nu_1 - \nu_0$. This provides a benefit in terms of gain since: (1) The amplitude of the down-mixed difference frequency can be larger than the amplitude of the original signal itself; (2) The difference frequency signal is proportional to the product of the amplitudes of the

local oscillator and signal electric fields. Thus, the larger the local oscillator amplitude, the larger the difference-frequency amplitude. Hence, there is gain in the photon conversion process itself. In terms of noise reduction, one of the advantages of heterodyne detection is that the difference frequency is generally far (in a spectral sense) from the potential noise radiated during the generation of either the signal or the local oscillator signal. Thus, making the spectral region near the difference frequency relatively noise-free. Hence, narrow electronic filtering near the difference frequency is highly effective at removing the remaining, generally broadband, noise sources. The application of heterodyne detection to OCT is straightforward, assuming that the local oscillator is the reference arm and the weak signal to be amplified is the reflected signal from the sample. The simplest way of achieving a heterodyne detection is by inducing a Doppler effect by scanning axially one arm of the interferometer, so that the frequency of the modulation is controlled by the speed of scanning. The Doppler-shifted optical carrier has a frequency expressed by Equation 1.7

$$f_D = \frac{2\nu_0 v_s}{c} \quad Eq.1.7$$

where ν_0 is the central optical frequency of the source, v_s is the scanning velocity of the pathlength variation, and c is the speed of light.

Depending on the speed of the axially scanning mirror, the beat frequency falls in the electrical domain, which allows applying standard analogical band pass filters for isolating a very small region, what improves the SNR, since less power spectrum of noise is taken into account. Besides, the "law square" property of photodetectors prevents the requirement of performing a Hilbert transform, so that only a rectification of the signal is needed (changing the signal from positive to negative). The heterodyne detection is illustrated in Figure 1.5, where the signal as it is produced by the photoreceiver is shown 1.5.a. Figure 1.5.b shows the electrical signal after a narrow bandpass filter, and Figure 1.5.c shows the rectification operation.

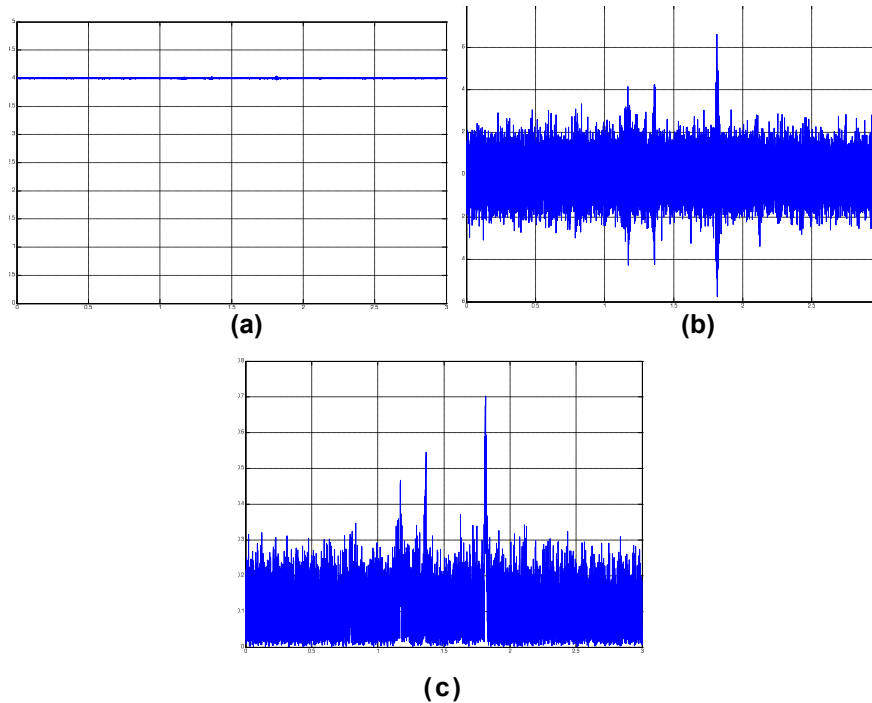


Figure 1.5. Signal produced by the photoreceiver of a TD-OCT b) Electrical signal after a narrow band bass filter. C) Signal result after the rectification process.

1.3.2. Fourier-Domain Optical Coherence Tomography

Fourier domain OCT (FD-OCT) was first demonstrated in 1995 by Fercher [Fercher et al 1995]. In contrast to TD-OCT, the setup involves a reference arm held fixed. The optical path length difference between sample and reference reflections is encoded by the frequency of the interferometric fringes modulating the power spectrum of the light source. Regardless of whether the spectrum is sampled in position across an array detector or in time, the frequency of the interferometric fringes as a function of spectrum encodes the location of the scatterer, with increasing frequency corresponding to larger optical path length mismatches. Two configurations have prevailed in Fourier domain systems: spectral domain (SD-OCT) uses a grating to spatially disperse the spectrum across an array-type detector [Wojtkowski et al, 2003, Häusler et al, 1998, and Park et al 2005], and swept source (SS-OCT) where a narrow band laser is swept across a broad spectrum, encoding the spectrum as a function of time [Chinn et al, 1997, Yun et al, 2003, and Choma et al, 2005].

Spectral Domain OCT

The SD-OCT essentially consists of a Michelson interferometer, which uses a broadband light source to produce the partial coherence

interferometry, and a spectrometer for decoding the spectral interferogram. The basic configuration of a spectrometer is shown in Figure 1.6, and it consists of a diffraction grating to separate the spectrum of light, of a lens to collect the dispersed light and of a linear array sensor (linear CCD or CMOS camera).

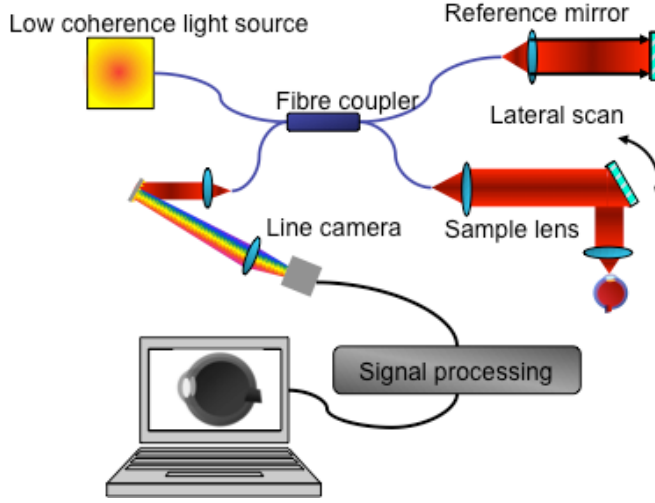


Figure 1.6. Schematic diagram of a sOCT based on a fiber optic Michelson interferometer.

If a population of n scatters is illuminated by an incoming beam, as in the PCI, the measured interferometric signal is the combination of n interferograms multiplied by the source spectrum. The resultant interferogram can be expressed as the sum of two non-interferometric spectral artefacts or DC terms, a cross correlation term, and an autocorrelation artefact.

$$I(k) \propto S(k) \left\{ I_R + \sum_n I_S^{(n)} + 2\sqrt{I_R} \sum_n \sqrt{I_S^{(n)}} \cos(2kOPD) + \right. \\ \left. 2 \sum_n \sum_{n \neq m} \sqrt{I_S^{(n)} I_S^{(m)}} \cos(2kOPD) \right\} \quad Eq.1.8$$

where $I(k)$ is the detector photocurrent being $k = 2\pi/\lambda$, $S(k)$ the source power spectral density, I_S the intensity from the reference arm, $I_S^{(n)}$ the backscattered intensity of the n th scatterer, and OPD is the optical path difference. The back-scattered axial profile can be obtained performing a Fourier transform. The procedure is illustrated in Figure 1.6 for a collection of three scatters located at different points of a depth profile. The mathematical properties of the Fourier transform allow the estimation of an A-scan, where each delta-function

corresponds to the depth location of a sample reflector. As a consequence of the symmetry properties of Fourier transform, a complex conjugate image is generated.

Swept Source OCT

The SS-OCT is based, as the Spectral Domain, in Wolf's solution to the inverse scattering problem, but instead of encoding the frequencies in space they are encoded in time. This allows overcoming the main drawbacks of the SD-OCT, which are the sensitivity drop-off, and the resolution imposed by the finite size of the pixels of the camera, which removes the contribution of the higher frequencies. The setup essentially consists of a Michelson interferometer, which uses a narrow band laser, which is swept in time across a broad spectrum, for producing the partial coherence interferometry, and a photodetector for converting the temporal encoded light into an A-scan (Figure 1.7).

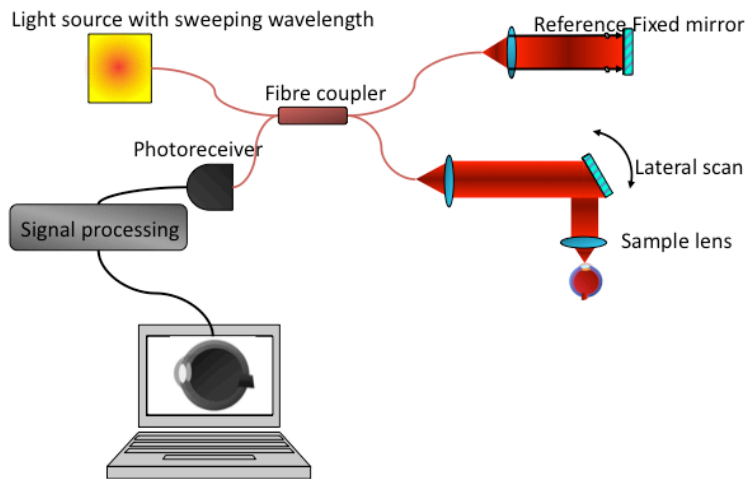


Figure 1.7. Schematic diagram of a SS-OCT based on a fiber optic Michelson interferometer.

In SS-OCT the wavenumber is parameterized in time by using the relationship between wavenumber and time. Assuming a starting wavenumber k_0 , the temporal variation can be expressed as the central wavenumber plus the contribution of the non-linear sweeping speed: $k(t) = k_0 + t dk/dt$. Introducing this definition in the previous expression for the interference and performing some algebra, the terms can now be transformed as a function of time as follows:

$$I(k) \propto S(k) \left\{ I_R + \sum_n I_S^{(n)} + 2\sqrt{I_R} \sum_n \sqrt{I_S^{(n)}} \cos(\omega_S^{(n)} + \phi_S^{(n)}) + \right. \\ \left. 2 \sum_n \sum_{n \neq m} \sqrt{I_S^{(n)} I_S^{(m)}} \cos(\omega_S^{(nm)} + \phi_S^{(nm)}) \right\} \quad \text{Eq.1.9}$$

where the angular frequencies $\omega_S^{(n)} = OPD^{(n)} dk/dt$ are the instant value of the cross-correlation, and $\phi_S^{(n)} = k_0 OPD^{(n)}$ is a non-dimensional parameter that expresses the phase shifting produced by a scatter centre. The variable $\omega_S^{(nm)} = OPD^{(nm)} dk/dt$ represents the instant value of the auto-correlation between scatters. Finally, $\phi_S^{(nm)} = k_0 OPD^{(nm)}$ is the phase shifting introduced by the distances between scatter centers. As in SD-OCT, the depth profile is obtained by means of a Fourier Transform, but now using the conversion between time and wavenumber, similarly, an echo artefact image is produced, which needs to be removed.

1.3.3 Comparative performances of different OCT modalities

Choma et al [Choma et al, 2003] developed a comprehensive analysis of the sensitivity of the different OCT modalities, and concluded that Fourier Domain OCT technologies are 20-30 dB more sensitive than TD-OCT. However, it is important to note that the theoretical SNR gain of SS-OCT and FD-OCT compared to TD-OCT derived above rests upon the assumption of shot noise-limited detection in each detection channel. The effective gain of current SD-OCT systems working with CMOS cameras, in comparison with TD-OCT is 10 dB, instead of the 20-30 of the theoretical gain. This lower sensitivity is due to the use of CMOS cameras in the detection process, which are faster than other detector types, but their higher readout noise reduces the theoretical gain in SNR. This it is not the case of the SS-OCT, since it uses PIN detectors for detection and the increase in sensitivity is maintained.

In terms of speed, as FD-OCT does not have any scanning mirror, the mechanical limits present in the TD-OCT technology are overcome, producing acquisition speeds hundreds or even thousands times larger than in TD-OCT. As example, the maximum acquisition speed of TD-OCT is around one thousands of A-Scans/s, while for the Fourier Domain the speed can reach more than one hundred thousands A-Scans/s.

However, Fourier Domain technologies have some drawbacks. In the case of the SD-OCT the main drawback is the sensitivity drop-off. The SNR drop-off in SD-OCT systems is caused by the finite wavelength resolution during the signal acquisition. In the SS-OCT systems, the

linewidth corresponding to each wavenumber is so small that this factor can be neglected. The SNR drop-off in SS-OCT systems is mainly caused by the nonlinearities in the wavenumber scan. Usually the nonlinearities in the swept source are not conspicuous, so the SNR drop-off is not prominent, and therefore can be ignored over the depth scan range. SS-OCT is the fastest, more extended scan range and with the highest sensitivity, although its main drawback to date is the intrinsic instability of the light sources.

1.4. Anterior segment optics and anatomy

The two main optical element of the eye (cornea and lens) refract the light, projecting images of the outside world onto the retina. From an anatomical point of view the anterior segment can be defined as all the former structures preceding to vitreous body of the eye (Figure 1.8): The tear film, cornea, iris, ciliary body and the lens. The cornea and crystalline lens project the images of the outside world onto the retina. The diameter of the incoming beam of light is controlled by the iris, which contracts and dilates when needed (myosis and mydriasis).

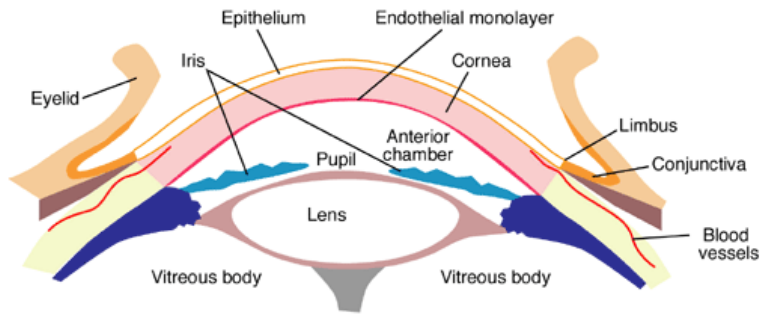


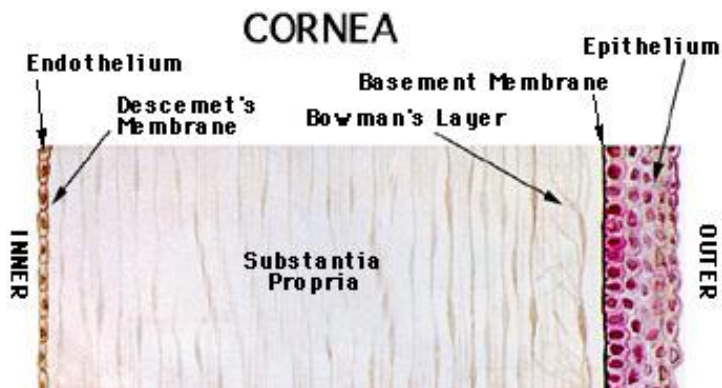
Figure 1.8. Anatomical cross-section of the anterior segment of the eye.

1.4.1 Tear film

The tear film can be defined as the liquid layer covering the cornea and conjunctiva. Its thickness can be considered between the range from 7-10 μm [Kaufmann, 1998, and, Prydal et al, 1992a]. The effective refractive index of the tear film is generally taken as 1.3367 [Prydal et al, 1992b]. Functionally speaking, the lipid layer helps to create a smooth outer layer thanks to the mechanical stability provided by the superficial tension of lipids that fills in the irregularities of the cornea, increasing its optical quality. Besides, it traps and flushes out foreign bodies and chemicals, and reduces the surface friction associated with eyelid blinking and eye movement. Finally, lipids preserve the liquid to be evaporated.

1.4.2. Cornea

The cornea is a quasi-transparent tissue (since it has no blood vessels) vault-shaped window placed at the front of the eye. It is composed of 5 main layers: epithelium, Bowman's membrane, stroma, Descemet membrane and endothelium (Figure 1.09). The cornea contributes to around two thirds of the power (around 40 diopters) of the relaxed eye. Although the anterior corneal surface is not a smooth surface due to its cellular structure, an optically smooth surface is achieved with a very thin tear film, which covers the cornea. The posterior surface of the cornea is less important in optical terms and subtracts around 6 diopters to the power of the cornea due to the lower refractive index in the aqueous humor.



http://files.fuchssupport.info/DLEK_definitions.htm

Figure 1.09. Histology of cornea section, with its five layers: Epithelium, Bowman's layer, Stroma (Substantia propria), Descemet Membrane and Endothelium.

Refractive Index

The refractive index of the cornea is considered generally as homogeneous with an accepted value of 1.376. Some authors have addressed the change of corneal refractive index with wavelength [Sivak et al, 1982] or described the cornea as a gradient structure. [Patel et al, 1995 and Barbero et al, 2006].

Corneal Shape

The average shape of the cornea is a not spherical meniscus but flattens in the periphery. It is commonly accepted that its shape can be represented as a conic [Atchison, 2000b], or a conicoid in 3D.

Equation 1.10 provides the analytical expression for a conicoid [Malacara, 1988], where ρ are the polar coordinates, z is the axial coordinate, R is the radius of the surface and Q the conic constant.

$$\rho - 2zR + (1+Q)z^2 = 0 \quad Eq.1.10$$

The cornea has been widely studied due to its accessibility. The first studies were performed on anterior corneal surface with keratometers. First proposed in 1779 by Ramsden, this device can only be applied to a very limited and central region of the cornea. Later in 1864 Donders provided the first anterior corneal data in males and females. Later, other authors used different generations of keratometers to characterize the anterior radius of the cornea [Sorsby et al, 1957, Kiely et al, 1982, Guillon et al, 1986, Patel et al, 1993 and Lam et al, 1997]. In 1948 Stenstrom published a study based on Roentgenology, using X-rays, to determine the axial length of the eye and the radius of curvature of the anterior surface of the cornea. Also slit-lamps have been widely used for evaluating the anterior and posterior corneal radii [Lowe and Clark, 1973, Dunne et al, 1992 and Garner et al, 1997] founding similar radii for the anterior corneal radius. Finally, Dubbelman et al used a Scheimpflug camera provided with correction algorithms to compensate the refraction of the anterior corneal surface [Dubbelman et al, 2002]. Placido disk based videokeratoscopes are the most widely used devices clinically today to measure corneal shape. The technique was first introduced by Javel in 1884 as an attempt to increase the sampled cornea area in comparison with keratometers. Later Studies from reported average central corneal power of $43.50D \pm 1.50D$ [Dingeldein et al 1989, Bogan et al 1990 and Rabinowitz et al in 1996]. Table 1.1 summarizes, in chronologically, reported values of the anterior corneal radius of curvature and asphericity using different devices.

Table 1.1. Chronological summary of anterior corneal shape reports

Author	Year	Method	Number of Eyes	Radius (mm)	Asphericity(Q)
Donders	1864	Keratometer	38 females	7.80	-
			79 males	7.86	
Stenstrom	1948	Roentgenology	1000	7.86±0.26	-
Sorsby	1957	Keratometer	194	7.82±0.29	-
Townsley	1970	-	350	-	-0.30
Mandell and St Helen	1971	-	8	-	-0.23
Lowe and Clark	1973	Slit Lamp	92	7.65±0.27	-
Kiely	1982	Keratometer	176	7.72±0.27	-0.26 ±0.18
Guillon	1986	Keratometer	220	7.77±0.25	-0.15 ±0.2
Royston	1990	Slit lamp	15	7.77	-
		Purkinje		7.77	-
Bogan	1990	Placido disk	212		
Patel	1993	Keratoscope	20	7.68±0.40	-0.01±0.25
Eghbali	1995	Videokeratoscope	41	7.67±0.20	-0.18±0.20
Rabinowitz	1996	Placido disk	195	7.75±0.25	-
Lam	1997	keratometer	60	7.80±0.25	-
Douthwaite	1999	Videokeratoscope	98	7.86±0.27	-0.21 ±0.10
Dubbelman	2002	Scheimpflug	83	7.87± 0.27	-0.18±0.18

There are few studies in the literature evaluating the posterior corneal shape. Some studies reported values using a slit-lamp [Lowe and Clark, 1973 and Royston et al, 1990], a larger number of studies used the Purkinje imaging to estimate the posterior radius of curvature and in some cases the asphericity [Royston et al, 1990, Dunne et al 1992, Edmund et al, 1994 and Garner et al, 1997]. Other studies using modified keratometers reported values of radius and asphericity. However, the most comprehensive study was performed by Dubbelman where a corrected Scheimpflug camera for optical distortion was used

to provide the values of posterior radius and asphericity [Dubbelman et al, 2002]. Table 1.2 summarizes, in chronologically, reported values of the posterior corneal radius of curvature using different devices.

Table 1.2. Chronological summary of posterior corneal shape reports.

Author	Year	Method	Number of Eyes	Radius (mm)	Asphericity(Q)
Lowe and Clarck	1973	Slit Lamp	92	6.46±0.26	-
Royston	1990	Slit lamp	15	6.35	-
		Purkinje		6.40	-
Patel	1993	Keratometer & Pachymetry	20	5.81±0.41	0.42
Dunne	1992	Purkinje	80	6.44	0.36
Edmund	1994	Purkinje	-	6.71±0.23	0.35
Garner	1997	Purkinje	120	6.42±0.31	-
Lam	1997	Modified keratometer	60	6.51±0.40	0.35
Dubbelman	2002	Scheimpflug	83	6.40 ± 0.28	0.38±0.27

Corneal Thickness

Corneal central thickness has been widely studied using different clinical instruments and techniques. Average reports from Ultrasonography range from 545 and 555 μm [Lackner et al, 2005, Amano et al, 2006 Hashemi, 2007 and Kim et al, 2007]. Scanning slit cameras provided average values from 527 to 580 μm . Clinical Scheimpflug camera provided ranges from 534 to 561 μm [Buehl et al, 2005, Lackner et al, 2005, Amano, 2006, Rosa et al, 2007, Kim et al, 2007, Matsuda et al, 2008, Menassa et al, 2008, Doors et al 2009 and Bernilla et al, 2009]. Anterior segment OCT has also used for this purpose providing an average value of 525 μm [Kim et al, 2008].

1.4.3 Iris

Overlying the lens, the iris is a structure made of thin elastic tissue with an opening in the center which is surrounded by a circular muscle called a sphincter [Gold et al, 2010]. It is responsible for controlling the

diameter and size of the pupils and the amount of light reaching the pupil. In response to the amount of light entering the eye, muscles attached to the iris expand or contract the aperture at the center of the iris, known as the pupil. The backside of this tissue is made up of cells containing brown pigment which acts to absorb light as well as prevent its scattering within the eye. As the pupil gets smaller in bright light, optical quality is primarily affected by diffraction and to a lesser extent by the optical aberrations of the eye. [Campbell et al, 1960]. There is also a relationship between the pupil size and the accommodation. As pupil size is reduced, the amplitude of accommodation is increased, approaching a fixed intermediate resting focus corresponding to approximately 1 m [Hennessy et al, 1976].

1.4.4. Lens

Histologically, the lens consists of three components: capsule, epithelium, and lens substance (Figure 1.10). The crystalline lens is composed of multiple layers of long, fiber cells that originate from the equator and stretch toward the poles of the lens. At the point where the cells meet, they form suture patterns. In the human, the embryonic lens has “Y” sutures, but as it ages, the suture patterns in the new layers become increasingly more complex, forming suture patterns that have a starlike appearance [Koretz et al, 1994].

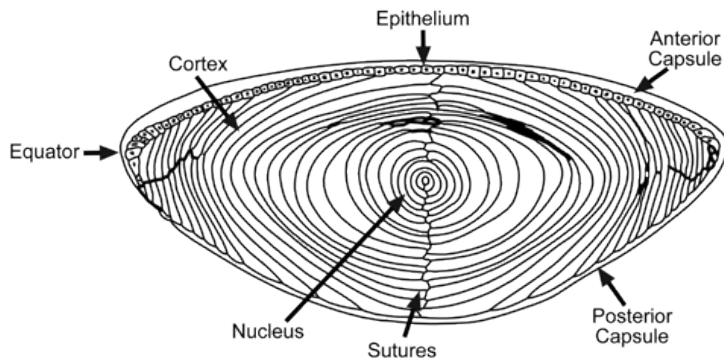


Figure 1.10. Illustration of the histology of the crystalline lens, including its layers: Epithelium, Anterior Capsule, Cortex, Nucleus, Sutures and posterior capsule.

The crystalline lens is a biconvex lens with aspheric surfaces. The lens is contained in the capsule which is a transparent membrane attached to the ciliary body by the zonules. In the crystalline lens, there is a layer of epithelial cells that extend from the anterior pole to the equator. This lens epithelium is responsible for the continuous growth of the lens throughout life with new epithelial cells forming at the equator. These cells elongate as fibers, which under the capsule and epithelium, meet at the sutures of the lens originating its characteristic onion-like layered

structure. The different concentration of a type of proteins produces changes in the refractive index across layers, being modeled modeled as a gradient index of refraction and commonly named as GRIN. From the beginning of 20-th century this change in refractive index has been introduced in model eyes [Helmholtz, 1924] using the values reported by Freytag among others [Freytag, 1907]. Different models have been proposed to describe this gradient index as, for instance, a large number of shells with different curvature [Pomerantzeff et al, 1971] or by modeling the crystalline lens with elliptical or bielliptical models that have been used [Smith et al, 1991, Atchison et al, 1995, and Al-Hadali et al 1995]. A later study proposed a parametric model where anterior and posterior hemispheres did not intersect at the equator but on a conicoid surface [Navarro et al, 2007]. The GRIN has also been described by functions: the first study modeled it as a four free parameters of a power Equation [Smith et al. 1992], or as a fourth-order Equation [Goncharov et al, 2007], or by sinusoidal functions [Diaz et al 2008 and 2011]. More recently, Campbell proposed the use of a shell model to account realistically the anatomy of the lens [Campbell 2010]. In 2010 Manns used a simple model similar power function to Smith [Manns et al, 2010]. Finally, de Castro introduced polynomial and power models together with genetical algorithms to estimate the variation of refractive index in humans lenses with aging from OCT images [de Castro et al, 2012], and found index variation ranged from 1.434 to 1413 in the nucleus to 1.386 to 1.376 in the lens cortex with a monotonic decrease in the young lenses, and a plateau-like function in the old lenses in agreement with previous mwasurements using Magnetic Resonance Imaging [Moffat et al, 2002b].

The first systematic studies of the shape of the *in vivo* crystalline lens were performed using phakometry systems. Most previous phakometric techniques were limited to the estimates of radii of curvature either from indirect measurements of light reflections from the lens surfaces (Purkinje imaging). Several algorithms [Smith and Garner, 1996; Garner, 1997] have been proposed to estimate the radii of curvature of the anterior and posterior surfaces, as well as, tilt and decentration of the lens with respect to the pupillary axis of the eye. Different works [Wulfeck, 1955; Sorsby et al., 1961; Veen and Goss, 1988; Phillips et al., 1988; Mutti et al., 1992; Rosales and Marcos, 2006; Taberbero et al., 2006; Rosales et al., 2008; Atchison et al., 2008] have studied the shape, power, and tilt and decentration of the crystalline lens using Purkinje images.

Scheimpflug cameras provide images of the full anterior segment. It is well known that the structures imaged through others suffer from

optical distortion. Correction of the images with the approximation of a constant refractive index in the lens have allowed the study of the shape of the crystalline lens and its change with age and accommodation [Brown, 1973a, 1974; Koretz et al., 1984, 2001; Dubbelman et al., 2003, 2005b; Rosales et al., 2006a and b; Rosales and Marcos, 2009].

Magnetic resonance imaging [Koretz et al., 2004] and ultrasound-based techniques [Silverman, 2009] have also been used to evaluate the lens. However their resolution is typically too low to fully characterize lens shape quantitatively.

In vivo measurements have shown that the anterior and posterior surface of the radii of curvature of the unaccommodated crystalline lens surfaces with age. This decrease is larger in the anterior surface (ranging values from around 12 mm in 20 year old subjects to 9 mm at 70) than in the posterior (ranging 6.5 mm at 20 to 5.5 mm in 70 year old subjects). The thickness increases with age from around 3.5 mm in young subjects to more than 4.5 mm in old subjects. If the index of the lens was homogeneous, this would result in an increase of power of the lens, yet there is not a tendency for myopia (so called lens paradox [Brown, 1974]). The changes in the GRIN distribution with age may be the reason behind the effect [Moffat et al., 2002b]. Table 1.3 summarizes *in-vivo* reported values of the radius of curvature of the anterior and posterior lens, using different techniques.

Table 1.3. Chronological summary of studies about radius of curvature of *in-vivo* lens shape.

Author	Year	Method	Number of Eyes	Anterior Radius (mm)	Posterior Radius (mm)
Lowe	1972	Slit Lamp	92	10.29±1.78	-
Brown	1974	Slit Lamp	200	12.40±2.60	8.10±1.60
Dubbelman	2001	Scheimpflug	65	9.00-14.00*	4.70-7.00*
		Scheimpflug	62	13.95±0.86	6.07±0.10
Koretz	2004	MRI	25	13.48±1.21	5.63±0.14
		Purkinje	46	10.95±1.10	6.7±0.8
Rosales	2006	Scheimpflug	17	11.10±1.10	6.10±0.55
		Purkinje		12.70-8.81	5.64-7.09

*Range of measurements

The measurement of the asphericity of the lens surfaces *in vivo* is still a challenge since the image of the crystalline lens is limited by the

diameter of the iris. Phakometry is generally limited to radii of curvature measurements only. Scheimpflug imaging has additional pupillary limitations to the visualization of the lens posterior surface. In addition, posterior asphericity estimates are limited by the assumption of constant refractive index in the lens. As mentioned above, the resolution of MRI is poor to attempt conic fittings of the lens surfaces. Brown [1973a, 1974] published data obtained from Scheimpflug images and reported that the curvature of the anterior lens surface decreased towards the periphery, while the posterior surface steepened toward periphery. In a more recent work Koretz et al. [1984] found a good fit of the surfaces using parabolas. Dubbelman and van der Heijde [2001] found that both anterior and posterior surface were hyperbolic, i.e. lens surface steepened towards periphery. To our knowledge, only Dubbleman et al. [2001a and b] reported lens asphericity measured *in vivo* from Scheimpflug imaging, also providing age-related expressions.

Equivalent Refractive index

The equivalent refractive index of the crystalline lens can be defined as the refractive index of a homogeneous lens with the same shape and dioptric power of the crystalline lens. Glasser and Campbell found no age dependence of the *in vitro* lens equivalent refractive index [Glasser et al, 1998]. Borja measured the focal length of a crystalline lens *in vitro* using a commercial lens meter and a custom developed optical system based on the Scheiner principle and, despite significant variability, found a decrease in the equivalent refractive index, as a function of age [Borja et al, 2008]. The change of the index of the crystalline lens index of refraction indicates that the change of the crystalline lens optics with age is not only due to the change of its shape but also to changes in the GRIN distribution. The relative surface refractive contribution is still under discussion. Borja et al. found that surfaces contribute only with a 40% to total lens power. This percentage was found to be nearly constant for the different age groups.

The *in vivo* equivalent refractive index was estimated *in vivo* in unaccommodated crystalline lenses with Scheimpflug [Dubbelman and van der Heijde, 2001] and Purkinje images [Garner and Smith, 1997; Atchison et al., 2008]. These studies also found a decrease in the equivalent refractive index with age, as reported *in vitro*.

Accommodation

First proposed by Helmholtz in 1855 [Helmholtz, 1855], the accommodation is an increase in the dioptric power of the eye that

enables the image of near objects to be focused on the retina. This is produced by the ciliary body relieving or releasing tension on the zonulae, connected to the elastic capsular bag which molds the lens into a more or less accommodative form. When the ciliary body contracts, the zonulae ligaments relax. This allows the lens to thicken, increasing the eye's ability to focus up close. When looking at a distant object, the ciliary body relaxes, causing the suspensory ligaments to contract. The lens becomes thinner, adjusting the eye's focus for distance vision. Studies *in vivo* on the change of the lens surfaces with accommodation [Koretz et al., 1984; Dubbelman et al., 2003, 2005a; Rosales et al., 2006, 2008] showed average changes in anterior and posterior radii, from around 12 and 6.5 mm (relaxed accommodation) to 7.5 and 5 mm (fully accommodated lens) respectively, and changes in lens thickness of around 0.5 mm over a 6 D accommodative range [Glasser et al, 1998 and 1999a,b].

1.4.5. Anterior Segment conditions studied in this thesis.

Ocular conditions and two specific treatments were monitored in this thesis, using the methods developed: Keratoconus and cataracts, and their treatment by intrastromal Rings Segments (ICRS) and Accommodative Intraocular Lenses (A-IOLs).

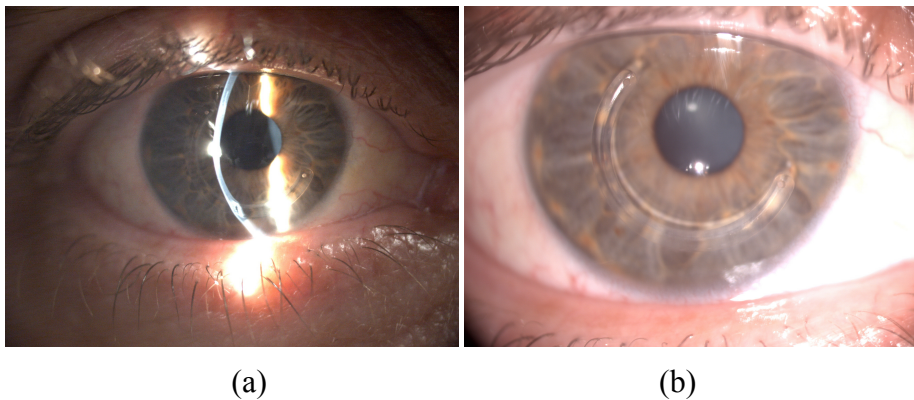


Figure 1.11. (a) Illustration of the keratoconus disease. (b) Implanted Intracorneal rings segments in a keratoconic cornea. Courtesy of Nicolas Alejandro, Fundación Jiménez Díaz, Madrid.

Keratoconus

This corneal condition is characterized by progressive, asymmetric, chronic and usually bilateral corneal disorder that affects the shape and the structure of the cornea, causing significant reduction in visual performance (Figure 1.12a). The progressive change of corneal geometry, steepening of both corneal surfaces and thinning, alters the

optical properties of the cornea, resulting in increase of corneal aberrations and decrease of visual quality, [Rabinowitz et al, 1998]. The significant increase of corneal astigmatism is the consequence of changes occurring in the corneal surfaces and structure. The estimated prevalence is about 1 per 2000 in the general population.

The hallmark of keratoconus is the presence of astigmatism and high order aberrations particularly coma, which cannot be corrected with conventional spectacles or rigid contact lenses. Patients in early stages of the disease are typically fitted with rigid contact lenses to compensate for the increase corneal asymmetry. In advanced stages, keratoplasty (corneal transplant) is frequently needed. Recently, alternative treatments aim at preventing or delaying corneal transplant. These include UV corneal collagen cross-linking and intrastromal ring (ICRS) implantation. Both treatments are under study in our laboratory. In Chapter 8, we evaluated patients implanted with ICRS (Ferrara et al, 1995, Colin et al, 2000, Siganos et al, 2002 and Alió et al, 2002) (Figure 1.11b).

Cataracts

The age-related increase of crystalline lens opacification, known as cataract, occurs as a result of the increase of the molecular weight of the lens proteins [Benedek et al, 1971], which leads to increased light scattering, producing the loss of the contrast and visual performance (Figure 1.12a).

In this thesis, the developed technology has been used to image and quantify the anterior segment of cataract patients, before surgery and after implantation of intraocular lenses. Cataract surgery has benefited significantly from technological advances. While eliminating the intraocular diffusion produced by the cataract is still the reason for the procedure, advances in optical measurements and intraocular lens (IOL) design have improved refractive outcomes, with recent designs actually aiming at correcting the corneal spherical aberration (Figure 1.12b). In addition to monofocal IOLs, advances have also been made in multifocal and accommodative IOL design. Accommodative lenses have been designed to allow vision at near, intermediate and far distances. These lenses rely on certain muscles in the eye to move the IOL forward and backward, thereby changing the focus.

Previous *in vivo* addressed the impact of IOL tilt and decentration on optical quality and found that the optical quality it is greatly related on an actual combination of tilt and decentration is critical, suggesting that the conclusions raised from *in vitro* models or computer models are of

limited value in they do not consider real measurements. Customized computer eye models built using individual anatomical data from patients allow accurate optical predictions and understanding of the contributing factors to optical degradation in eyes implanted with IOLs. In this regard, the capability of extracting topographies and biometry from the 3D data provided by the customized eye models. These accurate parameters are of particular interest in the evaluation of accommodative IOLs as it will be presented in chapter 10 of this thesis.

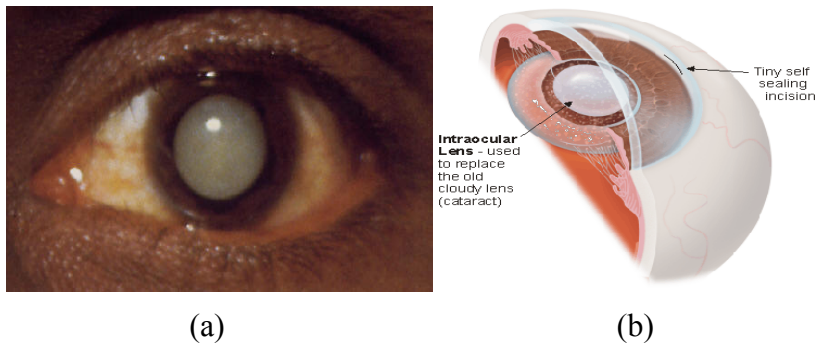


Figure 1.12. (a) Photograph of a patient with a cataract. (b) Implanted Intra ocular lens used to replace the cloudy lens

1.5. State of the art of anterior segment imaging.

There is a broad range of instruments capable of offering data from the anterior segment. In what follows we provide a brief review of existing technologies, currently used to quantitatively assess the optical and geometrical properties from the anterior segment of the eye.

1.5.1 Biometry

The axial length of the eye and the anterior chamber depth, along the foveal axis, are generally measured with ultrasound or low coherence interferometry. These measurements are widely used in the clinical practice, in monitoring refractive error development, as well as in cataract surgery planning, as an accurate estimation of axial length is key for optimal selection of IOL power

Ultrasonography: The physical principles that rule the ultrasounds technique [SantoDomingo-Rubido et al, 2002] rely on generating an acoustic wave typically at 10 Mhz. As the wave passes through the eye it strikes at the different interfaces present on the ocular tissue. The speed of the wave depends on the density of the medium, the stiffer the medium is the faster the wave is propagated. The amplitude of the echo depends on two factors: the relative difference of densities between media and the orientation of the interface with respect to the propagation vector of the wave. There are two ways to perform the

ultrasonography, by immersion (the gold standard) with a reported accuracy up to 0.03 mm at best, and by contact, with reported accuracy of 0.1 mm. Figure 1.13 shows an example of an A-Scan obtained by a clinical instrument.

Optical biometry: The physical principles that rule the device, a partial coherence interferometer, have been discussed in larger depth in section 1.2 [Fercher et al, 1988]. As discussed the accuracy depends on the bandwidth of the light source, but commercial devices reported accuracies of 0.02 mm. Figure 1.13 shows an example of an A-Scan obtained by the IOL Master.

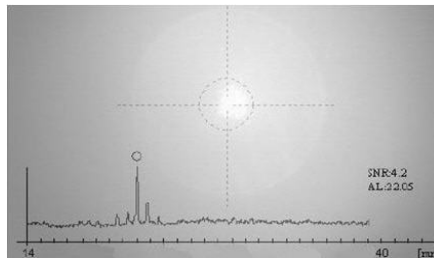


Figure 1.13. Example of an A-Scan obtained from an IOLMaster.

1.5.2 Anterior segment characterization

Purkinje: Purkinje images are reflections of the light from anterior and posterior corneal surfaces, first and second, Purkinje images (PI and PII), and from anterior and posterior crystalline lens surfaces, third and fourth Purkinje images, (PIII and PIV). Purkinje images I, III and IV can be captured by imaging the eye's pupil, as they are formed close to the pupillary plane. Purkinje imaging has been used to measure the radii of curvature of the crystalline lens (phakometry), as well as to measure tilt and decentration of crystalline and intraocular lenses. Purkinje-based IOL misalignment measurements rely on the proved assumption that there is a linear relationship between of the positions of the Purkinje images and the eye rotation [Barry et al, 1994a and b, Rosales et al, 2006a and b]. Figure 1.14.a shows the optical lay-out of a Purkinje imaging system. Figure 1.14.b picture shows the Purkinje images reflected by the anterior segment of a pseudophakic eye.

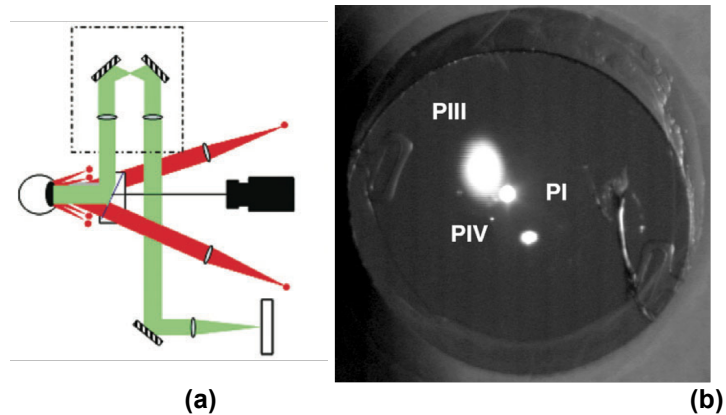


Figure 1.14. a) Optical schema of a Purkinje imaging system. b) Picture of the different Purkinje images reflected by the anterior segment of the eye. Adapted from Rosales and Marcos (2006a)

1.5.3 Corneal Measurements

There is a variety of instruments that provides information on the curvature or power of the cornea. These measurements are key for IOL calculations, refractive surgery or contact lens fitting. The most widespread instruments include keratometers, Videokeratoscopy, and scanning slit rastering.

Keratometers

In these instruments the estimation of corneal curvature are based on the reflection of 2 or more paracentral points, typically 6, on the cornea separated 3-4 mm. Then, the anterior corneal curvature is derived from the convex mirror formula, while the corneal power is estimated empirically based on Snell's law of refraction.

Videokeratoscopy

First proposed by Placido in 1880 and later incorporated by Gullstrand on his ophthalmoscope [Gulstrand, 1896]. This technique consists of projecting black-white disks on the cornea recording the contour lines. The reconstruction of the local elevation (and curvature) is performed by means of triangulation techniques. Knoll et al. [Knoll et all, 1957, knoll et all, 1961] introduced a hemispherical surface for the rings (Fig. 1.15.b). Campbell [1997] placed the hemisphere with its center of curvature at the center of the cornea. A camera acquiring images the reflected coaxial rings with variable width and spacing, with radial lines all passing through the center of the photographed rings, the profiles of several meridians are reconstructed.

Scheimpflug-based topographers

First proposed by Scheimpflug in 1904, Scheimpflug systems take advantage of the geometric rule that describes the orientation of the plane of focus of an optical system (such as a camera) when the lens plane is not parallel to the image plane. These devices use one or more special cameras to achieve greater depth of focus and thus sharp images of the anterior segment. In a normal camera, the 3 planes of the object, lens, and image are all parallel. However, in the Scheimpflug camera, these planes are rotated so that they intersect at a single point or plane to enable greater depth of field. When the slit image is on the cornea, it splits into a specular reflection and a refracted beam that penetrates the corneal surface and is scattered by the tissue of the cornea. An image of the backscattered light from the anterior segment light is formed by an observing imaging system. A Scheimpflug camera records images of the anterior segment of the eye by rotating the slit to obtain cross-sections across 25-50 meridians and reconstructing the maps of the structures. Typical commercial instruments allow cataract densitometry, tomography, anterior chamber analysis, as well as corneal maps (pachymetry, topography and elevation of both the anterior and posterior surfaces of the cornea). However, since the magnification is not constant and each surface is seen through the previous refractive surfaces, the images of the crystalline lens suffer geometrical and optical distortion. Correction of the images with the approximation of a constant refractive index in the lens allowed the study of the shape of the crystalline lens and its change with age and accommodation [Brown, 1973a, 1974; Koretz et al., 1984, 2001; Dubbelman et al., 2003, 2005b; Rosales et al., 2006; Rosales and Marcos, 2009]. Figure 1.15 shows an image obtained with a Scheimpflug camera.

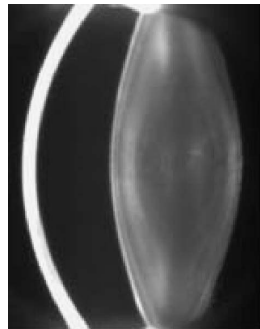


Figure 1.15. Shows an image obtained with a Pentacam camera. Adapted from Rosales and Marcos (2006b)

1.5.4. Imaging systems

These ophthalmic devices are able to image, and map the structures of the anterior segment.

Ultrasound Biomicroscope (UBM)

The first ocular UBM was introduced by Pavlin in 1990 [Pavlin et al, 1990]. In contrast to the conventional ultrasonography, it involves the use of much higher frequencies (35–50 MHz) than those used in ophthalmic B-scanners (10MHz), resulting in an improved reported resolution up to 40 μm . Figure 1.17 shows a cross sectional image of an in-vivo anterior segment collected by an UBM

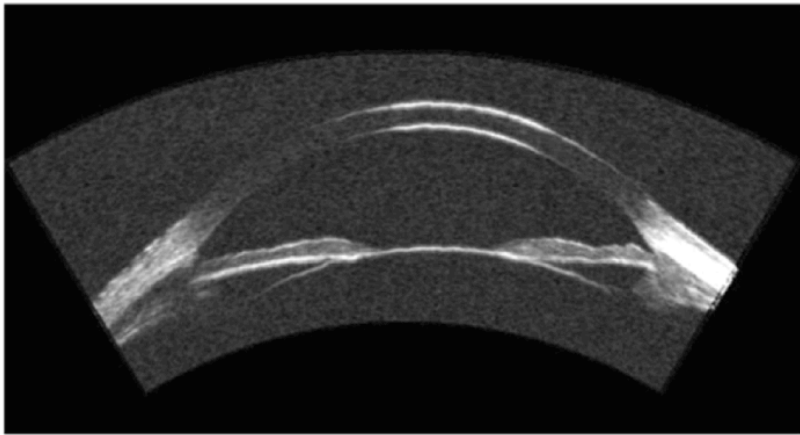


Figure 1.16. Cross sectional image of an in-vivo anterior segment collected by an UBM. Adapted from Silverman (2009)

Magnetic resonance imaging (MRI)

MRI is a non-ionizing technique that allows to visualize the internal structures of the body. The bases of the device rely on the use of a strong magnetic field to align the magnetic moments of the water hydrogen protons, applying a proper electromagnetic (Radio frequency) field, which makes the spin of some of the protons flip. When the exciting electromagnetic field is turned off the relative rates at which the protons decay to the initial state, depends on the tissue, what produces different relative contrasts across the image depending on the tissue structure. MRI systems specifically tuned to image the eye have been used to obtain quantitative information of the eye geometry and anterior segment biometry [Jones et al 2005, and Kasthurirangan, et al, 2011] and assessment of its spatial arrangement. Figure 1.17. shows a cross sectional image of an in-vivo eye globe.

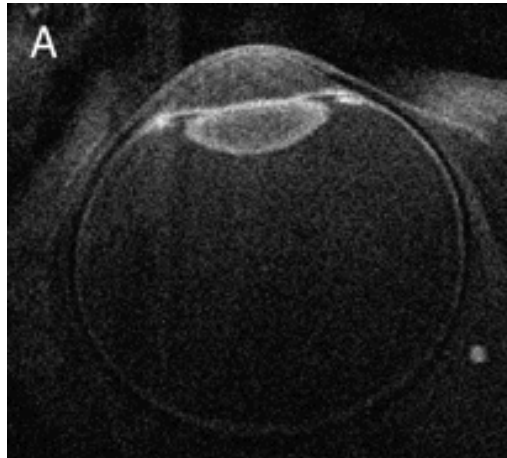


Figure 1.17. Shows a cross sectional image of an in-vivo eye globe. Adapted from Kasthurirangan, et al, (2011).

Wavefront Aberrometers

The optical performance of the human eye is not ideal since the aberrations of the eye's optics degrade contrast and limit the spatial resolution of the images projected on the retina. Wavefront aberrometers measure the deviation of the wavefront from ideal case. Typically, they measure the deviations of the local wavefront normals with respect to the principal ray, across the pupils. The set of deviations (ray aberrations) are proportional to the derivatives of the wave aberrations. Ingoing aberrometers such as the Laser Ray Tracing [Moreno-Barriuso et al, 2001] measure the deviations of rays of light scanned across the pupil, by collecting light reflected back from the retina at every entry pupil location. Outgoing aberrometers such as the Hartmann-Shack [Liang et al, 1994], project a spot of light on the retina and sample the deviations of the wavefront exiting the eye, with a microlens array. Wave aberrations are typically described by a set of Zernike coefficients. Knowledge of the optical surfaces and indices of the ocular components as well as the relative orientation of these surfaces allow computational estimation of the ocular aberrations by virtual ray tracing on customized computer eye models

Optical coherence tomography (OCT)

Anterior segment OCT systems are less common than retinal systems. Commercial systems have been recently introduced, but these are used more for inspection and qualitative analysis than to obtain comprehensive quantitative information of the cornea or lens. The setup proposed by Goldsmith [2005] derived into the first commercial OCT Visante (Carl Zeiss Meditec), which uses a Time Domain

configuration. Other commercially available anterior segment OCT instruments are Fourier domain systems. Some of these commercial devices are combined with other instruments in clinic like Topcon which commercializes an OCT that is combined with a slit lamp, or the Zeiss newest system (Visante Omni) combines an OCT with a Placido disk topography system. Figure 1.19 shows a cross sectional image of the eye up to the anterior lens.

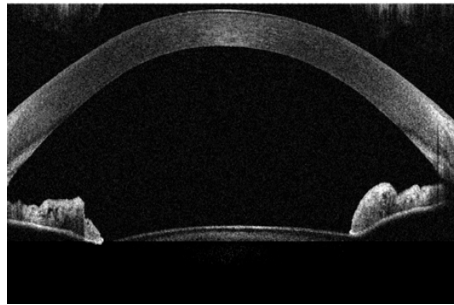


Figure 1.19. shows a cross sectional image of the anterior segment of the eye from the anterior cornea to the anterior lens surface.

1.6 State-of-the art of the OCT Technique

Optical Coherence Tomography was developed in 1991 [Huang et al, 1991], as a non-invasive technique for characterizing surfaces and faint tissue. Since then, the technique has experienced an increasing interest by engineering, research and clinical communities. In that seminal paper, the authors demonstrated the first *in vitro* OCT images of the human retina and coronary arterial wall, suggesting the potential of OCT as a new tool for imaging quasi-transparent or scattered media. The optical sectioning ability of the new device was soon recognized and exploited to image microscopic structures in tissue at depths beyond conventional confocal microscopes. Key benefits of the OCT include: (1) The high resolution of images up to submicron axial resolutions of $0.5\ \mu\text{m}$ in tissue [Pozavay et al 2002]. (2) The required light intensity (fluence) level of non ionizing radiation to illuminate the sample is sufficiently low to be used in sensitive tissue [Swanson et al, 1993].

OCT has been successfully applied in different medical fields. However, it is in ophthalmology where the method has been more extensively applied. To date OCT is both used in retinal and anterior segment imaging.

OCT applications in retinal imaging were the first developed, with the first OCT retinal images reported independently at the University of Viena [Fercher et al, 1993] and MIT [Swanson et al, 1993]. OCT

retinal imaging is specially promising for the diagnosis and monitoring of a variety of macular diseases such as macular edema [Hee et al, 1995, and Hee et al, 1998], macular holes [Hee et al, 1995], central serous chorioretinopathy [Hee et al 1995], aged-related macular degeneration and choroidal neovascularization [Hee et al, 1996], and monitoring of thickness in glaucoma [Schuman et al, 1995].

The Anterior Segment OCT (AS-OCT) was first reported in 1994 when the first real-time OCT, in a time-domain configuration, for anterior segment was developed at Duke University [Izatt et al, 1994, Radhakrishnan et al, 2001]. The system used a 1310 nm wavelength light source to illuminate the cornea, iris and lens, which reduces the amount of light that reaches the retina since the water present in the ocular tissue absorbs part of this energy [Van der Berg et al, 1997]. However, with the introduction of the Fourier or spectral domain OCT [Wojtkowski et al, 2003] the possibility of data acquisition of several thousands of A-scans per second was achieved, together with an improvement of the sensitivity [Choma et al, 2003] and signal to noise ratio [de Boer et al, 2003], and therefore allowing higher acquisition rates and lower energy exposure.

Numerous clinical applications of AS-OCT instruments have been reported. These include: pachymetric measurements of flap and stroma in LASIK surgery [Li et al, 2006 and 2007], post-refractive surgery corneal evaluation [Avila et al, 2006, Rosas et al, 2006], Intra-Corneal Rings Surgery (ICRS) [Lai et al, 2006], of keratoconus diagnosis [Li et al, 2009, and Li et al, 2009], tear meniscus evaluation [Savini et al, 2009,], for glaucoma diagnosis by angle measurements for narrow-angle [Radhakrishnan et al, 2005a, Radhakrishnan et al, 2005b], visualization of corneal scars [Khurana et al, 2007], biometric measurements for IOL power calculations [Goldsmith et al, 2005, Tang et al, 2006, and Tang et al, 2009], among others.

However, the main limitation for the direct quantitative analysis of surfaces is the so-called fan distortion. Fan distortion arises from aberrations associated with the scanning system architecture. It typically consists of two-mirror and two-axis, used to scan the beam laterally across the sample. Fan distortions results in the system coordinates not being linear, as a consequence a flat surface imaged by the system appears curved in that coordinate system. Therefore, the system cannot be used for the quantification of the geometrical aspects of surfaces. Some authors [Westphal et al, 2002] have addressed fan distortion in an OCT system, in which the rastering was produced by a non linear scanning system (consisting of resonant mirrors plus non-

telecentric scanning). They proposed to correct the distortion with the use of images taken axially around the confocal position of the beam, without taking into account the 3-D information provided by the OCT. Therefore the proposed procedure can be applied only to 2-dimensional imaging, not to 3-D topography.

Fan distortion correction allows quantitative analysis of the first surface (anterior cornea). However, the OCT is able to penetrate and to image inner structures of the eye, which apart from fan distortion, are also affected by the so-called optical distortion. Optical distortion is produced when a sample imaging embedded in a medium different from vacuum (air) is imaged. As light is bended at the media interfaces, it produces a very significant loss of the geometrical features of the observed surface, and therefore its geometrical parameters, such as curvature and thickness cannot be retrieved directly from the image. In order to provide accurate topographies of the internal surfaces of the eye, it is necessary to correct the optical distortion. This problem, to our knowledge, has not been addressed before in 3-D. Only a few studies have proposed methods for 2-D corrections of optical distortion in OCT images [Westphal et al, 2002, Podoleanu et al, 2004], based on the Fermat's principle. While this is an excellent first approach to the problem, and undoubtedly better than the standard correction consisting of dividing the OCT optical distances by the refractive index, surface parameters are better estimated in a 3-D correction rather than cross-sectional images. Only Podoleanu et al. [Podoleanu et al, 2004] showed corrections of cross-sectional images of an intraocular lens, an intralipid drop, and the anterior chamber angle in a living human eye. A limitation of the work is the use of analytical fits of circles (according to Gullstrand model) to the surfaces, and therefore ignoring local irregularities of the surfaces. Westphal et al [Westphal et al, 2002] recognized the potential improvement of applying the optical correction in 3-D, instead of 2-D.

There have been several attempts of quantifying parameters of the ocular optical components. For instance Izatt's group [Zhao et al, 2010] extracted the keratometric parameters of the cornea and they compared them with those obtained from standard ophthalmic devices. The cornea was scanned meridionally, and only corneal power, rather than corneal topography was reported. Gora et al [Gora et al, 2009] presented a preliminary quantitative corneal analysis based on a swept source OCT using a meridian rastering protocol for collecting data. They presented a volumetric and real time reconstruction of dynamic processes, such as pupillary reaction to light stimulus or blink-induced

contact lens movements. [Karnowski et al, 2011] presented a corneal topography in a keratoconic subject in comparison with corneal topographies obtained from clinical instruments: videokeratographer, Scheimpflug camera and slit scanning system, although compensation of fan distortion in this data set was not reported.

1.7. Open questions addressed in this thesis

Quantification of OCT anterior segment images. OCT provides high resolution and high contrasted images. However, OCT is primarily used for visualization of structures, most likely because the presence of distortions (fan an optical) have prevented from exploiting the potential of OCT to provide quantitative information in 3-D. Fan is inherent to the scanning architecture of the system, and can be minimized by hardware and fully corrected by software after calibration. The optical distortion is due to the refraction and affects structures that are imaged through preceding refracting surfaces. Most previous attempts of fan and optical distortion correction in the literature are in 2-D, and to our knowledge not systematically used in anterior segment OCT quantification

Accurate corneal topography. Corneal topography is normally obtained in the clinic with commercial Placido disk based topographers (videokeratographer) or Scheimpflug imaging. However, despite the clear advantages of OCT in axial resolution, high speed and posterior corneal surface quantification, OCT is typically only used quantitatively to retrieve central pachymetry, but not corneal topographies.

Crystalline lens surface topography. Several studies in the literature report the shape of the crystalline lens *in vivo*. In most cases the information is limited to phakometry (radii of curvature). Several instruments are limited by resolution, or by distortions requiring compensation. Topographic maps of the crystalline lens surfaces *in vivo* have not, to our knowledge, been reported.

Quantification of diseased and treated corneas. Understanding of the structural and geometrical changes induced on the diseased cornea is key in treatments to increase their predictability. Corneal irregularities, such as those present in keratoconus pose challenges to imaging and quantification of the anterior and posterior cornea, while the presence of intrastromal rings (increasingly used to treat this disease) with a different refractive index complicate the reconstruction of the internal surfaces.

Full 3-D quantitative biometry in normal, cataract and IOL implanted patients. Accounting for the full biometry and geometry of anterior segment is key for understanding the sources of degradation of the optical quality of the eye. Also, accurate estimates of biometric parameters such as the central corneal thickness, the anterior chamber depth, tilt and decentration of the lens or the radius of curvature and asphericities of cornea and lens, are crucial for IOL power calculation in cataract surgery.

1.8 Goals of this thesis

The specific goals of the thesis are:

1. To develop an OCT device capable of providing quantitative information of the anterior segment of the eye, *in vivo* and *in vitro*.
2. To develop theoretical and experimental methods for correcting fan distortion in OCT, including a calibration method for correction of any anterior segment OCT instrument
3. To develop a new efficient ray tracing algorithm, based on discrete number of points representing a surface, optimized for computers and easy to integrate and to be generally applied to the rest of the laboratory applications.
4. To establish an acquisition protocol and to develop robust automatic image processing tools to obtain topographies of *in vivo* anterior corneas, and to compare them with those obtained by other clinical devices.
5. To provide new algorithms to correct the optical distortion (refraction) of surfaces imaged through preceding surfaces and demonstrate its performance both *in vivo* and *in vitro*
6. To apply the developed technology to the characterization of pathological corneas affected by keratoconus before and after ICRS implantation.
7. To develop experimental protocols and image processing tools to obtain 3-D quantitative images of the anterior segment and to develop methods to provide for the first time the topography of the lens *in vivo*.
8. To obtain full 3-D OCT-based biometry of eyes implanted with IOLs

1.9 Hypothesis

It is possible, with the appropriate calibration and distortion correction algorithms, to obtain full three-dimensional geometrical and biometric information of the anterior segment of the eye, and apply it to the quantitative evaluation of normal, pathological corneal, an intracorneal and intraocular treatments.

1.10 Thesis structure

This thesis has been organized in the following chapters:

Chapter 1

A brief review of OCT technology is provided, with an emphasis of current anterior segment OCT instrumentation. The chapter also presents an overview of the anatomy of the anterior segment of the eye and current technologies to obtain quantitative information on the ocular components structures, with current limitations, current open questions in anterior segment OCT, and the thesis goals hypothesis and thesis structured are also presented.

Chapter 2

The OCT experimental systems developed for this thesis are described in detail: (1) time-domain OCT instrument, specifically developed for this thesis, and (2) a spectral OCT instrument, developed in collaboration with Copernicus University (Torun).

Chapter 3

A method of ray tracing for free-form optical surfaces is presented. The ray tracing through such surfaces is based on Delaunay triangulation of the discrete data of the surface and is related to finite-element modelling. Some numerical examples of applications to analytical, noisy, and experimental free-form surfaces (in particular, a corneal topography map) are presented. Ray-tracing results (i.e. spot diagram root-mean-square error) with the new method are in agreement with those obtained using a modal fitting of the surface, for sampling densities higher than 40×40 elements. The method competes in flexibility, simplicity, and computing times with standard methods for surface fitting and ray tracing, and will be the basis for the ray tracing algorithms used in the distortion correction of OCT images

Chapter 4

It addresses the measurement and correction of fan distortion in OCT. This effect arises from the scanning system configuration and prevents,

in general, from obtaining quantitative topographic data from OCT. Computer simulations allowed us to quantify the effect and evaluate its dependency on the scanning mirror separation and design of the collimating lens, as well as to estimate the optimal axial position of that lens to minimize the fan distortion. The chapter presents the developed a numerical algorithm based on 3-D ray propagation for the correction of the residual fan distortion. The effect was studied experimentally using a custom developed time-domain OCT in a Michelson configuration provided with a confocal channel, and the accuracy of the fan distortion correction algorithm tested on samples of known dimensions (flat surfaces and spherical lenses). The nominal radii of curvature of the surface were recovered. With a proper calibration of the system with use of confocal channel, this algorithm makes the time-domain OCT devices possible to be used as topographers.

Chapter 5

A method for 3-D optical distortion correction of anterior segment OCT images is presented. The correction has been applied theoretically to realistic computer eye models, and experimentally to OCT images of: artificial eye with a Polymethyl Methacrylate (PMMA) cornea and intraocular lens, an enucleated porcine eye, and a human eye *in vivo* obtained from two OCT laboratory set-ups (time domain and spectral). Data are analyzed in terms of surface radii of curvature and asphericity. Comparisons are established between the reference values for the surfaces (nominal values in the computer model; non-contact profilometric measurements for the artificial eye; Scheimpflug imaging for the real eyes *in vivo* and *in vitro*). The results from the OCT data were analyzed following the conventional approach of dividing the optical path by the refractive index, after application of 2-D optical correction, and 3-D optical correction (in all cases after fan distortion correction).

Chapter 6

It describes in detail the image processing tools developed to provide the quantitative data from anterior segment OCT images: Topographic and thickness maps, radii of curvature and asphericities or biometric data. Dedicated developed algorithms include: Denoising, statistical thresholding, clustering, boundary detection, further denoise reduction, 3-D merging and fitting.

Chapter 7 presents a method to obtain accurate corneal topography from a spectral Optical Coherence Tomography system. The method includes calibration of the fan (or field) distortion by the scanning architecture, and image processing analysis. We present examples of 3-

D surface topography measurements on artificial spherical and aspheric corneas and in 5 human corneas *in vivo*. Comparisons were made with non-contact profilometry (taken as reference) and Scheimpflug imaging in artificial lenses, commercial Placido ring videokeratoscopy and Scheimpflug imaging in patients. Corneal elevation maps from all instruments were fitted by conical surfaces (as well as by 8th order Zernike polynomials) using custom routines.

Chapter 8

It presents the developed OCT-based methods to characterize three-dimensionally (3-D) corneal topography in keratoconus before and after implantation of intracorneal ring segments (ICRS). Automatic tools were developed for the estimation of the 3-D positioning of the ICRS. Topographies of anterior and posterior cornea are obtained together to the thickness maps, as well as, the orientation and location of ICRS inside the cornea. The developed tools are illustrated in a keratoconic eye (grade III) pre-operative and 30 days post-operatively after implantation of two triangular-section, 0.3-mm thick Ferrara ring segments.

Chapter 9

It presents the use of our custom high-resolution high-speed anterior segment spectral domain Optical Coherence Tomography (OCT) for characterizing three-dimensionally the human crystalline lens *in vivo*. The OCT system was provided with custom algorithms for denoising and segmentation of the images, as well as for fan (scanning) and optical (refraction) distortion correction, to provide fully quantitative images of the anterior and posterior crystalline lens surfaces.

Chapter 10

It presents the use of our custom high-resolution high-speed anterior segment spectral domain Optical Coherence Tomography (OCT) for characterizing three-dimensionally the biometry of the eye. The method was tested on an *in vitro* artificial eye with known surfaces geometry at different orientations and demonstrated on an aging cataract patient *in vivo*.

Chapter 2

Custom-developed Optical Coherence Tomography systems

This chapter describes two anterior segment Optical Coherence Tomography (OCT) experimental devices developed to image optical surfaces, *in vitro* porcine eyes, and *in vivo* eyes (corneal and lens) in normal subjects and patients.

A Time-Domain OCT (TD-OCT) was used to obtain the experimental measurements on *in vitro* samples presented in Chapter 4 and Chapter 5, where the topographic capability of the OCT after distortion calibration (fan and optical) is presented. The measurements were compared to a commercial non-contact profilometer and clinical topographers. Specifically, we present a detailed description of the TD-OCT, optical and electronic layouts, and the custom-developed control software.

The Spectral-Domain OCT (sOCT), developed as a result of a collaborative effort between Copernicus University and the Visual Optics and Biophotonics Lab, was used to obtain the experimental measurements *in vitro* and *in vivo* of Chapter 5 and in the studies of Chapter 7 to Chapter 9. The *in vitro* measurements on optical surfaces were compared with a profilometer in Chapter 7, while the *in vivo* measurements on the anterior cornea were compared with clinical devices such as Scheimpflug camera and a corneal videokeratographer. The system was also used to measure the anterior and posterior surfaces in patients with corneal pathologies and treatments, as well as to obtain full anterior segment images pre-and post cataract surgery. In this Chapter we present the optical layout of the system.

The author of this thesis designed, implemented, calibrated and tested the TD-OCT in collaboration with Damian Siedlecki, Daniel Pascual, Laura Remon and Susana Marcos, and calibrated and tested the sOCT, in collaboration with Damian Siedlecki, Pablo Pérez Merino, Alberto de Castro Enrique Gamba, Judith Birkenfeld, and Susana Marcos. The sOCT was developed by Ireneusz Grulkowski, Michalina Gora and Maciej Wojtkowski among others.

2.1. Time Domain OCT

TD-OCT was the first proposed and developed OCT architecture [Huang et al., 1991]. However, it presents the limitation of its relatively low speed, with the most sophisticated configuration reaching of the order of 2000 A-scans/s at a relatively low sensitivity (90 dB). The first ophthalmological OCT devices commercially available were the TD-OCT developed by Carl Zeiss Meditec. As introduced in Chapter 1, the pathlength of the reference arm in TD-OCT is translated longitudinally in time. A property of the low coherence interferometry is the space gating [Schmidt et al., 1998], in such way that all the samples that fall out of the path matching the path in the reference arm of the interferometer do not produce interference fringes. This allows to measure distances between consecutive layers within the accuracy of the bandwidth of the low coherence source, provided that the material refractive index is known [Grajciar et al, 2008]. This axial measurement is commonly named A-Scan. In addition, it also allows obtaining 3-D images by incorporating a 2-D scanning system that rasters the surfaces [Rosen et al, 2009]. The name of the imaging technique depends on the way of scanning the surface. If it is a collection of A-Scans producing a cross sectional section of the sample, it is referred as B-Scan. Subsequently, if the sample is rastered first and the reference arm is moved it is named as C-Scan or en-face [Podoleanu, 1998]. The inherent ability of TD-OCT to resolve differences in distance within microns and the possibility of introducing fast optical scanners are valuable features for potentially converting OCT into a quantitative surface profilometer.

In this thesis we implemented a TD-OCT system, which we used to demonstrate quantitative surface topography.

Figure 2.1.a shows a schematic diagram of custom-developed TD-OCT (with the elements used in its implementation). Figure 2.1.b shows a photograph of the implemented set-up where the yellow lines represent the outgoing beam and the orange lines represent the returning.

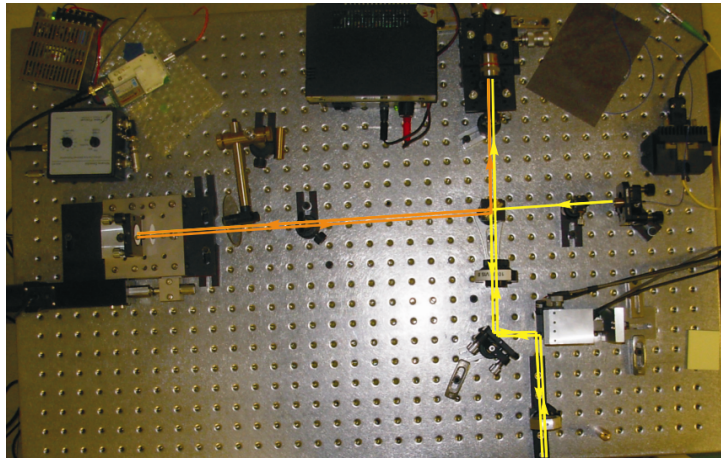
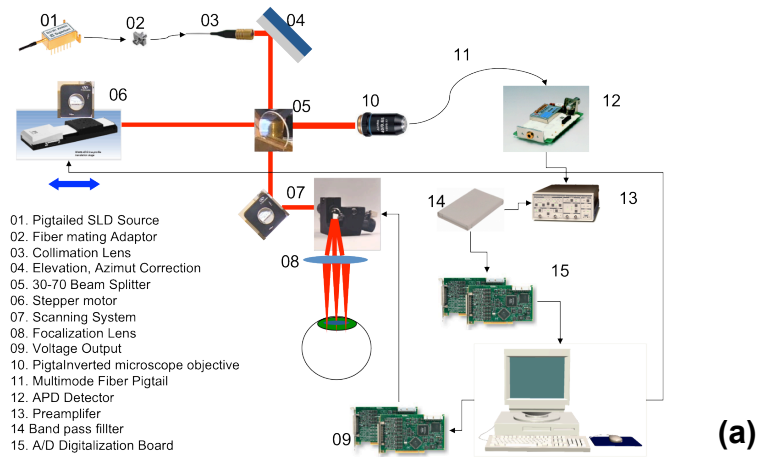


Figure 2.1. a) Optical and electronic schematic lay-out of the implemented TD-OCT with confocal channel. b) Photograph of the implemented TD-OCT with confocal channel.

2.1.1. Optical Lay-out

The system (Figure 2.1) consists of two units: a low coherence free-air Michelson interferometer for the tomographic measurements, and a confocal microscope for visualization and correction of distortions. Both channels share the same optical configuration, a reference arm and a sample arm. A low coherence light source: SLD (Superlum®, Carrigtwohill, Ireland) with a central wavelength of 810 nm and 20 nm of bandwidth, which provides a resolution of 14 μm was used for the illumination of the OCT and the confocal channel. The light coming from the SLD was collimated by a pigtailed lens (Princetel®, Pennington, NJ, USA) which provides a diameter beam of 3 mm. Then, a beam splitter (BS) divides the light toward the reference arm and the sample arm.

The reference arm is mounted on a stepper motor (Thorlabs®, Dachau Germany) configured with a speed of 23.75 mm/s, which provides a central Doppler frequency of 58.6 kHz.

The sample arm consists of a XY galvanometric scanner (mod. 6210, Cambridge Technologies®, Cambridge, MA, USA) with 3-mm clear aperture and a sampling frequency of 1 kHz, consisting of two rotating mirrors that deflect the incoming light to produce the rastering of the sample, and a plano-convex lens (Newport®, Irvine, CA, USA) of 100-mm focal length and 25-mm aperture acts as a collimating lens for chief rays and as focusing lens for the beam. This allows optimizing the irradiance impinging the sample, therefore improving the amount of scattering events. The light backscattered by the sample is collected by the collimating-focusing lens of the reference arm, it is de-scanned by the XY scanner and directed to the BS. The light coming from the reference arm and that backscattered of the sample are combined to produce the interference.

Finally, the light combined by the beam splitter is focused by an inverted microscope objective with magnification 4X (Olympus® Olympus, Japan) to a multimode fiber optic pigtail, which directs the light to an APD detector (C5460 Hamamatsu®, Hamamatsu, Japan). Electronic detection process is explained in section 2.1.2

An additional characteristic for the alignment of this setup is its capability to capture confocal images of the sample without any additional element. Taking advantage of the speed of the galvanometric scanner (1 kHz), it is possible to use this feature for almost a real-time preview (about 2 frames per second with satisfying resolution of 400x400 pixels) of the sample. This confocal mode is very useful to align the sample correctly or to place it in the proper (focal) distance from the lens in order to optimize OCT signal to noise ratio. Moreover, with use of the confocal channel it is possible to calibrate the system and to estimate the magnitude of the inherent distortion of the system, when a flat surface with a regular grid is imaged (Chapter 4).

2.1.2 Electronic lay-out.

Figure 2.2.a illustrates the process of detection in the TD-OCT. The resultant signal detected by the APD is composed of a DC term plus an AC part, and subsequently filtered by a custom band pass filter of central frequency of 58.6 kHz and bandwidth of 2.4 (Figure 2.2.b), digitized by a PCI card (PCI 6250 National Instruments®, Austin, TX, USA) and stored in the computer to produce the images.

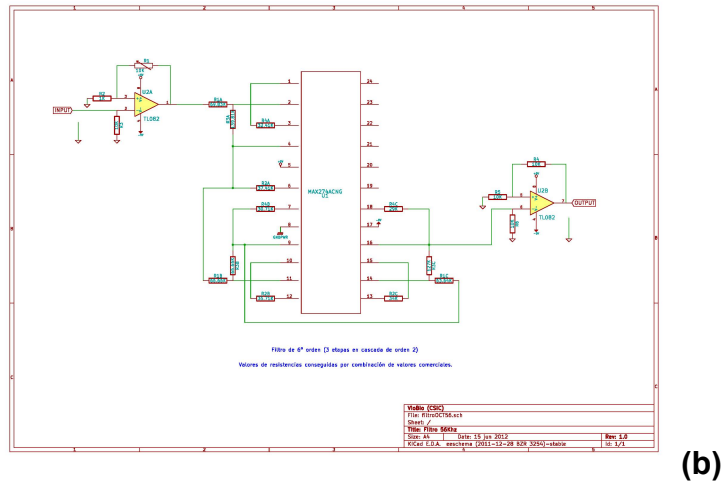
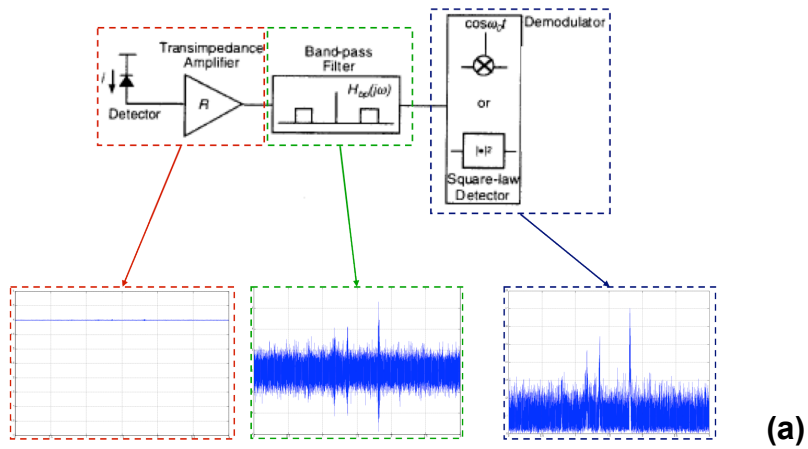


Figure 2.2. a) Detail of the detection process. Optical Detection in red, bandpass filter in green and demodulator in blue. b) Detail of the custom developed band-pass filter with central frequency of 58.6 kHz and bandwidth of 2.4 kHz.

The XY galvanometric mirrors (mod. 6210, Cambridge Technologies®, Cambridge, MA, USA) produce the sampling pattern of the acquisition. The mode of operations of these mirrors requires a stabilized DC current and an AC voltage to position them. The DC part is provided by a couple of microcontrollers (driver boards), model 6700 (Cambridge Technologies®, Cambridge, MA, USA), which are connected to a DC power supply with a low voltage ripple Vicor FlatPac with double Output of 28V (Vicor, Andover, MA, USA). The external voltage signal (AC) induces the movement of the mirrors in defelecting angles from -10 to 10 degrees, using a voltage of $\pm 10V$. The

external voltage signal is provided by a programmable PCI 6711 board, wired to a BNC box (BNC2110) by a SH68-68 cable (National Instruments®, Austin, TX, USA). The PCI 6711 card is completely programmable, allowing single voltage inputs, or acting as a generator of rectangular, triangular or saw tooth functions. Figure 2.3. shows the electrical layout to produce different sampling patterns with the galvanometric mirrors.

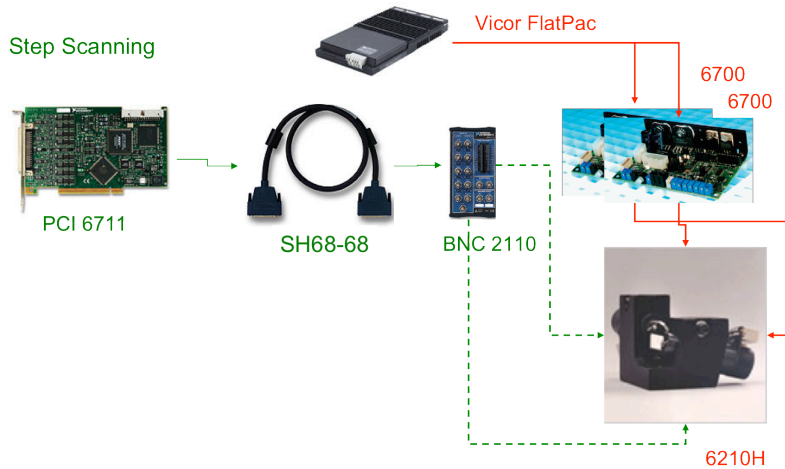


Figure 2.3. Detailed description of the controlling hardware for the galvanometric mirrors.

2.1.3. Software

Custom control software was developed in order to allow efficient data acquisition with a user friendly interface and flexible configurations. (Figure 2.4). The interface was written in C# (Microsoft .NET c#, Microsoft Corp., USA). The interface was combined with Matlab (Matlab; Mathworks, Natick, MA) scripts for visualization. The acquired data was structured according to an efficient interchange with Matlab.

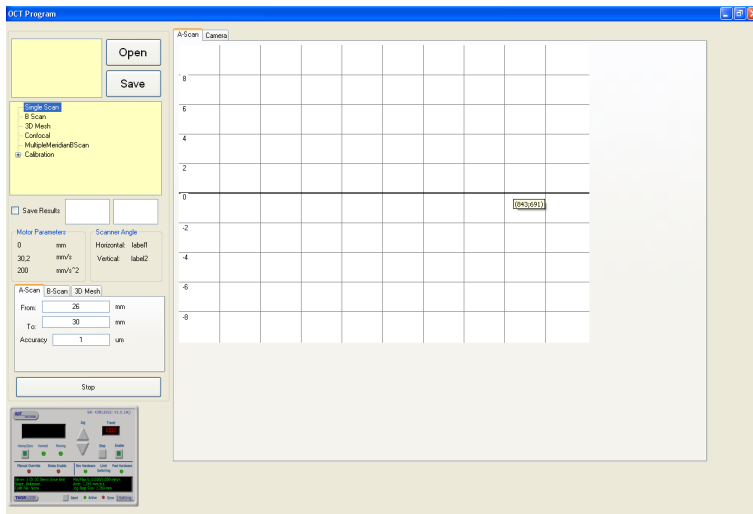


Figure 2.4. Snapshot of the control software developed for the TD-OCT.

The main purpose of the software for controlling the system was to optimize acquisition time and allow for flexible scanning configurations in one, two and three dimensions. Programmed scanning patterns were: A-Scan, B-Scan and C-Scan and 3-D as a collection of B-Scans or meridians. The software allows changing easily several parameters of the measurement collection: speed of the motor, range of acquisition, sampling density of the acquiring board and angles of rastering. The structure of the program has been arranged in classes to control every programmable device for producing an automated measurement: A-Scan, B-Scan Meridian B-Scan, 3-D-Mesh or Confocal. First, a class controls the stepper motor, producing the movement range; the class optimizes the scanning range speed taking into account the motor inertia (acceleration-deceleration). Then, a different class controls the movement of the XY galvanometric mirrors using a stair signal to provide the A-Scan collections and to saw tooth signals and triangular signal for the confocal. Finally, another class controls the acquiring board to generate triggers to start and to stop the acquisition and to start the motor movement.

Figure 2.5 illustrates how a B-Scan is collected as a number of A-Scans. The trigger, represented by the rectangular blue signal, encompasses all the operation when it is launched: the motor, the acquisition board and the XY mirrors start synchronously to move, to acquire data and to deflect the beam into position respectively. The red trapezoidal line represents the signal that it is required to generate for moving the axial scanning mirror. The green line segment (double arrow line) illustrates the detection and acquisition process, after a time

when the motor movement is stable, the acquisition card starts to record the signal provided by the APD detector and the bandpass filter. Finally, the orange broken line represents the voltage introduced to place mirror X, while the Y mirror continuous orange line, remain stable in the example illustrated in Figure 2.5. The A-Scan acquisition continues in a loop until the limits introduced to the routine are reached.

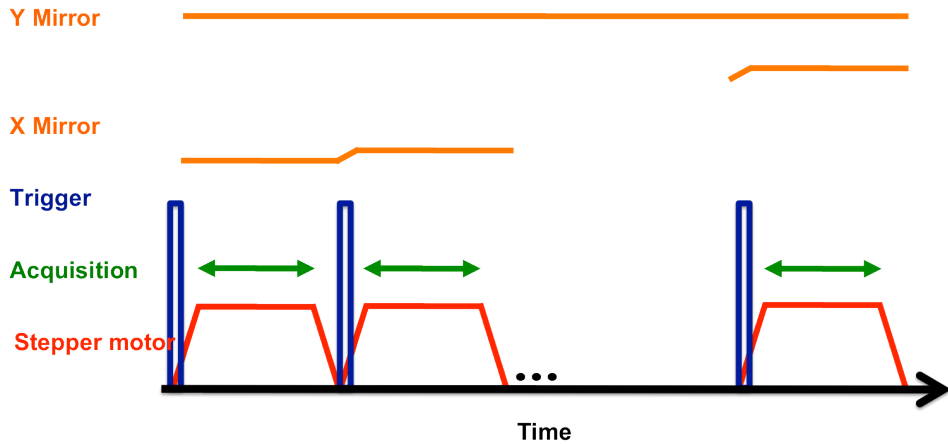


Figure 2.5. Time configuration of the electronic devices for a regular B-Scan acquisition.

The meridian collection is analogous to the regular B-Scan, as illustrated in Figure 2.6, except for the synchronous movement of both rastering XY mirrors. The trigger is launched and then the motor movement is initiated. The X and Y mirrors change their position, when the movement of the stepper mirror is stable. The acquisition card collects the data just before the deceleration movement is produced.

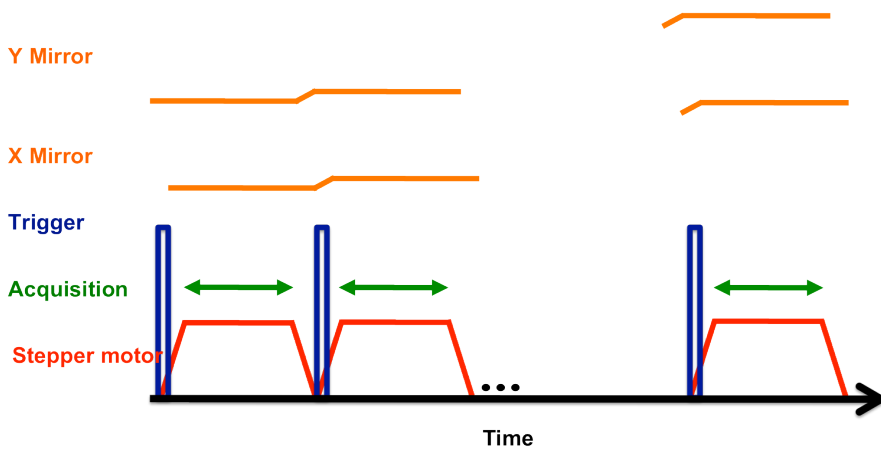


Figure 2.6. Time configuration of the electronic devices for a meridian B-Scan acquisition.

Figure 2.7 shows a typical cross-section obtained with the TD-OCT system on a porcine cornea *in vitro*. The upper structure is the cornea, the white bright structure in the lower left is the iris and the faint structure that appears beside the iris is the crystalline lens.

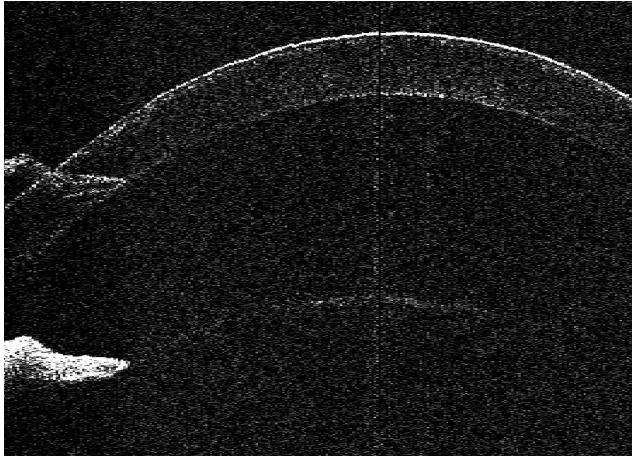


Figure 2.7. B-Scan from an ex-vivo porcine cornea obtained with the TD-OCT

The confocal channel acts as a microscope. It allows the alignment of the samples with respect to the axis of the system, and helps in the acquisition of images and in the calibration of the system for the correction of fan distortion. The signal is taken from the preamplifier since in confocal imaging the signal of interest is the DC component of signal rather than the AC like in the OCT measurements. A trigger generated by the PCI acquisition card 6250 is launched and then the PCI 6711 generates a pre-programmed saw-tooth function, to control the x mirror, and a stair function to control the y mirror. The acquisition routine is launched by the trigger and the acquisition card (PCI 6250) collects, digitizes and stores the APD signal. Figure 2.8.a shows a layout of timing of the confocal measurement. The result of this routine is shown in Figure 2.8.b where the image of a rectangular grid with resolution of 400x400 pixels is depicted.

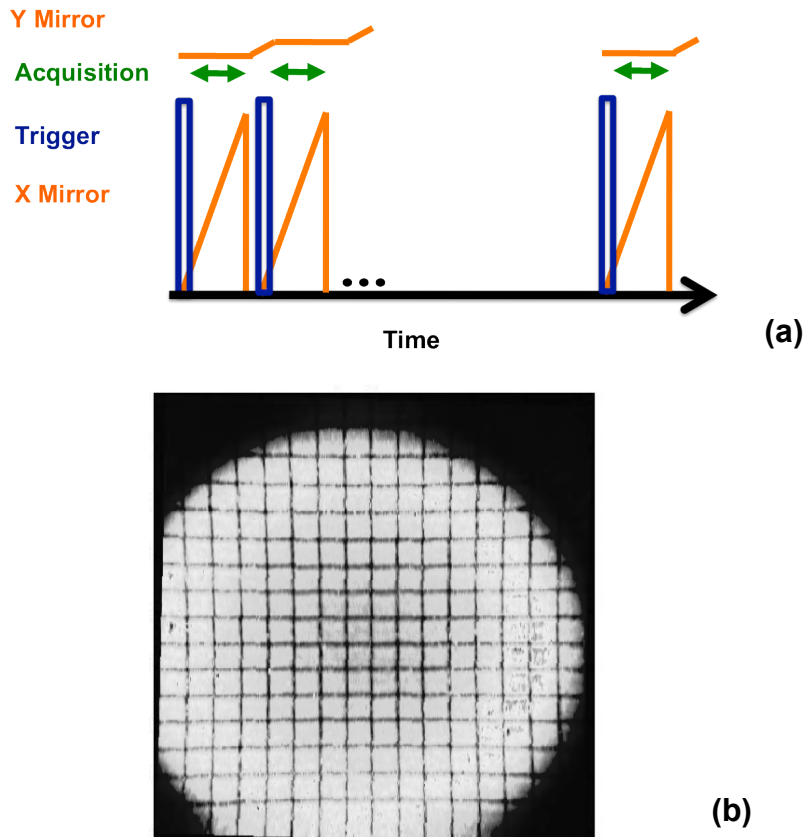


Figure 2.8. a) Time configuration of electronic devices to achieve a confocal measurement. b) Confocal measurement of a calibration grid.

2.2. Spectral Domain OCT

The other custom-developed OCT, implemented in this thesis, for anterior segment of the eye imaging is based on “Spectral-Domain” OCT (SD-OCT).

2.2.1 SD-OCT optical layout

The custom SD-OCT used in this thesis was developed in collaboration with Nicolaus Copernicus University (Torun, Poland) [Grulkowski et al, 2009]. A schematic diagram of the system is shown in Figure 2.9.a, and a photograph of the actual device is shown in Figure 2.9.b.

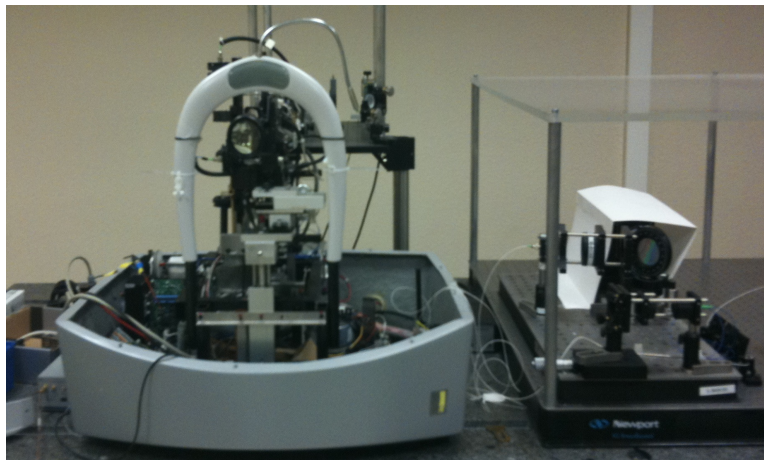
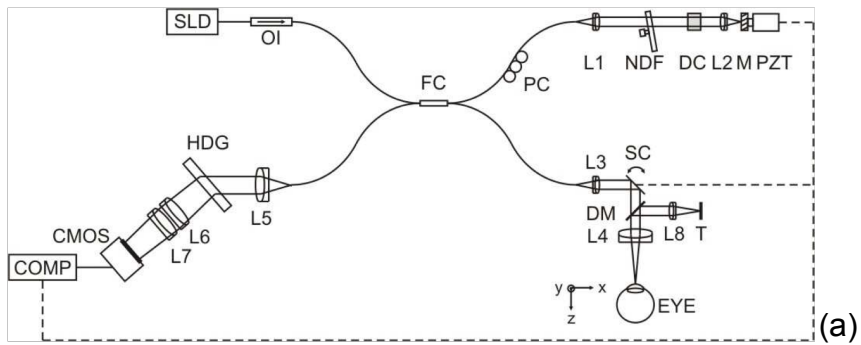


Figure 2.9. a) Experimental sOCT set-up: SLD superluminescent diode, OI-optical isolator, FC- 80:20 Fiber coupler, PC-polarization controller, NDF-Neutral density filter, DC-dispersion compensator, DM-Dichroic mirror, T-Target, HDG-holographic volume diffraction grating, CMOS linescan camera, COMP computer. Adapted from Grulkowski et al 2009 b) Actual implementation of the device.

The set-up is based on a fiber-optics Michelson interferometer configuration with a superluminescent diode SLD ($\lambda_0 = 840 \text{ nm}$, $\Delta\lambda = 50 \text{ nm}$; Superlum, Ireland) as a light source, followed by an optical isolator (OI) joined by a fiber mate to a Fiber coupler (FC) in order to avoid that backreflected light from the reference and sample arms returning to the SLD. The light is split by the fiber coupler in two arms (reference and sample arms). The reference arm consisted of polarization controller (PC) to optimize detection performance, a converging lens (L1) to produce a collimated beam, a neutral density filter (NDF) to increase or decrease the power of light in the reference arm, a converging lens (L2) that focuses the light on the mirror (M) and a piezotranslator (PZT). The sample arm consists of a converging lens (L3) that collimates the light onto a XY galvanometric optical scanner to produce the horizontal vertical rastering of the sample, and finally a

75 mm focal lens (L4) to collimate the chief rays of the beams and to focus the irradiance impinging the sample. The light backreflected by the reference and sample arm is recombined by the fiber coupler and it is led to the detection unit, which consists of a converging lens (L5) to collimate the light, a volume diffraction grating to spatially separate the spectrum and a magnifier objective composed of two converging lenses (L6) and (L7) to image the fringes on the detector a 12-bit line-scan CMOS camera with 4096 pixels (Basler sprint spL4096-140k; Basler AG, Germany). Figure 2.10.a shows an A-scan with the interferometric signal modulating the power spectrum of the light. Figure 2.10.b shows a cross sectional image of cornea, iris and lens.

The effective acquisition speed of this system is up to 150000 A-Scans/s, although the typical speed used for the experiments in this thesis was 25000 A-Scans/s, since it showed as a good compromise between speed and resolution. The axial range of the instrument is 7 mm, and the theoretical axial resolution $3.4 \mu\text{m}$ in air. The signal to noise rate (SNR) of the instrument was estimated to be 97 dB.

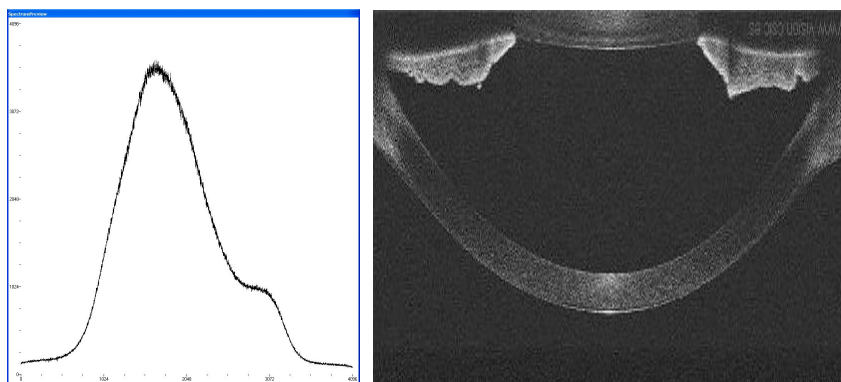


Figure 2.10. a) Power spectrum of an A-Scan and the interferences modulating it. b) Illustration of a B-Scan showing a corneal section, iris and anterior part of lens

Chapter 3

Three-dimensional Ray tracing on Delaunay-based reconstructed surfaces

This chapter is based on the article by Ortiz, S. et al “3-D Ray tracing on Delaunay-based reconstructed surfaces” *Applied Optics*, Vol. 48, Issue 20, pp. 3886-3893 (2009). The coauthors of the study are: Damian Siedlecki, Laura Remón and Susana Marcos. The study has been developed at Instituto de Óptica “Daza De Valdes”. The contribution of the author of this thesis was the mathematical development, coding and implementation of a ray tracing for free-form optical surfaces. The ray tracing through such surfaces was based on Delaunay triangulation of the discrete data of the surface and is related to finite-element modeling. Applications of this ray-tracing technique in analytical, noisy, and experimental free-form surfaces (in particular, a corneal topography map) are presented. Ray-tracing results (i.e., spot diagram root-mean-square (RMS) error) with the new method are in agreement with those obtained using a modal fitting of the surface, for sampling densities higher than 40x40 elements. The method competed in flexibility, simplicity, and computing times with standard methods for surface fitting and ray tracing and will be the basis for the ray tracing used in the distortion correction methods of OCT images developed in this thesis.

3.1. Introduction

A large variety of ray-tracing algorithms can be found in the literature. Many of them involve ray tracing through nonhomogeneous or gradient index media [Moore et al, 1976, Sharma et al, 1982, Marchand, 1988 and Egorchenkov et al, 2001]. Some others describe the light propagation in birefringent materials [Stavroudis, 1962, Liang et al, 1991, Beyerle et al, 1998 and Izdebski, 2008] or optical fibers (waveguides) [Tian et al, 1989 and Witkowski et al, 2008]. However, except for a few papers [Allen et al, Herzberger, 1957, Spencer et al, 1962 and Sharma et al, 1986], not many works in the literature explain a precise and efficient way of finding the intersection points of rays with optical surfaces. Although this problem seems to be relatively trivial, our experience in physiological optics shows that it is not, particularly if “noisy” or free-form surfaces are of interest. Interesting examples of such surfaces are surfaces of biological origin, for example, the cornea of the eye. The anterior corneal surface plays a very important role in focusing light on the retina. Its topography has a major influence on the optical performance of the eye, including higher-order aberrations [Applegate et al, 1994, Howland et al, 1994, Artal et al, 1998, Guirao et al, 2000a, Guirao et al 2000b, Barbero et al, 2002, Carvalho, 2003, Gwiazda et al, 2003, Navarro et al, 2006 and Rosales et al, 2007].

This chapter presents a three-dimensional (3D) technique of tracing rays through optical surfaces of any type. The method is based on the Delaunay triangulation [Delaunay, 1934 and Guibas et al 1992], which is a well-known method in finite-element modeling and graphical ray tracing that is used for rendering photorealistic images [Touma et al, 1998, Kohout et al, 2005 and Kang et al, 2006]. To the best of our knowledge, this method has never been implemented in geometrical optics. Typically, optical analysis software, such as ZEMAX [Zemax, 2007] uses a least-mean-square method together with linear or spline interpolation of the discrete surface points. The least-mean-square method is relatively fast and its accuracy, even for analytical, surfaces is acceptable. However, it depends strongly on the sampling density of the surface. The Delaunay method proposed in the current study can optimize computations of optical analysis of optical systems, regarding particularly the intersection points of a ray with an optical surface.

3.2. Delaunay decomposition

Delaunay decomposition is a well-described [Delaunay, 1934 and Guibas et al 1992] mathematical method used in computational

geometry. It uses the property of the convex hull (envelope) of the discrete set of points $\{X,Y\}$. By means of the Delaunay triangulation method, one can approximate any surface with a set of flat triangles, as is usually done in the finite-element method (FEM) [Strang, 1973, George et al, 1998, Vanselow, 2001, Calvo et al, 2003 and Babuska et al, 2004] (Figure 3.1). The number of obtained triangles is related to the number of points in the grid and the number of vertices on the convex hull. If m is the number of points in the grid, and l is the number of vertices, then the number of triangles t is defined by the following equation (Equation 3.1):

$$t = 2m - 2 - l \quad Eq.3.1$$

Because all the triangles are flat, one can easily calculate the vector normal to each of them and use it further in the Snell's law accomplishment. This makes the Delaunay triangulation method very convenient and relatively easy to implement to optical ray tracing.

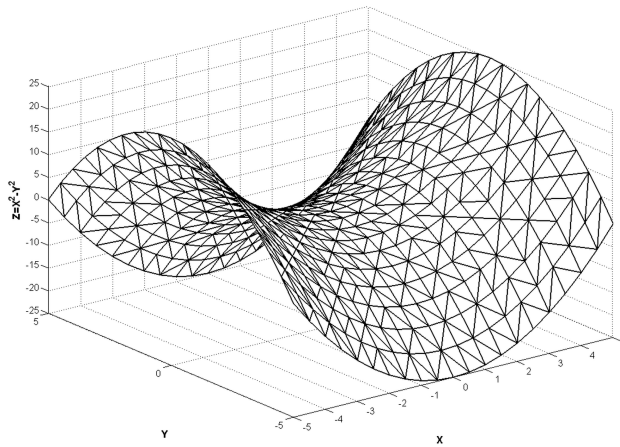


Figure 3.1. Function $z(x,y) = x^2 - y^2$ represented as a set of triangles to illustrate the Delaunay triangulation. The discrete data of the function are situated in vertices of triangles.

3.2.1. Description of the algorithm

In the first step it is needed to arrange adequately the data of the surface. The surface should be described by set of points $\{X,Y,Z\}$ corresponding to a discrete sample of the surface topography. If the surface is analytical, the set $\{X,Y,Z\}$ can be generated as a mesh with regular sampling. The optical surface can be the result of a

topographical measurement performed on irregular or even random sampling pattern. On a set of $\{X,Y\}$, one can perform 2-dimensional Delaunay decomposition, where each point from the discrete data set $\{X,Y\}$ is one of the vertices of at least two triangles. This results on a 3-D approximation of the surface $Z = f(X,Y)$.

The next step is to find one particular triangle, which is hit by the a ray denoted by its initial position, R_0 , and an optical vector at this point, \vec{K}_0 (Equation 3.2):

$$R_0 = \begin{pmatrix} x_0 \\ y_0 \\ z_0 \end{pmatrix}, \quad \vec{K}_0 = \begin{bmatrix} k_{x0} \\ k_{y0} \\ k_{z0} \end{bmatrix} \quad Eq.3.2$$

where k_{x0} , k_{y0} and k_{z0} represent directional cosines.

One can test each triangle separately, although this implies a relatively large computational effort, especially if the surface is large and the grid $\{X,Y\}$ is dense. Alternatively, a much more efficient way to do it is to assess the region of interest *a priori* by finding the minimum Euclidean distance between the straight line given by the optical vector (Equation 3.3).

$$R = R_0 + t\vec{K}_0 \quad Eq.3.3$$

(with as a length of the vector \vec{K}_0 and a real number) and each of the points from the set $\{X,Y,Z\}$. This distance is given by the Equation 3.4:

$$d_i = \left| \vec{w}_i - (\vec{w}_i \cdot \vec{K}_0) \vec{K}_0 \right| \quad Eq.3.4$$

where \vec{w}_i is a vector obtained by subtracting the coordinates of the point R_0 from the coordinates of the i -th point from the set $\{X,Y,Z\}$ ($(X_i, Y_i, Z_i) \in \{X,Y,Z\}$). If $d_m = \min(d_i)$ is found, this means that the ray hits one of the triangles surrounding the vertex $P_m = (X_m, Y_m, Z_m)$. Following this procedure, instead of testing thousands or even millions of triangles (Equation 3.1), one can limit the area of interest to (on average) six triangles (Figure 3.2). In the case of a random sampling

pattern, the number of triangles depends on the configuration of neighbors. The average number of triangles surrounding each vertex is characteristic of the Delaunay triangulation [Delaunay 1934; Guibas 1992]. With the number of possible triangles significantly reduced, one can easily find the common point to the ray given by the Equation 3.3, and each of the triangles of interest. This allows obtaining (on average) six different points on six different planes defined by six different triangles.

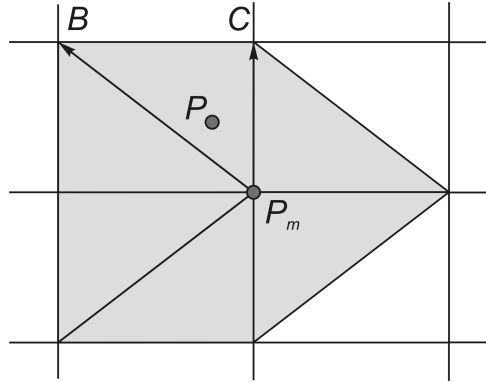


Figure 3.2. Graphical illustration of a point P_m being a common vertex of six neighbouring triangles and barycentric technique.

Additional calculations are required to obtain the exact triangle that is intersected by a ray. The proper facet can be found by means of the barycentric technique [Coxeter 1969], which is very commonly used together with Delaunay triangulation. Let us consider a triangle given by points P_m , B and C , with P_m as a reference point (Figure 3.2.). Each point of the plane containing the triangle P_mBC can be described as a linear combination of two vectors defining the plane (Equation 3.5):

$$P = P_m + u \cdot \overline{P_m B} + v \cdot \overline{P_m C} \quad Eq.3.5$$

where $\{u, v\} \in \mathbb{R}$. If we have the coordinates of the point P , after some simple mathematical operations one can get the following formulas for u and v (Equation 3.6):

$$\begin{aligned}
u &= \frac{(\overline{P_m B} \cdot \overline{P_m B})(\overline{P_m P} \cdot \overline{P_m C}) - (\overline{P_m B} \cdot \overline{P_m C})(\overline{P_m P} \cdot \overline{P_m B})}{(\overline{P_m C} \cdot \overline{P_m C})(\overline{P_m B} \cdot \overline{P_m B}) - (\overline{P_m C} \cdot \overline{P_m B})(\overline{P_m B} \cdot \overline{P_m C})} \\
v &= \frac{(\overline{P_m C} \cdot \overline{P_m C})(\overline{P_m P} \cdot \overline{P_m B}) - (\overline{P_m C} \cdot \overline{P_m B})(\overline{P_m P} \cdot \overline{P_m C})}{(\overline{P_m C} \cdot \overline{P_m C})(\overline{P_m B} \cdot \overline{P_m B}) - (\overline{P_m C} \cdot \overline{P_m B})(\overline{P_m B} \cdot \overline{P_m C})}
\end{aligned} \tag{Eq.3.6}$$

From the values of u and v one can assess if a particular point P belongs to the triangle or not. If u or v are < 0 , u or $v > 1$ and $u + v > 1$ the point P is out of the triangle. Alternatively if conditions $0 \leq u + v \leq 1$, $0 \leq u \leq 1$ and finally $0 \leq v \leq 1$ are accomplished, this means that the point P belongs to the particular triangle.¹

Once the triangles of the surface where rays intersect the surface have been determined, the z value can be found by means of linear interpolation, as the intersection of three planes, or alternatively, using more complex methods of interpolation, such as the values of the neighbors (B-splines) or radial base functions [Wedland, 2004]. The use of radial base functions does not require the use of a regular grid of sampling and potentially could allow reducing the density of the sampling (and computational time) without compromising accuracy. In this study, we have implemented several of these functions: cubic, multiquadric [Bookstein, 1989], and thin plate spline [Allison, 1993], besides the simplest linear interpolation. The algorithm [Liu, 2002] consists of fitting a number of coefficients using the values of x , y , and z of control points called nodes. The control points in our case are the points belonging to the triangle within the ray impacts. Once the coefficients are obtained, the value of the z coordinate can be easily obtained simply by substitution of the value of the x and y coordinates into Equation 3.7.

$$z(x, y) = c_0 + c_1 x + c_2 y + \sum_{i=1}^n \lambda_i \phi(r) \quad \text{where } r = \sqrt{x^2 + y^2} \tag{Eq.3.7}$$

¹ It may happen that the point P is located on the edge of the triangle (when either u or v from Eq. 3.6. is equal to 0, or $u + v = 1$), or even in the vertex (when both u and v are equal to 0 or either u or v is equal to 1), which means that it is common two or more of the triangles that have common edge (vertex), but the vectors normal to these triangles are different. In this situation it is convenient to consider the mean value of the normal vectors coordinates for further ray tracing calculations.

where c denotes the coefficients of the interpolation, φ is a radial base function (cubic, multiquadric, thin plate, etc.), d_i is the distance between the i -th node and the point to be interpolated, and n is the number of nodes. Further details can be found in the literature [Liu, 2002].

For the linearly interpolated method the normal to the surface at point P is associated to the characteristic vector of the facet to which this point belongs, with follows the Equations 3.8:

$$\hat{N} = \frac{\overline{P_m B} \times \overline{P_m C}}{|\overline{P_m B} \times \overline{P_m C}|} \text{ or } \hat{N} = \frac{\overline{P_m C} \times \overline{P_m B}}{|\overline{P_m C} \times \overline{P_m B}|} \quad Eq.3.8$$

for a convex or concave initial surface.

In the case of a more complex method of interpolation, the normals can be assessed using the partial derivatives with respect to x and y and, finally, performing the cross product.

Once we have a point P that belongs to the surface and a normal the surface at this point, \hat{N} , any of the 3-dimensional implementations of the Snell's law can be applied, i.e. the formula described by Sharma (Equation 3.9) [Sharma 1982]:

$$n' \overline{K_1} = n \overline{K_0} + w \hat{N} \quad Eq.3.9$$

where $\overline{K_1}$ is the optical vector after refraction, n and n' are refractive indices before and after the surface, respectively, and w is calculated as follows into Equation 3.10 [Barbero et al, 2002]:

$$w = \sqrt{n^2 - n'^2 + v^2} - v \quad Eq.3.10$$

where $v = \overline{K_0} \cdot \hat{N}$.

In Section 3.4 we present some numerical examples of application of the developed method to various surfaces that can be encountered in optical design and physiological optics. The three types of surfaces that we describe are analytical surface, noisy surface, and free-form surface, in particular, a corneal topography from a normal subject obtained from

a Placido disc corneal videokeratographer (Atlas, Zeiss). For this example, a semianalytical algorithm of a ray-tracing algorithm through a surface approximated by a set of Zernike polynomials was developed and programmed in MATLAB for the purposes of comparison. The free-form surface data under consideration was approximated by 36 Zernike polynomials [Schwiegerling et al, 1995, and Barbero et al, 2002] with a 3mm normalization radius, using a standard least-mean-square method. The intersection points of ray paths with the approximated surface were found by means of a least-mean-square method (because of the relative complexity of the expansion formula), while the normals to the surface at these points were calculated analytically by the partial derivatives. We refer to this algorithm as “semianalytical.”

3.3. Numerical examples

In order to demonstrate the possibilities and accuracy of the algorithm described above, we will present examples of 3-D ray tracing using the described methods on several types of surfaces (noise-free and noisy analytical surface, and free-form experimental surface).

3.3.1. Analytical surface with a regular and random grid

A conic surface has been considered for comparative purposes of ray tracing on the analytical and Delaunay decomposed surface. In particular, the first surface of an achromatic lens (AC508-100-B) from the Thorlabs optical elements catalog has been studied. The radius of the anterior surface of this lens is 65.77 mm, and the conic constant $k = 1$ (according to Malacara’s notation [Malacara, 1978]). The refractive index of the glass (LAKN22) is 1.64134164, for the operating wavelength of 855 nm. In order to test the accuracy of the method proposed, two different outcomes were evaluated (distance between the intersection points and refracted angle difference) from the ray tracing on the analytical (using Zemax, a commercial optical design and analysis software) and Delaunay decomposed surface with use of linear interpolation and with various sampling densities (programmed in MATLAB, Mathworks, Nantick, Massachusetts) for 200 rays entering the lens aperture at different heights. Our simulations showed that the average difference in distance estimated from the two methods ranged from 0.005 to 0.150 μm and the average difference in angles ranged from 0.005 to 1.79 arc min. For sufficiently high density sampling grids, these values are slightly larger than the Raleigh criterion (0.07 arc min, for the dimensions of the tested lens).

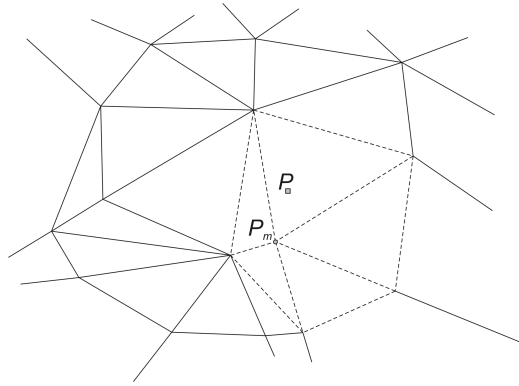
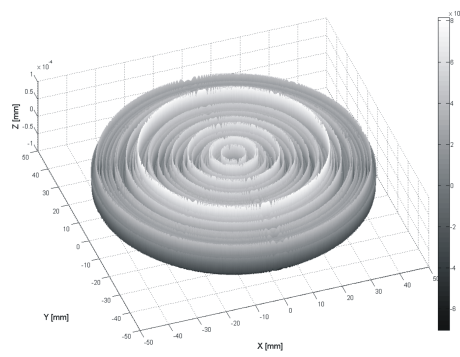


Figure 3.3 An example of a random grid on a plane. The dashed lines form triangles surrounding point.

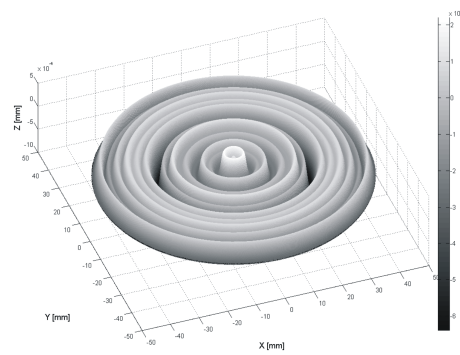
The same accuracy test has been performed for an analytical surface but defined on a random grid (Figure 3.3). The difference in distances between the two methods varied from 0.004 to 0.155 μm , and in angles from 0.17 to 1.94 arc min.

3.3.2. Noisy surface with a regular grid.

The next step is to explore the possibilities of the technique on noisy surfaces, for which random noise of Gaussian spectrum has been added to the analytical topography of the surface. The RMS of the height deviations has been kept below $\lambda/8$, and generated using the algorithm provided by Tsang [Tsang, 2001], with correlation lengths of 1 and 1000 μm (which meet the Beckmann [Beckmann, 1967] criterion for rough surfaces). The 1 dimensional Tsang's method has been extended to the 2-D surfaces assuming circular symmetry (Figure 3.4), and repeated 10 times for 6 different ranging from 100-2500 points per mm^2 . The simulated surface would be consistent to that produced by a lathe or optical driller.



a)



b)

Figure 3.4. Noise generated for simulations of realistic noisy surfaces: a) RMS = 855/8 nm and correlation length equal to 1mm; b) RMS = 855/8 nm and correlation length equal to 1000mm;

Table 3.1 and Table 3.2 show the results from these simulations. Difference values range from 0.021 to 0.204 μm and angles from 0.23 to 3.67 arc min.

Table 3.1. Accuracy of the algorithm in a relation to the sampling grid density (noisy surface). Results from 10 trials for 15 rays along the 25 mm diameter pupil.

Sampling grid density (1/mm ²)	Coherence length 1 μ m			
	Distance difference (μ m)		Angle difference (arc min)	
	mean	SD	mean	SD
100	0.156	0.016	0.749	0.109
400	0.045	0.023	0.233	0.132
900	0.020	0.018	0.598	0.344
1600	0.032	0.020	0.672	0.423
2500	0.021	0.014	1.013	0.521

Table 3.2. Accuracy of the algorithm in a relation to the sampling grid density (noisy surface). Results from 10 trials for 15 rays along the 25 mm diameter pupil.

Coherence length 1000 μ m			
Distance difference (μ m)		Angle difference (arc min)	
mean	SD	mean	SD
0.204	0.154	3.673	0.305
0.192	0.140	1.942	0.287
0.135	0.094	0.153	0.135
0.149	0.088	0.996	0.266
0.194	0.142	0.213	0.118

3.3.3 Free-form surface (corneal topography)

Free-form surfaces present a real challenge for optical design and analysis, as their surfaces cannot be easily described analytically. Examples of such surfaces include those of progressive addition lenses (PALs) designed to produce a power gradient across the lens to compensate for the accommodative loss in presbyopia [Charman, 2008, and Meister et al, 2008]. Another example of a free-form optical surface can be the topography of the human cornea. Currently it is possible to measure the anterior surface elevations of the human cornea

with satisfactory accuracy, although an analytical representation is challenging [Guirao et al, 2000a, Smolek et al, 2000 and Douthwaite, 2002].

Let us consider the raw data from a corneal topography measurement [Figure 3.5.a and Figure 3.5.b]. The surface is subject to noise due to experimental errors (camera, tear film, motion) and defined on an irregular grid. Although a common description of the corneal topography is a Zernike polynomial expansion [Schwiegerling et al, 1995, Barbero et al, 2002, Sicam et al, 2004, Turuwhenua, 2007], the optimal number of terms that best describes the surface has been debated [Iskander, 2001]. The algorithm presented gives the opportunity to trace rays through an optical surface given by raw elevation data points from corneal videokeratography without any additional approximation. Figure 3.5.c shows a ray tracing on a corneal elevation map from a Placido rings corneal videokeratographer reconstructed using the Delaunay decomposition. If the data are not subject to artefacts (i.e., because of eye lashes) the device is able to provide the elevation data sampled uniformly every 2° on each of the 24 Placido rings.

For purposes of comparison, the corneal topography from Figure 3.5.a was fitted by a seventh-order polynomial expansion (with 36 terms). The corresponding Zernike coefficients and the accuracy of the approximation are presented in Figure 3.6. The Zernike expansion was uniformly sampled over the area of interest and then the finite-element ray- tracing algorithm was applied.

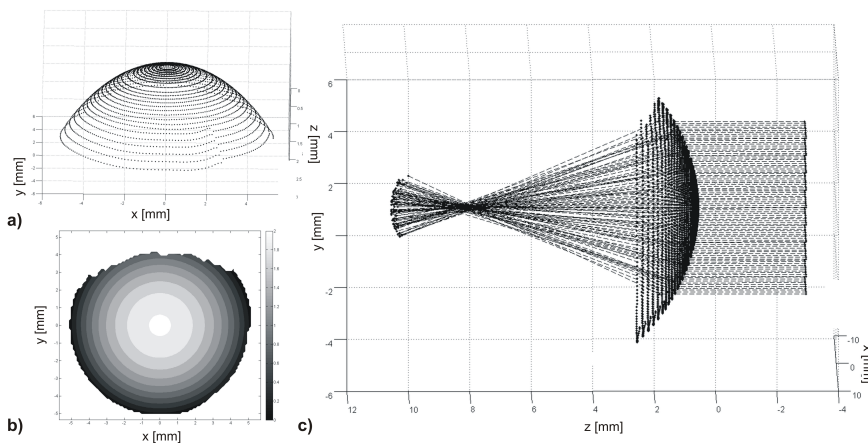


Figure 3.5. An example of a free-form surface: a) raw (discrete) data from corneal topographer; b) the elevation of the anterior corneal surface; c) ray tracing visualization through the anterior surface of the cornea.

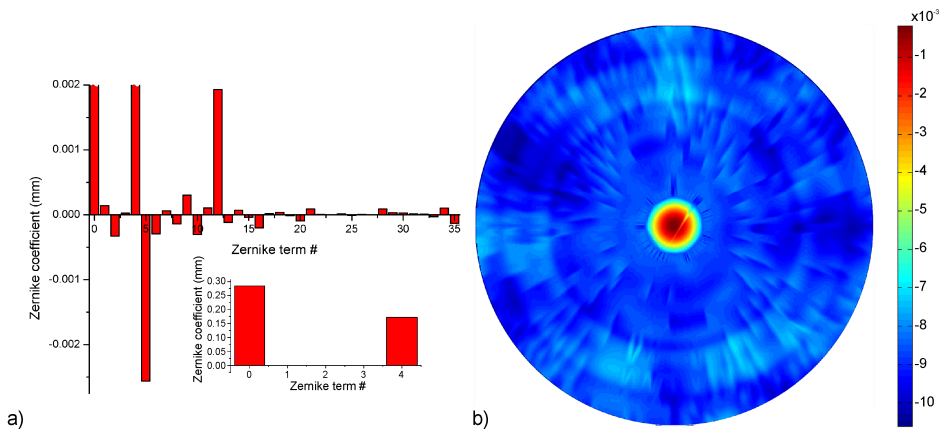
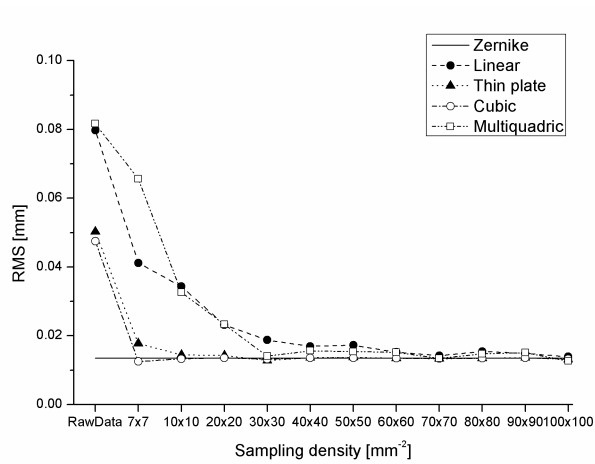


Figure 3.6. (Color online) Results of the 7th order Zernike polynomial expansion of the corneal elevation map of Figure 5 a) Zernike coefficients for a 3-mm normalization radius. The inset in figure a) shows the values of the 0-th and 4-th Zernike term as they are beyond the original scale. b) Difference between raw data (interpolated with cubic splines) and Zernike polynomial fit. The RMS of the difference is 1.4 μm . The surfaces were set to have the same Z value in the center.

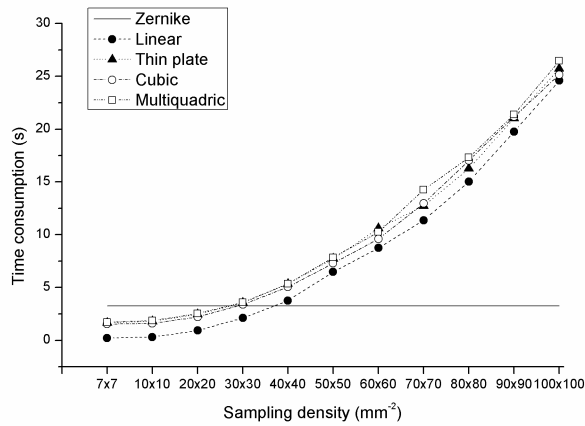
Figure 3.7.a compares the results of a ray tracing (200 randomly distributed rays) for various representations of the corneal surface and the ray-tracing algorithms. The values of the RMS of the spot diagrams were taken at a distance of 27.72mm, which is approximately the focal distance of this particular surface, and were used as a metric to compare the outcomes from different fittings (Zernike and Delaunay with different interpolation methods). The first data (labeled as “RawData”) correspond to a ray tracing performed directly on a reconstruction of the surface raw elevation data (without prior smoothing) with a Delaunay representation (with the different methods of interpolation, shown with different symbols). The horizontal line corresponds to the Zernike fitting and semianalytical method for ray tracing. The rest of the data represent results from a ray tracing of the same surface fit by a seventh-order Zernike polynomial expansion, followed by Delaunay reconstruction with different sampling densities (ranging from 7x7 up to 100x100 per mm^{-2} , in the horizontal axis) and different interpolation methods (represented by different symbols). It is remarkable that the values of RMS for finite-element ray tracing for raw data with the use of different interpolation methods is significantly higher than RMS for the surface approximated by Zernike polynomials. The Zernike representation smooths the data from the topographical measurement, while the FEM directly uses the raw data and performs the interpolation. The RMS values for FEMs on the data approximated by Zernike polynomials converge to the value of 13.6 μm achieved by

means of the semianalytical method ray tracing with use of Zernike approximation. For cubic and thin plate interpolation methods, the RMS values are very similar to the Zernike semianalytical ray tracing even for relatively low sampling densities (7×7), while the linear and multiquadric interpolation methods require denser samplings. Figure 3.7.b presents the computational time as a function of sampling density, for 200 rays randomly distributed in the aperture. The finite-element algorithms are competitive in terms of execution time of the ray-tracing procedure for low but sufficient sampling densities. Computational time increases exponentially with sampling density for the Delaunay methods, as expected given the increase of the number of facets.

Figure 3.8 presents a comparison of the computational time as a function of the number of rays to be traced for the different interpolation methods used in the finite-element algorithm (sampling 20×20 per mm^{-2}) and for the Zernike semianalytical method. In general, finite-element algorithms are competitive for the number of rays up to 300, above the typical number of rays used in visual optics applications [Llorente et al, 2007]. For a linear interpolation, the time consumption is significantly lower due to relatively small effort in finding the normals to the surface at each ray intersection with the surface.



a)



b)

Figure 3.7. (a) RMS of the spot diagram taken at the distance 27.72mm behind the cornea and (b) computational time, as a function of sampling density for different method of interpolation in the finite element ray tracing algorithm. The position “Raw data” in the horizontal axis denotes results from the ray tracing on a direct Delaunay reconstruction from the raw elevation data (with no sampling or Zernike smoothing). For all other cases, the raw data were first approximated by a 7th order Zernike polynomial and then sampled with different densities. The results for semi-analytical ray tracing on the Zernike surface are shown for comparison, as they do not depend on the sampling density (number of facets).

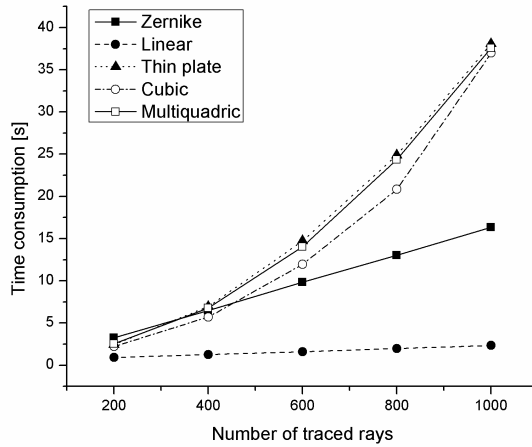


Figure 3.8. Time consumption as a function of number of traced rays for finite elements ray tracing algorithm with various method of data interpolation in comparison to semi-analytical procedure used with Zernike polynomials expansion.

3.4 Conclusions

The algorithm presented, based on a Delaunay-reconstructed surfaces, allows performing easily a ray tracing on a regular or random grids of points from either analytical, noisy or free-form surfaces. We have shown that the ray tracing through analytical surfaces is accurate even for reasonably low density samplings (when compared to analytical results provided by optical analysis software). However, as in many other finite element methods, denser sampling improves accuracy further when compared to the results obtained with use of analytical methods.

The algorithm is able to determine the points of intersection and normals on noisy surfaces. The accuracy depends on the surface roughness, and decreases with increasing height RMS and decreasing correlation length.

In principle, the Delaunay decomposition method is very flexible, allowing tracing rays through any optical surface given by discrete data points. Unlike with modal surface fitting (such as in Zernike polynomials), surfaces are not necessarily smoothed. Together with well-described algorithms for tracing rays through gradient index structures [Moore et al, 1976, Sharma et al, 1982, Marchand, 1988 and Egorchenkov et al, 2001] it can serve as a powerful tool for optical computations. The only limitation is the memory usage of the processing unit and the computational time which might be very large for tracing many rays through densely sampled surfaces. We have

shown that all methods tend converge for densities above 40x40 samples. When the Delaunay decomposition is combined with a thin plate or cubic interpolation, the results from ray tracing are similar to those when a Zernike fitting and semi-analytical ray tracing of surface is used, for densities as low as 7x7 samples. The advantages of the Delaunay decomposition rely on their relative simplicity, higher speed and a much more efficient way to estimate the surface normals.

The presented method can be used for to test the influence of the quality of the topographical surface reconstruction on the optical performance, as well as the influence of the noise or high frequency irregularities of the realistic surface on the performance of the optical elements; or the reversed question (i.e. what is the influence of the smoothening of the raw topography data of the real surfaces on their optical performance). Applications of this algorithm include the estimation of the aberrations produced by realistic surfaces and the application of optical distortion correcting algorithms.

Chapter 4

Optical Coherence Tomography for quantitative surface topography

This chapter is based on the article by Ortiz, S. et al “Optical Coherence Tomography for quantitative surface topography” Applied Optics, Vol. 48, Issue 35, pp. 6708-6715 (2009). The coauthors of the study are: Damian Siedlecki, Laura Remón and Susana Marcos. The development of this work was performed at Instituto de Óptica “Daza de Valdes”. The contribution of the author of this thesis was to address the measurement and correction of fan distortion in optical coherence tomography (OCT). Computer simulations were performed to quantify the effect and to evaluate its dependency of the scanning mirror separation and design of the collimating lens, as well as to estimate the optimal axial position of that lens to minimize the fan distortion, We also developed a numerical algorithm based on 3-D ray propagation for the correction of the residual fan distortion. The effect was studied experimentally using a custom developed time-domain OCT in a Michelson configuration provided with a confocal channel. The accuracy of the fan distortion correction algorithm was tested on samples of known dimensions (flat surfaces and spherical lenses).

4.1. Introduction

The OCT inherent ability to resolve differences in distance within microns and the possibility of introducing fast optical scanners makes of the OCT a perfect tool to act as a topographer. So far there are only few examples in the literature using OCT for quantitative surface characterization [Kim et al, 2009 and Podoleanu et al, 2004]. The main limitation for the direct quantitative analysis of surfaces is the so-called fan distortion. Fan distortion is a set of aberrations associated with the scanning system architecture of the optical setup that typically consists of two-mirror and two-axis scanning system [Li et al, 1995, Li et al 1997, Marshall, 1980, and Li et al 2008]. Such scanning systems are used in most of the OCT devices. One of the components that have the major contribution to the magnitude of fan distortion is field distortion and astigmatism. These Seidel's aberrations result on a deformation of the image of the tested sample [Xie et al, 2005 and Chen et al, 2007], and in the OCT devices arise primarily from the separation of the mirrors in the mentioned two-axis scanning system (see Figure 4.1). The other components to the distortion arise from the precision of the flatness of the scanner mirrors [Xie et al, 2005] or slight misalignment of the light beam to the axis of rotation of the mirrors. However, with a proper calibration of the fan distortion introduced by the optical scanner, OCT can be used as a tool to retrieve geometrical parameters of surfaces. Some authors [Westphal et al, 2002] have addressed fan distortion in an OCT system, in which the rastering was produced by a non linear scanning system (consisting of resonant mirrors plus non-telecentric scanning). They proposed to correct the distortion with the use of images taken axially around the confocal position of the beam, without taking into account the 3-D information provided by the OCT. Therefore the proposed procedure can be applied only to 2-dimensional imaging, not to 3-D topography. Therefore the topic still seems to be open and a solution timely, as current OCT systems start allowing real-time 3-D images acquisition in living samples.

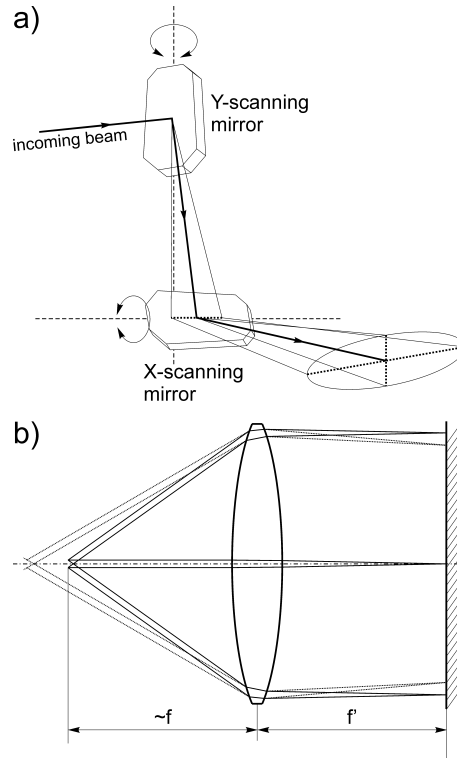


Figure 4.1. Separation of mirrors in the scanner (a) results in a different beam deflections after being refracted by a collimating lens (b) in an OCT setup.

In the current study we will present a proper and reliable calibration that is critical if the OCT setup is to be used for quantitative measurements of the surface topography. We also present some experimental results of topographic measurements of test samples of known geometry, in particular intraocular lenses (IOLs).

4.2. Methods

4.2.1. Modeling of the fan distortion

When imaging even perfectly flat surfaces by means of 3-D OCT devices, they become curved. This phenomenon can be described as a combination of at least two possible effects: (1) architecture of the scanning system, with relatively significant influence of spatial separation of the mirrors; (2) design, position and alignment of the collimation lens in relation to the mirrors of the scanner.

There exists a variety of designs and architectures of 2-D scanning systems [Montagu et al, 2004]. One feature that is common to most of them is that the mirrors responsible for angular beam deflection are

separated by some distance. In a pre-objective scanning configuration, it is equivalent to the situation presented in Figure 4.1b, when the origins of the fan in saggital, and meridional cross-sections (solid and dotted lines, respectively) are separated by the distance between mirrors in the scanner. Therefore, the incident angles of the marginal beams in two perpendicular cross-sections are different. This configuration results in different exit angles of off-axis beams (the further from the optical axis, the larger difference in angle). This leads to relevant differences in the optical path, which finally results in the distortion of a perfectly flat surface that can be seen in raw OCT images. The effect is shown schematically in Figure 4.2 which presents two OCT images of a flat optical surface (mirror) captured in two perpendicular directions. In this figure the effect of fan distortion can be clearly noticed: the flat surface became curved, and in one cross-section the curvature is larger than in the other.

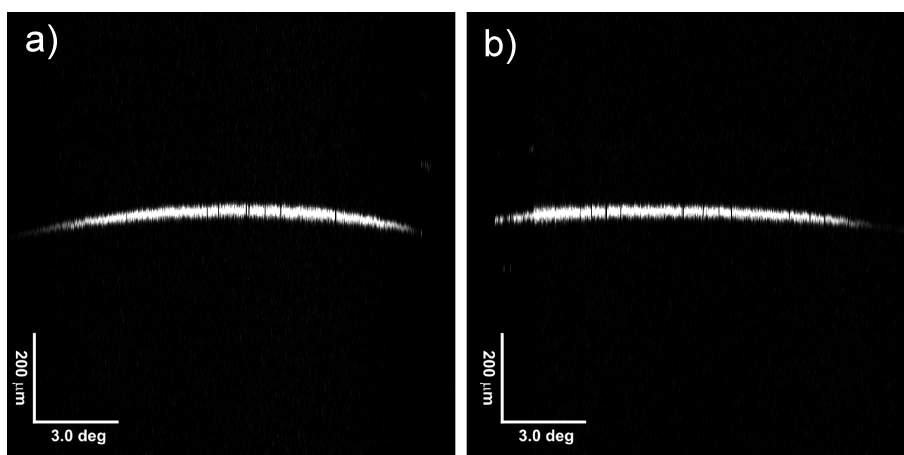


Figure 4.2 OCT images of a flat optical surface (mirror) captured in two perpendicular directions: a) vertical and b) horizontal.

The design, position and alignment of the collimating lens have a very significant impact on the magnitude of fan distortion. We developed an algorithm in Matlab® for simulations of the beam propagation in the OCT sample arm of the interferometer towards the sample. In this algorithm it was assumed that small-diameter beams used in the OCT scanning systems can be well described by single rays, and that the rays are propagated according to the laws of geometrical optics. In order to perform realistic simulations, the algorithm can take into account the eventual non co-axial alignment of the scanner mirrors with respect to the chief ray, various separations between the scanning mirrors and

various locations of the collimating lens (regarded as a thick lens) that focuses the beam on the sample. The algorithm is able to estimate the optimal lens position by minimizing the *rms* of the average value of the directional cosines of propagation vectors behind the lens. Experimentally, this can be achieved by moving the lens along the optical axis. It should be noticed that, if the system is free of aberrations, the propagation vectors of the rays are perfectly parallel to each other and their *rms* is equal to zero.

4.2.2. Estimation of the residual fan distortion

Even for the optimal lens position, there is some residual distortion that needs to be estimated and corrected numerically. For this purpose, a flat sample plate with a diffuse surface was used for calibration and tested on the experimental setup described in the Section 4.2.1. This calibration plate contains a black grid on a white background, with an interline separation of 1 mm. Series of grid images through the exact confocal position of the sample were obtained using both the confocal and the 3-D OCT channels. The images captured with use of confocal channel were processed using a Hough transform [Fernandes et al, 2008] (a more efficient algorithm than simple edge detection) to detect the lines of the grid in the image. The detected lines were fitted to parabolas (in the angular system of coordinates) and the intersections of vertical and the horizontal parabolas were recognized as the nodes of the grid (the steps of processing the confocal data are presented in Figure 4.3). This way each node can be expressed both in Cartesian coordinates $N_{ij}(x, y)$ and in angular coordinates $N_{ij}(\theta, \varphi)$, where i and j denote the number of row and column related to the reference node $(0, 0)$, which is not affected by distortion. It should be noted that in the confocal image the angular system of coordinates is rectangular, as shown in Figure 4.4. The conversion between these two systems is related to the length of arc calculated for the Equations of the parabolas given by $f(\theta)$ and $f(\varphi)$, which for each node can be expressed by Equation 4.1:

$$N_{ij}(x, y) = \begin{cases} x_i = \int_0^{\theta_i} \sqrt{1 + f'(\theta)} d\theta \\ y_j = \int_0^{\varphi_j} \sqrt{1 + f'(\varphi)} d\varphi \end{cases} \quad Eq.4.1$$

where (x_i, y_j) and (θ_i, φ_j) are the coordinates of the each node N_{ij} in Cartesian and angular coordinates, respectively. This way, each point in the confocal image can be converted to the Cartesian coordinates by calculating:

$$P_{kl}(x, y) = \begin{cases} x_k = \frac{\theta_k}{\Theta_m} X_m \\ y_l = \frac{\varphi_l}{\Phi_n} Y_n \end{cases} \quad Eq.4.2$$

where (x_k, y_l) and (θ_k, φ_l) are the coordinates of the each point P_{ij} in Cartesian and angular coordinates, respectively; (X_m, Y_n) and (Θ_m, Φ_n) are the coordinates (related to reference point $(0,0)$) of the node N_{mn} (in Cartesian and angular coordinates, respectively) which is closest to the point of interest P_{ij} . This conversion was used to obtain the angular input of the scanner into spatial coordinates.

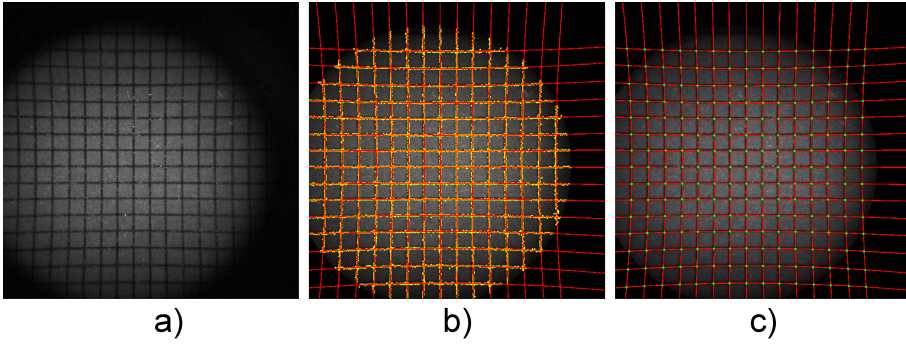


Figure 4.3. Steps of the calibration procedure using the confocal channel: a) original confocal image; b) grid line detection (points) and their approximation by parabolas (lines); c) detection of the grid nodes (intersection points of the parabolas).

The 3-D OCT images can be expressed in scanner angular coordinates plus a length to a reference point: (θ, φ, L) , where θ is the elevation angle, φ is the azimuth angle and L is the Euclidean distance (length) with respect to a reference point, being the minimum of the axial scanning range (to which any other axial scan range must be referred). The correspondence between the angular scanner coordinates and the

spatial coordinates on the image is achieved through the conversion factor obtained for each axial location from confocal channel, as explained before, allowing to express each OCT image of the series as (x, y, L) , where x and y are the horizontal and vertical coordinates, respectively and L is the uncorrected axial component (length). Correction of L is achieved by 3-D ray tracing in space. Rays can be described by the general ray Equation in a vectorial form (Equation 4.3):

$$\vec{R}_i = O_i + L\hat{T}_i \quad Eq.4.3$$

where O_i is the origin point of the i -th ray and \hat{T}_i is the normalized directional cosine of the ray.

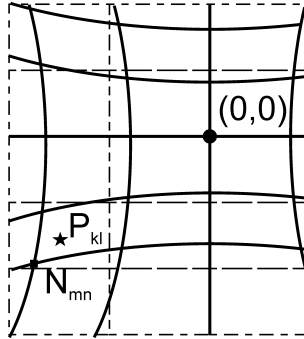


Figure 4.4. Point P_{kl} represented in angular (dashed lines) and Cartesian (solid lines) systems of coordinates. The origin of both systems is at the same point $(0,0)$ - the point not affected by distortion. Point N_{mn} is the closest node to point P_{kl} .

The directional cosines can be achieved by capturing a series of confocal images together with 3-D OCT measurements at each axial sample location around the confocal plane (the distances to the reference plane need to be known), and then identifying the coordinate positions of each pair of angles introduced to the scanner in each of the confocal images, tracking their relative movement spatial system coordinates (from one confocal image to the next one) as shown in Figure 4.5a. By fitting the x_i and y_i components to a line by linear regression, the vertical and horizontal coordinates at the origin, as well as the components of the directional cosine can be obtained. By using the regression analysis, the effect of the noise due to the introduction of

the diffuse plate and to mechanical instability of the motor is minimized:

$$\begin{cases} x_i = x_0^i + LT_x^i \\ y_i = y_0^i + LT_y^i \end{cases} \quad Eq.4.4$$

where x_0^i and y_0^i are the horizontal and vertical coordinates of the origin for i-th ray.

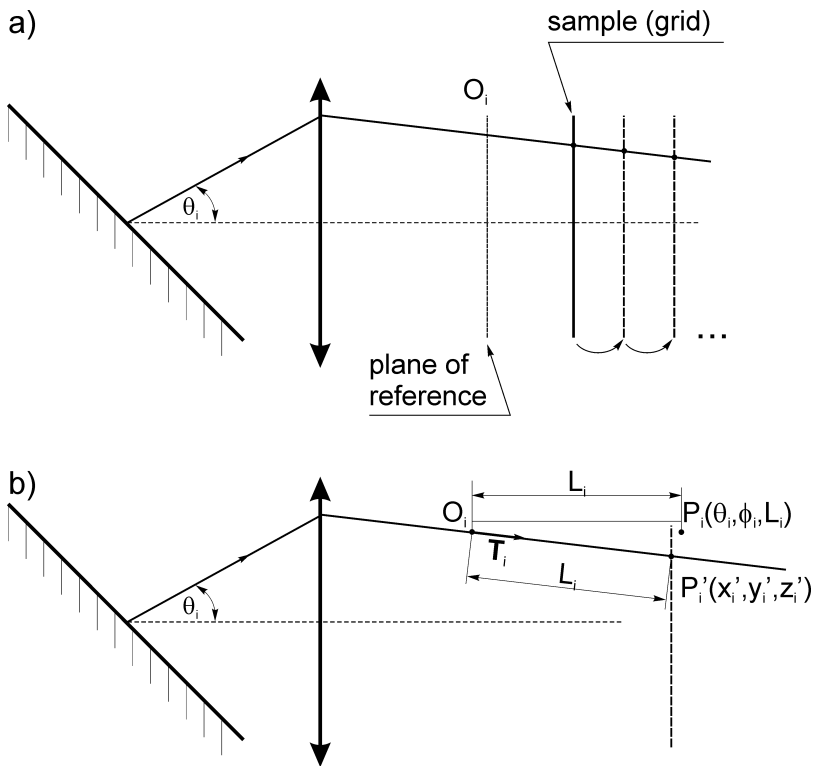


Figure 4.5. a) Capture of a series of confocal images at different axial grid positions for the purposes of system calibration; b) Schematic explanation of the correction procedure. Point P_i is obtained on the OCT and expressed in angular system of coordinates (θ, φ, L) , where θ and φ are the angles of the scanner, and L is the distance from the reference point O along the ray given by the propagation vector T . Point P'_i is the point after correction, in Cartesian coordinates.

Once the horizontal and vertical components of the directional cosine have been obtained, it is straightforward to get the axial component,

since this vector is normalized. Finally, by selecting the origin of the axial component as 0 the real axial coordinate can be obtained:

$$z_i' = L\sqrt{1 - (T_x^i)^2 + (T_y^i)^2} \quad Eq.4.5$$

4.2.3. Fan distortion correction

When the fan distortion of the setup is characterized, it can be easily removed using a general 3-D ray Equation: a reference point in space O and the directional cosine of a ray at this point \hat{T} . Any point at this ray can be placed by simple substitution of the angles in Equation (4.4). If the particular scanner angle was not measured experimentally, the correspondence can be obtained from a bicubic interpolation of the measured angle. Therefore, since the scanning beam can be approximated by a single ray, and each pair of angles of the scanning mirrors is related exactly to one normalized vector of propagation \hat{T}_i , the information achieved from the calibration of the setup (from the scheme presented above) can be used to obtain the coordinates of the normalized vector of propagation \hat{T}_i . Once it is obtained, the corrected coordinates of the point P_i' on a surface can be found by multiplying the distance obtained from OCT L_i by the directional cosine vector and adding the reference point for this specific ray.

$$P_i' = O_i + L_i\hat{T}_i \quad Eq.4.6$$

Figure 4.5b presents the schematic explanation of the method. A useful feature of this algorithm based on ray propagation expressed in angular notation is that the distortion is constant and does not depend on the axial position of the sample, unlike the Cartesian coordinates. For this purpose, the shape of the examined samples in the uncorrected OCT images does not change with the axial position of the sample (however, the image quality may change).

4.2.4. Validation on surfaces of known geometry

In order to validate the fan distortion correction method, its accuracy was tested on several surfaces of known geometries. These surfaces were: (1) a flat optical surface; (2) a spherical lens (used in previous studies as an artificial cornea [Gora et al, 2009]; (3) a biconvex commercial PMMA spherical IOL (anterior and posterior surface).

The spherical surfaces were measured additionally by confocal microscopy based non-contact profilometry (PLm 2300, Sensofar-Tech SL, Terrasa, Spain) in order to have the values of reference.

Each surface was measured by the described OCT setup (55 B-scans, 55 A-scans each). The angular dimensions used to scan the surface differed across samples: -4.5 to 4.5 deg for the flat surface, -3.3 to 3.3 deg for the artificial cornea, and -1.5 to 1.5 deg for the intraocular lenses. The 3-D data were processed with use of custom algorithms for line detection and surface identification. Once the cloud of points belonging to every surface was identified, the algorithm to correct fan distortion was applied and then the points were fitted by analytical Equations of spheres using a least-mean-square algorithm. The fits were performed on the raw points, as well as on the set points after fan distortion correction. The radii of curvature of each surface was obtained and compared to the values with use of non-contact profilometer.

4.3. Results

4.3.1. Simulation of fan distortion

We introduced the parameters of our OCT system in the simulation presented in Section 2.1, and applied a minimization algorithm to determine the optimal axial location of the collimating lens that provided the lowest level of fan distortion. The effect of the separation between the scanning mirrors and the focal length of the collimating lens were also tested.

The most relevant geometrical parameters for the model are the distance between centers of mirrors and collimation lens (4.67 mm), radii of curvature (39.070 mm and infinity), thickness (5.122 mm) and refractive index of BK7 for the wavelength 0.820 mm) of the collimated lens. Simulations were performed for a random pattern of 200 rays in the 3-D-ray tracing.

Figure 4.6a presents the results of simulation of the magnitude of aberrations (*rms*) as a function of the position of the lens and the separation between the scanning mirrors. The magnitude of the distortion is expressed in terms of the *rms* of the ray deviations with respect to theoretical collimation. The position of the lens is referred to the position of the vertical scanning mirror. The global minimum can be observed for a telecentric configuration, which is possible only for scanning in one direction (B-Scan). For any other distance between the scanning mirrors, there exists one position of the collimating lens,

which corresponds to the minimum of rms for this particular configuration. This means that the optimal position depends strongly on the separation distance between the scanner mirrors and the design of the lens (which affects its spherical aberration). Figure 4.6a shows the magnitude of the fan distortion as a function of the focal length of the collimating lens placed in its optimal position. Figure 4.6b presents a 3-D plot of the fan distortion simulated for the architecture used in our experimental system. Points on this plot correspond to the beams having the same optical path. The astigmatic shape of this distortion arises from the separation of the scanner mirrors: a larger separation results in a larger peak-to-valley difference of the distortion. For the collimating lens of our OCT system and the scanning mirror separation in our galvanometer system the optimal position for the collimated lens (marked with an asterisk in the Figure 4.6a) was 71.42 mm from the vertical scanner mirror.

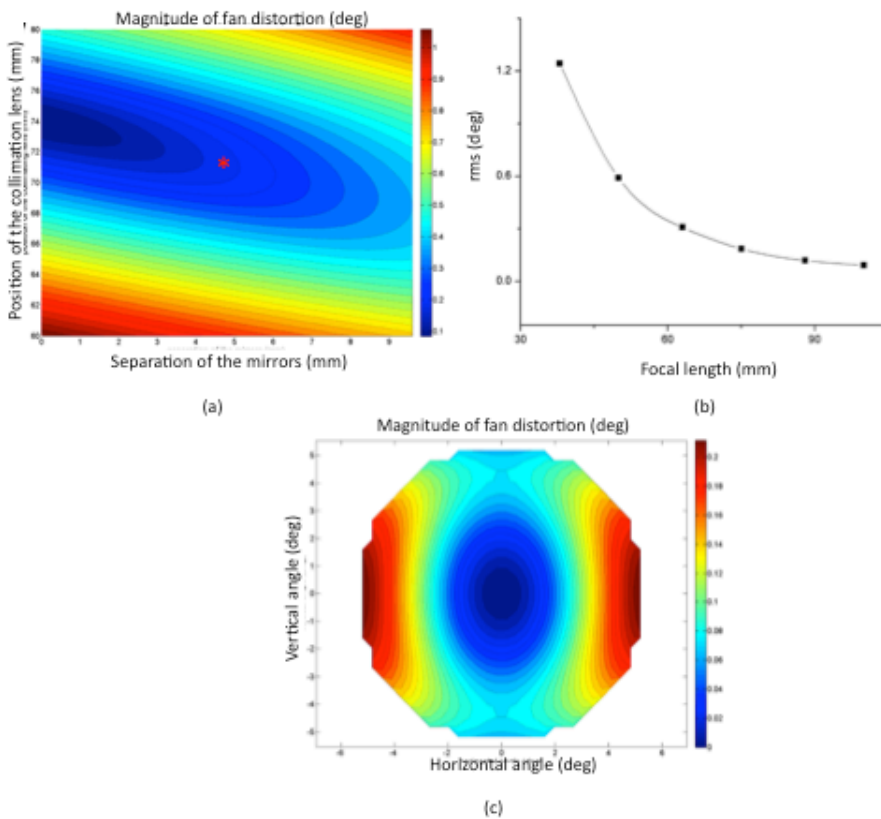


Figure 4.6. Results of simulations of the fan distortion: a) distortion as a function of the lens position and separation between scanner mirrors, b) distortion as a function of the focal length of the collimating lens (in its optimal position) and c) fan distortion for the architecture used in the experiment.

We found that the optimal lens position was also depended on the aperture size, due to the influence of the spherical aberration of the lens on the fan distortion. We repeated the simulation for different apertures (radius ranging from of 1 mm to full aperture of the lens in 1-mm steps). Figure 4.7 shows the dependence of the optimal distance with lens aperture, as predicted from the simulations.

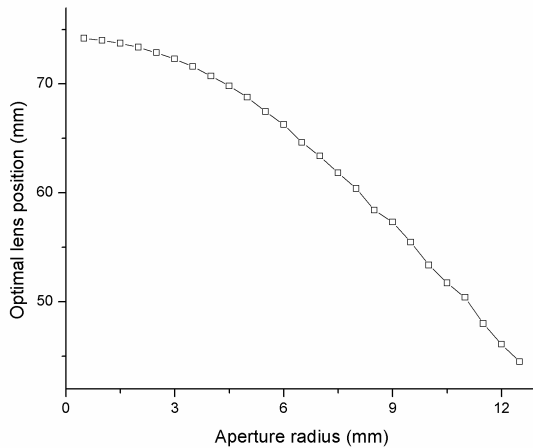


Figure 4.7. Optimal lens position as a function of lens aperture radius.

4.3.2 Residual fan distortion in the experimental system

In the experimental setup we placed the lens at the optimal distance estimated from the simulations, as both the lens parameters and scanner architecture of the experimental system were used in the model. Despite obvious technical difficulties in setting the exact distance, the reconstructed OCT data of a flat surface (optical mirror) is very similar to the simulated one (presented in Figure 4.6c.), which confirms our predictions.

4.3.3 Correction of fan distortion of OCT images

The developed fan correction distortion algorithm was applied to the correction of residual distortion in 3-D OCT images of a flat surface, shown in Figure 4.2. Figure 4.8 shows the efficiency of the correction applied to the distortion data of a flat surface. The deviation from flatness of the corrected surface is very small ($rms < 2 \mu m$, while the peak-to-valley magnitude of the distortion was about $90 \mu m$).

The correction of the residual fan distortion was also applied to 3 PMMA spherical surfaces of known radii of curvature. The results are shown in Table 4.1. Raw elevation data, profilometric data and

elevation data after fan distortion correction were fitted by spherical surfaces using the same fitting algorithm.

Table 4.2. Radii of curvatures of tested surfaces: measured with use of non-contact profilometry and OCT (before after distortion correction).

Type of data	Profilometer	OCT before correction ²	OCT after correction
Anterior IOL surface [mm]	17.66	17.40	17.70
Posterior IOL surface [mm]	10.70	10.86	10.76
Artificial Cornea [mm]	7.76	8.73	7.77

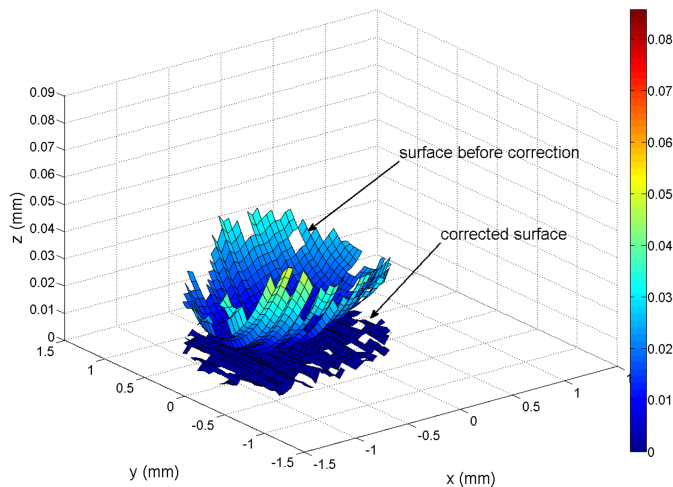


Figure 4.8 Comparison of topographies of a flat surface obtained by means of OCT before and after numerical correction. The shape of uncorrected surface is given by simple conversion from the angular to Cartesian coordinates.

4.4. Conclusions

We have shown the presence of fan distortions in OCT system and proposed a method for correction. The effect has been shown on a custom laboratory time-domain OCT system, in which a confocal has proved very useful tool for calibration and sample alignment.

The magnitude of fan distortion depends on the distance between scanning mirrors, as well as the position of the collimation lens and its

² Values calculated by simple conversion from the angular to Cartesian coordinates.

power and aperture. Fan distortion was minimized by positioning the collimated lens, according to predictions from 3-D ray tracing model. Fan distortion can be also reduced by increasing the focal length of the collimating lens. Algorithms to correct the residual fan distortion have also been proposed and applied to real surfaces imaged with the OCT device. After correction, we showed discrepancies of less than 2 mm RMS flatness on flat surfaces, and less than 0.2% in the radii of curvature of spherical lenses with respect to values measured with other method, while the uncorrected data showed discrepancies up to 90 mm for flat surface and up to 12% in the radii of curvature. We conclude that after application for fan distortion OCT can be reliably used for topography optical surfaces. OCT systems may be more versatile than other non-contact profilometry devices, as can work both on transparent and diffusing surfaces, and the lateral range of application is only limited by the angular range of the galvanometric scanners. The lateral resolution is hardware limited and depends mainly on the sample beam diameter and optics and the quality of scanners used in the setup, while the axial resolution depends on the light source bandwidth and subpixel precision of the edge detection algorithms. Also, with some modifications in the calibration method (based on other approaches rather than the use of a confocal channel), the fan distortion correction algorithms described here can also be applied to spectral OCT systems [Ortiz et al, 2010], which can then be used as reliable corneal topographers (Chapter 7) [Gora et al, 2009, Grulkowski et al, 2009 and Ortiz et al, 2011].

Chapter 5

Optical distortion correction in Optical Coherence Tomography for quantitative anterior segment three-dimensional imaging

This chapter is based on the article by Ortiz, S. et al “Optical distortion correction in Optical Coherence Tomography for quantitative anterior segment three-dimensional imaging” *Optics Express*, Vol. 18, Issue 3, pp. 2782-2796 (2010). The coauthors of the study are: Damian Siedlecki, Ireneusz Grulkowski, Laura Remon, Daniel Pascual, Maciej Wojtkowski and Susana Marcos. The work was developed at Instituto de Óptica “Daza de Valdes”. The contribution of the author of this thesis was the development of a method for 3-D optical distortion (refraction) correction on anterior segment OCT images has been developed. The method consists of 3-D ray tracing through the different surfaces, following denoising, segmentation of the surfaces, Delaunay representation of the surfaces, and application of fan distortion correction. The correction has been applied theoretically to realistic computer eye models, and experimentally to OCT images of an artificial eye with a Polymethyl Methacrylate (PMMA) cornea and an intraocular lens (IOL), an enucleated porcine eye, and a human eye *in vivo* images were acquired using two OCT laboratory set-ups (time domain and spectral systems). Data are analyzed in terms of surface radii of curvature and asphericity. Comparisons are established between the reference values for the surfaces (nominal values in the computer model; non-contact profilometric measurements for the artificial eye; Scheimpflug imaging for the real eyes *in vivo* and *in vitro*). The results from the OCT data were analyzed following the conventional approach of dividing the optical path by the refractive index, after application of 2-D optical correction, and 3-D optical correction (in all cases after fan distortion correction).

5.1. Introduction

Anterior segment imaging has received a strong attention in the last few years. The availability of different imaging modalities and the increased resolution and visibility of the ocular structures has allowed several of the new developments to have an impact on the clinical practice. However, the increased quality of the images obtained from these methods has not been in general paralleled by the quantitative analysis of the raw data. Quantitative biometry is essential in many areas in physiological optics (i.e. customized eye modeling [Rosales et al, 2007] understanding of the structural changes in the crystalline lens during accommodation [Rosales et al, 2007] and aging [Dubbelman et al, 2005], crystalline lens gradient index of refraction reconstruction, etc...) and ophthalmology (i.e. changes in the anterior and posterior corneal topography after refractive surgery [Moreno-Barriuso et al, 2001],[Perez-Escudero et al 2009] and the accuracy [Norrby, 2008] and evaluation of cataract surgery [De Castro et al, 2007],[Marcos et al, 2007], among others). Optical Coherence Tomography (OCT) is one of the most versatile and promising imaging techniques of the anterior segment of the eye, due to its high resolution, and the possibility of imaging the anterior and posterior cornea, the iris and the crystalline lens over a large cross- sectional area. Recent studies [Grulkowski et al, 2009] have shown the possibility of increasing the range of OCT imaging from the anterior cornea to the posterior surface of the crystalline lens. OCT presents advantages over other techniques such as Purkinje (limited to the estimation of lens alignment, keratometry and phakometry) and Scheimpflug imaging (which has lower resolution, and the posterior lens visibility is limited by the pupil aperture). However, unlike exceptionally in OCT, Purkinje and Scheimpflug imaging have been thoroughly validated and corrected from the optical distortions produced by the preceding ocular surfaces and the accuracy of the results demonstrated using model eyes with known geometry [Perez-Escudero et al, 2009, de Castro et al, 2007, Rosales et al, 2006, Dubbelman et al, 2002, and Rosales et al, 2009].

In general, OCT is subject to two types of distortion: fan and optical distortions. Fan (field) distortion, as it was explained in Chapter 4, is related to the rastering of the surfaces with optical scanners. If the fan of principal rays is not perfectly flat with respect to the optical axis of the system, then the first surface it is not well reproduced and even a flat surface becomes curved on the image. This effect as it was explained in Chapter 4 can be characterized and minimized numerically

by application of correction algorithms based on ray propagation, Snell law and Fermat principle.

Optical distortion is an effect produced while imaging a sample embedded in a medium different from vacuum (air), and therefore the rays are bended by the effect of refraction by preceding surfaces. This produces a very significant loss of the geometrical features of the observed surface, and therefore its geometrical parameters, such as curvature and thickness cannot be retrieved directly from the image. Imaging the inner layers in the eye is therefore subject to this type of distortion, as each layer differs in shape and structure [Jakobiec, 1982] and will show a different index of refraction. Apart from the strongest refractive effect at the air-anterior cornea (or tear film) interface, the major effects in a normal eye will happen in the posterior cornea-aqueous humor, aqueous humor-anterior lens, and posterior lens-vitreous humor interfaces.

The optical surfaces such as those in the eye are generally more complicated because they do not exhibit rotational symmetry and are not centered around an optical axis. As a consequence, the technique of distortion correction based on 2-D ray tracing seems to be insufficient. Therefore, a complete optical distortion correction requires a 3-D approach. Providing accurate topographies of the internal surfaces of the eye requires correction of the optical distortion, and this problem, to our knowledge, has not been addressed before in 3-D. Only a few studies have addressed the problem of optical distortion, and have proposed methods for 2-D corrections for OCT images [Podoleanu et al, 2004, and Westphal et al, 2002], based on the Fermat's principle. While this is an excellent first approach to the problem and undoubtedly better than the standard correction consisting of dividing the OCT optical distances by the refractive index, we will show that the errors of minimizing parameters that define the surfaces are better estimated correcting for 3-D instead of doing it only on cross-sectional images. Podoleanu et al. [Podoleanu et al, 2004] showed corrections of cross-sectional images of an intraocular lens (IOL), an intralipid drop and the anterior chamber angle in a living human eye. A limitation of the work is the use of analytical fits of circles (according to Gullstrand model) to the surfaces, and therefore ignoring local irregularities of the surfaces. Westphal et al. [Westphal et al, 2002] recognized the potential improvement of applying the optical correction in 3-D, instead of 2-D, since the normal has three components, as well as the refracted directional cosine.

In this chapter we present a numerical method to correct for the optical distortion of 3-D data from OCT systems. Experimental data on lenses (artificial cornea and IOL) with known geometrical parameters and in real eyes (porcine eye *in vitro* and human eye *in vivo*) were collected with two calibrated laboratory OCT set-ups, one time-domain OCT (TD-OCT) system and the other a spectral OCT (SDOCT) system. Previously to the optical correction, the raw images were corrected from fan distortion [Ortiz et al, 2009b]. The images are also segmented using custom-developed algorithms and fitted by a Delaunay surface decomposition [Ortiz et al, 2009a], which is used to perform 3-D Ray Tracing. The obtained geometrical parameters on the artificial cornea and IOL were validated against a non-contact profilometer, while a porcine and a human cornea were validated against a calibrated Scheimpflug imaging system.

5.2. Methods

5.2.1. Theoretical considerations

Any low-coherence interferometry system records optical paths. The easiest and most frequent method for reconstructing the position of the surfaces and interface distances is just by dividing the recorded optical paths by the value of refractive index without taking into account the refraction effect on the optical surfaces [Wang et al, 2002, and Kim et al, 2009]. Although this approach can be justified for the paraxial region and coaxial surfaces, where the axial ray goes through the optical system without being refracted, it cannot be applied for outer (peripheral) regions. The scanning rays in an OCT system are generally characterized by angular coordinates (θ, φ) of the scanner. Even though the OCT may be calibrated and the angular coordinates can be converted directly to spatial (x, y) coordinates, such calibration is valid only for the first surface, as it is the only one that is reached by parallel beams (assuming the fan distortion can be negligible or has been corrected [Ortiz et al 2009b]). For this reason, a simple division of the optical path by the value of refractive index of the media, which is the simplest and the most common way to correct the optical distortion, is insufficient for retrieval of the correct physical distances and dimensions of the sample.

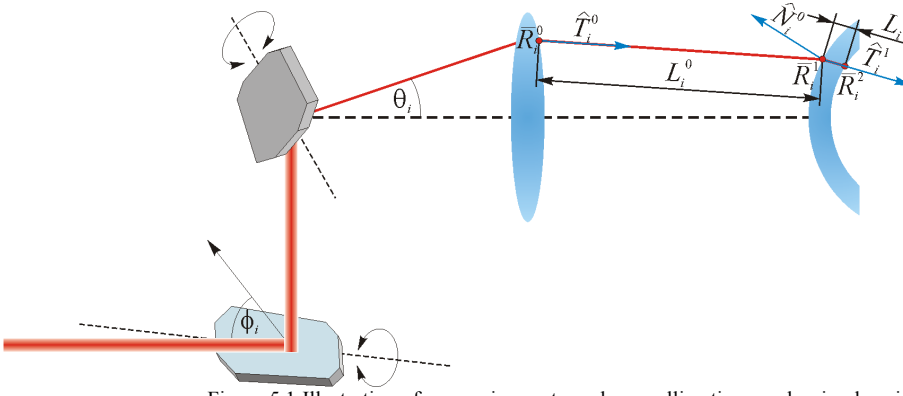


Figure 5.1 Illustration of a scanning system plus a collimation-condensing lens in an anterior segment OCT system. See text for details.

Figure 5.1 presents an illustration of the sample arm of the OCT measurement configuration, along with a curved sample (of refractive index n^1 , in blue) immersed in an external medium (in white) of refractive index n^0 . The elevation and azimuth angles θ_i and φ_i introduced to the galvanometric scanners define the i -th ray. Once, this ray has been propagated through the lens the outgoing ray defines a reference point \vec{R}_i^0 and a directional cosine \hat{T}_i^0 , where L_i^0 is the distance to meet the surface at the point \vec{R}_i^1 . The normal at the meeting point is denoted by \hat{N}_i^0 . Then, the ray is subject to refraction and it changes its directional cosine \hat{T}_i^1 . If the ray continues propagating through the second medium (in blue), it meets the second interface surface at point \vec{R}_i^2 travelling a geometrical distance denoted by L_i^1 . Therefore every pair of angles of the galvanometric scanner (θ_i, φ_i) can be related to a sampling ray and its Equation in a generalized vectorial form:

$$(\theta_i, \varphi_i) \rightarrow \vec{R}_i^{j+1} = \vec{R}_i^j + L_i^j \hat{T}_i^j \quad Eq.5.1$$

where the subscript i is the number of the ray, and the superscript j denotes the number of the interface.

However, in the OCT image representation the geometrical distances cannot be seen because each single A-Scan represents the optical path of one particular ray. In general the total path D_i of a particular ray (i) can be expressed as the summation of the partial optical paths of every media passed by the ray, assuming that the media are homogeneous the optical distance is simply the multiplication of the geometrical path and the value of the refractive index (see Equation 5.2).

$$D_i^j = \sum_{j=0}^m n^j L_i^j \quad Eq.5.2$$

where n^j is the refractive index of the medium between j -th and $(j+1)$ interface.

This way any OCT A-Scan can be described by two angular coordinates (θ_i, φ_i) and one spatial coordinate D_i .

In order to correct for the effect of optical distortion in general (fan distortion and refraction), it is required to propagate the optical distances obtained by the OCT along the directional cosines of the ray, taking into account refraction effects that happen at each interface between two media of different refractive indices. Starting from the calibrated zero position \bar{R}_i^0 and the initial directional cosine \hat{T}_i^0 the consecutive coordinates (spatial \bar{R}_i^2 and directional \hat{T}_i^2) can be estimated considering that the position of this point (\bar{R}_i^2) is actually a geometrical distance L_i^0 measured along the ray (see Equation 5.1). Once the ray goes through the first surface, it undergoes refraction if the consecutive medium has a refractive index different from air. In order to calculate the direction of ray propagation after refraction, the vectorial refraction Equation needs to be applied [Keller et al, 1950]:

$$\hat{T}_i^{j+1} = \left(\frac{n^j}{n^{j+1}} \right) \hat{T}_i^j - \left\{ \left(\frac{n^j}{n^{j+1}} \right) \hat{T}_i^j \hat{N}_i^j - \sqrt{1 - \left(\frac{n^j}{n^{j+1}} \right)^2 [1 - (\hat{T}_i^j \hat{N}_i^j)^2]} \right\} \hat{N}_i^j \quad Eq.5.3$$

In order to do this, it is required to know the cosine director \hat{T}_i^j of the incoming ray; the refractive index of every media in the ray path $\{n^{j+1}, n^j\}$, as well as the normal vector \hat{N}_i^j to the surface at point of refraction.

In order to apply this procedure computationally we have performed the calculation of the 3-D normal vectors by performing the cross products of the 3-D gradients for vertical and horizontal components. The gradients are obtained (Equation 5.4) by convolving a gradient mask vector in the horizontal direction (M_h) and in the vertical direction (M_v) with the component of the detected points of every surface $\{X^j, Y^j, Z^j\}$ arranged in matrices. Notice that the arrangement of

points corresponding to horizontal, vertical and axial coordinates is denoted in capital letters. The results of the operations are six matrices corresponding to the horizontal, vertical and axial coordinates for the horizontal $\{Gx_h^j, Gy_h^j, Gz_h^j\}$ and vertical $\{Gx_v^j, Gy_v^j, Gz_v^j\}$ components of the gradients.

$$\left\{ \begin{array}{l} \{Gx'_h, Gy'_h, Gz'_h\} = M_h \otimes \{X', Y', Z'\} = \begin{pmatrix} \frac{1}{2} & 0 & -\frac{1}{2} \\ 2 & & 2 \end{pmatrix} \otimes \{X', Y', Z'\} \\ \\ \{Gx'_v, Gy'_v, Gz'_v\} = M_v \otimes \{X', Y', Z'\} = \begin{pmatrix} -\frac{1}{2} \\ 2 \\ 0 \\ \frac{1}{2} \end{pmatrix} \otimes \{X', Y', Z'\} \end{array} \right. \quad Eq.5.4$$

In order to avoid the edge effects of filtering, the boundaries of the matrices are expanded by bicubic local extrapolation. This way the gradients for the three components are obtained in matricial form. Once the vertical and horizontal gradients are obtained, the resultant matrices are cropped by their boundaries to prevent them to be affected by filtering operations and to retrieve its original size.

The local gradient of a point (an element in matrix representation) is obtained by arranging again the matrices by the concatenation operation for the particular element of the gradient matrices. Let us to assume that the i -th ray corresponds to the element (m, n) in matricial notation. Then the horizontal and gradients vectors (\vec{G}_h^j and \vec{G}_v^j) can be expressed by:

$$\begin{aligned} \vec{G}_h^j(i) &= [Gx_h^j(m, n), Gy_h^j(m, n), Gz_h^j(m, n)] \\ \vec{G}_v^j(i) &= [Gx_v^j(m, n), Gy_v^j(m, n), Gz_v^j(m, n)] \end{aligned} \quad Eq.5.5$$

The cross-product of these gradients (\vec{G}_h^j and \vec{G}_v^j), for each point of these matrices, provides non-normalized normal vectors \hat{N}_i^j perpendicular to the surface. The vectors can be normalized as follows:

$$\hat{N}_i^j = \frac{\vec{G}_h^j(i) \times \vec{G}_v^j(i)}{\|\vec{G}_h^j(i) \times \vec{G}_v^j(i)\|} \quad Eq.5.6.$$

As explained above, the point which met the surface acts as the reference for the refracted ray \vec{R}_i^{j+1} , while the new cosine director \hat{T}_i^{j+1} is calculated by the refraction formula. In a last step, as the measured distance between layers is an optical path, it needs to be divided by the refractive index to retrieve the real geometrical aspects of the surface. In such a way, the points under the layer can be shifted following the new ray Equation. This processing should be repeated for every layer until all the points are corrected. Figure 5.2 illustrates the steps of the 3-D correction from the original surfaces to the reconstructed surface after correction.

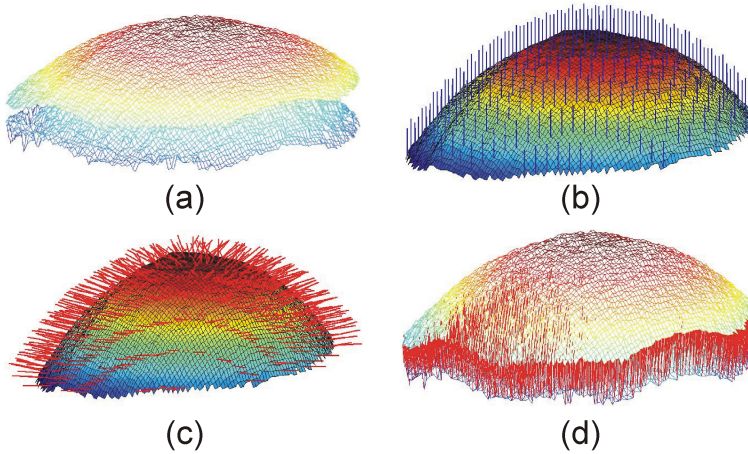


Figure 5.2. a) Original segmented surfaces of a human cornea. b) Anterior surface plus incoming rays in blue c) Normals to the surface the surface in red. d) Refracted rays in red and reconstruction of the second surface.

In this work, two more methods to correct the optical distortion have been implemented for comparison purposes with the 3-D correction previously described. The most common method consists of dividing the optical path by the refractive index of every layer. The so called 2-D Ray tracing method consists of applying the Snell law to every segmented curve of each collected B-Scan. This way the images are corrected from refraction in the very same plane as they are collected. Finally, the resultant layers or surfaces obtained by the three methods are fitted to 3-D conics in order to get relevant parameters (radius or conic constant) of the surface.

In order to predict the magnitude of the effect of the optical distortion in the eye, we simulated OCT imaging of the anterior chamber of a

simple 4-surface computer model (with conic anterior and posterior cornea and lens surface) with realistic amounts of lens tilt and decentration [de Castro et al, 2007, and Rosales et al, 2006] and foveal misalignment [Rosales et al, 2009]. The light was propagated across surfaces by exact 3-D Ray Tracing, the points of intersection between the surface and the beams recorded, and the geometrical (optical) distances evaluated. The resultant four surfaces were corrected from optical distortion by three approaches: (1) the most common method of dividing the optical path by the refractive index, (2) by performing a 2-D Ray tracing of every cross section (B-Scan) and (3) the method of 3-D correction of optical distortions.

5.2.2. *Experimental setups and protocols*

Experimental optical coherence tomography images were obtained using two laboratory anterior segment OCT systems set up at the Visual Optics and Biophotonics Lab (Instituto de Optica, CSIC, Madrid, Spain). One is a classical time domain OCT (TD-OCT) system with a confocal channel, described in detail before [Ortiz et al, 2009b]. The other system is a high-speed spectral OCT (SDOCT) using custom designed software, optics and spectrometer with CMOS camera (Basler Sprint), constructed in collaboration with Nicolaus Copernicus University, Torun, Poland based on commercially available Copernicus OCT device (Poland) [Grulkowski et al, 2009]. The parameters of light sources and resolutions of both systems can be found in our earlier publications.

These two devices were used to collect the 3-D data from different samples. *In vitro* samples (imaged with the time-domain OCT system) included (1) IOL made of PMMA, with spherical surfaces of known radii of curvature (as provided by the manufacturer, AJL Ophthalmics, Spain, and measured using non-contact profilometry); (2) a custom-made contact lens made of PMMA with spherical anterior and posterior surfaces, used in previous studies as an artificial cornea in physical model eyes [de Castro et al, 2007]; (3) a freshly enucleated porcine cornea from a local slaughterhouse. *In vivo* measurements were performed on one normal human eye with the spectral OCT system.

The correction was tested experimentally on a PMMA spherical biconvex IOL and a PMMA spherical convex-concave cornea. The radii of curvature of all the surfaces were measured with a microscopy-based non-contact profilometer (Sensofar Pl μ 2300) which allows surface topographies with an axial resolution of 0.15 μm using a 20X microscope objective. The OCT measurement was done using the

Time-domain OCT, optimized for fan distortion minimization [Ortiz et al, 2009b]. The central wavelength of this OCT is 819 nm. Measurements were taken on a grid of 30x30 scanning angles with an axial depth of 4 mm (and therefore the 3-D set consisted of 30 B-scans, each of 30 A-Scans). The samples were measured in air. The confocal channel was used to align the sample with respect to the optical axis of the sample arm. The 3-D data cloud after denoising, detection and segmentation algorithms was fitted by a spherical using a least-mean-squares algorithm. The index of refraction used in the calculations was 1.4856 for PMMA.

The correction was also tested experimentally on a porcine eye. As the TD-OCT is a slow system the measurements must be done on *in vitro* samples. Besides, the introduction of *in vitro* measurements allows comparing OCT and Scheimpflug at the same conditions without the movements inherent to living tissue. The sample was placed in an eye-holder without any additional pressure control. The experimental procedure consisted of a first measurement with a commercial Scheimpflug imaging rotating camera (Pentacam, Oculus), using 25 cross-sections and its built-in software for 3-D reconstruction, and immediately a 3-D measurement using the TD-OCT, with similar procedures to those explained before. For this experiment, the grid size was distributed regularly in 55 A-Scans x 55 B-scans, which resulted in a tested area of 7.35 x 7.35 mm. Fan distortion correction, and denoising, segmentation, Delaunay decomposition used for ray tracing and fitting to a sphere were performed as described above, prior to optical distortion correction. The corneal refractive index used in the reconstruction was 1.376.

Additionally, 3-D measurements on the left eye of one normal subject were obtained using the laboratory-based spectral OCT. The participating subject was 28 years of age. The study was approved by Institutional Review Boards and followed the tenets of the Declaration of Helsinki. The subject signed a consent form and was aware of the nature of the study. We used 100 horizontal B-scans equally spaced along 10 mm. Each B-Scan was (450x2048 pixels) with an averaging of the 3 rows, resulting in 150x2048 pixels across a 15 x 7 mm region, with a total measurement time of less than 2 s and 800 μ W corneal power exposure at a central wavelength of 840 nm. Surface elevations of the anterior and posterior cornea were fitted by conical surfaces on an optical zone of 9-mm diameter. The image processing procedures were performed as in previous examples with lenses and *in vitro* porcine eye. As in previous experiments, the data were analyzed using

the conventional processing (division by the refractive index of the cornea), and after application of optical distortion correction. The index of refraction used for the cornea was 1.376 and 1.336 for the aqueous humor. The same subject was measured with the Pentacam Scheimpflug imaging system, using conventional clinical protocols (corneal reflex centration, 50 meridians, chin and forehead rest stabilization).

5.2.3 Signal processing

The 3-D images consist of a stack of images (B-Scans) being horizontal cross-sections of the object at different vertical positions. Custom algorithms were developed to reduce noise and improve the detectability of the edge detection algorithms. The routines were written in Matlab® and developed to meet the particular detection architecture of the OCT system (a linear CMOS camera in the SDOCT set up and a photodetector in a balanced configuration in the time-domain OCT set-up). Some studies in the literature analyze the sources of noise in the images [Takada, 1998, Podoleanu, 2000, and, Haskelet al 2006]. If we assume that the noise is random, it can be characterized by its bandwidth, which is directly related to the amount of energy that reaches the detector. In OCT, the energy coming from the sample arm changes for every A-Scan, so that the data processing should be performed for every A-Scan. In the first denoising step a rotational kernel transform (RKT) was used [Rogowska et al, 2002]. Since the denoising processing in OCT images is one dimensional only, the actual vertical kernel was used. Alternatively, a wavelet low-pass filtering processing (from Matlab Wavelet Toolbox catalogue) was used, obtaining similar detection performance. The images were further improved using a contrast enhancement algorithm consisting of the average of a number of points along the A-Scan, which increased the signal in the peaks and averaged noise, which was then subtracted as an offset. Figure 5.3a shows an original image from an artificial eye as captured by the TD-OCT. Figure 5.3b shows the result after applying the denoising and contrast enhancement algorithms. The structural information was distinguished from noise using a simple statistical algorithm. The mean and standard deviation of every A-Scan was estimated within the noise (non-image) region, and then all points above the mean and the standard deviation (multiplied by a value of the threshold) were saved. The number of significant points is further reduced by selecting those belonging to the actual surfaces of the optical components, by finding the separation between consecutive peaks, as we assume that the maximum of the autocorrelation

distribution represents the surface where a scattering event occurs. The accuracy of the detection depends on the stability of superluminescent diode (SLED), on the mechanical stability of the components, and the resolution of the acquisition system. The procedures were applied to every single A-Scan, to create a mesh of points representing the signal from the imaged structures. The classification of peaks and the detection of the maximum value in each A-Scan allow identifying the structures that maximally reflect the light in each A-Scan. Apart from reducing the number of points in the mesh (by a factor of 5-20 per A-Scan) it also allows defining a set of consecutive of layers in the sample.

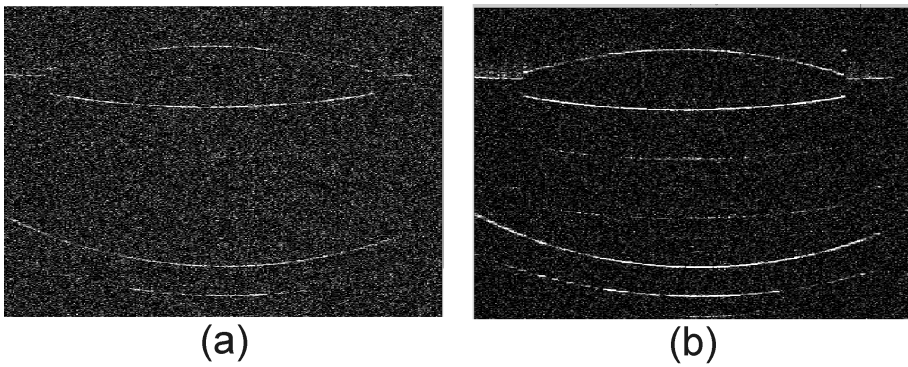


Figure 5.3. a) Cross section of an artificial eye composed by a plastic cornea of PMMA and an IOL obtained by the TD-OCT. b) Resultant image after denoising and contrast enhancement (the additional, lower contrast lines are ghost images and easily removed in the segmentation process).

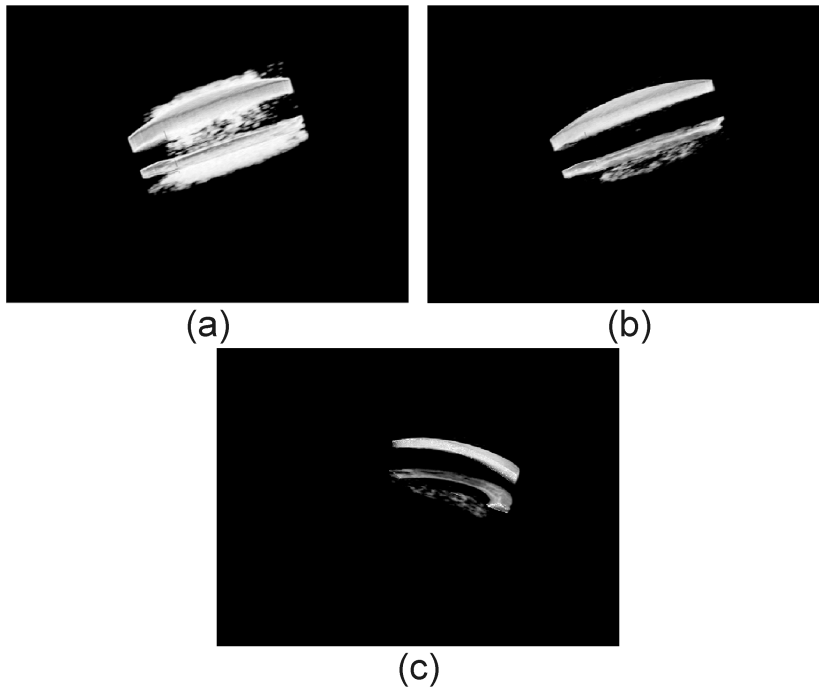


Figure 5.4. a) Movie with the data without filtering with the 3-D neighborhood algorithm. b) Movie showing the data after spurious points removal. c) Movie showing the points and the segmented layers.

Additionally, spurious points were eliminated using a neighborhood algorithm, which allows identifying a layer if there is continuity in at least one of the directions of the tensor mask (which is 3-D convolved with the tensor of data). A tensor data of the size $(m+2) \times (n+2) \times (p+2)$ was used, where m , n and p are dimensions of the data tensor corresponding to the number of images (m), number of pixels in the horizontal direction (n) and in the vertical direction of the image (p) and a tensor mask M_T of size $3 \times 3 \times 3$ Equation (5.7).

$$M_T = \begin{bmatrix} 1 & 1 & 1 \\ 1 & 0 & 1 \\ 1 & 1 & 1 \end{bmatrix} \times \begin{bmatrix} 1 & 1 & 1 \\ 1 & 0 & 1 \\ 1 & 1 & 1 \end{bmatrix} \times \begin{bmatrix} 1 & 1 & 1 \\ 1 & 0 & 1 \\ 1 & 1 & 1 \end{bmatrix} \quad Eq.5.8$$

The convolution provides a set of numbers between 0 and 24 indicating the degree of points detected in the mask neighborhood. The optimal threshold was determined and the algorithm applied to segment the different layers 3-Dimensionally (Figure 5.4).

Once the 3-D cloud of points is obtained, the data need to be corrected for fan distortion. The characterization of the fan distortion is important not only to correct the position of the points, but also to characterize the directional cosine of the propagation vector for every position of the scanner mirrors. Otherwise, the correction of the optical distortion must be done as if the ray that reaches the surface was collimated, resulting in improper propagation vector and therefore in a wrong location of the optically distorted point in space. An algorithm for fan distortion correction proposed in a previous study [Ortiz et al, 2009b] to retrieve the anterior surface quantitative topographical data was applied prior to the optical distortion correction algorithm developed in the current study.

5.3. Results

5.3.1. Computer simulations

We simulated the effects of optical distortion on OCT anterior segment images and studied the errors introduced when applying the most commonly used methods for processing the images: (1) simple division of the optical path by the index of refraction for each A-Scan; (2) 2-D correction of the optical distortion only; (3) 3-D correction of optical distortions. In all cases the fan distortion correction, arising from the scanning architecture of the OCT system was applied [Ortiz et al, 2009b]. The parameters of the elements of the OCT systems used in the experiment (galvanometer scanner and achromatic lens) were introduced in the simulation. The optical system of the model eye consisted of four surfaces simulating cornea and lens. The nominal geometrical features for the ocular surfaces (radii, conic constant and refractive index) of the computer eye model used in the simulations are summarized in Table 5.1. The data for refractive indices of the cornea, lens and ocular media are taken from the literature [Weddell, 1971, Stafford, 2001, Smith, 2003, and Pope et al, 2002], where no gradient index but an equivalent index is assumed for the crystalline lens. The simulation was performed for a square grid of 100 x 100 pixels with a 6-mm side.

Table 5.1. Nominal data for computer eye model used in computer simulations

	Radius [mm]	Conic Constant		Refractive Index	Thickness [mm]
Anterior Cornea	7.87	0.82	Air	1	-
Posterior Cornea	6.4	0.9	Cornea	1.376	0.56
Anterior Lens	11.76	-4	Aqueous humor	1.336	1.56
Posterior	-5.96	-3	Lens	1.399	5.6

Table 5.2 shows the results of radii of curvature of the lens surfaces and the thickness from simulated OCT surfaces by exact 3-D Ray Tracing with the values of the Table 5.1. The data were obtained from the simulated OCT images and reconstructed using the standard processing (division by refractive index), correction of 2-D data, and correction of 3-D data.

For the posterior corneal radius of curvature, the difference between the nominal value and the retrieved value correcting by the refractive only is 3.7 % (equivalent to 0.23 diopters). Applying the optical correction in 2-D the difference is smaller 1.4% (equivalent to 0.09 diopters). The difference between the nominal value and that obtained after 3-D correction is negligible. For the anterior lens radius of curvature, the difference between the nominal value and the refractive index correction is 8.9% and 3.7% applying the 2-D correction (equivalent to 0.38 and 0.17 diopters respectively). For the posterior lens surface radius of curvature the discrepancies are 59.7% and 12.2% (equivalent to 3.4 and 1.0 diopters respectively). In both cases, the difference between the nominal radius of curvature and the value obtained after application of the 3-D correction is lower than 0.3%. For the conic constant the discrepancies with respect to the nominal value when applying only the refractive index correction range from 16.9% for the posterior cornea to 207% for the posterior lens surface. Applying the 3-D correction produces discrepancies of less than 1% in all surfaces.

Table 5.2. Retrieved data from the simulated OCT images, with three different type of data processing

	Refractive Index Correction	2-D optical distortion correction	3-D optical distortion correction
Cornea			
Anterior Radius [mm]	7.88	7.88	7.88
Posterior Radius [mm]	6.64	6.49	6.39
Anterior conic constant	0.83	0.83	0.83
Posterior conic constant	0.77	0.93	0.91
Lens			
Anterior Radius [mm]	12.80	12.20	11.77
Posterior Radius [mm]	-9.55	-6.69	-5.96
Anterior conic constant	-3.22	-2.98	-3.96
Posterior conic constant	-1.45	-1.09	-2.99

5.3.2 Experimental data

In the next stage of our study we acquired images of IOL and cornea of known parameters. Table 5.3 shows the measurements of the surfaces radii of curvature on the IOL and on the PMMA cornea (reference values from non-contact profilometry and estimates from OCT). Figure 5.5 illustrates the effect of the correction. The anterior surface radius of the IOL from TD-OCT shows a difference of 1.0% from the reference value. The posterior radius of curvature of the IOL from TD-OCT (with no correction) differs by 66.7% from the reference value, while after 3-D correction the difference is only 1%. For the PMMA the anterior cornea radius of curvature differs 1.0% from the value of reference. Non-contact profilometry of the posterior PMMA corneal surface was not due to the limitations of the profilometer in measuring convex

OPTICAL DISTORTION CORRECTION IN OPTICAL COHERENCE TOMOGRAPHY FOR
QUANTITATIVE ANTERIOR SEGMENT THREE-DIMENSIONAL IMAGING

surfaces. Nominal values were available from the manufacturer, and those differ less 1.0% from the estimates from TD-OCT after 3-D correction.

Table 5.3. IOL and artificial cornea dimensions: values from manufacturer, and estimates from non-contact profilometry and TD-OCT measurements

	Nominal value	Non Contact profilometry[mm]	OCT without optical distortion correction [mm]	OCT with optical distortion correction [mm]
Intraocular lens				
Anterior[mm]	17.29	17.66	17.82	17.82
Posterior[mm]	-11.04	-10.70	-6.42	-10.82
Thickness [mm]	0.93	0.89	1.37	0.92
PMMA Cornea				
Anterior[mm]	7.8	7.72	7.77	7.77
Posterior[mm]	6.48	-	10.29	6.35
Thickness [mm]	0.55	-	0.87	0.6

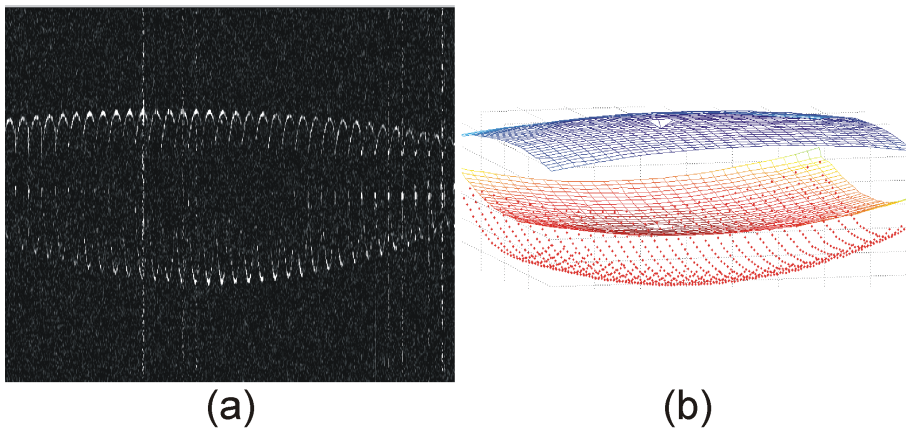


Figure 5.1. a) 2-D representation of all cross sections obtained from the IOL using the TD-OCT. b) 3-D Representation of the surfaces extracted from the IOL, the anterior and the corrected posterior surfaces are wire represented while the raw data without correction is represented by the red discrete points.

In the second stage, experiments were performed using a porcine eye as the object. Table 5.4 shows results of the anterior and posterior corneal curvature of the porcine eye. Data from the Pentacam Scheimpflug imaging (using the commercial software), as well as the values

obtained after standard correction (division by the index of refraction), and the optical distortion correction of TD-OCT images are included. Figure 5.6 shows a cross-section of the porcine eye as obtained from the OCT, after segmentation, and the corrected 3-D result. The agreement between measurements on the anterior cornea obtained with Scheimpflug and OCT confirm the appropriate fan distortion correction of the OCT data. Correction of the optical distortion on the posterior corneal changes the estimate by 6% (the difference is equivalent to 0.39 D) with respect to estimates obtained only dividing by the refractive index. Differences in the measured posterior corneal surface radius of curvature between Scheimpflug and corrected OCT are 1.0%.

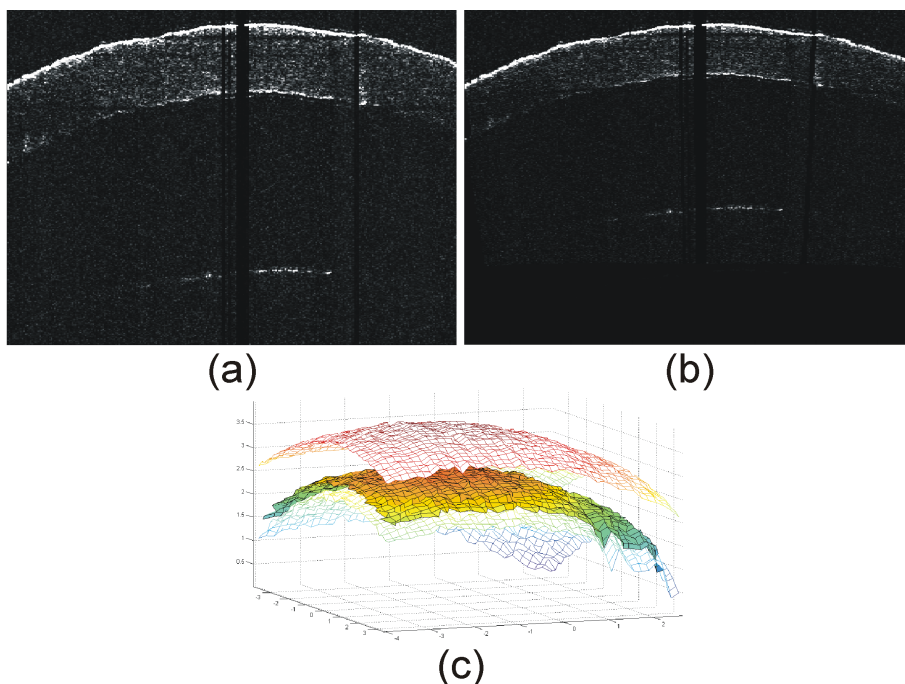


Figure 5.6. a) 2-D representation of a cross-section obtained from the porcine cornea using the TD-OCT. b) The same cross section corrected using a 2-D ray tracing algorithm. c) 3-D representation of the anterior and posterior surfaces extracted from the porcine cornea. The raw data are represented by a mesh and the corrected posterior surface by solid color.

OPTICAL DISTORTION CORRECTION IN OPTICAL COHERENCE TOMOGRAPHY FOR
 QUANTITATIVE ANTERIOR SEGMENT THREE-DIMENSIONAL IMAGING

Table 5.4. Anterior and posterior corneal dimensions of an enucleated porcine cornea: estimates from Scheimpflug imaging and TD-OCT measurements

	Scheimpflug imaging	OCT refractive index corrected	OCT optical distortion corrected
Anterior[mm]	8.62	8.63	8.63
Posterior[mm]	7.37	7.89	7.33
Thickness [mm]	0.87	0.90	0.90

Finally, the correction algorithms were tested on the *in vivo* images of the human eye. In the case of *in vivo* OCT imaging there is a good correspondence between Scheimpflug and OCT anterior corneal radii of curvature (after fan distortion correction): (7.46 and 7.66 mm for the radius of curvature, and 0.42 and 0.54 for the asphericity). Table 5.5 shows results for the posterior cornea of a human eye *in vivo* (data from Scheimpflug imaging, as well as from SDOCT after 2-D optical distortion correction). The differences in the radius of curvature from Scheimpflug and 3-D corrected SDOCT is 2.8%, while the correction of the optical distortion changes the estimate of the posterior radius by 6.2% (with respect to data only divided by the refractive index), equivalent to 0.37 Diopters. The highest differences are observed in the conic constant, where the application of the 3-D correction distortion algorithm modifies the estimate by 73% with respect to the simplest corrections (also increasing the agreement with respect to the Scheimpflug estimate). Figure 5.7 illustrates the differences of correcting by dividing by the refractive index and the 3-D distortion correction in the living human eye.

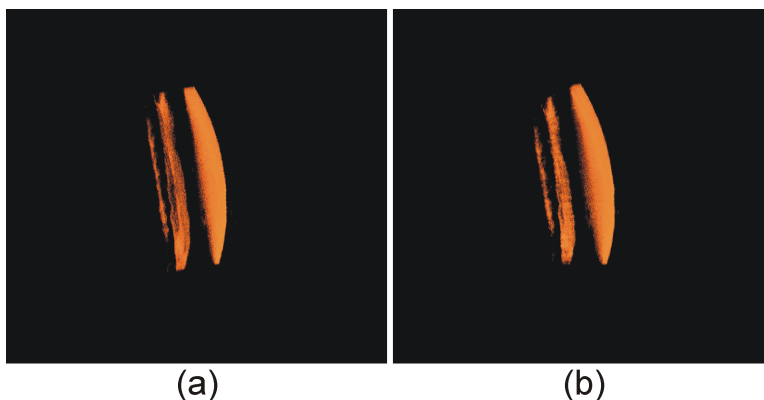


Figure. 5.7. a) Movie of the 3-D cloud of points by correcting by the refractive index, b) Correcting in 3-D.

Table 5.5. Posterior cornea dimensions of a human eye *in vivo*: estimates from Scheimpflug imaging and SDOCT.

	Scheimpflug	OCT Refractive Index Corrected	OCT 2-D distortion corrected	OCT 3-D distortion corrected
Radius[mm]	6.14	6.70	6.28	6.31
Conic Constant	-0.40	-0.28	-0.26	-0.45
Thickness [mm]	0.59	0.59	0.59	0.58

5.4. Conclusions

We have proposed a method for 3-D correction of optical distortion in OCT images, and demonstrated that after application of fan and optical distortion correction, reliable quantitative reconstruction of the ocular surface internal topography can be achieved.

The method has been validated using simulations of OCT imaging in a realistic computer eye model, *in vitro* on intraocular lenses and a PMMA artificial cornea of known parameters (from profilometry), and in real eyes (a porcine eye *in vitro* and a human eye *in vivo*) –where comparisons have been established with Scheimpflug imaging. Application of 3-D optical distortion correction increases the accuracy of the radii of curvature estimates by significant amounts, with respect to the simple division of the optical path by the index of refraction and over 2-D correction. Differences between the retrieved 3-D corrected and nominal values are less than 1% in most cases. The correction is particularly important for the surface asphericities, where the simulations predict discrepancies as large 200% for the posterior lens, and large differences with respect to applying the conventional correction have been also found experimentally in the posterior cornea. Experiments have been performed using two different laboratory-developed OCT systems (time-domain and spectral)

Correcting for optical distortion (along with for fan distortion) is therefore critical to reliably use OCT for quantitative estimates of ocular surfaces geometry, particularly that of internal surfaces. This correction is important in numerous applications that rely on quantitative analysis of the ocular surfaces (corneal changes after refractive surgery, cataract surgery and IOL implantation, corneal biomechanics, etc...) as well as those that involve quantitative measurements in the crystalline lens. While the current study has primarily addressed the cornea (in the examples in real eyes) the

technique would be applied similarly (and subsequently) for the reconstruction of the crystalline lens surfaces. An additional complication (with respect to the examples of artificial eyes *in vitro* presented here) is the presence of a gradient index distribution in the crystalline lens [Borja et al, 2008 and Siedlecki et al, 2012].

Two previous studies in the literature have discussed the presence of optical distortion and addressed it in 2-D. We have demonstrated higher accuracies when the correction is applied in 3-D. The importance of the correction has been demonstrated using laboratory-developed instrument, but it is inherent to the technique, and therefore has potential of being applicable to standard OCT commercial devices.

Chapter 6

3-D Image processing tools for clinical applications

This Chapter is based on the articles by Ortiz, S. et al “Corneal topography from spectral Optical Coherence Tomography (SD-OCT)” *Biomedical Optics Express*, Vol. 2, Issue 12, pp. 3232-3247 (2011), “Corneal topography from spectral Optical Coherence Tomography (SD-OCT)” *Biomedical Optics Express*, Vol. 3, Issue 5, pp. 814-825 (2012), and “In vivo human crystalline lens topography” submitted to *Biomedical Optics Express* Vol. 3, Issue 10, pp. 2471-2488 (2012).

The coauthors of the study appear in Chapters 7-9. The work was developed at Instituto de Óptica “Daza de Valdes”. The contribution of the author of this thesis was in development, implementation and testing the algorithms for extracting the 3-D Data from volumetric data provided by the custom-developed OCT. The algorithms include denoising, statistical thresholding, volume clustering, Multilayer segmentation, Further surface denoising, pupil centration, 3-D merging and surface fitting by quadrics, conicoids and topographic maps

6.1. Introduction

The OCT generates a huge amount of data due to the fast data acquisition and the high resolution used to collect the A-Scans. Manual processing for reconstruction and measurement is time consuming and also operator-dependent and automatic routines for image processing are therefore essential. A first step for analysis of the images is noise reduction. There are several studies in the literature characterizing the sources of noise in OCT [Takada et al, 1998, Podoleanu et al, 2000, and Haskell et al 2006] and proposals for noise reduction in OCT images, such as reduction of speckle noise by RKT algorithm [Rogowska et al 2002] or noise reduction by the application of wavelets [Adler et al, 2004]. A second step for retrieving surface information is segmentation of the surfaces of interest from the images. For segmentation two main strategies are normally used: Region segmentation techniques that search for the regions satisfying a given homogeneity criterion, and edge segmentation techniques that search boundaries between regions with different characteristics [Gonzalez et al, 2002]. Those algorithms normally are not automatized and they require the operator to select manually from the B-Scans the region of interest. However, those standards cannot be applied in a straightforward way to segment the anterior segment of the eye. First, the intensity of signal varies for every A-Scan, as well as, the noise statistics. Second, voxel sizes are different across lateral or axial dimension, with lateral resolution in the order of tenth's-hundreds of microns (0.033-0.100 mm), the axial resolution within microns (3.42 μm is sOCT system). This different orders of magnitude of voxel size makes difficult to adapt 2-D boundary detectors (i.e Canny, Roberts, Sobel,...) to 3-D conventional measurements.

In order to produce automated image processing and analysis techniques that can overcome the above mentioned limitations. We have developed a series of custom algorithms, which include algorithms to reduce noise, statistical thresholding, volume clustering, multilayer segmentation (edge improved detectability), pupil centering, merging 3-D volumes, geometrical distance calculation, distortion corrections and surface fitting by Zernike terms and quadrics. The routines were written in Matlab® and developed to meet the particular detection architecture of each of the OCT systems used in this thesis, although we have tested that they can be easily adapted to other commercial systems [Siedlecki et al, 2012].

6.2. Pre-processing in Fourier Domain OCT

For the particular case of Fourier domain systems, there is a consideration prior to further processing, which is related to a residual signal, localized at the low frequencies, coming from the zero order of Fourier Transform. This residual signal is the sum of the value of every point of one A-Scan spread over the cross correlation function. If these pixels are not removed, the images have very low contrast as their intensity is much higher than the average signal. As the SD-OCT output data contain this zero order information the first step is to trim this zone (Figure 6.1).

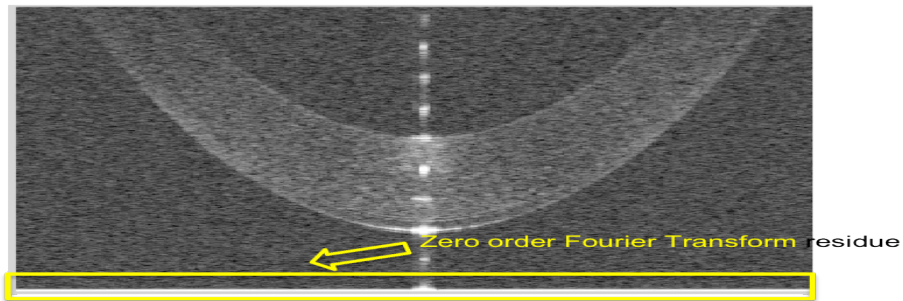


Figure 6.1. Measurement acquired with the SD-OCT device. In yellow the zero order of the Fourier transform

6.3. Denoising

The large amount of noise appearing in the OCT images produces low contrast data. Some studies in the literature analyze the sources of noise in the images [Takada et al, 1998, Podoleanu et al, 1998, and Haskell et al, 2006]. If we assume that the noise is random, it can be characterized by its bandwidth, which is directly related to the amount of energy that reaches the detector. In order to reduce the noise and to enhance the contrast, therefore improving the detection ratio, a combination of two denoising algorithms has been introduced. First, a Rotational Kernel Transform for an edge preserving denoising is applied, followed by a wavelet denoising to reduce the high frequency regime contribution of the noise.

In the first denoising step a rotational kernel transform (RKT) was performed for an edge-preserving denoising, using a programmable mask of variable size. The RKT algorithm is a method for nonlinear image processing that is especially well suited for removing the speckle noise. The method uses directional information contained in a circular neighbourhood centered at each point of the input image. It has the ability to enhance straight-line features in an image regardless their

orientation. In this method the input image is convolved with a two-dimensional kernel that is rotated 360 deg, either continuously or discretely in a large number of steps. The result of performing the convolution output denoted by $S_{\theta}(x, y)$ is described by Equation 6.1

$$S_{\theta}(x, y) = I(x, y) \otimes K_{\theta}(x, y) \quad Eq.6.1$$

where $I(x, y)$ the intensity value of determined pixel of a B-Scan and $K_{\theta}(x, y)$ a Kernel function for a rotation angle θ .

As the kernel rotates, the convolution output $S_{\theta}(x, y)$ is monitored, and the maximum and minimum values at each point (x, y) are stored. The output image $I_{out}(x, y)$ is given by some function of $Max(x, y)$ and $Min(x, y)$. This is known as nonlinear mapping of the input image to output image in a rotating kernel Min-Max transformation (RKMT). The specific implementation consisted of generating square matrices containing a rotating line of ones. The number of orientations and size are related to the size of the kernel n , being n an odd number, in such a way that the size of the matrices are $n \times n$ and the number of orientations is $2n - 2$. This way, for a kernel value of 3, there are 4 aspects each one rotated 45° , while for 5 there are 8 rotated every 22.5° . Sometimes, the rotation does not match the elements of the matrix. This drawback is solved setting the closer element values to one.

$$Kernel\ 3 = \left\{ \begin{pmatrix} 0 & 1 & 0 \\ 0 & 1 & 0 \\ 0 & 1 & 0 \end{pmatrix} \begin{pmatrix} 0 & 0 & 0 \\ 1 & 1 & 1 \\ 0 & 0 & 0 \end{pmatrix} \begin{pmatrix} 0 & 0 & 1 \\ 0 & 1 & 0 \\ 1 & 0 & 0 \end{pmatrix} \begin{pmatrix} 1 & 0 & 0 \\ 0 & 1 & 0 \\ 0 & 0 & 1 \end{pmatrix} \right\}$$

For processing of OCT images collected in the studies presented in Chapters 5-8 the mask size was 9 pixels. In Chapter 5 only the vertical kernel was used, instead of the 2-D.

In addition, a low-pass filter based on log Gabor wavelets was developed to improve the signal-noise to ratio (SNR). The denoising filter is applied by averaging the pixel information across multiple scales and orientations. A total of seven parameters are required to produce the denoising. The final denoised image ($S_f(x, y)$) was obtained by convolving the previous denoised image ($S_{\theta}(x, y)$) resulting from RKT algorithm with the log Gabor wavelet (G) Equation 6.2.

$$S_F(x, y) = S_\theta(x, y) \otimes G(x, y; \lambda, \theta, \varphi, \sigma, \gamma) \quad Eq.6.2$$

where the number of scales λ describes the sinusoidal response, θ represents the number of orientations, φ the phase offset, σ the standard deviation of the Gaussian envelope and γ the spatial aspect ratio, which specifies the ellipticity of the support of the Gabor function Equation 6.3.

$$G(x, y; \lambda, \theta, \varphi, \sigma, \gamma) = \begin{cases} \exp\left(-\frac{x_R^2 + \gamma^2 y_R^2}{2\sigma^2}\right) \cos\left(2\pi \frac{x_R}{\lambda} + \varphi\right) \\ \exp\left(-\frac{x_R^2 + \gamma^2 y_R^2}{2\sigma^2}\right) \sin\left(2\pi \frac{x_R}{\lambda} + \varphi\right) \end{cases} \quad Eq.6.3$$

$$where \begin{pmatrix} x_R \\ y_R \end{pmatrix} = \begin{pmatrix} \cos\theta & \sin\theta \\ -\sin\theta & \cos\theta \end{pmatrix} \begin{pmatrix} x \\ y \end{pmatrix}$$

Figure 6.1 shows an illustration of a B-Scan before and after applying the full denoising algorithm. The parameters were RKT kernel size 9, $\lambda = 7$, $\theta = 6$, $\varphi = 0$, σ is calculated, all points below and upper 2 the value are rejected and $\gamma = 1$.

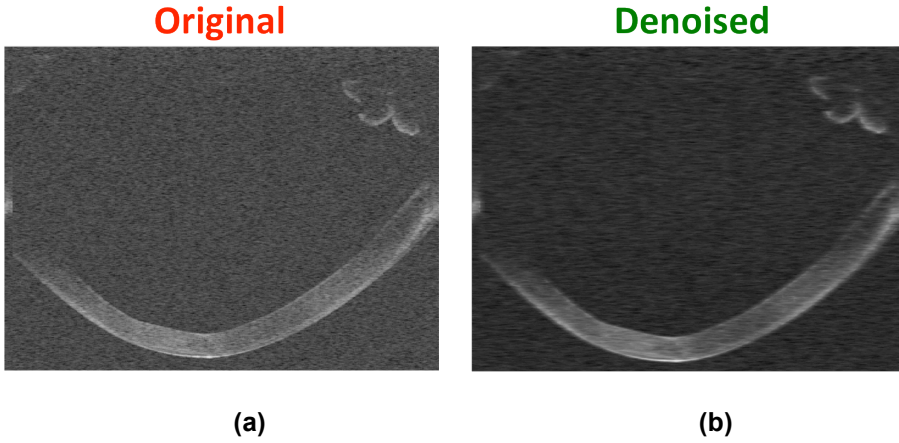


Figure 6.2. a) Raw image as it is obtained from the SD-OCT. b) Result after the application of low-pass filtering based on log-Gabor wavelets.

6.4. Statistical thresholding

After denoising the OCT images, the signal is separated from the background taking into account the existing difference in statistics of the signal and the background. Throughout this thesis we have used two different types of statistical thresholding methods: standard Otsu method (Chapter 7) and multimodal method (Chapter 8-10).

The standard Otsu statistical thresholding method was performed on individual A-Scans rather than on the B-Scans, which allows an adaptive treatment of the noise and signal levels of every A-Scan. The algorithm assumes that the data to be thresholded contain two classes of pixels or bi-modal histogram (signal and background), and it calculates the optimal threshold separating those two classes so that their combined spread (intra-class variance) is minimal. The intra-class variance can be defined as a weighted sum of variances of the two classes:

$$\sigma_{\omega}^2(t) = \omega_1(t)\sigma_1^2(t) + \omega_2(t)\sigma_2^2(t) \quad Eq.6.4$$

where σ_i^2 are the variances and ω_i are the probabilities of the two classes, separated by threshold t . The implemented algorithm computes the histogram and probabilities of each intensity level, it establishes initial values for $\omega_i(0)$ and $\mu_i(0)$, and it steps through all the possible thresholds. Then, it updates ω_i and μ_i , and it computes intraclass variance. Finally, the desired threshold for the intraclass variance is found.

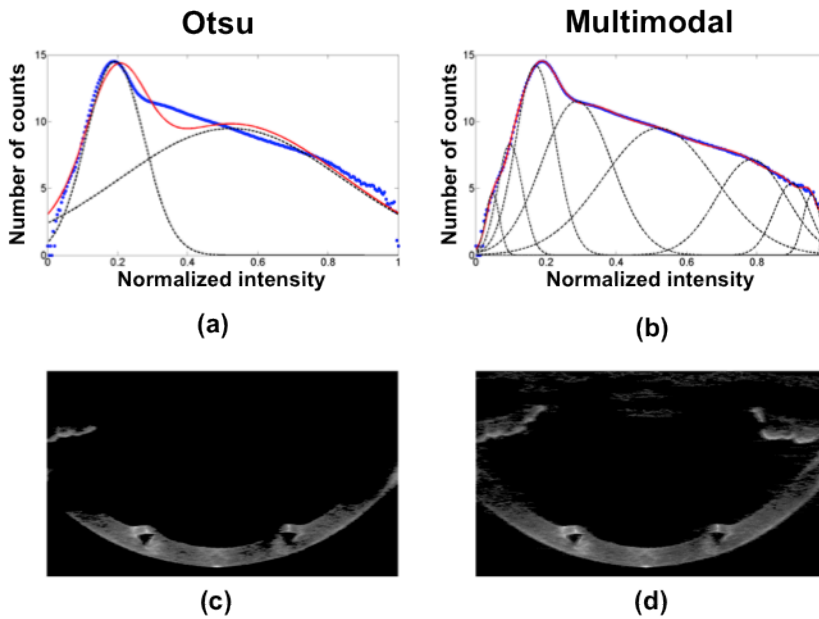


Figure 6.3. (a) Semi-logarithmic representation of the 3-D image histogram using normalized intensity (blue points) and fitted data provided by the statistics of the Otsu's statistical thresholding method (red points). (b) Result of the multi-modal fitting in red (9 different number of classes were found). In (a) and (b) classes are represented by dash black lines (c) Result of the application of the Otsu's algorithm on a cross sectional image. (d) Result of the application of the multimodal algorithm on the same cross sectional image.

For Chapters 7 and 8, an alternative strategy was developed, which allowed global application of the thresholding method. Instead of a bimodal histogram a multimodal histogram distribution for the entire 3-D data was introduced. Using a non-linear least squares algorithm, the normalized intensity histogram of the entire 3-D- data is fitted to a sum of Gaussian distributions, which provides the statistics (average and bandwidth) of a number of discrete classes. The algorithm classifies every single pixel of the data by its maximum of likelihood of belonging to a certain class, and only those points belonging to classes different from noise are considered. Figure 6.3 shows a semi-logarithmic representation of the histogram using normalized intensity provided by the Otsu's method (Figure 6.3.a) and the multi-modal fitting, providing 9 classes in this case (Figure 6.3.b). Figure 6.3.c illustrates the result of the thresholding provided by the Otsu's method on a cross sectional image, Figure 6.3.d shows the result of the same thresholding when the multimodal fitting is applied.

6.5. Volume Clustering

As a result of the overlapping statistics of the noise and signal, randomly distributed noise is still present in the images after thresholding. We developed a volume clustering algorithm based on area or volume classification. Volumes of connected points are identified as classes. To perform the volume clustering, a mask tensor M_T of size $3 \times 3 \times 3$ (Equation 6.5) was convolved with a binary representation of the 3-D cloud of points provided by the statistical thresholding. It allows identifying a layer if there is continuity in at least one of the directions of the tensor mask (which is 3-D convolved with the tensor of data).

$$M_T = \left\{ \left(\begin{array}{ccc} 1 & 1 & 1 \\ 1 & 1 & 1 \\ 1 & 1 & 1 \end{array} \right) \left(\begin{array}{ccc} 1 & 1 & 1 \\ 1 & 1 & 1 \\ 1 & 1 & 1 \end{array} \right) \left(\begin{array}{ccc} 1 & 1 & 1 \\ 1 & 1 & 1 \\ 1 & 1 & 1 \end{array} \right) \right\} \quad Eq.6.5$$

Assuming B the resultant binary tensor representing the binarization of the signal tensor after thresholding S_F , being 1 the position (x, y, z) corresponding to signal and 0 the points corresponding to the background, the result of the convolution $N(x, y, z)$ is expressed as:

$$N(x, y, z) = B(x, y, z) \otimes M_T \quad Eq.6.6$$

Equation 6.6 provides a tensor with a range values from 1 to 27 for every point (x, y, z) . The value of the (x, y, z) indicates the number of detected points which are in the neighborhood or surrounding the point. The value 1 corresponds to a point with no neighbors, while 27 corresponds to a point which is completely surrounded by other points belonging to the signal. Finally, only the points which value is 27 are considered as members of a class. The classes with a volume size below a certain threshold are eliminated. The threshold is estimated as a certain percentile within the range of 95-99% of the total number of connected points. This way, only large volumes are extracted and small groups of points are neglected. After statistical thresholding and clustering, some small holes can appear in the clustered volumes. In order to fill those holes, morphological operations are used: a dilation operation followed by erosion was programmed for 1-D, 2-D and 3-D as subroutines from the volume clustering. In the case of 1-D, a line is used as a mask allowing joining separated points of the same A-scan. For the 2-D case, rectangular and elliptical masks (with rectangular and

circular cases as degenerate cases from rectangular and elliptical respectively) were programmed, with floating size, allowing filling those holes that are sufficiently small to be considered as a part of the volume. Finally, in the 3-D case, rectangular or ellipsoidal tensor masks are generated to fill the holes smaller than the size of the mask tensors. Figure 6.4 shows the result of a volume clustering showing the automatic classification of the cornea (in red) and iris (in green).

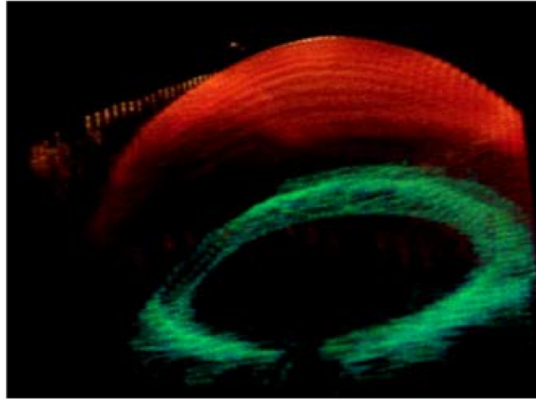


Figure 6.4. Volumetric clustering of the data after denoising (cornea is represented in red and the iris is represented in green)

6.6. Multilayer segmentation

Several algorithms for multilayer segmentation have been implemented in this thesis for detecting layers in OCT images. In Chapters 4 and 5, a simple algorithm based on maximum intensity detection was used. In Chapters 7 to 10, more sophisticated algorithms based on first derivative were applied in order to produce a better boundary determination. In simple terms, these operators calculate the gradient of the image intensity at each point, and provide the direction of the largest possible increase from light to dark and the rate of change in that direction. The result therefore shows how "abruptly" or "smoothly" the image changes at that point, and therefore how likely it is that that part of the image represents an edge, as well as how that edge is likely to be oriented. In practice, the magnitude (likelihood of an edge) calculation is more reliable and easier to interpret than the direction calculation.

In Chapter 7, the Robert's operator was used to produce the anterior surface segmentation of IOL's and *in vivo* corneas. The algorithm consisted of an extension to 3-D of Roberts algorithm in 2-D. Given that the Robert's method can only be applied in 2-D, we applied the

algorithm to the different cross-sections of the tensor $S_F : XY, XZ$ and YZ . Therefore, if it is assumed that the size of tensor S_F is $l \times m \times n$ it means that in direction XY there are n images of size $l \times m$, and direction XZ direction there are m images of size $l \times n$, and in YZ the set of images consisted of l images of size $m \times n$. Then, we convolved every section with the following kernels Equation 6.7.

$$M_1 = \begin{pmatrix} 1 & 0 \\ 0 & -1 \end{pmatrix} \quad M_2 = \begin{pmatrix} 0 & 1 \\ -1 & 0 \end{pmatrix} \quad Eq.6.7$$

After the sequential application of the convolution in the images the resultant tensors for the three orientations are binarized. The binarization is produced by thresholding them, and removing the points that are not a local maxima. These results in resulting on three binary tensors obtained for each orientation $B_{XY}(x,y,z)$, $B_{XZ}(x,y,z)$, and $B_{YZ}(x,y,z)$. Finally, the resultant tensor $B(x,y,z)$ (Equation 6.8) is the product of the three binary representations.

$$B(x,y,z) = B_{XY}(x,y,z) \times B_{XZ}(x,y,z) \times B_{YZ}(x,y,z) \quad Eq.6.8$$

The main advantage of this algorithm is its simplicity, while its main drawbacks are its intrinsic sensitivity to the noise and its time for calculation, since it needs three loops to travel the three aspects of the cross-sections.

For Chapter 8 a more sophisticated algorithm was developed, allowing determining boundaries and intra-tissue objects with a larger degree of accuracy. The algorithm was based on boundary region identification (and not only maximum intensity), and allows automatic resolution of very close layers of different reflectivity. The algorithm extracts the position of the peaks of every A-Scan, and they are sorted by position and intensity. In this case two separated operations are performed: a smoothing perpendicular to the derivative direction with a triangle filter and simple central difference in the derivative direction. A number of kernels was developed to find the derivatives: Sobel (Equation 6.9), Prewitt (Equation 6.10) and Scharr (Equation 6.11).

SOBEL OPERATOR

$$\begin{aligned}
 M_x(x,y,z) &= \begin{bmatrix} 1 & 0 & -1 \\ 2 & 0 & -2 \\ 1 & 0 & -1 \end{bmatrix} \times \begin{bmatrix} 2 & 0 & -2 \\ 4 & 0 & -4 \\ 2 & 0 & -2 \end{bmatrix} \times \begin{bmatrix} 1 & 0 & -1 \\ 2 & 0 & -2 \\ 1 & 0 & -1 \end{bmatrix} \\
 M_y(x,y,z) &= \begin{bmatrix} 1 & 2 & -1 \\ 0 & 0 & 0 \\ -1 & -2 & -1 \end{bmatrix} \times \begin{bmatrix} 2 & 4 & 2 \\ 0 & 0 & 0 \\ -2 & -4 & -2 \end{bmatrix} \times \begin{bmatrix} 1 & 2 & -1 \\ 0 & 0 & 0 \\ -1 & -2 & -1 \end{bmatrix} \\
 M_z(x,y,z) &= \begin{bmatrix} 1 & 2 & 1 \\ 2 & 4 & 2 \\ 1 & 2 & 1 \end{bmatrix} \times \begin{bmatrix} 0 & 0 & 0 \\ 0 & 0 & 0 \\ 0 & 0 & 0 \end{bmatrix} \times \begin{bmatrix} -1 & -2 & -1 \\ -2 & -4 & -2 \\ -1 & -2 & -1 \end{bmatrix}
 \end{aligned} \tag{Eq.6.9}$$

PREWITT OPERATOR

$$\begin{aligned}
 M_x(x,y,z) &= \begin{bmatrix} 1 & 0 & -1 \\ 1 & 0 & -1 \\ 1 & 0 & -1 \end{bmatrix} \times \begin{bmatrix} 1 & 0 & -1 \\ 1 & 0 & -1 \\ 1 & 0 & -1 \end{bmatrix} \times \begin{bmatrix} 1 & 0 & -1 \\ 1 & 0 & -1 \\ 1 & 0 & -1 \end{bmatrix} \\
 M_y(x,y,z) &= \begin{bmatrix} 1 & 1 & -1 \\ 0 & 0 & 0 \\ -1 & -1 & -1 \end{bmatrix} \times \begin{bmatrix} 1 & 1 & 1 \\ 0 & 0 & 0 \\ -1 & -1 & -1 \end{bmatrix} \times \begin{bmatrix} 1 & 1 & -1 \\ 0 & 0 & 0 \\ -1 & -1 & -1 \end{bmatrix} \\
 M_z(x,y,z) &= \begin{bmatrix} 1 & 1 & 1 \\ 1 & 1 & 1 \\ 1 & 1 & 1 \end{bmatrix} \times \begin{bmatrix} 0 & 0 & 0 \\ 0 & 0 & 0 \\ 0 & 0 & 0 \end{bmatrix} \times \begin{bmatrix} 1 & 1 & 1 \\ 1 & 1 & 1 \\ 1 & 1 & 1 \end{bmatrix}
 \end{aligned} \tag{Eq.6.10}$$

SCHARR OPERATOR

$$\begin{aligned}
 M_x(x,y,z) &= \begin{bmatrix} 3 & 0 & -3 \\ 10 & 0 & -10 \\ 3 & 0 & -3 \end{bmatrix} \times \begin{bmatrix} 6 & 0 & -6 \\ 20 & 0 & -20 \\ 6 & 0 & -6 \end{bmatrix} \times \begin{bmatrix} 3 & 0 & -3 \\ 10 & 0 & -10 \\ 3 & 0 & -3 \end{bmatrix} \\
 M_y(x,y,z) &= \begin{bmatrix} 3 & 10 & -3 \\ 0 & 0 & 0 \\ -3 & -10 & -3 \end{bmatrix} \times \begin{bmatrix} 6 & 20 & 6 \\ 0 & 0 & 0 \\ -6 & -20 & -6 \end{bmatrix} \times \begin{bmatrix} 3 & 10 & -3 \\ 0 & 0 & 0 \\ -3 & -10 & -3 \end{bmatrix} \\
 M_z(x,y,z) &= \begin{bmatrix} 3 & 10 & 3 \\ 6 & 20 & 6 \\ 3 & 10 & 3 \end{bmatrix} \times \begin{bmatrix} 0 & 0 & 0 \\ 0 & 0 & 0 \\ 0 & 0 & 0 \end{bmatrix} \times \begin{bmatrix} -3 & -6 & -3 \\ -10 & -10 & -10 \\ -3 & -6 & -3 \end{bmatrix}
 \end{aligned} \tag{Eq.6.11}$$

The gradients (G_x , G_y and G_z) in the different directions were obtained as the convolution of the data tensor obtained from volume clustering S_f and three tensor kernels Equation 6.12.

$$G_i(x,y,z) = I(x,y,z) \otimes M_i \quad \text{where } i = X, Y \text{ and } Z \quad \text{Eq.6.12.}$$

The magnitude of the gradient M was obtained from the square root of the gradients along the three orientations (G_x , G_y and G_z).

$$M(x,y,z) = \sqrt{G_x^2 + G_y^2 + G_z^2} \quad \text{Eq.6.13}$$

The resultant tensor was binarized, and the maxima non corresponding to maxima below a threshold were removed. The application of the Scharr algorithm to the segmentation of surfaces in the cornea of a patient implanted with an intrastromal ring (Chapter 8) is illustrated in Figure 6.5. The algorithm segments successfully the anterior and posterior surface of the cornea as well as the surfaces of the intrastromal implant.

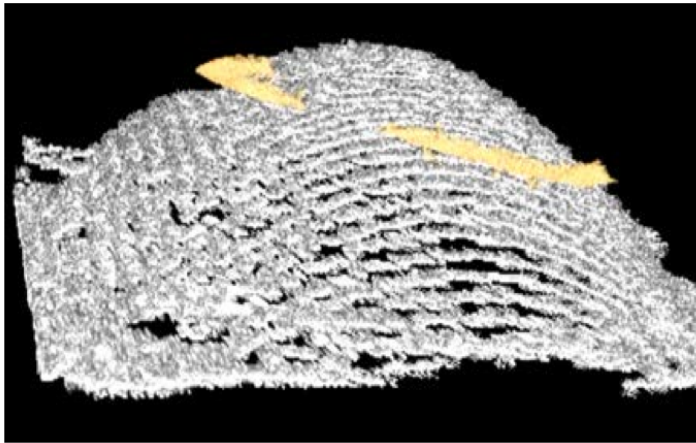


Figure 6.5. Illustration of the multilayer segmentation in a keratoconic cornea implanted with an ICRS, showing the posterior corneal surface (white) and ICRS (yellow).

The main drawbacks of the algorithm were still relatively noisy data even after application of denoising, and the large difference of resolution in the three dimensions of the voxels. The axial resolution of the voxel was $3.42 \mu\text{m}$, while the lateral size was $0.1 \times 0.2 \text{ mm}$ in Chapter 7, and 0.033×0.2 in Chapter from 8 to 10. These differences in voxel resolution produce a lack of connectivity in the neighborhood of a local maxima.

In order to solve these drawbacks, a new approach for automatic segmentation was developed for Chapter 9 and 10, based on Canny detection in each A-scan (1-D signals). In an initial step, a Gaussian filter (standard deviation $s=5$ pixels) was convolved with the signal to reduce spurious peaks associated to noise detection (Figure 6.6.a). The

anterior and posterior cornea surfaces (in green and yellow, respectively), following the application of the neighborhood algorithm.

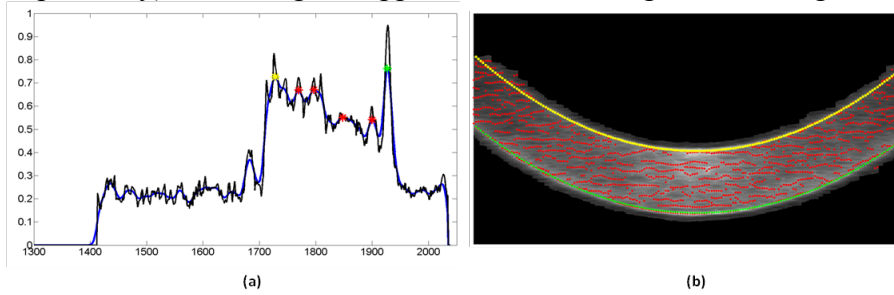


Figure 6.6. (a) Illustration of the algorithm for maxima detection: Original A-Scan black; Filtered signal by Gaussian filtering, blue; Detected local maxima (red asterisks) by First derivative 9-pixel kernel computation. The anterior and posterior corneal peaks are marked by the green and yellow asteriks, respectively. (b) Detection of maxima in corneal B-Scan (in red), and multilayer segmentation of the anterior surface (green line) and posterior surface (yellow line) by the neighborhood algorithm.

6.7 Further surface denoising.

Even after the denoising algorithm and boundary detection algorithms the segmented surfaces are still noisy. This fact is due to the detection process of the OCT system, which adds noise to the signal. The noise can be described as a ripple in the smooth surface of the anterior segment of the eye. The method that we used to remove the ripple in the surfaces is based on a Zernike description of the surface. The Zernike polynomials are a set of orthogonal polynomials, typically used to describe the elevation, or the associated wave aberrations in optical systems with circular pupils. Zernike have been traditionally used in visual optics for describing the aberrations from the human eye, and Zernike polynomials are usually defined in polar coordinates (ρ, θ) , where ρ is the radial coordinate ranging from 0 to 1 and θ is the azimuthal component ranging from 0 to 2π . Each of the Zernike polynomials (Equation 6.14) consists of three components: a normalization factor (Equation 6.15), a radial-dependent component (Equation 6.16), and an azimuthal-dependent component. The radial component is a polynomial, whereas the azimuthal component is sinusoidal. Zernike polynomials are usually represented using a double indexing scheme, with n standing for the order of the radial coordinate and, m for azimuthal frequency of the sinusoidal component.

$$Z_n^m(\rho, \theta) = \begin{cases} N_n^m R_n^{|m|}(\rho) \cos(m\theta) & \text{for } m \geq 0 \\ -N_n^m R_n^{|m|}(\rho) \sin(m\theta) & \text{for } m \leq 0 \end{cases} \quad Eq.6.14$$

Where the normalization factor N_n^m is given by:

$$N_n^m = \sqrt{\frac{2(n+1)}{1 + \delta_{m0}}} \quad Eq.6.15$$

Where $R_n^{|m|}(\rho)$ is given by

$$R_n^{|m|}(\rho) = \sum_{s=0}^{(n-|m|)/2} \frac{(-1)^s (n-s)!}{s!((n+|m|)/2-s)!((n+|m|)/2-s)!} \rho^{n-2s} \quad Eq.6.16$$

Apart from its traditional use in the representation of the optical aberrations and elevation data, Zernike description (Figure 6.8) can be used to obtain smooth surfaces from noisy raw elevation maps, acting as a sort of low pass filter for noise. Figure 6.8 shows the Zernike polynomials up to the 7th radial order.

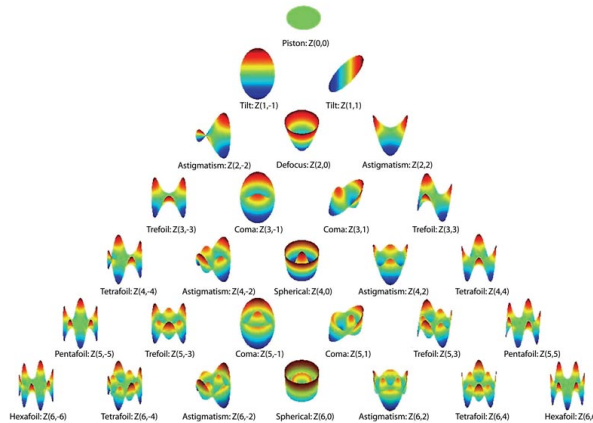


Figure 6.8. Shows the Zernike polynomials up to the 7th radial order.

3-D segmented surfaces corresponding to an anterior segment layer are fitted to Zernike modal expansions in a least square sense. The method is implemented in an iterative procedure, which allows further rejection of spurious points in the surface by evaluating the local distance of every point with respect to the surface fitted to the Zernike modal expansion. The number of terms is introduced by the user up to tenth order. Points further than three times the standard deviation of the distances between the actual surface and the fitted surface are eliminated, and a new Zernike fitting is performed. The procedure is repeated until the fitted Zernike coefficients change less, from the previous iteration, than a percentage introduced by the user. Figure 6.9 shows an example of the result of the application of the described algorithm on the anterior surface of a cornea in vivo, where red points

are the elevation data after segmentation, and blue points are the resultant surface (after 8 iterations) to a 10th order polynomial.

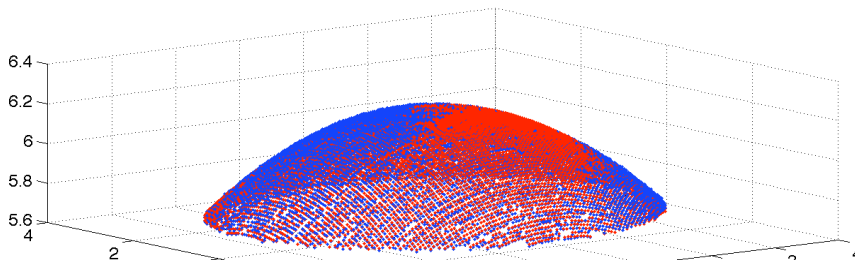


Figure 6.9. shows an example of the result of the application of the described algorithm on the anterior surface of a cornea in vivo, where red points are the elevation data after segmentation, and blue points are the resultant surface (after 8 iterations) to a 10th order polynomial.

6.8 Pupil center reference.

The pupil center was used as a reference across measurements (i.e. cornea, anterior and posterior lens) and to define the optical zone (effective area within the pupil), the selection of this point seems reasonable, as the pupil center has been reported to change little across pupil sizes and light conditions [Yang et al, 2002]. In the application described in Chapter 7 the pupil center was taken as a reference for pre- and post- operative corneal topographies, as well as to define the relative lateral location of the implanted intrastromal ring segments. In the application described in Chapter 8, the pupil coordinates in 3-D along with the normal to the pupil plane were used for merging. The images collected at different foci, containing the cornea and the iris, and the lens surfaces and the iris, respectively, were used to reconstruct the entire anterior segment of the eye. The pupil center was efficiently calculated from the clustered iris volume (Figure 6.9.a), by collapsing the cloud of points onto a 2-D image. The pupil center (lateral coordinates X_{pc} and Y_{pc} and radii (R_x and R_y) were obtained from an ellipse fitting of the segmented edges using a Sobel edge detector (Figure 6.10.b).

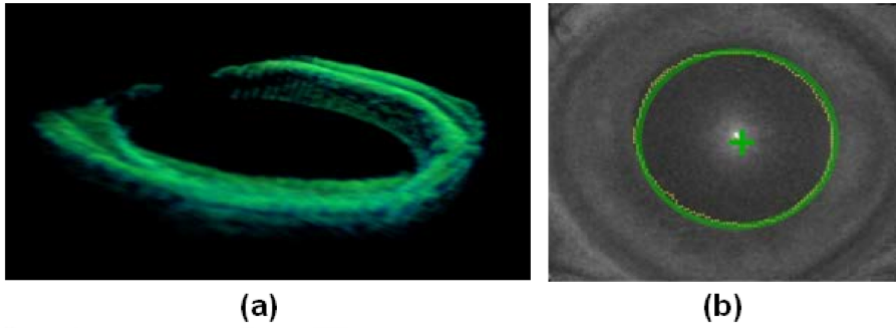


Figure 6.10 (a) Clustered iris volume. (b) Pupil fitted to an ellipse with the center represented as a green cross.

The collapsed iris provides a plane that is fitted by non linear least-square fitting to a 3-D plane. The evaluation of the plane at the estimated pupil lateral coordinates (X_{pc} and Y_{pc}) provides the axial component of the pupil center Z_{pc} (Equation 6.17).

$$Z_{pc} = -(AX_{pc} + BY_{pc} + D)/C \quad Eq.6.17$$

In addition, the coefficients A, B, C and D allowed calculation of the normal vector to the pupil plane \hat{N}_{pp} (Equation 6.18), which provided the tilt angle of this plane with respect to the OCT coordinate system.

$$\hat{N}_{pp} = \{A, B, C\} / \sqrt{A^2 + B^2 + C^2} \quad Eq.6.18$$

6.9. Merging 3-D volumes

Applications where the full anterior segment was quantified (Chapter 9 and 10) used up to three sets of data at different depths that were merged using the pupil center and pupil plane orientation for registration, assuming the pupil center as a common reference across images of the anterior segment collected at different depths. Variations in the pupil diameter were negligible across images. In a first step prior to merging, the corneal image was inverted, as for efficiency in the focus range shifts, this was obtained in the opposite side of the Fourier transform (in comparison with the crystalline lens acquisition). The 3-D volumes of the anterior cornea/iris and posterior lens/iris are shifted to the pupil center reference, and rotated in order to superimpose the characteristic vectors of the corresponding pupil plane to those of the anterior lens/iris. Figure 6.11 illustrates the process to obtain the full anterior segment 3-D image merging from the three volumetric

acquisitions. A full overlapping of the iris from the 3 sets of images can be observed.

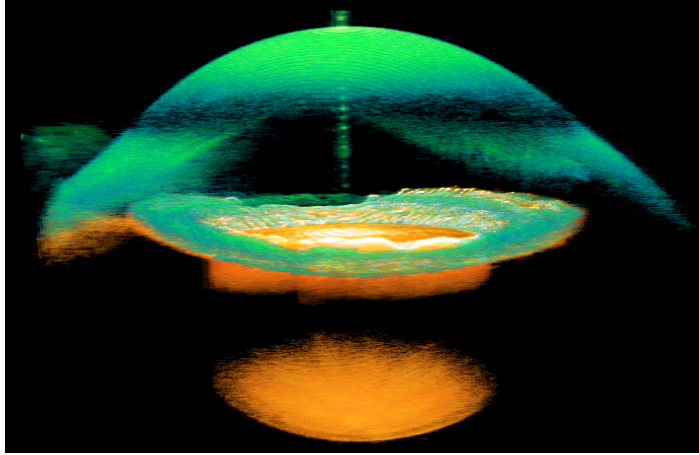


Figure 6.11. Illustration of the merging of three volumetric acquisitions to obtain a 3-D full anterior segment image.

The transformation operation that allows translating and rotating the points for the cornea and posterior lens is a 4×4 matrix, and it consists of the product of the translation matrix (T) with the Rotation matrix (R).

$$R = \begin{pmatrix} R_{11} & R_{12} & R_{13} & 0 \\ R_{21} & R_{22} & R_{23} & 0 \\ R_{31} & R_{32} & R_{33} & 0 \\ 0 & 0 & 0 & 1 \end{pmatrix} \quad T = \begin{pmatrix} 1 & 0 & 0 & D_x \\ 0 & 1 & 0 & D_y \\ 0 & 0 & 1 & D_z \\ 0 & 0 & 0 & 1 \end{pmatrix} \quad Eq.6.19$$

where R_{ij} elements of matrix R are related to the rotation angles between the pupil normal vector (the one extracted from the iris in the anterior lens acquisition) and the pupil normal vectors to be rotated (obtained from the iris of the posterior lens acquisition and the cornea acquisition iris). The D_k elements are the distances that the different pupil centers must be translated to match the pupil center of the anterior lens. In order to assess the R_{ij} coefficients efficiently, we used a method not based on square roots neither trigonometric functions but based on dot and vectorial products of two vectors. Denoting the unitary reference pupil vector as f and the unitary pupil normal vector

to be rotated as t , the rotation matrix can be described by Equation 6.20.

$$R = \begin{pmatrix} c + hv_x^2 & hv_xv_y - v_z & hv_xv_z + v_y & 0 \\ hv_xv_y + v_z & c + hv_y^2 & hv_yv_z - v_x & 0 \\ hv_xv_z - v_y & hv_yv_z - v_x & c + hv_z^2 & 0 \\ 0 & 0 & 0 & 1 \end{pmatrix} \quad Eq.6.20$$

where v_i are the (x,y,z) components of vector \vec{v} assessed as $\vec{v} = f \times t$, c is the dot product between f and t vectors, and $h = (1 - c)/(\vec{v} \cdot \vec{v})$.

6.10. Geometrical distances calculation

The registration described above, involved shift and rotation by coordinates in optical distances, which actually differ across the different depths. Estimation of the geometrical parameters from the volumetric images (still subject to fan and optical distortion) required re-sampling of the surfaces in a rectangular equally distributed mesh. In Chapter 9 the selected grid was of 100 x 100 points in the rectangle circumscribed by the pupil ellipse. The geometrical distances calculation was based on an interpolation method by means of the Delaunay description of the surfaces, and the use of Radial Base Functions (RBF) (as those functions do not require the use of a regular grid of sampling without compromising accuracy).

$$z(x,y) = c_0 + c_1x + c_2y + \sum_{i=1}^n \lambda_i \varphi(\rho) \quad \text{where } \rho = \sqrt{(x - x_i)^2 + (y - y_i)^2} \quad Eq.6.21$$

where x and y are the lateral coordinates of the point to be interpolated, c_k are the coefficients of the linear part of the RBF, and λ_i are the n coefficients for the nodes, while x_i and y_i are the lateral coordinates for the nodes. The function φ is the radial function and it can be selected from a catalogue (Figure 6.12): linear, cubic, multiquadrics, Thinplate or Gaussian.

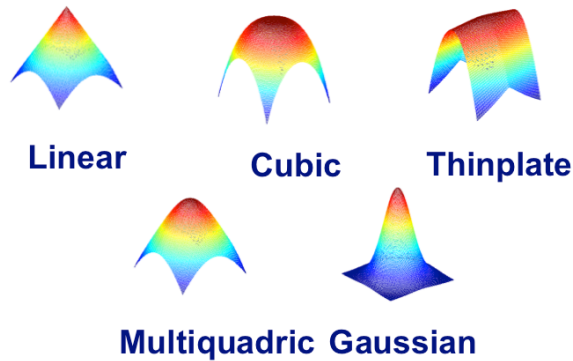


Figure 6.12. Catalogue of the Radial basis Functions used in this thesis.

The interpolated coordinates are obtained from the nodes of the triangle elements that tile the surfaces in the Delaunay description. The procedure is performed for all surfaces of the volumetric data, in the case of the anterior segment: anterior-posterior cornea and anterior-posterior lens. The optical distance can be then calculated by direct subtraction of the coordinates of the different surfaces, while the geometrical distances were obtained by dividing the optical distance by the corresponding group refractive index at the illumination wavelength.

6.11. Surface fitting by quadrics, conicoids and topographic maps

Once the surfaces have been corrected from the fan distortion (Chapter 2) and optical distortion (Chapter 6) data are expressed in euclidean coordinates, and can be fitted by standard functions (conic, Zernike polynomials, etc...). The same custom routines for fitting were also used to fit the corneal elevation maps provided by other instruments (Scheimpflug and Placido disk videokeratography) used for reference.

The algorithm uses fit four analytical functions fitting two non-degenerate biologically compatible quadrics (Sphere and ellipsoid) a conicoid and a biconicoid. The fitting is produced in a non linear least square sense, and it was implemented in an iterative procedure, which allows further rejection of spurious points in the surface, by evaluating the local distance of every point with respect to the surface fitted to the analytical function selected by the user. Points further than three times the standard deviation of the distances between the actual surface and the fitted surface are eliminated, and a new iteration is performed. The procedure is repeated until the output variables change less than a percentage (defined by performer) from the previous iteration.

From the sphere (Equation 6.22) it is possible to obtain both radius a and the center of the sphere (x_0, y_0, z_0) .

$$(x-x_0)^2 + (y-y_0)^2 + (z-z_0)^2 = a^2 \quad Eq.6.22$$

From the ellipsoid (Equation 6.23) the algorithm extracts the three radius of curvature (a, b, c) and the center of the ellipsoid (x_0, y_0, z_0) . There is a relationship between the ellipsoid and the biconicoid, which allows by simple operations, to express the radii and asphericities of the anterior segment surfaces in a format that can be compared to the values found in the literature.

$$\frac{(x-x_0)^2}{a^2} + \frac{(y-y_0)^2}{b^2} + \frac{(z-z_0)^2}{c^2} = 1 \quad Eq.6.23$$

The usual definition of the conicoid (Equation 6.24), described by the following Equation, matches the ellipsoid definition with $a = b$.

$$(x-x_0)^2 + (y-y_0)^2 - 2(z-z_0)R + (Q+1)(z-z_0)^2 = 0 \quad Eq.6.24$$

where (x, y) being the horizontal and vertical coordinates relative to their origin (x_0, y_0) , z and z_0 are the axial and axial origin coordinates. Finally, the fitting parameters are the radius R and the conic constant Q . The conic constant is defined as $Q = -(1 - b^2/c^2)$ and the radius $R = a^2/c$.

In the case of the biconicoid (Equation 6.25) the following definition has been used, matching the definition of the ellipsoid.

$$z(x, y) = z_0 + \frac{c_x(x-x_0)^2 + c_y(y-y_0)^2}{1 + \sqrt{1 - (1+Q_x)c_x^2(x-x_0)^2 - (1+Q_y)c_y^2(y-y_0)^2}} \quad Eq.6.25$$

Where c_x is the inverse of the radius of curvature in the horizontal direction, c_y is the inverse of the radius of curvature in the vertical direction, Q_x is the asphericity in the horizontal direction, Q_y is the asphericity in the vertical direction and $\{x_0, y_0, z_0\}$ are the coordinates of the apex.

The horizontal conic constant is related to the ellipsoid radii by $Q_x = -(1 - a^2/c^2)$ and the vertical by $Q_y = -(1 - b^2/c^2)$ and the radii are related to the radii provided by the ellipsoid by $R_x = a^2/c$ for the horizontal and $R_y = b^2/c$ for the vertical respectively.

Finally the corneal topographies are represented as elevation maps (Figure 6.13), where the measured elevation data are represented as the difference of surface elevation data from the reference sphere (best fitted sphere estimated using nonlinear least squares algorithm). The corneal elevation maps are displayed in a square grid for the selected diameter, where warm colors depict points that are higher than the reference surface while cool colors designate lower points.

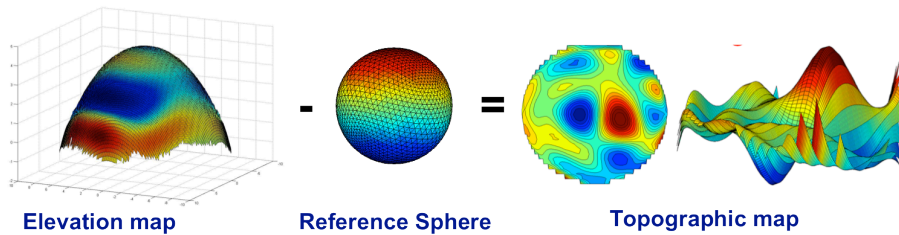


Figure 6.13 Illustration of the calculation of a topographic map as a direct subtraction of the elevation data minus the best fitted sphere.

Chapter 7

Topography from spectral domain optical coherence tomography for *in vivo* and *in vitro* surfaces

This chapter is based on the article by Ortiz, S. et al “ Corneal topography from spectral Optical Coherence Tomography (sOCT)” Biomedical Optics Express, Vol. 2, Issue 12, pp. 3232-3247 (2011). The coauthors of the study are: Damian Siedlecki, Pablo Pérez-Merino, Noelia Chia, Alberto de Castro, Maciej Szkulmowski, Maciej Wojtkowski, and Susana Marcos. The work was developed at Instituto de Óptica “Daza De Valdés”. The contribution of the author of this thesis was to develop a method to obtain accurate corneal topography from a spectral Optical Coherence Tomography (sOCT) system. The method included calibration of the device, compensation of the fan (or field) distortion introduced by the scanning architecture, and image processing analysis for volumetric data extraction, segmentation and fitting. Some examples of three-dimensional (3-D) surface topography measurements on spherical and aspheric lenses were presented, as well as on 10 human corneas *in vivo*. Results of sOCT surface topography (with and without fan-distortion correction) were compared with non-contact profilometry (taken as reference) on a spherical lens, and with non-contact profilometry and state-of-the art commercial corneal topography instruments on aspheric lenses and on subjects.

7.1. Introduction

The amount of quantitative information provided by anterior segment OCT is typically limited to axial distances between consecutive layers i.e. corneal thickness [Kim et al,2008, and Muscat et al, 2002], anterior chamber depth [Dawczynski et al, 2007, and Lavanya et al, 2007] or anterior chamber angle [Radhakrishnan et al, 2008], within the accuracy provided by axial resolution and exact knowledge of the refractive index of the tissue. Although the use of OCT as a pachymeter [Li et al, 2007, and Steinert et al, 2008] and for optical biometry [Ruggeri et al, 2010, Dunne et al, 2007] is widespread, its capability to produce surface elevation maps, and therefore to be used as a corneal topographer, has only been limitedly exploited. Although several studies address the use of OCT to estimate corneal power [Tang et al, 2006, Li et al, 2008], only a few recent papers explore the accuracy and perform validations of corneal topography and keratometry from OCT 3-Dimensional imaging [Gora et al, 2009, Plesea et al, 2008, Zhao et al, 2010, and Karnowski et al, 2009].

As it was mentioned in Chapter 4 one of the limitations of the most typical configuration of OCT systems is the presence of so-called fan (or field) distortion. In general, the effect is related to the scanning architecture of most 3-D OCT systems [Ortiz et al, 2009, Westphal et al, 2002, Xie et al, 2005, and Li et al, 2008], so that when imaging perfectly flat surfaces they appear curved. This phenomenon can be described as a combination of at least two possible effects: a) the architecture of the scanning system, which is primarily affected by the spatial separation of the mirrors, and b) design, position and alignment of the collimating lens in relation to the mirrors of the scanner. Therefore such images are not well represented in a Cartesian system of coordinates (x,y,z) , but rather in (x_{oct},y_{oct},L) , where L is the optical path along the ray, and (x_{oct},y_{oct}) are the angles (horizontal and vertical) of the scanner mirrors, which can be explicitly associated to the coordinates (origin and directional cosines) of rays entering the sample. This representation allows conversion from angular to spatial coordinates following relatively simple calibration.

OCT systems are designed to detect usually faint back-scattered light from tissue. However, both backscattered as well as back-reflected (from directional and specular reflections) light is detected, particularly for surfaces normal to the optical axis of the instrument, such as the corneal apex in anterior corneal imaging. The presence of back-reflected light results in saturation of the A-scan signals. Upon Fourier

Transform, fully saturated A-scans appear as completely modulated white lines, whereas partially saturated A-scans give rise to replications and ghost signals. These effects produce additional distorting factors in the detected corneal surfaces from sOCT images, and may result in an artificial steepening of the estimated cornea. However, the consequences of these effects on the quantification of geometry of the surfaces have been generally miss-regarded.

Another practical limitation for quantification of *in vivo* sOCT is imposed by motion artifacts [Yun et al, 2004, and Zhu et al 2004], which are associated to breath, pulsation [Ditchburn et al, 1953], dynamics of the tear film [Benedetto et al, 1984], among others, and occur, even when forehead support or bite bars are used. In order to minimize the impact of motion artifacts, the common solution is to increase the acquisition speed [Potsaid et al, 2010]. A widespread solution in anterior segment OCT, also common to other imaging modalities such as Scheimpflug corneal topography, is the use of a meridional scanning configuration, instead of a denser rectangular scanning [Tang et al, 2006, Li et al, 2008, Zhao et al, 2010, de Castro et al, 2010]. However, this approach assumes that the center of rotation is fixed and requires from radial interpolation, generating other sources of error. On the other hand, a dense, homogeneous sampling of the corneal elevation prevents from interpolation errors of radial or meridional sampling approaches.

In this chapter, the effect of fan distortion correction on surface asphericity both on artificial surfaces and *in vivo* is demonstrated. Corneal topographic maps corrected from fan distortion in patient's eyes are shown, and compared to topographic maps obtained with state-of-the-art clinical topography systems (Scheimpflug imaging and Placido-based videokeratography) in the same patients.

7.2. Methods

7.2.1 Image processing, automatic segmentation and surface fitting

Anterior segment OCT systems are designed for imaging quasi-transparent media, as corneal and lens tissues, and therefore, their dynamic range is adapted for the very weak signals provided by the diffuse reflection of the ocular surfaces. Images of plastic surfaces, or even the cornea, typically show a "white" area corresponding to zones producing a specular or directional back-reflection. In sOCT systems saturation results in the images showing a repetitive structure along the "white" A-scans, as a result of the Fourier Transform. We implemented the following strategy to avoid the saturation, of the whole 3-D scan

acquisition: We reduced the amount of irradiance impinging the surface up to prevent the interference fringes (carrier) coded in the autocorrelation spectrum (envelope) from saturating the detection system. This procedure can be applied by shortening the exposure time of the CMOS camera or by lowering the radiant intensity from the autocorrelation spectrum of the reference arm to values below four times the detection range of the camera. This way, the maximum of the interference fringes placed at the maximum of the cross-correlation for the specular reflection is within the range of the camera. This allows separating the information of the specular-directional reflection area from the “white background”, as the artificial echoes introduced by the Fourier transform are reduced.

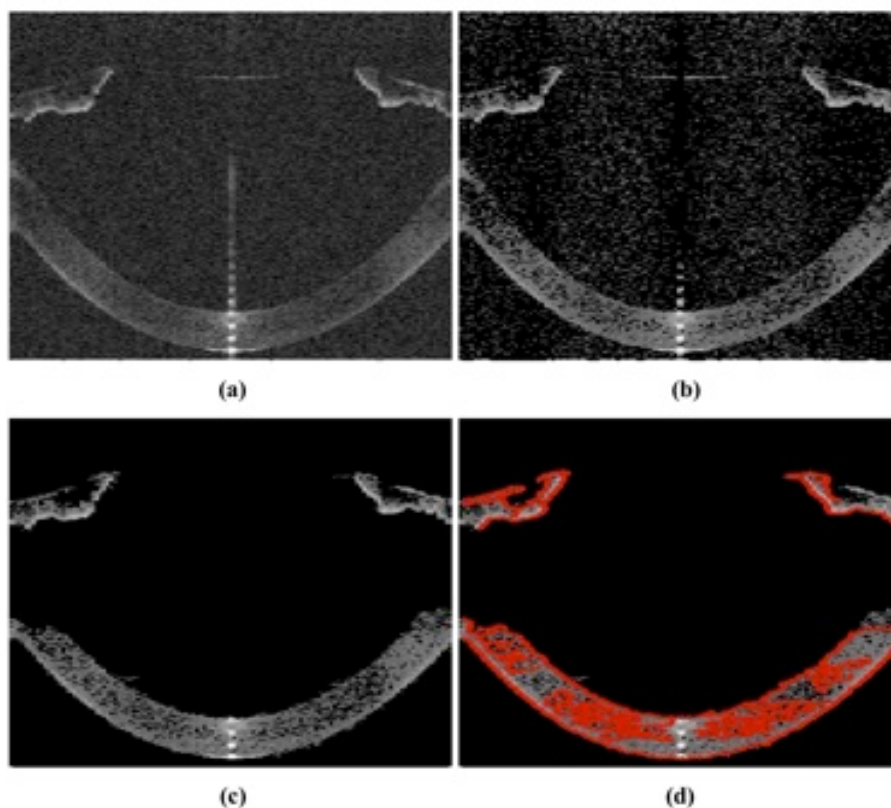


Figure 7.1. Single-frame excerpts from video recordings of the processing algorithms: a) Collection of original B-Scans, containing the data acquired from an in vivo healthy eye. b) Result of application of the statistical thresholding algorithm. c) Data after denoising image processing. d) Boundary detection in red.

In a previous work [Ortiz et al, 2010] we presented a segmentation algorithm to extract the 3-D data from sOCT B-Scans. This image processing incorporates important improvements for faster and more sensitive automatic segmentation of the surfaces in comparison with the signal processing of Section 5.2.3. The algorithm can be summarized in six steps (Figure 7.1):

(1) Statistical thresholds are calculated based on a derivation of the Otsu's [Otsu, 1979] method as it is explained in Section 6.2 (see Figure 7.1.a for a typical noisy raw B-scan) after the thresholding the Spurious noise is removed by using Morphological operators, areas in the B-scan smaller than 10 pixels are cleaned. Finally, an algorithm that finds the connected points in a neighborhood, allows identifying those belonging to a cluster >10 pixels in each B-scan (Figure 7.1.b)

(2) Application of the volume clustering algorithm as it is explained at Section 6.2.

(3) Identification of the boundaries of volumes as it is explained in Section 6.3, by performing a 3-D edge algorithm (extension to 3-D of Roberts algorithm in 2-D). This algorithm allows detecting the maximum intensity in each boundary region, allowing a multilayer segmentation (Figure 7.1.c).

(4) Multilayer segmentation. The approach, based on boundary region identification (and not only maximum intensity), allows to automatically resolve very close layers of different reflectivity (Figure 7.1.d).

(5) Application of the further surface denosing explained at Section 6.6 on the 3-D segmented surfaces corresponding to the layer identified as the anterior corneal surface are fitted to Zernike modal expansions (55 terms, 10th order) [Schwiegerling et al, 1995, Barbero et al, 2002].

(6) Surface fitting by quadrics, conicoids and topographic maps routine explained at Section 6.10 is applied to the final surfaces (Zernike fits) are also fitted by different quadrics (sphere or conicoids), using a non-linear least mean square procedure [Roberts, 1996, Cano et al, 2004 and Perez-Escudero et al, 2010].

We have developed a procedure that accounts for potential tilts of the surface, with two modes of operation: (1) The apex or center of the quadric is defined by the user. This mode is useful for comparison purposes across different topographers (where, for instance, the specular reflection can be used for reference in longitudinal measurements on patients following corneal treatment). In this case, tilt

can be corrected using the information provided by the tilt Zernike coefficients, Z_1^{-1} and Z_1^1 . (2) The location of the apex is considered an additional variable to those defining the surface shape (radii of curvature, conic constants or eccentricity [Perez-Escudero et al, 2010]). This mode is useful when the surfaces do not have a particular point that acts as a reference (i.e. in surface profilometry). The fitting process and correction of tilt is illustrated in Figure 7.2, for the first mode, considering the specular reflection as the reference Figure 7.2.a, and after tilt correction and denoising through the Zernike fitting procedure described above (Figure 7.2.b). The points in blue represent the surface used for fitting, and the red points, the surface fitting to quadrics.

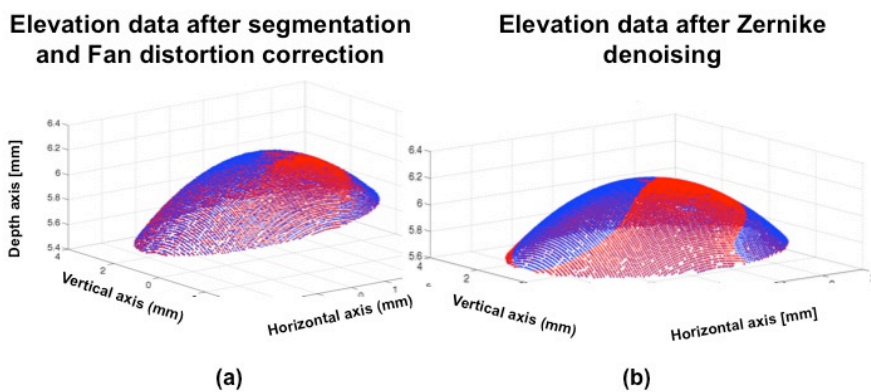


Figure 7. 2 a) Elevation data (using the specular reflection as a reference) in blue and, the surface fitted to conicoid in red (note the tilt of the surface, well accounted by the fit). b) Surface fitting after tilt correction, and further denoising using Zernike fitting. Blue points are raw points used in the fitting and red points represent the fitted surface

7.2.2. Fan distortion measurement and correction: general considerations

In Chapter 4 we have presented a method for hardware minimization and software correction of the residual fan distortion in a time-domain OCT system, which was applied to in vitro samples. A key step in the fan distortion correction is the estimation of the directional cosines at each point in the surface. The method relies on the assumption that the outgoing beam from single mode fibers can be described as TEM00 mode, and therefore following geometrical optics, the propagation of the beam can be described through their directional cosines.

Figure 7.3 shows a typical implementation of a sample arm for anterior segment OCT: A two mirror-scanner system, showing a certain separation between the mirror centers and the collimating lens. Simple ray tracing on this optical layout shows that the output directional cosines after the lens are not parallel to the optical axis. As it was

demonstrated in Chapter 4, even when the lens is placed at the optimal position from the scanner the directional cosines are skew rays, with the geometry affecting not only the axial coordinate but also the lateral coordinates, since the optical scanner deflects the light in both, elevation and azimuth angles.

As a result of the separation between the scanning mirrors, an elliptical wavefront is formed. Therefore, rays in different orientations travel different distances, and as a consequence, the lateral coordinates of the OCT become ellipsoidal (not Euclidian), producing path differences between the ray that defines the optical axis of the system and the rest of rays.

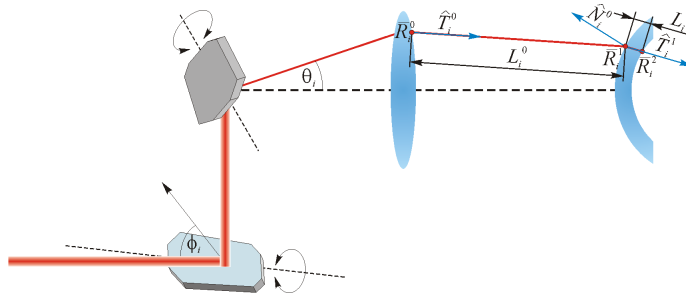


Figure 7.3. Illustration of a scanning system plus a collimation-condensing lens in an anterior segment OCT system. See text for details.

In Chapter 4 we made use of a confocal channel in the system to calibrate fan distortion. However, that channel is not generally available. Therefore we developed an alternative method, which could be easily implemented for calibration any OCT system, and we applied it, in particular, to a custom-developed sOCT [Grulkowski et al, 2009]. The method allows obtaining the axial distances that need to be added to each axial coordinate to compensate for the variable distances with respect to the optical axis at each location, as well as the transformation that must be performed to obtain lateral distances in Euclidean coordinates.

The procedure consists of collecting series of 3-D volumes (sOCT images) of a calibrated grid at different axial positions within the axial range of the device (7 mm). The grid was placed on a linear stage of 50 mm of travel path with micrometer accuracy. A 3-D volume was collected, every 0.5 mm.

The collected volumes were used to generate 2-D axial-integrated images [Targowski et al, 2006] by simple addition of the intensity along each A-scan. Figure 7.4.a shows an example of an axially integrated image of the grid used in the calibration (taken 1 mm from the best focus).

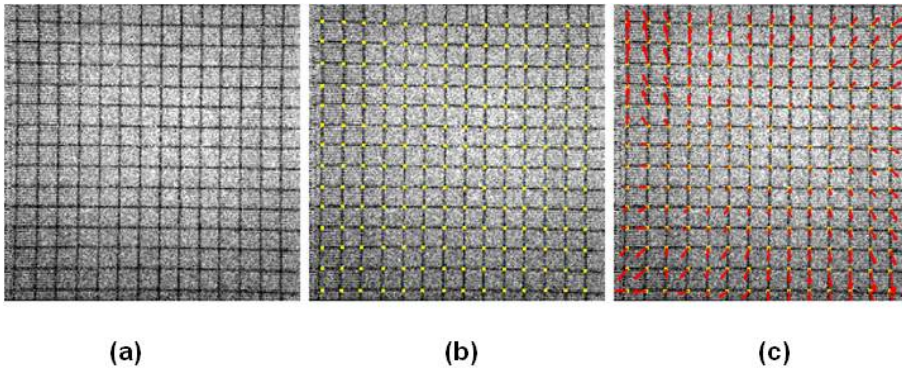


Figure 7.4. a) Axially integrated images of a grid used in the calibration (200x200 A-Scans, 11.25 wide system local units). b) Automatic nodes identification c) Vectorization of the node movement across the axial length

Each particular ray (and pixel in the image) is described by the local coordinates of the OCT x and y . We used the location of the nodes in the grid (crossing points between vertical and horizontal lines) to identify a set of 3-D coordinates in the system local coordinates, and relate them to the actual positions of the object in space. The Hough transform, in combination with circular and elliptical filters, was used to determine automatically the grid. The lines in the grid image were fitted by parabolic curves, and the nodes of the grids estimated from their intersections (Figure 7.4.b). The parabolic fit also allowed us to establish the transformation of the system local coordinates into lateral Euclidean units for each point in the volume of interest. Also, since the nodes are labeled for each axial location of the grid, the axial Euclidean coordinates are also obtained. Figure 7.4.c represents the amount and direction of the shift of the nodes at the boundary positions of the axial range. The axial length for the voxel of the collected 3-D images was estimated to be $3.42 \pm 0.01 \mu\text{m}$.

Once the actual 3-D coordinates are estimated, the quantitative estimation of axial fan distortion was performed by 3-D sOCT imaging of a flat optical surface (mirror) along the axial range of the sOCT system (7 mm). The mirror was placed at the same axial positions used in the collection of grid images. Normality of the mirror with respect to the optical axis was ensured by a pan/tilt mount (within 8 mrad).

The corresponding magnitude of the fan distortion is the distance of one point expressed in local OCT coordinates with respect to the optical axis. This distance is subtracted (in OCT local coordinates) from the raw optical path difference of detected surfaces to obtain their actual position.

7.2.3 Experiments on artificial lens surfaces (spherical and aspheric)

Measurements were performed on a spherical lens of known geometry (27.91-mm of radius of curvature) and an aspheric PMMA surface. The nominal surface geometry of the spherical artificial lens (Edmund optics) was obtained from the Edmund® catalogue. The aspheric surface was obtained by ablating a PMMA cornea (of initially 12.7-mm radius of curvature) with a refractive surgery excimer laser (Technolas, Bausch and Lomb), programmed with a standard algorithm to correct 6-D (on corneal tissue) over a 6-mm diameter optical zone [Dorrnsoro et al, 2006, Dorrnsoro et al, 2009]. The ablated surface was measured by non-contact profilometry (Sensofar P Lu 2300 Software version 2300) which allows surface topographies with an axial resolution of 0.15 μm (for a 20X microscope objective). 3-D elevation maps were obtained by evaluating the surface in a squared grid of 1157 points over a region of 15 mm for the spherical surface, and of 10 mm for the aspheric surface. In addition, the aspheric lens was measured using a Placido based videokeratography (Humphrey Atlas model 990, Humphrey Instruments, San Leandro, CA, USA, for cornea). Finally, sOCT images were obtained of both the spherical and aspherical surfaces. Measurements were collected on a 15 \times 15 mm zone, using 300 \times 300 A-scans for the spherical lens, and on a 10 \times 10 mm zone for the aspheric lens, using 200 \times 200 A-Scans, which resulted on a lateral resolution of 0.05 mm. The data were processed with and without the fan distortion correction. A total of 5 measurements were collected for each sample and device.

Elevation maps obtained for spherical surfaces (from profilometry, OCT, and OCT after fan distortion correction) were fitted by spherical surfaces, on a 6-mm diameter area. Elevation maps obtained for aspheric surfaces (from profilometry, corrected OCT and Placido based videokeratography) were fitted by conicoids [Roberts, 1996, Cano et al, 2004 and Perez-Escudero et al, 2010], on a 6-mm diameter (optical zone of the ablation). Difference maps were obtained subtracting OCT fitted topography maps from those obtained from the reference instruments. RMS (root mean square) of the difference map was used

as a metric of the accuracy of the OCT anterior corneal topographic measurement.

For statistical analysis we applied an analysis of variance (ANOVA; general linear model for repeated measurements, with the data collected from different instruments the only factor). The evaluated data were the Zernike coefficients describing the surface (as proposed by Llorente et al. [Llorente et al, 2007]), as well as radii and asphericities from the surface fitted data. Significant levels (ANOVA and pair wise comparison t-tests) were set at $p < 0.05$. The statistical tests were performed using SPSS software (SPSS, Inc., Chicago, Illinois).

7.2.4 Experiments on human corneas in vivo.

A total of 10 eyes from five human subjects participated in the experiment. The ages ranged from 24 to 38 years. The subjects were considered normal in a clinical ophthalmological examination. Refractions ranged between 0 to -4.75 D sphere and 0 to 1 D of cylinder. All protocols had been approved by Institutional Review Boards, and the subjects signed informed consents after the nature of the study had been explained, in accordance to the tenets of the declaration of Helsinki.

The subjects were aligned to the sOCT system by using the specular reflection of the cornea as a reference. Measurements were collected on a 10×12 mm zone, using 50 B-Scans composed by a collection of 360. In order to enhance the signal to noise ratio, 3 A-Scans in a B-Scan, were averaged, resulting in a final sampling of 50×120 , which provides a spatial sampling interval of 0.1 mm for the horizontal direction and of 0.2 mm for the vertical direction. The corneal power exposure was 800 μ W. Three-dimensional sOCT corneal images were collected in less than 0.8 seconds. This acquisition time was deemed as an appropriate compromise between resolution and presence of motion artifacts on control experiments on 20 subjects in which consecutive corneal images were obtained with decreasing acquisition times (0.5-2.0 sec). Five repeated images were collected per subject.

In addition to the sOCT measurements, corneal topographies were obtained from commercial Scheimpflug topography (Pentacam, Oculus Optikgeräte GmbH, Wetzlar, Germany) and Placido based videokeratography (instrument of section 2.4). These instruments were used for comparison with state-of-the art clinical standards, not as gold-standard references. The 50-scan acquisition protocol was used in the Pentacam instrument. Each Pentacam measurement was collected in about 2 seconds, while the subject fixated foveally the built-in red

fixation spot, and the corneal reflex of the fixation spot used as a reference. Each Placido based videokeratography measurement was collected in about 300 ms. Alignment was achieved by centering the image of the reflected rings on the cornea with the corneal reflex. Five repeated sets of data were obtained per subject with each instrument.

Elevation data from all three instruments were fitted by Zernike polynomial expansions (up to the 10th order) using the algorithms described in Section 7.2, in order to remove noise. Quadrics (sphere and conicoid) were subsequently fitted to the elevation maps described by Zernikes. Radii of curvature (R) and asphericity (Q) were used to describe the surfaces. A variance analysis (ANOVA) was used to estimate the statistical significance of measurements from each instrument. A Bland-Altman test [Bland et al, 1986] was applied to evaluate the agreement across methods (OCT, Scheimpflug and Placido based videokeratography), taking the Placido based videokeratography as the reference. The SPSS software was used for statistical data analysis.

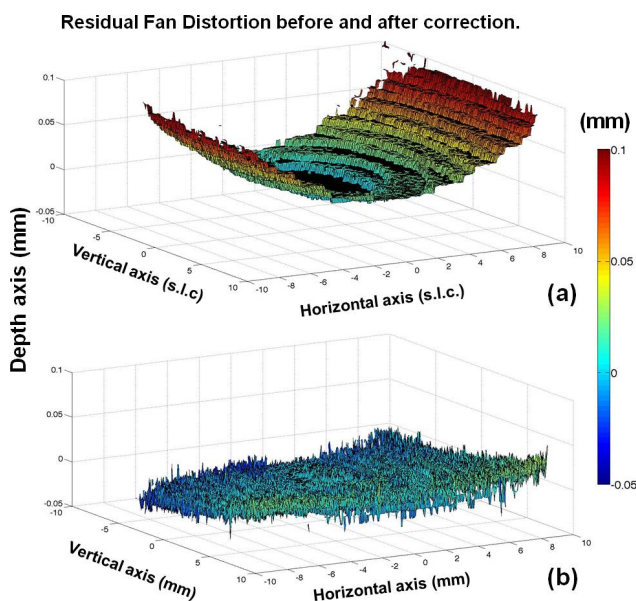


Figure 7.5. a) Map of residual fan distortion obtained from a flat optical surface with the sOCT system of the study. The surface is presented after segmentation of the image captured by the OCT and it is represented in system local coordinates (slc), except for the axial axis what it has been transformed into Euclidean coordinates for comparison purposes. b) Map of residual fan distortion after fan distortion correction.

There are several ways in which the shape of corneal surfaces can be represented and quantified [Roberts, 1996, Waring, 1989, and Klyce et

al, 1989]. We selected the so-called “height representation” where the measured elevation is represented as the difference of corneal elevation data from the reference sphere (best fitted sphere estimated using a nonlinear least squares algorithm) [Warnicki et al, 1988]. The corneal elevation maps are displayed in a square grid of 100×100 points (6-mm diameter), where warm colors depict points that are higher than the reference surface while cool colors designate lower points as it is explained in Section 6.2.

7.3. Results

7.3.1 Fan distortion

Figure 7.5.a shows the raw elevation map of flat optical surface obtained by the sOCT system (i.e. without fan distortion correction), by using a mesh of 300×300 A-Scans rastering a square zone of 19 system local coordinates width. The distortion of this surface is a direct measurement of the amount of residual fan distortion. As we had previously predicted [Ortiz et al, 2009b], the residual fan distortion is constant and does not depend on the axial position of the sample. The measured peak-to-valley difference (fan distortion) in our sOCT is 96 mm in the horizontal direction and 24 mm in the vertical direction. This asymmetry is well predicted by simulations [Ortiz et al, 2009b]. Figure 7.5.b shows the result of applying the algorithm for fan distortion correction to the sOCT images collected of a flat mirror placed on a holder mount.

7.3.2 Topographic measurements on artificial lens surface (spherical and aspheric)

Surface topographies from sOCT on a spherical lens and an ablated artificial cornea were compared to 3-D profilometric data, which were taken as a reference. Table 7.1 shows radii of curvature: nominal, and fits to profilometric and OCT data (average and standard deviation of repeated measurements). The radius of curvature from sOCT without fan distortion correction differs from profilometric data 3.9%, while after the fan distortion correction the difference decreases to 0.9%. The result of the variance analysis was that only statistically significant differences were found for the non corrected sOCT measurement.

Table 7.1. Nominal and fitting parameters to surface elevation maps measured with different instruments (spherical surface)

Spherical surface	Nominal	Profilometry	OCT (Without Fan distortion correction)	OCT (With Fan distortion correction)
Radius [mm]	27.91	27.78±0.27	27.69±0.11	28.03± 0.08

Figure 7.6 shows difference maps between sOCT and profilometric topography before (Figure 7.6.a) and after fan distortion correction (Figure 7.6.b) on spherical surfaces. The RMS error of the difference maps for the spherical surface decreases from 2.3 μm without fan distortion correction to 0.8 μm with fan distortion correction, for an area of 6-mm diameter. Figure 7.6.c shows relevant Zernike terms of the Zernike fit to the sOCT measurements (before and after correction of fan distortion), in comparison to profilometric measurements. Non-corrected sOCT surfaces show significant amount of astigmatism (Z_2^2) that decreases dramatically with fan distortion correction (from 1.25 to -0.08 μm). Differences for this coefficient between non-corrected sOCT data and profilometry were statistically significant.

The geometrical aspects (radius and asphericity) of the conicoid fitting to the aspheric PMMA surface are summarized in Table 7.2 for the three instruments: Non-contact profilometer (taken as gold standard), Placido based videokeratography, and sOCT without and with fan distortion correction. Even though Scheimpflug measurements were collected it was not possible use them, since the Pentacam software was not capable to produce reliable segmentation of the PMMA surface. Radii of curvature differed from profilometry by 0.8% for the Placido based videokeratography, 4.6% for the sOCT without fan distortion correction (being statistically significantly different), and 1.6% for sOCT with fan distortion correction. Asphericities differed substantially across methods, as well the repeatability of the asphericity estimates from repeated measurements. Asphericities differed from profilometry by 65% for the Placido-disk topographer, 130% for the sOCT without fan distortion correction, and 5% for sOCT with fan distortion correction.

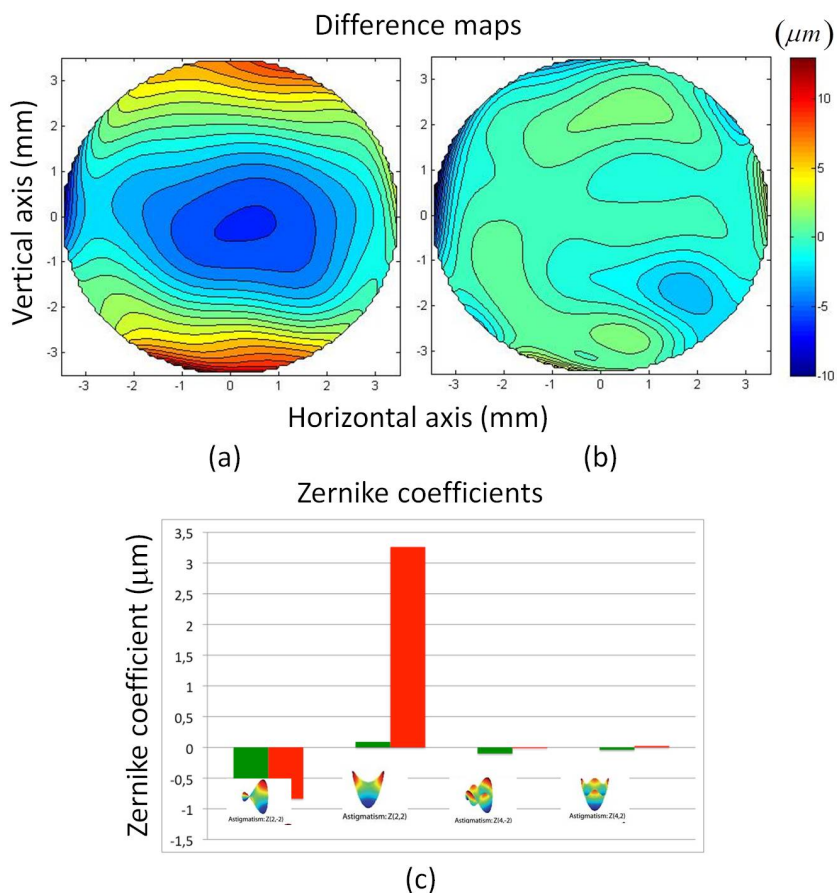


Figure 7.7. a) Difference map (sOCT elevation map – profilometric elevation map), without fan distortion correction. b) Difference map (sOCT elevation map – profilometric elevation map), with fan distortion correction, for a spherical surface. c) Second and fourth order astigmatism Zernike terms from a Zernike polynomial fit to the surfaces for sOCT topographies without fan distortion correction (red) and with fan distortion correction (green). Data in μm are averages across 5 repeated measurements for each instrument, and 6-mm diameter zones.

Table 7.2. Fitting parameters to surface elevation maps measured with different instruments (aspheric surface)

Aspheric surface	Profilometer	Placido based	sOCT (Without Fan distortion correction)	sOCT (With Fan distortion correction)
Radius (mm)	8.53±0.11	8.46±0.01	8.92±0.01	8.67±0.00
Asphericity	-0.20±0.25	-0.07±0.08	0.47±0.05	-0.21±0.02

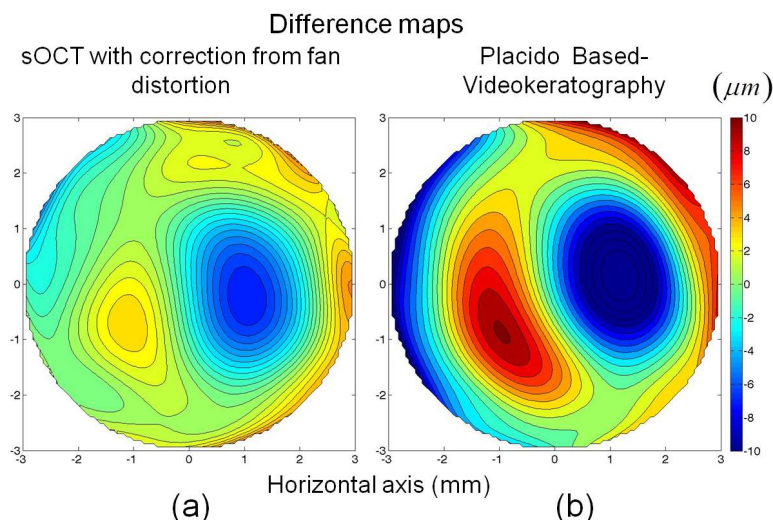


Figure 7.7 a) Difference map (OCT elevation map with fan distortion correction – profilometric elevation map). b) Difference map (Placido based videokeratography elevation map – profilometric elevation map), for an aspheric surface. Data are for a 6-mm area (optical zone of the ablation).

Figure 7.7 represents difference elevation maps (with respect to the non-contact profilometric maps) of the sOCT topography after fan distortion correction (Figure 7.7.a) and of the Placido based videokeratography (Figure 7.7.b). The RMS error of the difference maps, for a 6-mm diameter area, was $2.6 \mu m$ for sOCT with correction and $5.6 \mu m$ for the Placido based videokeratography. The differences with the profilometric topography (analyzed in terms of the Zernike coefficients) were not significant for neither instrument, although the differences for the sOCT tended to be smaller.

7.3.3 Topographic measurements on human corneas *in vivo*

Corneal topographies were obtained on 10 eyes from 5 subjects from sOCT and commercial instruments. Table 7.3 and 7.4 show radii and asphericities from conicoid fits to all corneas in a 6-mm diameter zone. Data are averages (and standard deviations) of 5 repeated measurements on each eye. Radii of curvature (Table 7.3) from sOCT without fan distortion measurements were systematically lower than those from sOCT measurements with fan distortion correction (2% on average). Discrepancies of the latter with respect to radii of curvature from Scheimpflug topography were between 1 and 2%, and from Placido based videokeratography <1%. A variance analysis showed significant differences between the Placido based videokeratography and Scheimpflug in S#1-OD, S#1-OS, S#2-OD and S#3_OD. Non-corrected sOCT data showed statistical differences compared to the

other methods for S#4-OD. Corrected sOCT was statistically significantly different from other methods for S#1-OS. The Bland-Altman plot for radii of curvature did not show any significant difference across instruments, providing a range of [-0.13, 0.05] for the comparison between Placido based videokeratography and Scheimpflug, [-0.16, 0.16] for the sOCT without fan distortion correction, and [-0.09, 0.10] for the sOCT with fan distortion correction.

Table 7.3. Radii of curvature (from a conicoid fitting) of anterior corneal elevation maps measured with different instruments (10 eyes from 5 subjects)

	Conicoid Radius (mm)	Placido based videokerato.	Scheimpflug	sOCT (Without Fan distortion)	sOCT (With Fan distortion correction)
S#1	OD	8.16±0.01	8.12±0.02	8.23±0.11	8.14±0.02
	OS	8.18±0.01	8.10±0.02	8.10±0.07	8.14±0.01
S#2	OD	7.51±0.04	7.45±0.01	7.54±0.03	7.53±0.04
	OS	7.45±0.03	7.45±0.03	7.45±0.01	7.46±0.02
S#3	OD	7.59±0.02	7.54±0.01	7.54±0.06	7.60±0.02
	OS	7.53±0.01	7.52±0.03	7.47±0.06	7.52±0.01
S#4	OD	8.02±0.11	7.90±0.00	8.19±0.04	8.09±0.03
	OS	7.88±0.09	7.83±0.00	7.94±0.03	7.89±0.02
S#5	OD	7.50±0.02	7.49±0.02	7.54±0.04	7.56±0.06
	OS	7.52±0.05	7.50±0.03	7.51±0.04	7.48±0.05

Asphericities (Table 7.4) from sOCT without fan distortion differed dramatically in comparison with the rest of the instruments (even changing signs), in consistency with the findings on the artificial aspheric surfaces. Only two eyes S#4-OS and S#5-OS show statistically significant differences between Scheimpflug and Placido-based videokeratography. When the sOCT without fan distortion correction was compared to the Placido-based videokeratography three eyes showed significant statistical differences (S#2-OD, S#2-OS and S#4-OS). In the case of the sOCT with fan distortion correction the only eye showing significant statistical difference was S#4-OS. The Bland-Altman plot for asphericity showed relatively narrow limits of agreement comparing Placido-based videokeratography with Scheimpflug and sOCT with fan distortion correction ([-0.17, 0.21; Scheimpflug], [-0.19, 0.18; sOCT with fan distortion correction]). In the case of sOCT without fan distortion correction the limits of agreement in comparison with Placido-disk were higher [-0.21, 0.37].

TOPOGRAPHY FROM SPECTRAL DOMAIN OPTICAL COHERENCE TOMOGRAPHY FOR *IN VIVO* AND *IN VITRO* SURFACES

Table 7.4. Asphericities (from a conicoid fitting) of anterior corneal elevation maps measured with different instruments (10 eyes from 5 subjects)

Asphericity		Placido based videokerato.	Scheimpflug	sOCT (Without Fan distortion)	sOCT (With Fan distortion correction)
S#1	OD	-0.12±0.07	-0.02±0.09	-0.22±0.16	-0.13±0.02
	OS	0.06±0.11	-0.04±0.15	-0.01±0.12	-0.12±0.09
S#2	OD	-0.13±0.04	-0.19±0.04	-0.04±0.04	-0.07±0.02
	OS	-0.18±0.08	-0.10±0.09	0.07±0.01	-0.18±0.01
S#3	OD	0.01±0.08	-0.02±0.01	-0.01±0.08	-0.07±0.02
	OS	-0.02±0.07	-0.01±0.07	0.01±0.09	-0.03±0.03
S#4	OD	-0.25±0.11	-0.32±0.00	-0.15±0.05	-0.24±0.03
	OS	-0.39±0.00	-0.30±0.02	0.07±0.04	-0.34±0.01
S#5	OD	-0.04±0.09	0.01±0.04	-0.04±0.04	0.01±0.04
	OS	-0.11±0.04	0.02±0.08	-0.06±0.05	-0.12±0.03

Figure 7.8 shows topographic height maps from 4 eyes, obtained from Placido-based videokeratography, Scheimpflug and sOCT (without and with fan distortion correction). Difference maps are not shown, as none of the instruments is considered as a “gold standard”. All maps are presented on the same scale for each eye, and are averages of 5 repeated measurements. All data are represented over a 6-mm diameter zone, centered at the specular reflection for foveal fixation. The topographic maps were obtained by fitting the raw elevation maps to a 10th degree Zernike expansion, relative to the best fitting sphere. The numbers below each map represent the average and standard deviation of the radius of curvature of best fitting sphere in mm.

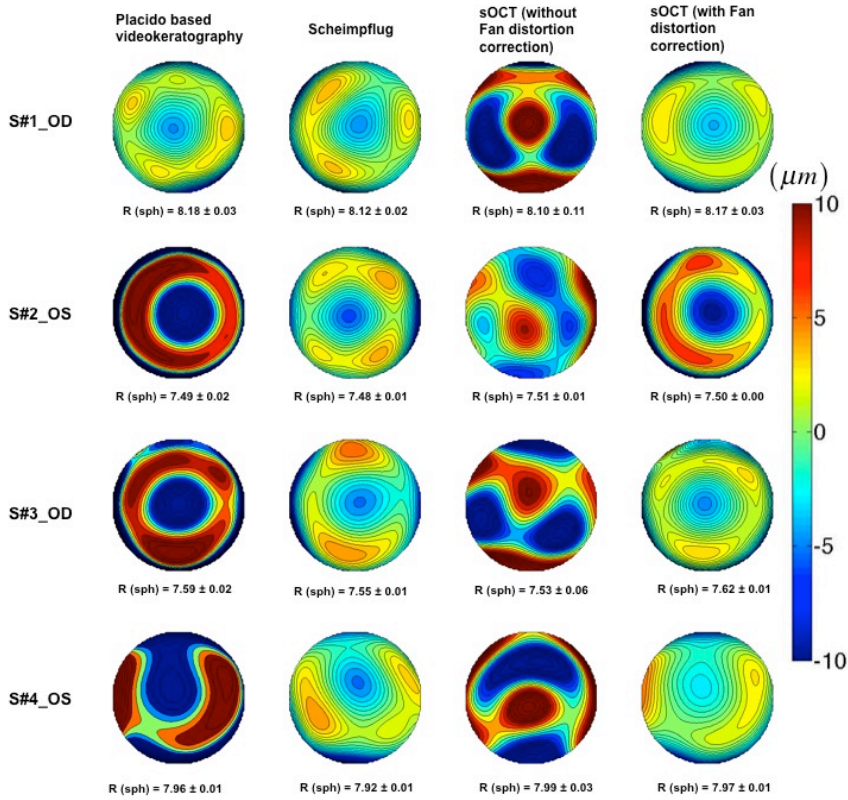


Figure 7.8. Corneal elevation maps obtained in 4 eyes obtained from different instruments (relative to the best fitting sphere). R = radii of curvature of the best fitting sphere (from fits to sphere quadrics).

7.4. Discussion

We have presented a method for correcting the distortion of OCT systems, due to the architecture of the sample arm. The calibration has been combined with new algorithms for denoising, segmentation and surface fitting, which have allowed automatic estimation of the surface topography. The presence of fan distortion and its correction in a non-telescopic scanning system was first reported by Westphal et al [Westphal et al, 2002]. In a previous study we presented theoretical predictions and measurements, as well as a method for correction of fan distortion in a time-domain OCT system provided with a confocal channel [Ortiz et al, 2009b]. In this study, we have demonstrated that the sOCT corrected for fan distortion produces accurate topographic estimates of artificial surfaces, as compared to non-contact profilometric data. Correcting fan distortion has proved particularly critical for accurate estimates of asphericity. In fact, sOCT with fan distortion correction produced the closest estimates of asphericity with respect to the gold standard (non-contact profilometry) values than

other commercial topographers (such as Placido-based videokeratography). A proper measurement of corneal asphericity is critical in clinical applications of corneal topography (refractive surgery, contactology, etc...).

Even though there are small statistically significant differences in terms of quadric parameters for the sOCT without correction, it is in terms of the topographic maps where differences are most notorious. The presence of astigmatism in the data prior to fan distortion correction is clearly observed in the measurements of artificial surfaces, where (unlike in real eyes) no other astigmatism arising from alignment or shape should be present.

Placido-based videokeratography, and to a less extent Scheimpflug imaging, are widely used clinically to measure the geometry of corneal surfaces. The high level of accuracy and precision of Placido-based videokeratography in measuring spherical and aspheric samples has been demonstrated in several studies [Tang et al, 2000, and Cho et al, 2002]. We have recently reported on the accuracy of the Pentacam anterior and posterior corneal topography on artificial (plastic and hybrid porcine/plastic) eyes. Although the radii of curvature of the surfaces were retrieved within 98.3% accuracy [Pérez-Escudero et al, 2009] we did not attempt to explore the accuracy of the asphericity estimates. The repeatability of clinical instruments has also been studied. In general, Placido-based videokeratography showed higher repeatability due to its high-speed acquisition; however the posterior corneal surface or the geometry of the corneal apex cannot be measured [Nakagawa et al, 2009]. Although some studies reported high repeatability in anterior corneal parameters in normal corneas measured with Pentacam [Chen et al, 2007, Shankar et al, 2008, and Read et al, 2009], a recent study reported relatively high variability in the corneal elevation data obtained with this instrument [Shankar et al, 2008]. The relative long acquisition times and the rotating slit scanning scheme may result in motion artifacts and changes in the center of slit rotation.

The relatively sparse information in certain dimensions (radially in Placido-based videokeratography, where the information in the 1-mm central region is lost, and the cornea is sampled radially, and meridionally in Scheimpflug, where the information is sampled only on 25-50 meridians) poses some limitations to these techniques. For example, the meridional pattern is not well suited in patients with irregularities with higher azimuthal frequencies [read et al, 2009].

In contrast, OCT allowed a more sensitive analysis of the geometrical shape of the corneal surface due to its larger axial and lateral resolution. In order to minimize the impact of motion artifacts, we decreased the acquisition times without compromising sampling density (>25000 A-Scans were used). The homogenous sampling pattern in the current study differs from that chosen in recent reports of OCT-based topography, where the information is collected in a series of meridians [Tang et al, 2006, Li et al, 2008, Zhao et al, 2010]. While this strategy is time-efficient and non-problematic in symmetric surfaces, it potentially encompasses similar limitations than those indentified for Scheimpflug imaging (reduced sensitivity in the detection of asymmetries, dependence on the center of rotation, etc). Optimizing both sampling density and sampling pattern will potentially contribute to more accurate corneal elevation reconstructions.

In summary, correction of fan distortion is important for accurate surface/corneal topography with OCT systems. Spectral OCT has the potential for becoming a system for state-of-the-art topography, and overcome the limitations of current standard topographic system. It is essential however to provide the systems with appropriate calibration tools, as well as automatic procedures for accurate detection and evaluation of the surfaces. Although the technique has been demonstrated on a laboratory-based OCT system, it can be easily extrapolated to other OCT systems.

7.5. Conclusions.

We have presented a full experimental method for correction of fan distortion, which can be universally applied to any anterior segment OCT system. This method that allows achieving accurate corneal topographies from spectral anterior segment OCT. The method for correction has been combined with robust automatic image processing techniques. The sOCT topography after fan distortion correction has proved extremely accurate (compared to non-contact profilometry) on artificial lenses (less than 1% discrepancy for both radius of curvature and asphericity), and provided the most accurate estimate of surface asphericity. The statistical comparison of these corrected topographies with topographies from state-of-the art clinical topography systems represents a valuable contribution toward the development “All-OCT-based” topographic systems. Fan distortion correction (along with fast acquisition and powerful segmentation strategies) is essential to obtain reliable corneal elevation maps from sOCT in patients.

Chapter 8

Quantitative OCT-based corneal topography in keratoconus with intracorneal ring segments

This chapter is based on the article by Ortiz, S. et al “ Corneal topography from spectral Optical Coherence Tomography (sOCT)” *Biomedical Optics Express*, Vol. 3, Issue 5, pp. 814-825 (2012). The coauthors of the study are: Pablo Pérez-Merino, Nicolas Alejandre, Enrique Gamba, Iñigo Jimene- Alfaro, and Susana Marcos. The work was developed at Instituto de Óptica “Daza de Valdés”. The contribution of the author of this thesis was the 3-D characterization of corneal topography in keratoconus before and after implantation of intracorneal ring segments (ICRS) using our Custom high-resolution high-speed anterior segment spectral domain Optical Coherence Tomography (OCT). Surfaces were automatically detected for quantitative analysis of the corneal elevation maps (fitted by biconicoids and Zernike polynomials) and pachymetry. Automatic tools were developed for the estimation of the 3-D positioning of the ICRS. The pupil center reference was estimated from the segmented iris volume. The developed algorithms are illustrated in a keratoconic eye (grade III) pre- and 30 days post-operatively after implantation of two triangular-section, 0.3-mm thick Ferrara ring segments. Automatic tools also allowed estimation of the depth of the implanted ICRS ring, as well as its rotation with respect to the pupil plane.

8.1. Introduction

Keratoconus is a bilateral, asymmetric and chronic disease of the eye caused by the weakening of the cornea with a prevalence of 1 per 2000 in the population [Rabinowitz et al,1998]. It is characterized by a progressive thinning and steepening of the cornea, resulting in a cone-shaped cornea, which leads to increased astigmatism and high order aberrations [Barbero et al, 2002], and a loss of visual quality [Kymes et al, 2008]. In the early stages of the disease, the use of spectacles or contact lenses might provide sufficiently functional visual quality to the patient [Nordan, 1997]. However, the progressive corneal thinning and steepening usually results in the need of corneal transplant in advanced stages [Mamalis et al, 1992, and Javadi et al, 2003]. Several emerging treatments of keratoconus, such as collagen cross-linking [Ferrara et al, 1995] or the implantation of poly(methyl methacrylate) (PMMA) intracorneal ring segments (ICRS) [Colin et al, 2000, Siganos et al, 2002 and Alió et al, 2002], attempt at preventing or delaying corneal transplant. The rationale behind the ICRS is the use of passive spacing elements to increase the keratoconic corneal structural integrity, shorten the arc length of the corneal surface, and achieving a refractive adjustment by flattening the central cornea [Barraquer, 1966, and Blavatskaya, 1968]. One of the advantages of the ICRS surgery is the possibility of reshaping the cornea without removing tissue, although a potential drawback is the lack of predictability of its outcomes [Burriss et al, 1993 and 1998, and Piñero et al, 2010].

Understanding of the structural and geometrical changes induced on the cornea upon implantation of ICRS is key in the optimization of the ICRS surgery to treat keratoconus and increase its predictability. Quantitative information from advanced anterior segment imaging techniques may be challenged by the irregular cornea, by the limited range of application of some of the existing instruments, and by the presence of the implant with a different index of refraction from tissue. Several studies report geometrical corneal changes in keratoconic corneas [Maguire et al, 1989, Rabinowitz et al, 1989, Maeda et al, 1994 and Tomikodoro et al, 2000] and upon ICRS implantation, measured by slit-scanning corneal topography (Orbscan, Orbtek, Inc) [Dauwe et al, 2009], Scheimpflug camera (Pentacam, Oculus, Inc) [Kamburoglu et al, 2009] or high-frequency ultrasound (UBM) [Reinstein et al, 2001]. Although these instruments have allowed to identify unusual topographic patterns in the anterior cornea, and provided posterior corneal elevation and pachymetry maps, they are subject to limitations, particularly in the application under study. Slit-scanning topography

presents limited depth resolution and several studies have reported underestimation of corneal thickness in keratoconic patients [Kawana et al 2005]. Furthermore, the lack of an appropriate correction of the optical distortion produced by the anterior corneal surface limits the reliability of the retrieved posterior corneal surface. In comparison with slit-scanning systems, Pentacam Scheimpflug imaging system has shown to provide good reproducibility and repeatability in measuring curvature and thickness in normal and keratoconic eyes [de Sanctis et al, 2007], although some studies reported variability in corneal elevation maps [Shankar et al, 2008, Read et al, 2009]. In a previous study we showed that posterior corneal curvature measured with this instrument was not influenced by refraction of the anterior surface [Perez-Escudero et al, 2009]. However, it is likely that the optical distortion correction assumes a constant corneal refractive index, compromising the estimates of posterior corneal elevations viewed through a different optical material. UBM requires immersing the eye in a coupling fluid, which limits control of the visual fixation). Also, although unlike optical techniques UBM is not subject to refraction distortion, the axial resolution is poorer than that of optical techniques.

OCT appears therefore as an ideal tool to quantify both the geometry of the cornea, and its changes with treatment, as well as the implantation of the ICRS (i.e. three dimensional positioning of the implants within the corneal volume). However, quantitative geometrical parameters can only be retrieved accurately upon correction of the fan (scanning) distortion of the sample arm of the OCT instrument, and (for all structures behind the anterior cornea) correction of the optical (refraction) distortion [Ortiz et al, 2009a, 2009b, 2010, and 2011, Zhao et al, 2010]. Optical correction of the refraction of the anterior cornea is particularly critical in keratoconic corneas, with increased irregularities and steepening, and in the presence of ICRS with a different refractive index.

In this study, we present quantification of the keratoconic cornea before and after ICRS implantation. To our knowledge, this is the first time where fully quantitative OCT (following fan and optical distortion correction) has been applied to retrieve anterior and posterior corneal elevations and pachymetric to irregular and treated corneas. The chapter also reports the development of a series of automatic algorithms of volume identification in general (and of the ICRS in particular), automatic segmentation of the edges of the ICRS, which allowed accurate automatic estimate of the location, depth and rotational angles of the ICRS.

8.2. Material and Methods

8.2.1. Patient and ICRS surgery

Ferrara ICRS were implanted using a manual surgical technique in one keratoconic patient (29 y.o) [Siganos et al, 2002]. The surgical procedure was carried out under topical anesthesia. The technical specifications of the Ferrara ICRS were: triangular cross-section, 0.3-mm thickness, 90-deg arc length, 5-mm inner diameter, and 5.6-mm outer diameter. The tunnels were performed at 80% of the corneal thickness, and the ICRS subsequently implanted in the tunnels. Two segments were implanted symmetrically at an angle of 70° deg from the steepest meridian. The study was approved by Institutional Review Boards and followed the tenets of the Declaration of Helsinki. The subject signed a consent form and was aware of the nature of the study.

8.2.2. Experimental acquisition protocols

Measurements on the patient were performed pre-operatively and 30 days after ICRS implantation. The patient was stabilized using a bite bar. Alignment of the patient was achieved with respect to the anterior corneal specular reflection. All the measurements were performed in a dark room under the same conditions without the use of dilating drops. A total of five sets of 3-dimensional measurements were collected pre-operatively and post-ICRS implantation. The SLD power exposure was fixed at 800 μ W. Each set of 3-D measurements was acquired in 0.72 seconds in order to minimize the impact of motion artifacts (Section 8.2.4). Measurements were collected on a 10 \times 12 mm zone, using 50 B-Scans composed by a collection of 360 A-Scans, providing a resolution of 0.03 mm for horizontal and 0.2 mm for vertical meridian.

8.2.3. 3-D image analysis: denoising, segmentation and surface fitting.

Corneal topographic maps from normal subjects using sOCT by extracting volumetric data were described in detail in previous chapters (2-5 and 7). This study incorporates improvements for a faster and a more sensitive automatic segmentation of the surfaces, as well as new routines that have been specifically developed for the requirements of the current application. Newly developed algorithms for automatic clustering of volumetric objects have been particularly instrumental in the detection of ICRSs within the corneal volume, and the automatic pupil detection, used for referencing. The algorithm is summarized in nine steps. Only dedicated new routines are described in detail:

- (1) Denoising: As it is explained in Section 6.2 a rotational kernel transform was performed for an edge-preserving denoising, using a mask of size 9 pixels. In addition, a wavelet low-pass filtering processing based on log-Gabor wavelet for 7 scales and 6 orientations was used.
- (2) Statistical thresholding: In this chapter, a multimodal histogram distribution for the entire 3-D data was introduced in application of Section 6.3
- (3) Volume Clustering: As a result of the overlapping statistics of the noise and signal, randomly distributed noise is still present in the images after thresholding. We developed the volume clustering introduced at section 6.4. The classes with a volume size below a certain threshold are eliminated. The threshold is estimated as a certain percentile within the range of 95-99% of the total number of connected points.
- (4) Multilayer segmentation: As it is introduced in Section 6.5 the Sobel operator extended for 3-D was applied and after a 3-D neighborhood algorithm is applied to this 3-D matrix producing layers of connected points and rejecting random peaks due to noise. Examples of surface segmentation of the posterior corneal surface, ICRS surfaces, and the anterior corneal surface are shown in Figure 8.1.

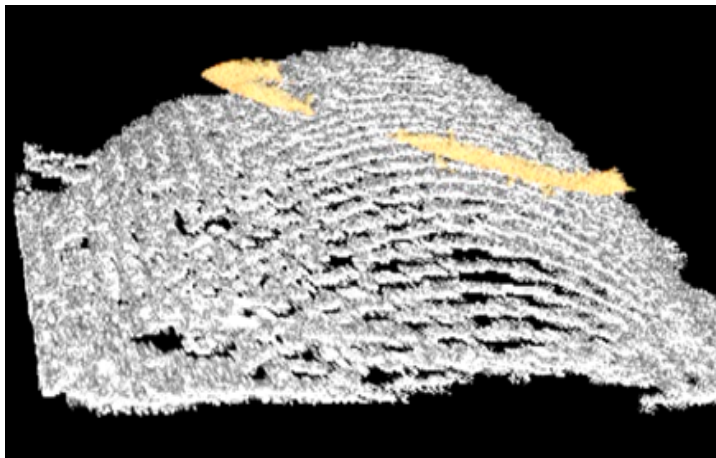


Figure 8.1. Illustration of the multilayer segmentation in a keratoconic cornea implanted with an ICRS, showing the posterior corneal surface (white), ICRS (yellow) and the anterior corneal surface (orange, movie only).

- (5) Distortion corrections: Fan distortion correction was applied for the anterior cornea, and both fan and optical distortion corrections were applied for the multiple surfaces after the anterior surface. We applied

these algorithms as previously described in Chapter 4 and in Section 8.2.2, assuming a corneal index of refraction of 1.376. However, the presence of the ICRS (index of refraction= with 1.4914) required adjustments in the algorithm to account for the new refractive interfaces across the cornea in 3-D.

(6) Surface fitting by quadrics (biconicoid): Raw corneal elevation data from anterior and posterior surfaces were denoised by using a fitting Zernike modal expansions (55 terms, 10th order) (Section 6.5). The denoised surfaces were also fitted by quadrics (Section 6.8). For the purposes of this study a spherical surface was used as a reference surface in corneal elevation maps, A biconicoid was used to obtain corneal shape descriptive parameters (radii of curvature R_x and R_y and conic constants Q_x and Q_y) [Perez-Escudero et al, 2010].

(7) Pupil center reference. The pupil center was used as a reference across measurements (i.e. pre- and post-operative) and to define the optical zone (effective area within the ICRS inner diameter). According to previous studies, the pupil center shifts little across pupil sizes and light conditions [Yang et al, 2002]. The pupil center was efficiently calculated from the clustered iris volume (Figure 8.2.a), by collapsing the cloud of points onto a 2-D image. The pupil center and radii were obtained from an ellipse fitting of the segmented edges using Sobel edge detector (Figure 8.2.b). The center of the ICRS inner area was calculated from the clustered ICRS volume, and ellipse fitting (Figure 8.2.c). The shift between the pupil center and the center of the inner area of the ICRS was estimated. The center of optical zone was therefore defined from post-operative parameters and used of registration of the pre-operative cornea (Figure 8.2.d). The biconic fitting of pre- and post-operative corneas was performed on 4-mm pupil diameter.

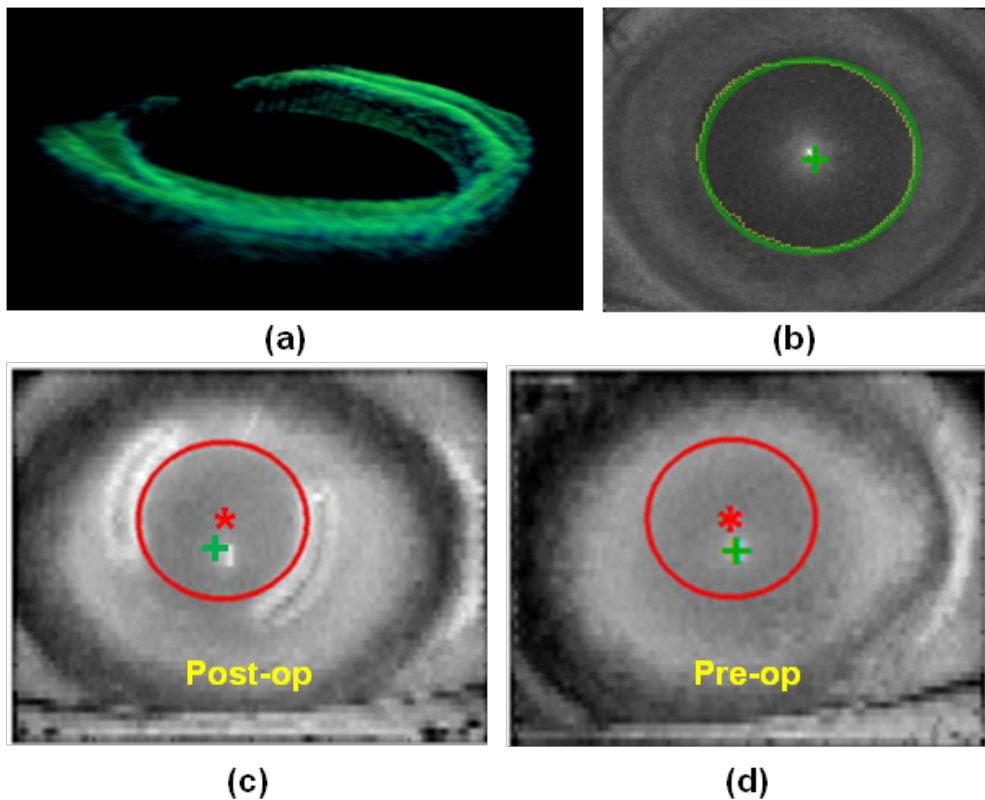


Figure 8.2. (a) Segmented (green). (b) Pupil edge fitting (detected edge in yellow and ellipse fitting in green). (c) ICRS inner diameter edge fit in the post-operative cornea (red line, and center as a red asterisk) and pupil center (green cross) (d) Evaluation of the same optical zone (in red) in the pre-operative cornea, using the pupil center as a reference.

(8) Corneal elevation maps: As it is explained in section 6.8 the maps are displayed in a square grid of 100x100 points in a 6-mm of diameter, with respect to the pupil center. This representation does not require interpolation of the data, as (unlike other approaches in Scheimpflug imaging and OCT [Shankar et al, 2008, and Li et al 2010]) the data were obtained as a dense collection of B-scans, rather than across meridians. The measured elevation is represented as the difference of corneal elevation data from the reference sphere [Warnicki et al, 1988], where warm colors represent points that are higher than the reference surface and cool colors represent points below the reference. The pachymetry maps were calculated from direct subtraction of the posterior corneal surface from the anterior corneal surface, after distortion corrections, and are represented using the HSV color map.

8.2.4. ICRS implantation evaluation

The automatic identification of the edges of the implanted ICRS volumes obtained from the clustering algorithm allows the analysis of the ICRS location in 3-D within the cornea: depth, orientation and lateral position at every corneal location. These parameters were obtained from estimations of the vertices of the ICRSs, and their geometrical center at every location. The resulting points in 3-D along an arc (for each segment) allowed estimation of the depth and position of the ICRS with respect to the anterior corneal surface. The plane containing those arcs (and its corresponding normal) was used to estimate the overall rotation of the ring (using the pupil plane as a reference).

8.3. Results

8.3.1. Posterior corneal surface change after ICRS distortion correction

Raw OCT images suggested an even larger increase of corneal thickness in the peripheral areas of the cornea, as a result of higher optical path difference through the ICRS. However, after correction of optical distortion and consideration of the actual PMMA refractive index within the segment, corneal thickness decreased by up to $35\ \mu\text{m}$ in those areas. Figure 8.3 shows a cross-section of the cornea implanted with the ICRS ring, illustrating the effect of correcting the refraction in the left segment while the right one remained un-corrected. It can be observed qualitatively that the correction reveals a more symmetric segment with flat edges.

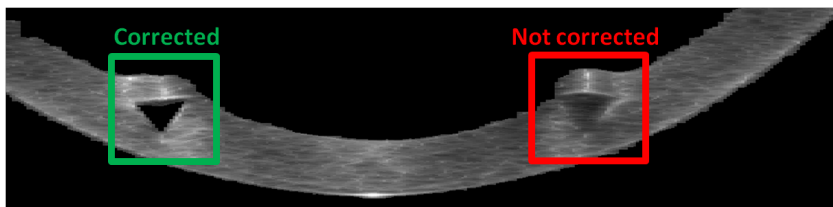


Figure 8.3. Effect of the ICRS distortion on the corneal posterior surface. Left: Non-corrected image (red). Right: image after optical distortion correction of the ICRS (green).

8.3.2. Corneal shape: radii of curvature and asphericities

Table 8.1 summarizes the values of radius and asphericity for anterior and posterior corneal surface before and after ICRS implantation, obtained from corneal elevation fitting within the optical zone (4 mm). Data are the mean of five repeated measurements.

ICRS implantation produced a significant flattening of the anterior corneal surfaces (vertical 1.85%; horizontal 6.00%), and posterior corneal steepening (vertical 11.38%; horizontal 3.94%). Similarly, changes in asphericity were also higher in the vertical than in the horizontal meridian, both in the anterior (vertical 3.74%; horizontal 10.10%) and posterior (vertical 24.42%; horizontal 9.09%) cornea.

Table 8.1. Radii and asphericities of the cornea before and after ICRS surgery

	Radii of curvature (mm)			
	Pre-op		Post-op	
	<i>Horizontal</i>	<i>Vertical</i>	<i>Horizontal</i>	<i>Vertical</i>
Anterior	8.03±0.08	6.51±0.14	8.16±0.16	6.90±0.11
Posterior	5.97±0.13	6.32±0.09	5.36±0.14	6.08±0.17

	Asphericity			
	Pre-op		Post-op	
	<i>Horizontal</i>	<i>Vertical</i>	<i>Horizontal</i>	<i>Vertical</i>
Anterior	-1.03±0.02	-0.89±0.03	-1.07±0.03	-0.99±0.02
Posterior	-1.07±0.08	-1.20±0.07	-0.86±0.08	-1.10±0.10

8.3.3 Full corneal topography

Figure 8.4 shows quantitative topographies of the anterior and posterior corneal surfaces before and after ICRS implantation. The pre-operative anterior corneal surface shows a 40 µm bulging (with respect to the reference sphere) near the ectatic zone, next to a -45 µm depression. Large asymmetries are also observed in the posterior cornea.

After ICRS implantation, the anterior surface of the cornea shows a more regular pattern, a shift of the area of maximum elevation and a decrease in the maximum height (down to 15 µm.). The ICRS produces a stretching that decreases elevation (-20 µm) in the area above the ICRS. The posterior topographic map is consistent with a lateral stretching in the optical zone induced by the action of ICRS, and shows an effective protrusion of the cornea areas behind the ICRS.

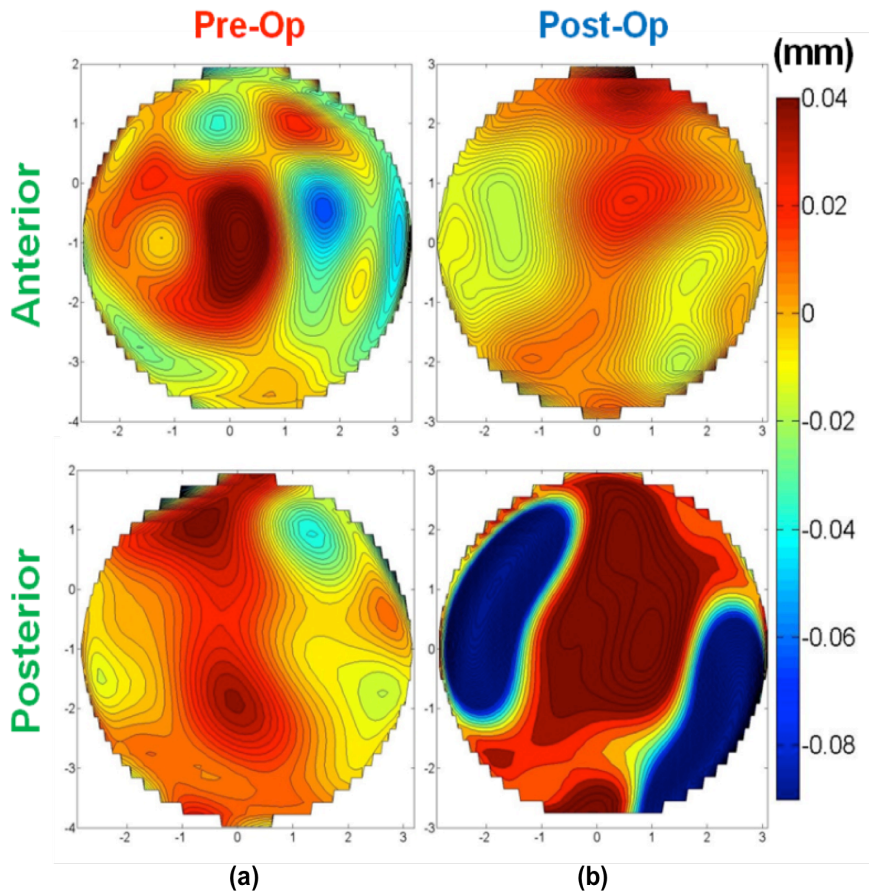


Figure 8.4. (a) Quantitative anterior and posterior corneal elevation maps of a keratoconic cornea. (b) Quantitative post-ICRS anterior and posterior corneal elevation map. All data are after refraction distortion correction, and for a 6-mm zone.

8.3.4. Corneal pachymetry

ICRS implantation increased the minimum corneal thickness (from $353 \pm 15 \mu\text{m}$ pre-operatively and $429 \pm 15 \mu\text{m}$ post-ICRS), and decreased the overall corneal thickness asymmetry (Figure 8.5). The post-ICRS pachymetry map is consistent with a lateral stretching within the optical zone induced by the action of ICRS. At the location of the ICRS (i.e. beyond the optical zone) corneal thickness effectively increased,

indicating an axial stretching of the cornea by the ICRS

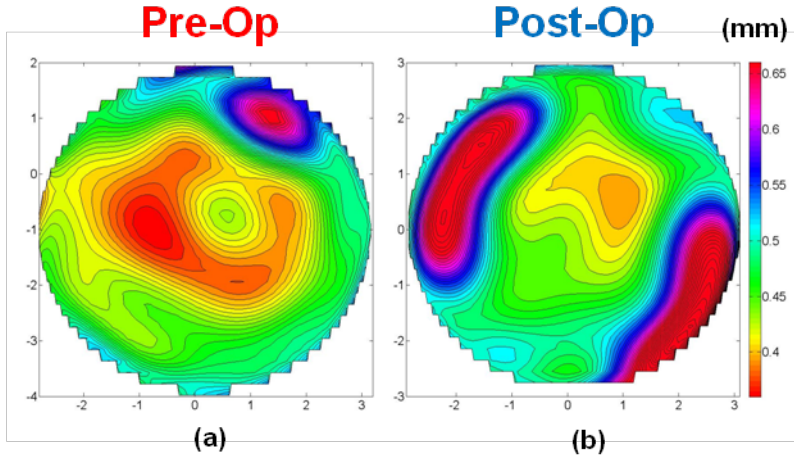


Figure 8.5 Quantitative pachymetry map of keratoconic cornea (a) before and (b) after ICRS implantation. Data are for a 6-mm zone.

8.3.5. ICRS location

Figure 8.6 shows an illustration of the estimated location and orientation of the ICRS inside the cornea in 3-D. The ICRS center of mass was measured to be at a depth from the anterior corneal surface ranging from 350 to 470 μm (left segment) and from 360 to 450 (right segment). The ICRS was tilted $5.46 \pm 1.16^\circ$ (left segment) and $12.41 \pm 1.65^\circ$ (right segment) with respect to the pupil plane, and laterally decentered (-0.10 ± 0.05 mm in the horizontal direction and -0.34 ± 0.10 mm in the vertical direction) with respect to the pupil center.

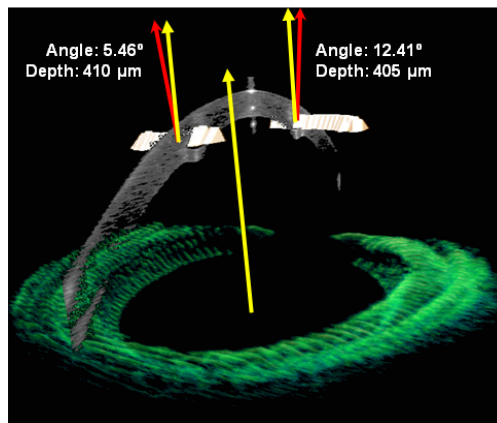


Figure 8.6. 3-D analysis of the orientation (with respect to the pupil plane) and average depth (with respect to the anterior cornea) of the left and right ICRS. The red arrows are normal to the plane of the ICRS, and the yellow arrows are normal to the pupil.

8.4. Discussion

The capability of the OCT for obtaining accurate topographies from the anterior corneal surface has been explained in Section 8.2.2. In this chapter, the application of the algorithms for reconstructing accurate corneal elevation maps after application of optical and fan distortion correction (Chapter 4-5 and Section 8.2.2) as well as new dedicated processing algorithms for automatic segmentation and volume clustering has opened the possibility for automatic corneal topographies and quantitative characterization of keratoconic eyes before and after ICRS implantation. This application is particularly demanding, as keratoconic corneas are irregular, and the ICRS are foreign objects within the cornea with a different refractive index. The high-resolution of the OCT, together with the acquisition of 3-D corneal images (rather than meridional cross-section) allows reconstruction of a dense corneal volume. The methods of analysis of the OCT corneal images presented in this study have resulted in powerful tool for quantitative evaluation of the keratoconic cornea and its change after ICRS implantation, even beyond the optical zone limited by the inner diameter of the ICRS. While the anterior corneal topography in keratoconic patients has been reported extensively with different corneal topographers, primarily Placido videokeratoscopy, the changes in the posterior corneal changes are debated. It is thought that the first topographical changes in keratoconus are presented on the posterior corneal surface, corresponding to an increased posterior corneal elevation and a focal thinning [Maguire et al, 1989, Maeda et al, 1994 and Tomikodoro et al, 2000], although further investigations are needed, as some of the commercially available devices to measure posterior corneal surface are either not well validated or suffer from optical distortions from the anterior corneal surface. Therefore, a more sensitive posterior corneal elevation measurement, corrected from the refractive effects of the (very irregular) anterior corneal surface can be critical in the diagnosis and monitoring of keratoconus.

The automatic tools developed for analysis of the keratoconic cornea in this study provide extensive information of the geometrical features of the keratoconic corneas based on OCT imaging, including anterior and posterior corneal elevation maps, pachymetric maps, 3-D location of the ectatic area, corneal apex and pupil center for referencing (reported as a more suitable reference than the specular reflection [Li et al, 2010]). This information is essential in planning treatment, in particular ICRS implantation. Additional automatic tools have been developed to characterize the ICRS implant, and the geometrical corneal changes

following ICRS, all based on OCT imaging. In this patient, the ICRS produced a significant anterior corneal flattening within the optical zone. We also showed a steepening of the posterior corneal surface inside the ICRS optical zone. It is likely that the distortion produced by the ICRS on the posterior corneal surface, if not corrected using the ICRS index of refraction, may result in inaccuracy of the curvature data provided by other instruments, even within the optical zone. Furthermore, the correction of the optical distortion produced by the anterior corneal surface, as well as by the ICRS in the OCT images, allows analysis of the corneal topography even in peripheral corneal areas. The quantitative corneal surface maps (Figure 8.4) suggest a lateral stretch produced by the ICRS. The quantitative pachymetric maps (Figure 8.5) suggest a redistribution of corneal thickness which could help in delaying the progression of keratoconus. The automatic volume clustering and surface segmentation tools allowed a comprehensive description of the 3-D location of the ICRS, and therefore to evaluate the implantation and monitor potential longitudinal changes, as well as correlations between the geometrical and optical outcomes and the geometrical properties and location of the ring.

8.5. Conclusions

Anterior segment OCT provided with fan and optical distortion correction and automatic analysis tools is an excellent instrument for evaluating keratoconus. Furthermore, OCT quantitative imaging allows comprehensive 3-D quantitative analysis of the keratoconic cornea and the changes produced by ICRS treatment, as well as monitoring of the ICRS three-dimensional location. ICRS produced a flattening of the anterior surface, steepening of the posterior surface, meridional differences in the changes of radii of curvature and asphericities, a symmetrization of the anterior corneal and a redistribution of corneal thickness.

Chapter 9

In vivo human crystalline lens topography

This chapter is based on the articles by Ortiz, S. et al “In vivo human crystalline lens topography” published in *Biomedical Optics Express* Vol. 3, Issue 10, pp. 2471-2488 (2012). The coauthors of the study are: Pablo Pérez-Merino, Enrique Gamba, Alberto de Castro, and Susana Marcos. The work was developed at Instituto de Óptica “Daza de Valdés”. The contribution of the author of this thesis was to characterize three-dimensionally (3-D) the human crystalline lens in vivo using a custom developed OCT, which was provided with custom algorithms for denoising and segmentation of the images, as well as for fan (scanning) and optical (refraction) distortion correction, to provide fully quantitative images of the anterior and posterior crystalline lens surfaces. Quantitative surfaces are compared to those not correcting for distortion. Lens surfaces were fitted by biconicoids and Zernike polynomials: difference, topographic and thickness maps and in terms of geometrical aspects (Radii and asphericities). The repetitivity of the measurement is also shown.

9.1. Introduction

The optical quality of the human eye is mainly determined by the geometrical and optical properties of two elements, cornea and crystalline lens. The cornea accounts for two-thirds of the optical refractive power, while the crystalline lens provides approximately one third of the total static refractive power of the eye, and it is the responsible for accommodation [Helmholtz, 1855, Gulstrand, 1924, Kiely et al, 1982, Smith et al, 1991, Schwiegerling et al, 1995, Glasser et al, 1998, Garner et al, 1997a and 1997b and Dubbelman et al, 2002]. Accurate description of the geometry of the eye's optical components is critical for understanding their contribution to optical quality. Though the geometrical properties of the cornea have been widely studied due to its accessibility [Kiely et al, 1982, Schwiegerling et al, 1995 and Dubbelman et al, 2002], accurate quantitative data of the crystalline lens geometry are limited to *in vitro* studies [Glasser et al, 1999, Manns et al, 2004 and Rosen et al, 2006], while *in vivo* data is referred in most cases to axial properties (i.e. thickness) and central areas (i.e. central radius of curvature) [Sakamoto et al, 1992, Cook et al, 1998, Dubbelman 2001a, 2001b and 2005, Goss et al, 1997, Rosales et al, 2006].

The shape, location and phakometry of the crystalline lens have been reported *in vivo* and *in vitro* using different imaging techniques. Radii of curvature, tilt and decentration of the lens have been measured using a Purkinje-imaging based method [Rosales et al, 2006a, 2006b and 2008]. However, although Purkinje-based phakometry is a rapid, systematic, and reliable, it does not provide the full geometry of the crystalline lens surfaces, nor a direct view of the lens. In contrast, Scheimpflug imaging allows acquisition of cross-sectional images of the crystalline lens, and with proper correction of the geometrical and optical distortion, radius of curvature and asphericity of the lens surfaces can be obtained [Dubbelman 2001a, 2001b and 2005, Koretz et al, 2004, and Rosales et al 2009]. The slit-lamp based geometrical configuration of Scheimpflug imaging-based systems (where the front view of the pupil appears superimposed to the cross-sectional image) frequently limits the view of the posterior lens. Besides, commercial instruments, although providing images of the lens, are typically not corrected from optical distortion, preventing quantitative evaluation of lens parameters. To our knowledge, custom correction algorithms have been only provided for few Scheimpflug instruments in a laboratory

setting, and the reported crystalline lens parameters restricted to a single cross-section of the lens. [Dubbelman 2001a, and Rosales et al 2009]. In addition to optical techniques, the anterior chamber of the eye can be imaged through non-optical imaging techniques such as ultrasound [Goss et al, 1997, and Vilpuru et al, 2003] and Magnetic Resonance Imaging (MRI) [Jones et al, 2005, Hermans et al, 2009 and Kasthurirangan et al, 2011]. These non-optical techniques allow visualization of the entire crystalline lens and its neighboring ocular structures. However, these are either invasive or time-consuming imaging methods, with significantly lower resolution than optical techniques, which impose major problems (low acquisition speed, motion artifacts or low sampling density) which prevent quantifying the crystalline lens geometry with high accuracy.

To our knowledge, the 3-D structure of the crystalline lens has not been investigated quantitatively with any method, likely as a result of the associated problems of the imaging techniques used to image the crystalline lens. Several geometrical crystalline lens parameters surfaces have been reported previously with OCT, such as lens thickness and anterior and posterior lens radius of curvature in the horizontal meridian [Dunne et al, 2007, Yadav et al, 2010 and Shen et al, 2010]. In addition, OCT has been used recently to quantify the crystalline lens shape in 2-D in human and primate lenses *in vitro* [Uhlhorn et al, 2008, Kim et al, 2011, Maceo et al, 2011], and to estimate the Gradient Index (GRIN) distribution (from the optical distortion produced by GRIN on the posterior lens surface) in the porcine lens in 3-D and the human lens in 2-D [de Castro 2010, 2011a and 2011b, Borja et al, 2010 and Siedlecki et al, 2012].

Imaging the crystalline lens with sOCT poses some challenges: (1) The axial imaging range is limited by the resolution of the spectrometer, and this can be insufficient to image the entire anterior segment (from the anterior cornea to the posterior lens) in a single acquisition [Grulkowski et al, 2009]. (2) Motion artifacts can limit the repeatability of the measurements, making it necessary to reduce acquisition time [Ortiz et al, 2011]; (3) Fan (arising from the scanning architecture) and optical (refraction) distortions, if left uncorrected, prevent quantitative analysis of the crystalline lens images [Ortiz et al, 2009b 2010, and 2011, Zhao et al, 2010 and Karnowski et al, 2011].

In this chapter we measured and quantified the crystalline lens surface in 3-D. Further developments of the methods that we previously developed and applied to achieve quantitative corneal topography [Ortiz et al, 2009b 2010, and 2011] were applied to the quantification

of the crystalline lens, overcoming limitations (2) and (3). Newly developed methods for registration and merging of sOCT images at different focus allowed full anterior segment imaging, overcoming limitation (1).

Accurate measurement of the lens geometry is crucial in the understanding of crystalline lens optical properties, and of the physical changes of the lens in accommodation and presbyopia, as well as in the design and evaluation of accommodation-restoration solutions for presbyopia, and to increase the predictability of intraocular lens implantation procedures.

In this study, we present the capability of sOCT imaging to provide 3D quantitative parameters of the anterior and posterior lens surfaces (radii and asphericity) and lens thickness. To our knowledge, this is the first report of 3-D topographic maps of the anterior and posterior lens surfaces of the eye *in vivo*.

9.2. Material and Methods

9.2.1. Validation experiments on samples in vitro

The accuracy of the method to retrieve the shape of the lens was tested on a physical water cell model eye and on a donor lens.

The physical model eye has been described in previous studies where it was used to assess the accuracy of measurements of lens tilt and decentration from Scheimpflug and Purkinje imaging [de Castro et al, 2011] and of topographic measurements with a Time Domain OCT system [Ortiz et al, 2010]. The water cell model consists of a PMMA cornea and a spherical biconvex intraocular lens with known spherical radii, as measured by a non-contact profilometer (PLu, Sensofar, Barcelona Spain), filled with saline solution. The index of refraction of the materials (1.486 for the artificial cornea and lens and 1.336 for the saline solution) were provided by the manufacturers. Measurements on the physical model eye were obtained with the SLD power exposure fixed at 800 μ W. Each set of 3-D measurements was acquired in 0.72 seconds, similar to acquisition time used in *in vivo* eyes, with two acquisitions at two different planes of focus. Measurements were collected on a 10 \times 15 mm zone, using 50 B-Scans composed by a collection of 360 A-Scans, providing a resolution of 0.04 mm for horizontal and 0.2 mm for vertical meridian.

Experiments were also performed on one crystalline lens from a 65-year donor eye, within 24 hours post-mortem (Eye Bank Transplant Services Foundation, Barcelona, Spain). Protocols for human tissue

handling followed the guidelines of the Declaration of Helsinki, and had been approved by the Institutional Review Boards. Crystalline lens was extracted immediately before measurements and immersed in preservation medium (DMEM/F-12, D8437, Sigma, St. Louis, MO) at 25° C. The imaging procedure of the crystalline lens *in vitro* was similar to that described by de Castro et al. [40]. Images were acquired with the lens in two orientations, first with the anterior surface facing the OCT beam, “anterior up”, and then with the posterior surface facing the OCT beam (“posterior up”), after carefully flipping the lens. A homogeneous lens index of refraction of 1.413 was assumed in the calculations. Each single 3-D collection consisted of 70 B-scans with 1668 A-scans, with a lateral range of 12x12 mm, providing a resolution of 170x7 μm . The acquisition time of a full 3-D image was 4.5 s.

9.2.2. *Experimental protocols for anterior segment image acquisition in vivo*

Images were collected on the right eye of 3 young subjects (ages 28-33). The subjects were considered healthy in a clinical ophthalmological examination. Refractions ranged between 0 to -4.75 D sphere and 0 to 1 D of cylinder. All protocols had been approved by Institutional Review Boards, and the subjects signed informed consents after the nature of the study had been explained, in accordance to the tenets of the declaration of Helsinki. Measurements were performed under mydriasis (by Tropicamide 1%). The subjects were stabilized using a bite bar. Alignment of the subject was achieved with respect to the anterior corneal specular reflection, while the subject fixated on a reference a maltese cross target projected on a minidisplay at optical infinity.

A total of 15 sets of 3-D data were collected in each eye: 5 repeated images of the cornea, 5 repeated images of the anterior part the lens, and 5 repeated images of the posterior part of the lens. All 3-D sets of data contained also the iris.

The SLD power exposure was fixed at 800 μW . Each set of 3-D measurements was acquired in 0.72 seconds in order to minimize the impact of motion artifacts, as it was explained in Section 7.2.4. Focus was changed by an automatic displacement to achieve the different anterior segment structures. Images of each axial region were collected in 0.72 s. Measurements were collected on a 10 \times 15 mm zone, using 50 B-Scans composed by a collection of 360 A-Scans, providing a resolution of 0.04 mm for horizontal and 0.2 mm for vertical meridian.

9.2.3. 3-D Image analysis: denoising, segmentation, merging, distortion correction and surface fitting.

In previous works corneal topographical maps from normal and pathological subjects were obtained using sOCT and dedicated algorithms for volumetric data extraction explained in Chapter 6. The image processing algorithm can be summarized in nine steps. Only dedicated new routines are described in detail:

(1) Denoising: It was applied as it is described in Section 6.2: The rotational kernel transform was performed using a mask of size 9 pixels. In addition, the wavelet low-pass filtering processing based on log-Gabor wavelet was used for 7 scales and 6 orientations.

(2) Statistical thresholding: The adaptive algorithm explained in section 6.3 has been applied using the multimodal Gaussian fitting of the histogram intensity.

(3) Volume Clustering: The statistics of the noise and signal are overlapped. As a result, small randomly distributed volumes are mixed with the large volumes representing the objects of interest in 3-D (cornea, iris, lens surfaces, etc...). Applying the clustering algorithm of section 6.4 the number of pixels belonging to certain a volume is obtained by means of the connectivity of points. The volumes of interest are obtained by thresholding the number of elements according to the expected total number. Figure 9.1(a) shows examples of the volumes clustered in each of the 3-D data set collected at different depths: (a) cornea and iris, (b) anterior lens and iris, (c) posterior lens and iris.

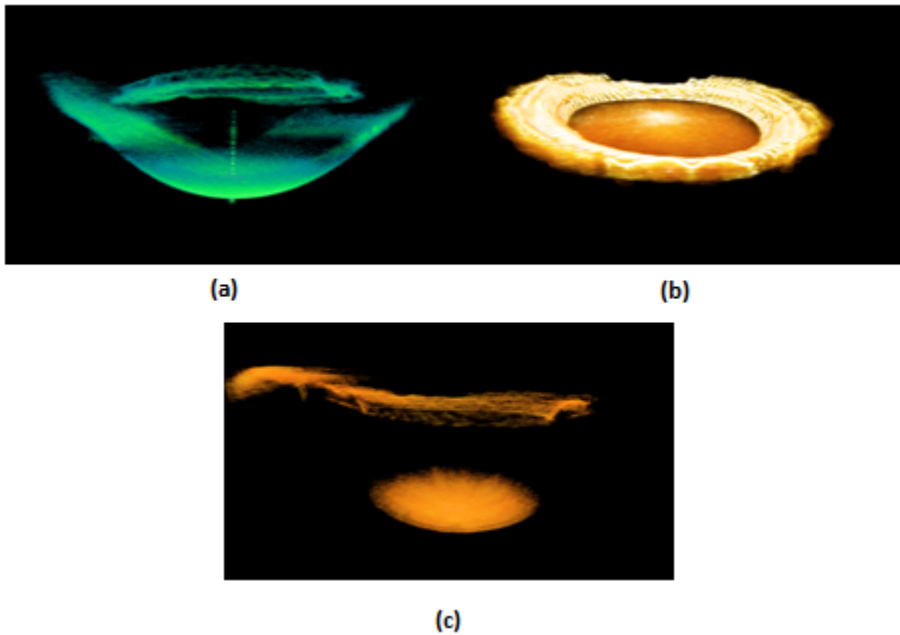


Figure 9.1. Illustration of the three acquisitions of one of the repeated data collection in subject S#1. (a) cornea volume and iris; (b) anterior lens and iris; (c) posterior lens and iris.

(4) Multilayer segmentation: The Canny detection algorithm explained at section 6.5 has been applied with a Gaussian kernel of 5 pixels and thresholding level of 0.25 times the standard deviation plus the average value.

(5) Pupil center reference. The pupil center was used as a reference across measurements (i.e. cornea, anterior and posterior lens) and to define the optical zone (effective area within the pupil). According to previous studies [Yang et al, 2002], the pupil center shifts little across pupil sizes and light conditions. In a previous work (Chapter 8) we estimated the pupil center and optical zone by fitting the outer edge of pupil in 2-D en face images (computed by adding all images of a 3-D data set) to an ellipse. However, the current application requires 3-D position of the pupil center (including the axial coordinate), and estimation of the pupil plane in 3-D, as this information is used for registration and merging of the corneal and lens images. In this study, the lateral pupil coordinates were obtained as in the previous study (Chapter 8), while the axial coordinate was obtained by non linear least-square fitting of the iris plane in 3-D (and evaluation of the plane at the estimated pupil lateral coordinates). In addition, the characteristic vector of the iris plane was obtained, which provided the tilt angle of this plane with respect to the OCT coordinate system.

(6) Merging 3-D volumes: The procedure for merging the 3-D volumes was explained in Section 6.7. Figure 9.2 illustrates the process to obtain the full anterior segment 3-D image merging from the three volumetric acquisitions. A full overlapping of the iris from the 3 sets of images can be observed.

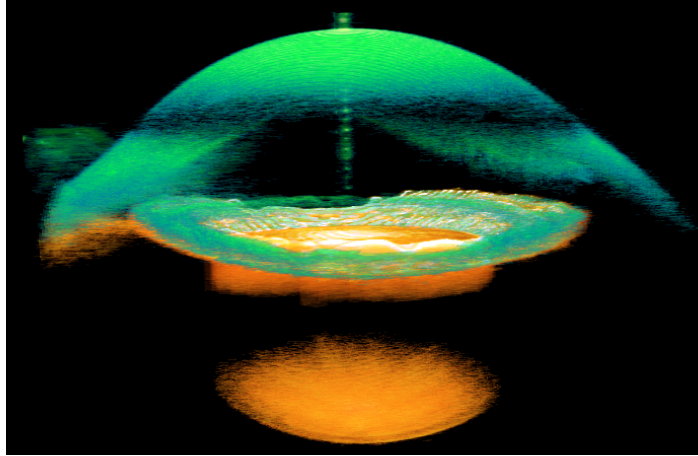


Figure 9.2. Illustration of the merging of three volumetric acquisitions to obtain a 3-D full anterior segment image.

(7) Geometrical distances calculation and further denoising: Once the surfaces have been extracted as the pupil centering requires shifting and rotation, surfaces must be resampled in order to retrieve the geometrical distances. The procedure is fully explained in Section 6.9, the selected refractive index of the anterior segment of the eye were: 1.376 for the cornea, 1.336 for the aqueous humor, while the crystalline lens refractive index was obtained from the age-dependent average refractive index expression derived by Uhlhorn et al. [Uhlhorn et al, 2008] (1.4176-1.4186 for the subjects of our study). The sampled anterior segment elevation data from anterior and posterior surfaces of the cornea and the lens were denoised using the fitting Zernike modal expansion explained

(8) Distortion corrections: In order to correct the interface layers for the effect of distortion in general (fan distortion and refraction), it is required to propagate the geometrical distances obtained from the previous point along the directional cosines of the ray, taking into account the refraction that occurs at each interface between two media of different refractive indices as it is explained in chapter 4. A procedure similarly to that described in the previous chapter 8 and practically applied to the cornea was followed, expanding it sequentially from the cornea to the posterior surface of the crystalline lens. Correction of the fan and optical distortions produces large

geometrical changes in the anterior optical surfaces, which are particularly qualitatively observable in the diameter of the visible areas of the anterior, and to a larger extent, the posterior lens. Figure 9.3 shows the difference in the segmented surfaces fully corrected from optical distortion correction (in green), and the segmented surfaces corrected from fan distortion but not from refraction effect (dividing only by its refractive index, in red).

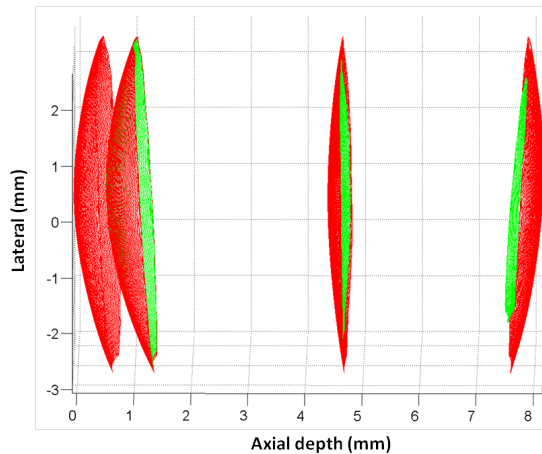


Figure 9.3 Illustration of the effect of optical (refraction) correction (in green) in comparison with the correction of the surfaces by simple division by their corresponding refractive indices in an anterior segment image (in red). From left to right: segmented anterior and posterior corneal surfaces, and anterior and posterior lens surfaces.

(9) Surface fitting by quadrics (biconicoid, conicoid), and topographic maps as it is explained in Section 6.10 allows estimating the geometrical aspects of lens for conicoid and biconicoid fitting and topographic, difference and thickness maps.

9.3. Results

9.3.1. *In vitro* samples

The images obtained from the physical model eye were processed using the developed image analysis and distortion correction algorithms. Table 9.1 shows the nominal radii of curvature of the cornea and lens surfaces in the model eye, along with the values before and after application of optical distortion correction algorithms. Fan distortion correction was applied in all cases. Discrepancies in the retrieved radii of curvature were 7.5% for the posterior cornea, 9.7% for the anterior lens and as high as 23.5% for the posterior lens. The accuracy in the radius of curvature retrieval increased dramatically after optical distortion correction, with discrepancies of 0.3% for the anterior

cornea, 2.0% for the posterior cornea, 1.4% for the anterior lens, and 2.8% for the posterior lens.

Table 9.1. Surface radii of curvature from sphere fittings in the model eye: nominal values, values estimated from OCT measurements before and after correction of optical distortion.

	Cornea			Lens		
	Nominal (mm)	OCT Uncorrected (mm)	OCT Corrected (mm)	Nominal (mm)	OCT Uncorrected (mm)	OCT Corrected (mm)
Anterior	7.80	7.77	7.77	17.29	18.96	17.05
Posterior	6.48	6.96	6.35	11.04	13.64	10.74

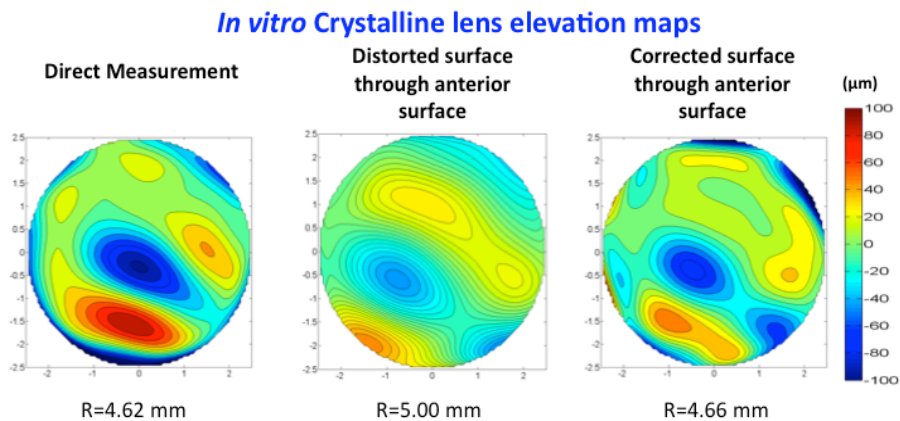


Fig 9.4. Quantitative elevation maps of the posterior lens surface for the *in vitro* 65-year donor lens. Left panel: Measurements with the posterior surface of the lens facing the OCT beam (“posterior up”); Middle panel: Measurement of the posterior surface of the lens viewed through the anterior surface of the lens, and no optical distortion correction (simple division by the index of refraction); Left panel: Measurement of the posterior surface of the lens viewed through the anterior surface of the lens, after application of optical distortion correction. Maps are Zernike fits to the elevation maps, relative to the best fitting sphere. R = radii of curvature of the best fitting sphere (from fits to sphere quadrics).

The images obtained from the donor lens *in vitro* were processed using the developed image analysis and distortion correction algorithms. Figure 9.4 shows the elevation maps obtained of the posterior surface of a donor lens *in vitro* (direct view of the posterior lens, view of posterior lens distorted by the anterior lens, and posterior lens corrected from optical distortion by the anterior lens). Optical distortion correction decreases the error in the retrieved posterior lens radius of

curvature from 8.23% to 0.9%. Correction also decreased the discrepancies in the RMS surface elevation map (referred to the best fitted sphere) from 48.3% (no optical distortion correction) to 4.5% (after optical distortion).

9.3.2. Cornea shape parameters

Corneal surface quantification is necessary to provide accurate optical distortion correction of the lens surfaces. Table 9.2 summarizes the anterior and posterior corneal parameters in the 3 subjects of the study after full distortion corrections, obtained from conicoid and biconicoid fittings of corneal surfaces in a 5-mm diameter zone.

Table 9.2. Radii of curvature and Asphericity (Q-value) of the anterior and posterior cornea from biconicoid and conicoid fittings

	Radius of curvature					
	Anterior Cornea			Posterior Cornea		
	Biconicoid		Conicoid	Biconicoid		Conicoid
	Rx (mm)	Ry (mm)	R (mm)	Rx (mm)	Ry (mm)	R (mm)
S#1	7.40±0.07	7.53±0.03	7.47±0.05	6.76±0.13	6.59±0.07	6.69±0.10
S#2	7.95±0.06	7.82±0.10	7.87±0.11	6.96±0.07	6.95±0.11	6.96±0.08
S#3	7.47±0.05	7.42±0.14	7.43±0.09	6.93±0.06	6.70±0.13	6.72±0.11
	Asphericity (Q-Value)					
	Qx	Qy	Q	Qx	Qy	Q
S#1	0.10±0.01	-0.19±0.05	0.01±0.04	-0.03±0.05	0.06±0.08	-0.01±0.09
S#2	0.20±0.05	-0.18±0.08	0.10±0.03	0.03±0.05	0.01±0.11	0.04±0.03
S#3	0.11±0.06	-0.02±0.09	-0.01±0.07	-0.08±0.04	0.01±0.03	0.01±0.08

9.3.3. Effects of optical distortion on crystalline lens shape

To quantify the effect of optical distortion from preceding surfaces on the crystalline lens shape, we evaluated difference maps, obtained as the subtraction of the elevation map estimated after full optical correction from the map obtained after fan distortion correction and a simple division of the optical distances by the refractive indices, both for the anterior and posterior lens surface. Not correcting for optical distortion produced discrepancies ranging from 0 μm (in the center of the lens) up to 50 μm in the periphery of the anterior lens surface, and

up to 200 μm in the periphery of the posterior lens. The difference maps (Figure 9.5) reveal the progressive overestimation of the lens curvatures in the non-corrected maps. Although dominated by the differences in curvature, slight irregularities in the difference maps indicate the effect of optical distortion in astigmatism and other higher order terms.

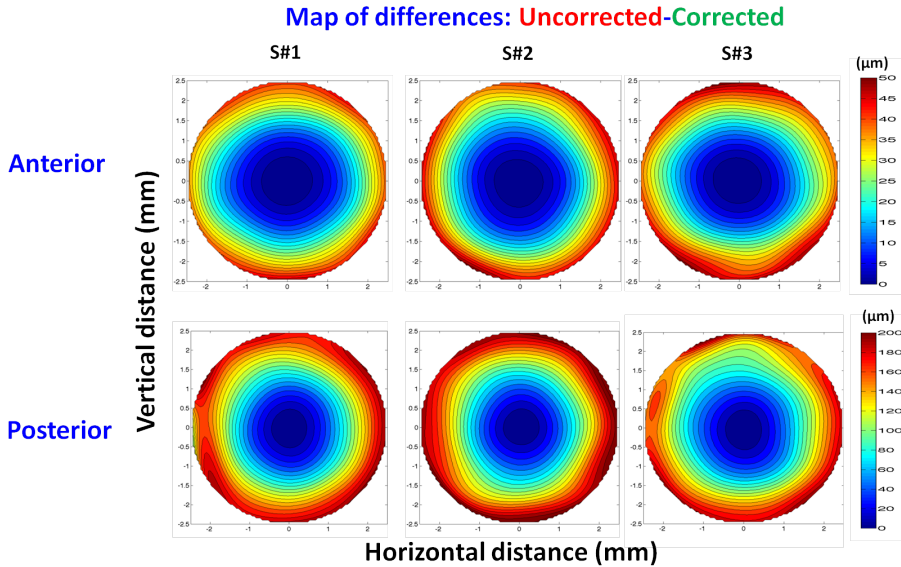


Figure 9.5. Difference lens anterior (top) and posterior (bottom) elevation maps after optical distortion correction relative to elevation maps obtained by simple division of the optical distances by their corresponding refractive indices.

9.3.4. Crystalline lens shape

Lens surfaces (with and without optical distortion corrections) were obtained, and fitted to conicoids and biconicoids, within 5-mm diameter zones. Table 9.3 and 9.4 show the fitted radii of curvature and asphericities. Data represent averages (and standard deviations) of 3 repeated measurements on each eye. Not correcting for optical distortion produced a systematic overestimation of the lens radii of curvature (Table 9.3), between 20.46 and 22.77% for the horizontal meridian, and between 20.96 and 32.81% for the vertical meridian (in the anterior lens), and between 63.40 and 72.70% for the horizontal meridian, and between 68.14 and 80.27% for the vertical meridian (in the posterior lens). For a conic fitting, radii for overestimated between 20.20 and 23.56% in the anterior lens, and between 69.28 and 78.72% in the posterior lens.

Table 9.3. Radii of curvature from biconicoid and conicoid fittings of the uncorrected and optical distortion corrected crystalline lens surfaces

		Anterior Lens			Posterior Lens		
		<i>Biconicoid</i>		<i>Conicoid</i>	<i>Biconicoid</i>		<i>Conicoid</i>
		<i>R_x (mm)</i>	<i>R_y (mm)</i>	<i>R (mm)</i>	<i>R_x (mm)</i>	<i>R_y (mm)</i>	<i>R (mm)</i>
S#1	Uncorrected	17.36±0.11	13.95±0.21	15.42±0.19	11.64±0.01	13.51±0.22	12.48±0.11
	Corrected	14.14±0.13	11.24±0.30	12.48±0.20	6.74±0.11	7.54±0.20	7.25±0.25
S#2	Uncorrected	13.83±0.07	13.64±0.24	13.74±0.09	10.06±0.26	10.66±0.29	10.36±0.20
	Corrected	11.47±0.09	10.27±0.29	11.43±0.04	6.10±0.12	6.34±0.04	6.12±0.15
S#3	Uncorrected	15.60±0.04	13.79±0.38	14.64±0.21	11.52±0.12	13.43±0.23	12.85±0.04
	Corrected	12.95±0.12	11.40±0.19	12.18±0.06	7.04±0.12	7.45±0.16	7.19±0.03

Table 9.4. Asphericity (Q-value) from biconicoid and conicoid fittings of the uncorrected and optical distortion corrected crystalline lens surfaces

		Anterior Lens			Posterior Lens		
		<i>Biconicoid</i>		<i>Conicoid</i>	<i>Biconicoid</i>		<i>Conicoid</i>
		<i>Q_x (mm)</i>	<i>Q_y (mm)</i>	<i>Q (mm)</i>	<i>Q_x (mm)</i>	<i>Q_y (mm)</i>	<i>Q (mm)</i>
S#1	Uncorrected	-0.40±0.34	-0.33±0.12	-6.02±0.03	-0.09±0.06	-0.49±0.11	-0.67±0.25
	Corrected	-0.41±0.15	-0.36±0.20	-2.57±0.31	-1.87±0.93	-1.96±0.76	-1.64±0.33
S#2	Uncorrected	-0.33±0.37	-0.42±0.32	-0.29±0.07	-0.45±0.33	-0.24±0.20	-0.66±0.16
	Corrected	-0.40±0.16	-0.26±0.29	-0.43±0.21	-0.06±0.02	-0.09±0.07	-0.01±0.00
S#3	Uncorrected	-0.35±0.41	-0.23±0.20	-1.21±0.43	-0.40±0.10	-0.25±0.23	-0.84±0.22
	Corrected	-0.19±0.23	-0.25±0.32	-0.93±0.40	-0.46±0.22	-0.07±0.08	-0.59±0.07

Lens asphericities (Table 9.4) were negative in all eyes, although values differed significantly across subjects. While optical distortion correction modified the asphericity parameter, there was not a consistent trend toward overestimation or understimation without correction.

9.3.3. Crystalline lens topography

Lens surfaces were fitted by Zernike polynomial expansions (up to the 10th order) within a 5-mm optical zone. Figure 9.6 shows representative second and third order Zernike terms (astigmatism, coma and trefoil). Data are averages of 3 repeated measurements on each eye, and the

error bars represent the standard deviation. Only fits corresponding to fully distortion corrected surfaces are shown. The most relevant term is astigmatism at 0 and 90 deg (Z_2^2). Not correcting optical distortion produced an underestimation of the magnitude of astigmatism by 33% on average. Interestingly, all eyes showed vertical astigmatism in the anterior lens (negative Z_2^2 , i.e. steepest vertical meridian), but a horizontal astigmatism in the posterior lens (positive Z_2^2 , i.e. steepest vertical meridian).

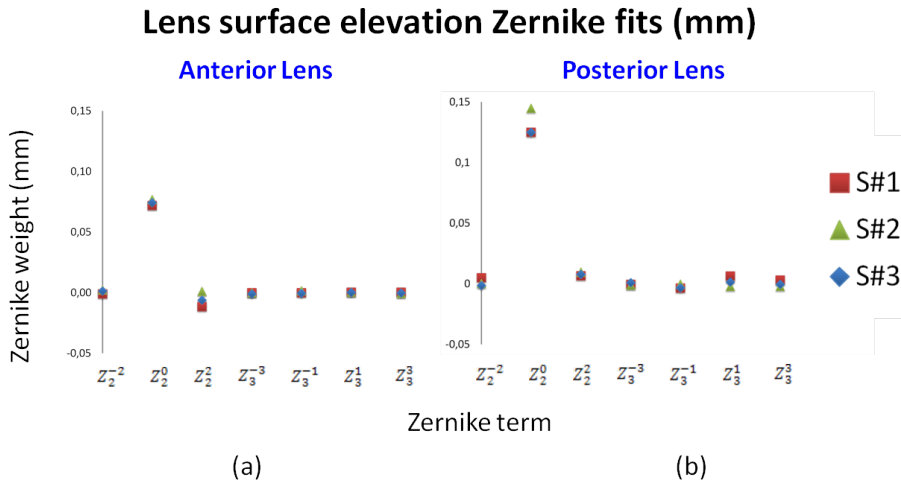


Fig 9.6. Representative second and third order Zernike terms from the Zernike fit to full distortion corrected (a) anterior lens surface, and (b) posterior lens surface. Data are average values of 3 repeated measurements on S#1 (red squares), S#2 (green triangles), and S#3 (blue diamonds). Error bars are not represented since the error is smaller than the marker.

Figure 9.7 shows topographic maps of the anterior and posterior lens surface in the 3 subjects of the study, within a 5-mm diameter zone. The topographic maps represent 10th order Zernike fits of the elevation maps relative to the best fitting sphere. The numbers below each map indicate the radii of curvature of best fitting sphere.

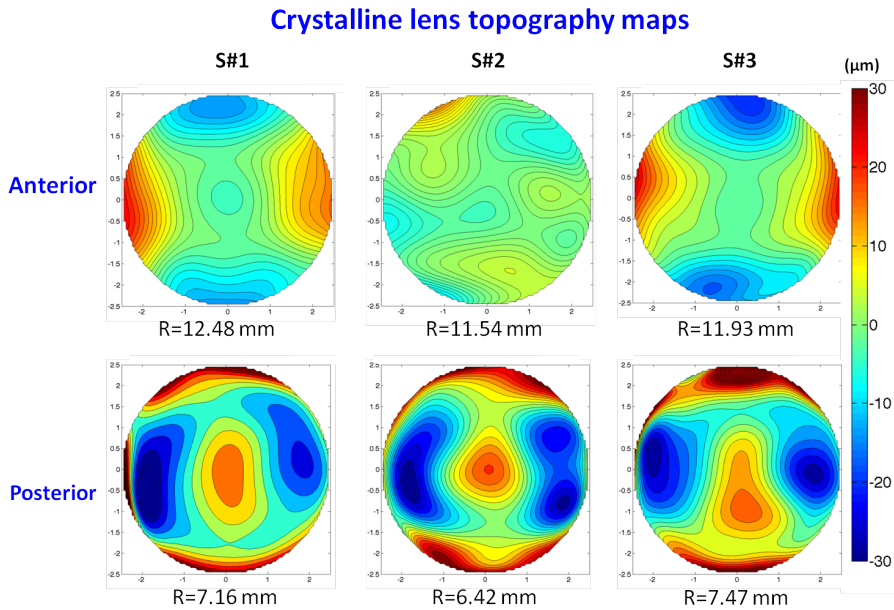


Figure 9.7. Quantitative anterior (top) and posterior (bottom) crystalline lens topography maps in 3 eyes, after full distortion correction. Maps are Zernike fits to the elevation maps, relative to the best fitting sphere. R = radii of curvature of the best fitting sphere (from fits to sphere quadrics).

Figure 9.8 shows an illustration of the repeatability of the lens topography maps in Subject #3, for both the anterior and posterior lens surfaces (5-mm optical zone). The numbers below each map represent the radii of curvature of best fitting sphere in mm. The average anterior lens radius of curvature was 12.02 ± 0.21 mm (1.7% of variability). The average posterior lens radius of curvature was 7.37 ± 0.09 mm, (1.2% variability). The average RMS lens topography (relative to the best fitting sphere) was 2.08 ± 0.09 mm for the anterior lens (4% variability) and 9.92 ± 0.83 mm for the posterior lens (8% variability).

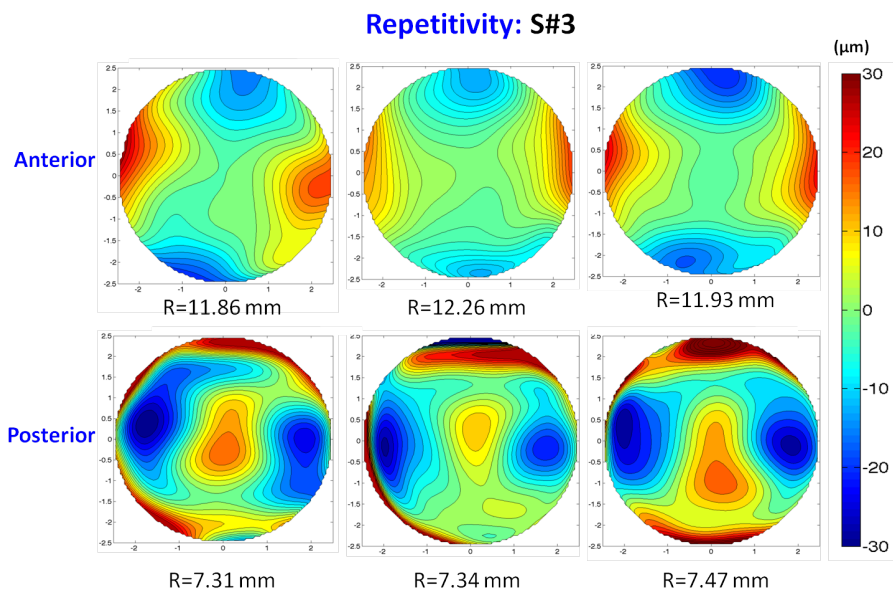


Figure 9.8. Three repeated anterior and posterior lens surface topography maps in subject #3. R = radii of curvature of the best fitting sphere (from fits to sphere quadrics).

9.3.3. Crystalline lens thickness

Figure 9.9 shows thickness maps estimated using uncorrected surfaces (obtained by simple divisions the optical distances by the average lens refractive index, and fan distortion corrections) and fully corrected surfaces (within a 5-mm diameter zone, centered at the pupil center). Central thickness was $3.18 \pm 0.02\text{ mm}$ for S#1, $3.36 \pm 0.02\text{ mm}$ for S#2 and $3.06 \pm 0.04\text{ mm}$ for S#3, and did not change with optical distortion correction of the surfaces. However, not correcting for optical distortion overestimated thickness by more than 15% on average in peripheral areas (2.5 mm from the center)

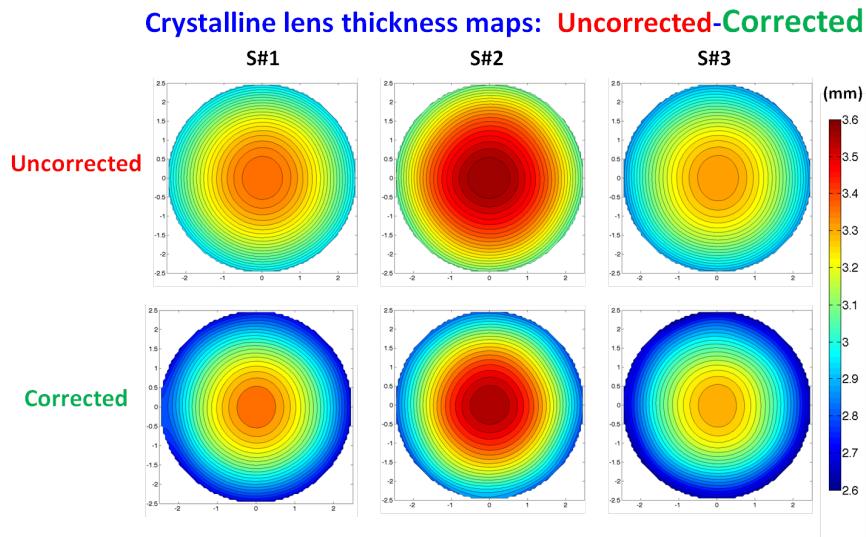


Figure 9.9 Crystalline lens thickness maps obtained as direct subtraction from anterior to the posterior elevation maps, for uncorrected surfaces (top) and for fully corrected surfaces (bottom). Data are for 5-mm optical zone.

4. Discussion

We have presented a new methodology for obtaining accurate shape and 3-D topographies of the crystalline lens surfaces. To our knowledge, this is the first time that OCT has been applied to obtain quantitative 3-D geometry of the crystalline lens *in vivo*. The method has been tested using a model eye and a human donor lens *in vitro*, showing a good correspondence between nominal data of the model eye and the retrieved data after correction, and the posterior lens surface (obtained with the posterior lens surface facing the OCT beam) and the reconstructed posterior lens surface in the donor lens. The presented method builds on previous methods developed to obtain quantitative corneal elevation from OCT images Chapters 7 and 8, including fan and optical distortion correction (Chapters 3-5, 7 and 8), and image processing tools, which along with newly developed routines for volume clustering (of cornea, iris, and lens), and 3-D merging and registration, allowed quantitative lens surface segmentation, correction and topography. The lens surfaces were fitted by conics and biconics, as well as Zernike polynomial descriptions, which allowed estimates of the anterior and posterior lens radii of curvature, asphericity, astigmatism and high order irregularities.

Correction of optical distortion proved particularly relevant in the crystalline lens imaging, giving the accumulated refraction changes by multiple preceding surfaces, and the ray convergence. In keeping with

theoretical predictions introduced in Chapter 5, correcting optical distortion improved accuracy in the estimates of the lens radii of curvature by 25% and 65% in the anterior and posterior lens respectively.

Most previous phakometric techniques were limited to the estimates of radii of curvature either from indirect measurements of light reflections from the lens surfaces (Purkinje imaging) or anterior segment imaging (such as Scheimpflug imaging). Our lens radii of curvature estimates (11.90 ± 1.34 mm for the anterior lens and 6.86 ± 0.63 mm for the posterior lens) fall within the ranges reported in the literature. Classical eye model [Helmholtz, 1855] used 10 mm for the anterior lens and 6 mm for the posterior lens, whereas more recent models [Liou et al, 1997] use 12.4 and 8.1 mm respectively. Dubbleman et al. [Dubbelman et al, 2001a] reported an age dependent expression for the anterior and posterior lens radius of human lenses in vivo based on corrected Scheimpflug measurements, which applied to the average data of our three subject would predict 11.02-11.3 mm and 5.8-5.86 mm for the anterior and posterior lens radius respectively. Rosales et al. [Rosales et al, 2006a] in a comparative study of the radii of curved estimated from Purkinje and Scheimpflug imaging on the same group of young subjects reported 10.8 mm and 11.1 mm from each technique, and 6.7 mm and 6.1 mm from each technique, for anterior and posterior lens radius of curvature respectively. Differences with respect to the OCT-based estimates may arise from the assumption of spherical surfaces in the Purkinje method [Rosales et al, 2006a], or the fit within a 3-mm optical zone in the Scheimpflug method [Dubbelman et al, 2001a], while we use a conic/biconic fitting within a 5-mm zone, where the reported radii of curvature correspond to the apical zone. Nevertheless, the reported intersubject variability (within the same age range than our three subjects) is huge: 9-14 mm for the anterior and 4.7 -7 mm for the posterior lens radii in Dubbleman et al. [Dubbelman et al, 2001a]; 8.1-13.8 mm for the anterior and 5.1-7.15 mm for the posterior lens radii in Rosales et al. [Rosales et al, 2006a] in another study using Scheimpflug imaging, and 7.9-14.3 mm for the anterior lens radii and 5.2-8.65 mm for the posterior lens radii in Rosales et al. [Rosales et al, 2006b] using Purkinje imaging. The data reported in this study appear less variable across subjects, and well within the reported ranges.

To our knowledge, only Dubbleman et al. [Dubbelman et al, 2001a] reported lens asphericity measured in vivo from Scheimpflug imaging, also providing age-related expressions. The predicted asphericity from that study on the age range of our studies (-4.56 and -3.04 for the

anterior and posterior lens surfaces) is significantly more negative than that obtained in the current OCT-based study (-1.31 ± 1.12 and -0.75 ± 0.83 for the anterior and posterior lens surfaces). However, the intersubject variability found by Dubbleman et al. [Dubbleman et al, 2001a] was huge (-20 to 7 for the anterior lens and -13 to 2 in the posterior lens). It is likely that the specific fitting method used by Dubbleman (two-stage fitting to a spherical surface followed by a fitting of the residuals to conic), the use of 2-D data sets, and the reported interactions of radius of curvature and asphericities in conic fitting [Pérez-Escudero et al, 2010] play some role in the differences.

The 3-D acquisition and reconstruction of the lens surfaces with OCT allowed us to obtain 3-D lens geometry in vivo, for, to our knowledge the first time in the literature. We had previously measured the 3-D geometry of crystalline lenses in vitro in the porcine [de Castro et al, 2010] and human [Birkenfeld et al, 2011] lens. The correction of optical distortions from the cornea allowed reconstructions of lens surface topographies, very much like the conventional surface topography of the cornea, widespread in the clinical practice. As our previous OCT-based corneal topographies, topographic measurements are based on a collection of regular B-scans, rather than meridians [Zhao et al, 2010 and Karnowski et al, 2011].

Unlike previous cross-sectional measurements of lens geometry which were limited to one meridian, 3-D measurements allow to investigate lens surface astigmatism. Very interestingly, our three subjects show perpendicular orientation in the astigmatism of the anterior versus the posterior lens surface. To date, astigmatism of the crystalline lens in vivo is usually assessed by subtracting corneal from total aberrations [Artal et al, 2002, Barbero et al, 2002 and Kelly et al, 2004]. Compensation of the corneal astigmatism by internal astigmatism has been postulated [Kelly et al, 2004], as well as changes of this balance with age [Artal et al, 2002]. Measurements of the crystalline lens topography in vivo will offer the possibility of investigating the sources of this compensation and potential age-related changes. In a previous study we investigated lens surface contribution to lens astigmatism in a porcine lens in vitro, and found that the lens gradient index of refraction (GRIN) may also play a compensatory role [de Castro et al, 2010]. Undergoing research in our laboratory explores the role of GRIN in astigmatism and spherical aberration both in porcine and human lenses in vitro.

Our OCT-based crystalline lens topographies show minimal amounts of trefoil, coma or other high order aberrations. It is likely that the coma

measured by direct subtraction of total minus corneal aberrations arises from the misalignment of the ocular components, including the off-axis position of the fovea [Marcos et al, 2008, Berrio et al, 2010]. Measurements of optical aberrations in isolated lenses using lateral images of the ray tracing in primate lenses [Roorda et al, 2004], or by diffraction point interferometry [Acosta et al, 2010] indicate presence of trefoil and other high order aberrations. The fact that the lens surface topographies are relative smooth suggests a contribution of the internal lens structure (likely line sutures) to the reported lens optical irregularities.

We provided the first report of lens surface shapes from OCT upon correction of optical (refraction) distortion, although (as previous reports based on Purkinje or Scheimpflug) we did not considered a GRIN in the lens.

Borja et al. [Borja et al, 2010], stated the optimal refractive index for the correction of OCT images, was closer to the average refractive index [Uhlhorn et al, 2008] than to the equivalent refractive index. In previous studies [Borja et al, 2010, and Siedlecki et al, 2012] we analyzed the potential effect of GRIN in the visualization and quantification of the posterior lens surface, and developed a tool for thru-GRIN optical distortion correction of OCT images, which we applied in vitro. We concluded that using a homogeneous index of refraction as opposed to actual lens GRIN profile did not produce significant discrepancies on the estimated radius of curvature, although it could over estimate the posterior lens asphericity in a 6 mm pupil diameter [Borja et al, 2010]. However, the results using a 4mm pupil diameter [Siedlecki et al, 2012] showed an improvement only in the RMS or peak to value differences. Estimates of the posterior lens surface topography and lens thickness in vivo could therefore benefit slightly by increasing knowledge (and potential retrieval in vivo) of the lens GRIN.

9.5. Conclusions

Anterior segment OCT provided with full distortion correction and automatic analysis tools allowed quantification of the human crystalline lens in vivo in 3-D. Correction of optical distortion is critical as simple division of the OCT optical distances by the refractive index produces an overestimation of the crystalline lens anterior and posterior radii of curvature by 25% and 65% respectively. The retrieved lens radii of curvature from OCT agree with phakometric data previously reported using Scheimpflug and Purkinke image along one meridian. We found

slight negative lens surface asphericities, crossed astigmatism in the anterior and posterior lens surface, and negligible high order irregularities in the lens surfaces. OCT-based lens topography is a promising tool to investigate the lens optical properties, the contribution of the lens to the overall retinal image quality, and understanding the change of the physical properties of the lens with accommodation and aging.

Chapter 10

Anterior segment biometry: an application in cataract surgery

This chapter is based on the articles by Ortiz, S. et al “Full OCT anterior segment biometry: an application in cataract surgery” submitted to Biomedical Optics Express. The coauthors of the study are: Pablo Pérez-Merino, Sonia Durán, Miriam Velasco-Ocana, Judith Birkenfeld, Alberto de Castro, Ignacio Jiménez-Alfaro, and Susana Marcos. The work was developed at Instituto de Óptica “Daza de Valdés”. The contribution of the author of this thesis was to develop the methodology for evaluating three-dimensional (3-D) anterior segment biometry before and after cataract surgery. The method was tested on an *in vitro* artificial eye with known surfaces geometry at different orientations and demonstrated on an aging cataract patient *in vivo*.

10.1 Introduction

Cataract is one of the major causes of vision loss in the aging population, as the crystalline lens progressively loses transparency and opacifies. Upon replacement of the crystalline lens by an intraocular lens (IOL), the source of scattering is eliminated. Current cataract surgery also aims at correcting the refractive errors of the eye, and even optimizing optical quality by reducing high order aberrations. Recently, the customization of IOL design to the anatomical parameters of each patient has been proposed [Barbero et al, 2007, and Bellucci et al, 2007]. Although cataract surgery has advanced considerably with recent improvements in IOLs designs, phacoemulsification (and even all-laser) technologies, and biometry techniques, a limitation to the accuracy of the IOL power selection is the accuracy of pre-operative ocular biometry and the approximations inherent to IOL power calculation formulae [Norrby, 2008]. In addition, understanding of performance of current IOL designs, and insights for new IOL designs will definitely benefit from quantitative imaging of the eyes after cataract surgery.

Regression IOL power calculation formulas (such as the SRK or SRK-II) [Olsen et al, 1990] are based on statistical retrospective analysis of post-operative data, although these are decreasingly used today. Theoretical IOL power (i.e. SRK-T) generally uses a thin lens approach, and different approximations for the cornea and lens, normally in the paraxial regime [Olsen, 2007]. These formulas require at least pre-operative data of axial length and corneal power, as well as estimates of the post-operative anterior chamber depth (ACD), known as Estimated Lens Position (ELP). More recently, the use of exact ray tracing, requiring geometrical and position data of the patient's cornea and lens have been proposed [Preusner et al, 2002]. In fact, custom computer models of eyes implanted with IOLs (including corneal elevation, anterior chamber depth, IOL and ocular alignment) have been shown to predict with high accuracy even the high order aberrations of individual pseudophakic eyes [Tabernero et al, 2006, and Rosales et al, 2007]. Improved estimates of the Estimated Lens Position, and Custom Eye Models for ray tracing IOL power calculation, as well as for post-operative evaluation of optical performance, require a more complete characterization of ocular geometry than that normally performed clinically, and which in most cases is obtained from multiple instruments.

Improvements in cataract surgery have been paralleled by improvements in biometry techniques. Increasingly used Partial Coherence Interferometry (PCI) for measuring axial length surpasses in resolution A-scan ultrasonography (0.01 vs 0.1 mm) [Drexler et al, 1998, and Haigis et al 2000]. Corneal power is typically measured using keratometry, Placido-based videokeratography, slit-lamp scanning or Scheimpflug imaging [Swartz et al, 2007]. However, the traditional lack of measurements of the posterior corneal surface has led to approximations (i.e. keratometric index)[Olsen et al, 2007], which do not hold in abnormal corneas [Tang et al, 2010]. In addition, non-paraxial ray tracing approaches would require complete corneal shape information beyond corneal power. Additionally, it is likely that more accurate estimates of the post-operative ELP require more extensive 3-D information of the anterior segment of the eye, and pre-operative crystalline lens. For example, it has been shown that pre-operative ACD correlates with post-operative ACD [Canovas et al, 2010], as well as with lens thickness [Olsen, 2006]. A-scan ultrasound, some low coherence interferometry instruments, and Scheimpflug imaging (provided with distortion correction algorithms [Dubbelman et al, 2001, and Rosales et al, 2009]) offer ACD and lens thickness data, although generally the information provided by commercial instruments is limited to the axial dimension. The alignment of the optical components also plays a role in determining the optical performance in the normal and pseudophakic eye, with impact on coma and astigmatism [Artal et al, 1996]. Laboratory-based Purkinje-imaging and Scheimpflug imaging methods have been demonstrated and used to measure *in vivo* tilt and decentration of the crystalline lens and IOLs [Philips et al, 1998, Rosales et al, 2006, and de Castro et al 2006]. The mechanical stability of the IOL and its alignment in the eye are important factors considered in the design of new IOLs.

Although different imaging techniques are able to quantify biometrical properties of the anterior segment of the eye, currently there is no instrument that provides a full quantitative analysis of the anterior segment geometry, which can be used for planning cataract surgery and for complete assessment of cataract surgery performance.

Spectral Optical Coherence Tomography (sOCT) presents several advantages over other techniques to evaluate ocular anterior segment biometry. It is non-invasive, high-speed, allowing the collection of three dimensional (3-D) anterior segment data in hundreds of milliseconds with high axial and lateral resolution [Grulkowski et al 2009 and 2012]. Previous studies described the measurement of corneal

[Li et al, 2010] and lens [Dunne et al, 2007, Yadav et al 2010, and Shen et al, 2010] geometrical properties from 3-D OCT images, as well as ACD [Cleary et al, 2010] and tilt in a 2-D cross-sectional OCT image [Kumar et al, 2010]. However, 3-D OCT quantitative geometrical parameters can only be retrieved accurately upon correction of the fan (scanning) and optical (refraction) distortion [Ortiz et al 2009, 2010a, 2011 and 2012a, Zhao et al 2010, and Karnowski et al, 2011]. In addition, automatic image processing tools, which allow accurate segmentation and merging of the different volumes (cornea, iris and lens or IOL) are essential for full biometrical quantification [Ortiz et al, 2012b].

In this study we demonstrate OCT-based methodologies to estimate 3-D biometrical parameters of the anterior segment of the eye, including interocular distances, as well as tilt and decentration of the lens. The technique is illustrated in an eye with cataract, before and after implantation of an IOL. Along with ocular biometry and alignment, the quantification of the surface topography of the anterior and posterior cornea and anterior and posterior lens previously demonstrated and reported [Ortiz et al, 2012 a and b], the method allows full quantification of the anterior segment of the eye. To our knowledge, this is the first report of 3-D lens alignment measurements with OCT, and of the full *in vivo* anterior segment quantification for a patient before and after cataract surgery.

10.2. Methods

10.2.1. Validation experiment on in vitro sample

The accuracy of the method to retrieve the shape, tilt and decentration of the lens was tested on an *in vitro* physical model eye. The model eye has been described in prior publications, and also used to validate measurements of IOL tilt and decentration with Purkinje and Scheimpflug imaging [de Castro et al 2006, Ortiz et al 2010, Ortiz et al 2012]. The water cell model consists of a PMMA cornea and a spherical biconvex IOL with known spherical radii filled with saline solution. The refractive index of the materials (1.486 for the artificial cornea and lens and 1.336 for the saline solution) were provided by the manufacturers. The lens is mounted on a M-RS40 (Newport corporation, Irvine,CA) manual rotating and x-y translational stage. Measurements on the physical model eye were obtained with the SLD power exposure fixed at 800 μ W. Each set of 3-D measurements was acquired in 0.72 s with two acquisitions at two different planes of focus (artificial cornea and IOL). The IOL was tilted from -5 to 5 degrees, in

2.5 degrees-steps. Measurements were collected at each orientation on a 7x15 mm zone, using 50 B-Scans composed by a collection of 360 A-Scans, providing a resolution of 0.04 mm for horizontal and 0.2 mm for vertical meridian.

10.2.2. Experiments on cataract surgery patient

Images were collected on the left eye of a 73 year-old cataract patient before (15 days) and after (90 days) IOL implantation. The study was approved by Institutional Review Boards and followed the tenets of the Declaration of Helsinki. The subject signed a consent form and was aware of the nature of the study.

Clinical ophthalmological examination and surgery were performed at the Fundación Jiménez-Díaz hospital. A Crystalens AO IOL (Bausch & Lomb Surgical, Aliso Viejo, CA) was implanted through a 2.75-mm corneal incision. The IOL power was calculated with the SRK-T formula selecting the closer value to emmetropia (+23.5 D).

Measurements were performed under natural conditions pre-operatively and under mydriasis (phenylephrine 10%) post-operatively. The subject was stabilized using a bite bar. Alignment of the subject was achieved with respect to the anterior corneal specular reflection, while the subject fixated on a reference E-letter target projected on a minidisplay at optical infinity.

A total of 15 sets of 3-D data were collected pre-operatively (3 repeated images for the cornea, anterior lens and posterior lens, respectively), and 9 sets post-operatively (3 repeated images for the cornea and IOL, respectively). All 3-D sets of data contained the iris volume (fixed reference for merging).

The SLD power exposure was fixed at 800 μ W. Focus was changed by an automatic displacement to achieve optimal imaging of the different anterior segment structures (cornea, anterior and posterior lens). In order to minimize the impact of motion artifacts, images of each axial region were collected in 0.72 s. Measurements were collected on a 7x15 mm zone, using 50 B-Scans composed by a collection of 360 A-Scans, providing a resolution of 0.04 mm for horizontal and 0.2 mm for vertical meridian.

10.3. 3-D image analysis

The image processing algorithm can be summarized in 10 steps. The first 9 steps have been described in detail in previous studies [Ortiz et al 2009a, Ortiz et al 2009b, Ortiz et al 2010, Ortiz et al 2011, Ortiz et al 2012a] and only the new dedicated routine for estimating anterior

chamber depth, and 3-D tilt and decentration of the crystalline lens and IOL is described in detail (step 10).

(1) Denoising: A rotational kernel transform was performed for edge-preserving denoising, using a mask of size 9 pixels. In addition, a wavelet low-pass filtering processing based on log-Gabor wavelet was used for 7 scales and 6 orientations. (2) Statistical thresholding: An adaptive algorithm based on a multimodal Gaussian fitting of the histogram intensity (in a non-linear least squares sense) was performed on the entire 3-D sets of data, which allowed the separation of a noise class from the signal. (3) Volume clustering: the pixels belonging to large volumes representing the objects of interest in 3-D (cornea, iris, anterior crystalline lens surface, posterior crystalline lens surface and IOL) are separated from small volumes through point-connectivity algorithm and thresholding algorithms (4) Multilayer segmentation: Automatic segmentation was based on Canny detection in each A-scan (1-D signals), following Gaussian ($\sigma=5$ pixels) filtering (5) Pupil center reference: The pupil center was used as a fixed reference across and to define the optical zone (effective area within the pupil). The current application uses the pupil plane in 3-D for registration and merging of both conditions. The characteristic vector of the iris plane of every acquisition was obtained, which provided the tilt angle of this plane with respect to the OCT coordinate system. (6) 3-D volume merging: Images of the cornea, anterior and posterior lens were merged using the pupil center and pupil plane orientation for registration. In a first step prior to merging, the corneal images were inverted, as for efficiency in the focus range shift, the cornea was acquired in the opposite side of the Fourier transform (in comparison with the crystalline lens acquisition). (7) Geometrical distances calculation and further denoising: The registration of the 3-D volumetric data sets involved shift, rotation and resampling using a Delaunay surface description for interpolation. Optical distances were calculated by direct subtraction of the coordinates of the different surfaces, and geometrical distances were obtained by dividing the optical distance by the corresponding group refractive index (1.376 for the cornea, 1.336 for the aqueous humor, 1.403 for the crystalline lens of the subject in the study as per a previously published age-related expression [Uhlhorn et al, 2008], 1.430 for the Crystalens IOL, 1.486 for the PMMA cornea and IOL of the physical model eye, and 1.336 for the saline solution). (8) Fan and optical distortion correction, by propagating the geometrical distances along the directional cosines of each ray, taking into account the refraction that occurs at each interface between media of different

refractive indices [Ortiz et, 2010]. (9) Surface fitting to spherical surfaces in a 3-mm diameter optical zone with respect to corresponding surface apex.

(10) Anterior segment biometry: central corneal thickness (CCT), anterior chamber depth (ACD), crystalline lens thickness (CLT), intraocular lens thickness (ILT), intraocular lens position (ILP), and lens IOL tilt (IT) were computed from the corrected 3-D OCT images. CCT is defined as the distance between the anterior and posterior corneal apices. ACD is defined as the distance between the posterior corneal surface apex and the anterior crystalline lens surface apex. CLT and ILT are defined as the distance between the anterior and posterior lens surface apices. ILP is defined as the distance between the posterior corneal surface apex and the anterior IOL surface apex. The 3-D Euclidean distances were obtained by direct subtraction of the apices coordinates obtained from the fittings of the surfaces to spheres, after optical distortion correction. Figure 2 illustrates these definitions, in a 3-D OCT section of the anterior segment in an eye with a natural crystalline lens (prior to cataract surgery) -left panel- and the same eye after IOL implantation -right panel-.

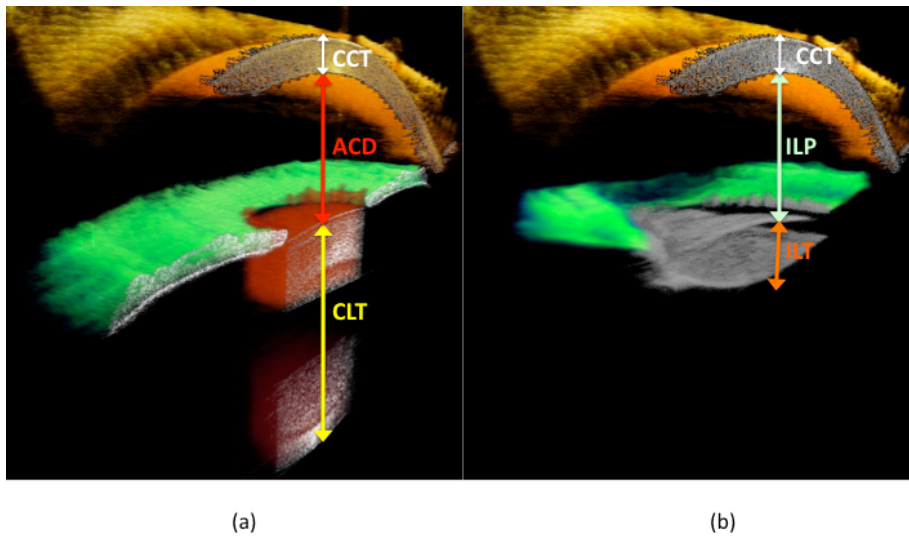


Fig. 10.1. Illustration of the biometry evaluation from 3-D anterior segment sOCT. (a) Pre-cataract surgery: CCT Central Corneal Thickness (in white) ACD Anterior Chamber Depth (in red) and CLT central Lens Thickness (in yellow). (b) Post-cataract surgery with IOL implantation: CCT Central Corneal Thickness (in white), ILP Intraocular Lens Position (in light green) and ILT Intraocular Lens Thickness (in orange).

Crystalline lens/ IOL decentration is defined as the lateral Euclidean distance between the IOL center and the pupil center. Lens tilt is defined as the angle between the axis of the lens and the pupillary axis.

The Lens/IOL axis (\vec{L}) has been defined as the vector that joins the apexes of the anterior and posterior lens surfaces [de Castro et al 2007]. The pupillary axis (\vec{P}) has been introduced as the vector that joins the center of curvature of the anterior cornea and the pupil center. The angle between axes is obtained by the scalar product of those vectors, from which (Equation 10.1). The horizontal and vertical components of the tilt are obtained, following a sign convention similar to that reported by Rosales et al [2008] Figure 10.2 Illustrates the crystalline lens (left panel) and IOL (right panel) axes, and the pupillary axis, defining lens tilt.

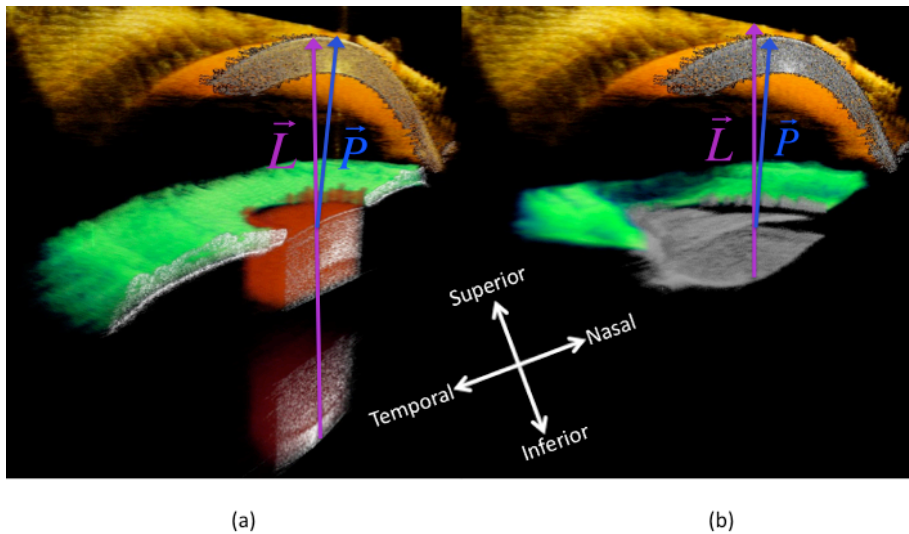


Figure 10.2. Illustration of the lens tilt evaluation: Pre-cataract surgery (a), and post-cataract surgery with IOL implantation (b). Vector P (in blue) is the pupillary axis, and L (in purple) is the Lens/IOL axis.

10.3. Results

10.3.1. OCT-based lens tilt measurement: validation on an in vitro physical model eye

The images obtained from the physical model eye were processed using the developed image analysis and distortion correction algorithms. Validation of the retrieved radii of curvature of the artificial cornea and lens, in comparison with nominal data were described in a recent study [Ortiz et al 2012b]. Figure 10.3 shows the measured horizontal tilt values in the physical model eye versus the nominal amount of tilt set in the micrometer stage that holds the lens (varied between -5 and 5 deg). There is an excellent correlation between nominal and measured values, with an average deviation of less than 0.3 deg from nominal values. As expected, the y-axis tilt remains constant through

measurements (measured y-axis values ranging between -3.76 and -4.07 deg). Slight variations could be associated to manual rotation of the IOL.

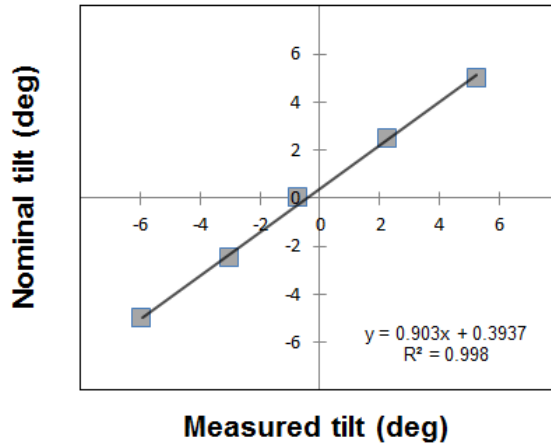


Figure 10.3. Comparison of the nominal tilt introduced in the lens of the physical model eye, and the tilt estimated from the OCT images.

10.3.2. *In vivo 3D anterior biometry: cornea and crystalline lens/IOL*

3D anterior segment biometry (cornea and lens/IOL) is described after full distortion corrections. Radii of curvature of all the surfaces (Table 10.1) were obtained from sphere fitting. There is a high measurement repeatability, including pre- and post-operative corneal measurements. The 3.9% variation in the anterior corneal surface in the anterior corneal radius of curvature could be caused by a slight corneal relaxation with the incision [Merriam et al 2003].

Table 10.1. Radii of curvature of the corneal and crystalline lens/IOL surfaces from sphere fitting

	Radii of curvature (mm)			
	Anterior cornea	Posterior cornea	Anterior lens	Posterior lens
Pre-op (lens)	7.41±0.03	6.82±0.08	8.34±0.25	6.39±0.14
Post-op (IOL)	7.70±0.01	6.80±0.11	6.97±0.06	8.73±0.14

Table 10.2 shows thickness and interocular distances of the ocular components (CCT, ACD/ILP and CLT/ILT), and tilt and decentration of the crystalline lens/IOL). The anterior surface of the IOL was placed 400 μm behind the natural crystalline lens. CLT is consistent with the average 73-year old lens thickness [Dubbelman et al, 2001]. Both the crystalline lens and IOL were tilted decentrated with respect to the pupillary axis and center in the same direction, but significantly different amounts. According to existing conventions [Rosales et al, 2008], negative horizontal decentration stands for nasal (in left eyes), and positive vertical decentration for superior. Positive tilt around the horizontal axis (Tilt x) indicates that the superior edge of the lens is moved forward. Negative tilt around the vertical axis (Tilt y), in left eyes, indicates that the nasal edge of the lens is moved forward.

Table 10.2. Anterior segment biometry of the corneal and crystalline lens/IOL

	Anterior segment biometry(mm)						
	<i>CCT</i>	<i>ACD/ELP</i>	<i>CLT/cIOLt</i>	<i>Tilt (x)*</i> (deg)	<i>Tilt (y)**</i> (deg)	<i>Decentration</i> (x)	<i>Decentration</i> (y)
Pre-op (lens)^o	0.49±0.01	3.14±0.04	4.24±0.05	1.89±0.32	-2.47±0.16	-0.66±0.05	0.17±0.06
Post-op (IOL)	0.47±0.01	3.56±0.10	1.33±0.05	0.04±0.03	-0.77±0.10	-0.26±0.02	0.39±0.07

*Tilt (x) stands for tilt around x-axis (superior/inferior tilt); **Tilt (y) stands for tilt around y-axis (nasal/temporal tilt)

10.4. Discussion

We have presented new methodology for 3-D biometry of the anterior segment of the eye based on quantitative OCT, and its application in cataract surgery. 3-D measurements allowed interocular distances and thickness to be measured along the objectively identified axes (as opposed to single A-scan measurements which rely on patient's fixation). In addition, this is, to our knowledge, the first time that the crystalline lens and IOL tilt and decentration have been measured in 3-D using OCT. This information, along with full corneal topography [32,35,36] and axial length measurements, is extremely valuable to improve biometric pre-operative evaluations of cataract surgery, and therefore the selection of the most appropriate IOL design and power, as well as to fully characterize surgical outcomes and optical performance in pseudophakic eyes. In particular, quantitative 3-D OCT

anterior segment geometry and biometry will help to improve IOL selection by: (1) providing true corneal power, from anterior and posterior corneal radius of curvature; (2) providing 3-D data for non-paraxial 3-D ray tracing calculations of IOL power calculations and beyond this, full customization of the IOL design; (3) improving accuracy in interocular distances estimations; (4) greatly improving the Estimated Lens Position, which is a key parameter in IOL power calculations [Norrby et al, 2008]. 3-D quantitative views of the full anterior segment of the eye pre- and post-operatively will provide important insights into the pre-operative anatomical parameters affecting the positioning of the implanted IOL beyond the recently explored pre-operative ACD and ILT [Olsen, 2006].

The geometrical values retrieved for the patient reported in this study are consistent with previously reported values in the literature. Dubbelman et al. [Dubbelman et al, 2001a, and 2006], using corrected Scheimpflug imaging in a population of 102 subjects of different ages, reported values of corneal radii of curvature [Dubbelman et al, 2006], and a linear regression of crystalline lens radii of curvature and lens thickness as a function of age [Dubbelman et al, 2001b]. For a 73-year old eye, the predicted radii of curvature from Dubbelman's expression are: 7.79 and 6.53 mm (anterior and posterior cornea), 8.74 and 5.32 mm (anterior and posterior lens), and 4.30 mm for LT, which are very close to the values that we found in this study for a patient of the same age (7.41, 6.82, 8.32, 6.39 and 4.24 mm, respectively). The measured ACD in our patient (3.14 mm) is within the range of values reported in the literature for a similar age (2.87 to 3.80 mm).

Post-operative measurements are interesting to assess possible changes in corneal shape with incision [Merriam et al, 2003]. We found the pre-operative anterior cornea to be slightly steeper than the post-operative cornea. Further analysis of the corneal elevation maps, available from OCT, could reveal changes in astigmatism and other high order terms [Marcos et al, 2007]. Post-operative 3-D biometry reveals interesting features concerning IOL positioning, which are essential to refine estimates of the IOL position (ELP, used in IOL power calculations), and understand the stability of the IOL and its optical performance. ELP depends on individual anatomical parameters (fully available with the reported methodology) and the IOL platform and haptic design. The particular design of the IOL of the example (an accommodating IOL, expected to move axially upon an accommodative effort) may explain the relatively forward position of the lens –and therefore relatively lower post-operative ACD compared to that obtained with common

monofocal IOLs (i.e. 3.91 ± 0.28 mm, as obtained for the single-piece aspheric IOL using OCT [Zhang et al, 2010]).

As the IOL design becomes more sophisticated, there is an increasing interest in the assessment of IOL tilt and decentration, and its potential impact on optical quality. Previous studies used Purkinje or Scheimpflug imaging to measure IOL alignment in normal young eyes, and pseudophakic eyes implanted with aspheric monofocal IOLs [de Castro et al, 2006, Taberero et al, 2006a and b, Rosales et al, 2007,]. In this study, we report for the first time full measurements and validations of IOL tilt and decentration obtained from OCT images. We found amounts and orientations in the natural lens of the patient of study within the range of previous studies [Philips et al, 1988 and Rosales et al, 2006]. In addition, as observed in previous studies, the IOL showed decentration and tilt in the same direction as the natural lens, although the amounts varied slightly. The analysis of the anatomical and IOL design factors (i.e. haptic design) influencing IOL tilt and decentration is interesting for improvement of IOL design parameters.

Customized model eye's using anatomical information for each patient has been shown to provide excellent predictions of wave aberrations (estimated from ray tracing) in pseudophakic eyes, compared to measurements of ocular aberrations performed in the same eye [Rosales et al, 2007]. As cataract surgery heads towards ray-tracing calculations of IOL power, and to customized IOL designs, it becomes more important to obtain accurate biometric parameters. Fully quantitative OCT-based 3-D geometry, and biometry obtained from the same instrument holds promise to become a primary tool in the cataract surgery practice.

10.5. Conclusions

Anterior segment OCT provided with full distortion correction and automatic analysis tools allowed quantification of the human biometry *in vivo* in 3-D previous and after cataract surgery. The retrieved radii of curvature from OCT, previous operation, agree with phakometric data previously reported using Scheimpflug and Purkinje image along one meridian. Biometric pre and post-operative parameters CCT, ACD/ILP, CLT/ILT Tilt and decentration are retrieved with a very high degree of accuracy. IOL was placed $400 \mu\text{m}$ behind the natural crystalline lens. In the reported patient the IOL tilt and decentration preserved the orientation of the natural lens (lens tilted with the superior and nasal edge forward, and decentered superiorly and nasally); pre-operative tilt

was 3.11 deg and decentration 0.77 mm; post-operative tilt was 0.77 deg and decentration 0.47 mm. OCT-based biometry is a promising tool to investigate the changes after cataract surgery; the contribution of the IOL location and tilt to the overall retinal image quality, and in the design of new IOLs.

Chapter 11

Conclusions

This thesis addresses the development of Optical Coherence Tomography technology for imaging and quantification of the anterior segment of the eye. The developed methodology includes hardware and quantification of OCTs for 3D imaging of the anterior segment of the eye. These developments have been applied to the geometrical characterization of the cornea and the lens, in normal, pathological and treated eyes.

In this thesis we accomplished the following achievements.

- Design, development and implementation of a TD-OCT with a confocal channel.
- A novel ray tracing method based on Delaunay triangulation and radial basis functions as interpolants for optical propagation of rays.
- Theoretical fan distortion prediction based on the optical configuration of the TD-OCT, including simulations and calculations to find the optimal optical configurations of the instrument.
- Calibration of the TD-OCT for compensating the residual fan distortion, providing quantitative topographies of artificial surfaces and ex-vivo corneas.
- A procedure for calibrating OCT applicable to any anterior segment OCT instrument, with quantitative applications in artificial surfaces, ex-vivo and in-vivo corneas.
- A method for correcting the optical (refraction) distortion in 3-D for retrieving accurate geometry of surfaces imaged through preceding refracting surfaces. The method was evaluated through with simulations for the anterior segment of the eye and experiments on artificial surfaces of known geometry, ex-vivo and in-vivo corneas and lenses.
- A set of image processing tools for analysis of OCT 3D images including: denoising, statistical thresholding, clustering, distortion corrections, 3-D merging, optical distances interpolation, surface denoising and quadric fittings
- Fan-distortion correction of anterior corneal maps from OCT and comparison with other clinical devices such as Scheimpflug and videokeratography.
- Characterization of a keratoconic cornea before and after the implantation of intra corneal ring segments (ICRS), providing anterior and posterior corneal radii of curvature, asphericities, topographic maps and thickness maps, and positioning in depth and rotation of the ICRS with respect to the pupil plane.

- 3-D geometrical characterization of the crystalline shape in vivo, including anterior and posterior lens radii of curvature, asphericity, thickness and elevation maps.
- Full biometry of the anterior segment of the eye pre- and post-cataract surgery, including crystalline lens and intraocular lens position and alignment.

The development of the experimental methodology proposed in this thesis allows to conclude that:

1. It is possible to perform an accurate and efficient ray tracing, based on Delaunay decomposition and Radial Basis Functions, on regular or random grids of points surfaces from either analytical, noisy or free-form surfaces, as the obtained by clinical instruments.

2. A proper and reliable correction of fan distortion is critical for OCT-based quantitative measurements of the surface topography. After calibration, measurement discrepancies on ophthalmic surfaces were less than 0.2% for the radius of curvature compared with measurements obtained with a profilometer. Not correcting for fan distortion produced discrepancies of up to 12%.

3. It is possible to correct for fan distortion in any anterior segment OCT instrument. Topography after fan distortion correction proved extremely accurate, in comparison with non-contact profilometry, tested on artificial surfaces of known geometry. Discrepancies less than 1% were obtained in measurements of both corneal radius of curvature and asphericity were observed.

4. It is possible to obtain OCT-based anterior corneal topographies comparable to state-of-the-art clinical topography systems (Scheimpflug and Placido-disk videokeratoscopy).

5. 3-D correction of optical distortion in OCT images allowed reliable quantitative reconstruction of the ophthalmic and ocular surface internal topography. Differences less than 3.1% and 8.1% in radius of curvature were observed in the reconstruction of an in-vivo human cornea, compared with data obtained from corrected Scheimpflug camera.

6. OCT quantitative imaging allows comprehensive 3-D quantitative analysis of the keratoconic cornea, and of the changes produced by ICRS treatment, as well as monitoring of the ICRS 3-D location. Preoperatively, average vertical and horizontal corneal radii of curvature were 7.03 and 6.51 mm, 5.97 and 6.32 mm for the anterior and posterior cornea respectively, and the minimum corneal thickness was 353 μm . ICRS implantation produced a significant flattening of the anterior corneal surfaces (vertical: 7.16 mm, and horizontal: 6.90 mm) and a steepening of the posterior cornea was (vertical 5.36 mm; horizontal 6.08 mm) a redistribution of thickness within the optical zone (minimum thickness: 429 μm).

7. Anterior segment OCT provided with full distortion correction and automatic analysis tools allowed quantification of the human crystalline lens in vivo in 3-D. The retrieved lens radii of curvature from OCT agree with phakometric data previously reported using Scheimpflug and Purkinje image along one meridian. The anterior lens radii of curvature ranged from 10.27 to 14.14 mm, and the posterior lens radii of curvature ranged from 6.12 to 7.54 mm. Surface asphericities ranged from -0.04 to -1.96. Surface lens astigmatism was significant, with the anterior lens typically showing horizontal

astigmatism (Z_2^2 ranging from -11 to -1 μm) and the posterior lens showing vertical astigmatism (Z_2^2 ranging from 6 to 10 μm).

8. It is possible to obtain OCT-based 3-D quantitative biometry of the human anterior segment *in vivo* previous and after cataract surgery. The method was tested on an *in vitro* artificial eye with known surfaces geometry at different orientations and demonstrated on an aging cataract patient *in vivo*. Biometric parameters CCT, ACD/ILP, CLT/ILT Tilt and decentration were retrieved with a very high degree of accuracy. IOL was placed 400 μm behind the natural crystalline lens. The IOL was aligned with a similar orientation of the natural lens (2.47 deg superiorly), but slightly lower amounts (0.77 deg superiorly). The IOL was decentered superiorly (0.39 mm) and nasally (0.26 mm).

Future work

Calibration of fan distortion in commercial devices. The developed technology for distortion correction and quantification can be applied to commercial devices. The first results on an Optopol HR system are promising [Siedlecki et al, 2012b].

Fan distortion optimization for 3-D acquisition. The possibility of producing new sample arms architectures should be explored in order to reduce the magnitude of fan distortion without compromising its acquisition speed.

Radiometric calibration of OCT. The possibility of calibrating the OCT radiometrically will open the new venues of exploring the amount of light back-reflected by the sample in every pixel and relate it to the tissue scattering properties

Follow-up of the keratoconus patients. The location and effect of ICRS implanted in keratoconus patients on anterior and posterior corneal topography, corneal thickness and corneal aberrometry are being studied longitudinally on a larger sample of patients. Topographic and thickness maps along time, as well as, the possible changes in location (depth and orientation) of the ICRS.

Correction of GRIN in-vivo. In other studies in our laboratory (de Castro et al.) OCT has been used in combination with tomographic algorithms to reconstruct the GRIN distribution in the crystalline lens in vitro. We will address the optical distortion correction if OCT crystalline lenses in vivo assuming a GRIN distribution inside the lens, and attempt the reconstruction of the lens GRIN in vivo.

Accommodation topography. When a near object is imaged the lens changes its anterior and posterior surfaces being more curved [Helmholtz, 1855]. Crystalline lens topography will be also studied as a function of accommodation. High speed OCT also allows acquisition of cross-sections of the crystalline lens dynamically as a function of accommodation.

Changes in Crystalline lens topography with accommodation and aging. The current thesis has provided for the first time the topography of the human lens in vivo, using OCT. We will study the shape a topography of the crystalline lens as a function of accommodation in vivo. Similarly, the changes in the topography of the anterior and posterior lens (and their relationship) will be studied as a function of age.

CONCLUSIONS

Cataract surgery and performance of new IOLs. In this thesis we have demonstrated quantitative full 3-D imaging in eyes before and after cataract surgery. We will use this technology to fully characterize the performance of state of the art IOLs, such as accommodating IOLs, with the use of fully OCT-based custom eye models.

Bibliography

A

E. Acosta, J. M. Bueno, C. Schwarz, and P. Artal, "Relationship between wave aberrations and histological features in ex vivo porcine crystalline lenses," *J. Biomed. Opt.* 15(5), 055001 (2010).

J. L. Alió, T. F. Salem, A. Artola, and A. A. Osman, "Intracorneal rings to correct corneal ectasia after laser in situ keratomileusis," *J. Cataract Refract. Surg.* 28(9), 1568–1574 (2002).

J. Allison, "Multiquadric radial basis functions for representing multidimensional high energy physics data," *Comput. Phys. Commun.* 77, 377-395 (1993).

W. A. Allen and J. R. Snyder, "Ray tracing through uncentered and aspheric surfaces," *J. Opt. Soc. Am.* 42, 243-249 (1952).

S. Amano, N. Honda, Y. Amano, S. Yamagami, T. Miyai, T. Samejima, M. Ogata, and K. Miyata, "Comparison of central corneal thickness measurements by rotating Scheimpflug camera, ultrasonic pachymetry, and scanning-slit corneal topography," *Ophthalmology.* 113(6), 937-941 (2006).

G. P. Agrawal. "Fiber Optic Communication systems" John Wiley and sons (2002).

I. H. Al-Ahdali and M.A. El-Messiery, "Examination of the effect of the fibrous structure of a lens on the optical characteristics of the human eye: a computer-simulated model," *Appl. Opt.* 34(25), 5738–5745 (1995).

R. A. Applegate, H. C. Howland, J. Buettner, A. J. Cottingham, Jr., R. P. Sharp, and R. W. Yee, "Corneal aberrations before and after radial keratotomy (RK) calculated from videokeratometric measurements," in *Vision Science and Its Applications*, Vol. 2 of 1994 OSA Technical Digest Series (Optical Society of America, 1994), pp. 58-61.

P. Artal, S. Marcos, I. Iglesias, and D.G. Green, "Optical modulation transfer function and contrast sensitivity with decentered small pupils in the human eye," *Vision Res.* 36(22), 3575-3586 (1996).

P. Artal and A. Guirao, "Contributions of the cornea and the lens to the aberrations of the human eye," *Opt. Lett.* 23, 1713-1715 (1998).

P. Artal, E. Berrio, A. Guirao, and P. Piers, "Contribution of the cornea and internal surfaces to the change of ocular aberrations with age," *J. Opt. Soc. Am. A* 19(1), 137–143 (2002).

D. A. Atchison and G. Smith, "Continuous gradient index and shell models of the human lens," *Vision Res.*, 35(18):2529–2538 (1995).

D. A. Atchison, and G. Smith. "Optics of the Human Eye". (Oxford, Butterworth-Heinemann) (2000).

D. A. Atchison, E. L. Markwell, S. Kasthurirangan, J. M. Pope, G. Smith, and P. G. Swann, "Age-related changes in optical and biometric characteristics of emmetropic eyes," *J Vis.*, 8(4), 1–20 (2008).

M. Avila, Y. Li, J. C. Song, and D. Hang, "High-speed optical coherence tomography for post-LASIK management," *J. Cataract Refrac. Surg.*, 32(11), 1836-1842 (2006).

B

I. Babuska, U. Banerjee, and J. E. Osborn, "Generalized finite element methods: main ideas, results, and perspective," *Int. J. Computat. Methods* 1, 67-103 (2004).

S. Barbero, S. Marcos, and J. Merayo-Llodes, "Corneal and total optical aberrations in a unilateral aphakic patient," *J. Cataract Refract. Surg.*, 28, 1594-1600 (2002a).

S. Barbero, S. Marcos, and J. Merayo-Llodes, "Corneal and total optical aberrations in a unilateral aphakic patient," *J. Cataract Refract. Surg.*, 28(9), 1594–1600 (2002b).

S. Barbero, "Refractive power of a multilayer rotationally symmetric model of the human cornea and tear film," *J. Opt. Soc. Am. A* 23, 1578-1585 (2006).

S. Barbero, and S. Marcos, "Analytical tools for customized design of monofocal intraocular lenses," *Opt. Express* 15(14),8576-8591 (2007).

J. I. Barraquer, "Modification of refraction by means of intracorneal inclusions," *Int. Ophthalmol. Clin.*, 6(1), 53–78 (1966).

J. C. Barry, R. Effert, M. Reim, and D. Meyer-Ebrecht, "Computational principles in Purkinje I and IV reflection pattern evaluation for the

- assessment of ocular alignment,” *Invest. Ophthalmol. Vis. Sci.*, 35(13), 4205-4218 (1994a).
- J. C. Barry, R. Effert, A. Kaupp, and A. Burhoff, “Measurement of ocular alignment with photographic Purkinje I and IV reflection pattern evaluation,” *Invest. Ophthalmol. Vis. Sci.*, 35(13), 4219-4235 (1994b).
- P. Beckmann, “Scattering of light by rough surfaces,” in *Progress in Optics*, E. Wolf, ed. (North-Holland, 1967), pp. 55-69.
- A. P. Beers and R. G. L. Van der Heijde, “Age-related changes in the accommodation mechanism,” *Optom Vis Sci*, 73(4):235–242 (1996).
- R. Belluci, and S. Morselli, “Optimizing higher-order aberrations with intraocular lens technology,” *Curr. Opin. Ophthalmol.* 18(1),67-73 (2007).
- G. B. Benedek, “Theory of transparency of the eye,” *Appl. Opt.*, 10(3), 459-473 (1971).
- D. A. Benedetto, T. E. Clinch, and P. R. Laibson, “In vivo observation of tear dynamics using fluorophotometry,” *Arch. Ophthalmol.*, 102(3), 410–412 (1984).
- T. J. Van den Berg, and H. Spekreijse, “Near infrared light absorption in the human eye media,” *Vision Res.*, 37(2), 249-253 (1997).
- E. Berrio, J. Taberero, and P. Artal, “Optical aberrations and alignment of the eye with age,” *J. Vis.*, 10(14), 34 (2010).
- G. Beyerle and I. S. McDermid, “Ray-tracing formulas for refraction and internal reflection in uniaxial crystals,” *Appl. Opt.*, 37, 7947-7953 (1998).
- J. Birkenfeld, A. de Castro, S. Ortiz, P. Pérez-Merino, E. Gamba, and S. Marcos, “Three-dimensional reconstruction of the isolated human crystalline lens gradient index distribution,” *Invest. Ophthalmol. Vis. Sci.* 52, E-Abstract 3404 (2011).
- K. Bizheva, B. Povazay, B. Hermann, H. Sattmann, W. Drexler, M. Mei, R. Holzwarth, T. Hoelzenbein, V. Wacheck, and H. Pehamberger, “Compact, broad-bandwidth fiber laser for sub-2-microm axial resolution optical coherence tomography in the 1300-nm wavelength region,” *Opt. Lett.*, 28(9), 707–709 (2003).
- J. M. Bland and D. G. Altman, “Statistical methods for assessing agreement between two methods of clinical measurement,” *Lancet* 327 (8476), 307–310 (1986).

- E. D. Blavatskaya, "Intralamellar homoplasty for the purpose of relaxation of refraction of the eye," *Arch. Soc. Am. Ophthalmol. Optom.*, 6, 311–325 (1968).
- J. F. de Boer, B. Cense, B. H. Park, M. C. Pierce, G. J. Tearney, and B. E. Bouma, "Improved signal-to-noise ratio in spectral-domain compared with time-domain optical coherence tomography," *Opt Lett.*, 28(21), 2067-2069 (2003).
- S. J. Bogan, G. O. Waring, O. Ibrahim, C. Drews, and L. Curtis, "Classification of normal corneal topography based on computer-assisted videokeratography," *Arch Ophthalmol.*, 108(7), 945-949 (1990).
- C. F. Bohren, "Absorption and Scattering of light by small particles," John Wiley and Sons. (1983).
- F. L. Bookstein, "Principal warps: thin plate splines and the decomposition of deformations," *IEEE Trans. Pattern Anal. Machine Intell.* 11, 567-585 (1989).
- D. Borja, F. Manns, A. Ho, N. Ziebarth, A. M. Rosen, R. Jain, A. Amelinckx, E. Arrieta, R.C. Augusteyn, and J.M. Parel, "Optical power of the isolated human crystalline lens," *Invest. Ophthalmol. Vis. Sci.*, 49(6), 2541–2548 (2008).
- D. Borja, D. Siedlecki, A. de Castro, S. Uhlhorn, S. Ortiz, E. Arrieta, J.-M. Parel, S. Marcos, and F. Manns, "Distortions of the posterior surface in optical coherence tomography images of the isolated crystalline lens: effect of the lens index gradient," *Biomed. Opt. Express*, 1(5), 1331–1340 (2010).
- M. Brzezinski, "Optical Coherence Tomography: Principles and Applications," (Academic, 2006).
- N. Brown, "The change in shape and internal form of the lens of the eye on accommodation," *Exp. Eye Res.*, 15(4): 441–459 (1973a).
- Brown, N, "Slit-image photography and measurement of the eye," *Med. Biol. Illus.*, 23(4), 192–203 (1973b).
- N. Brown, "The change in lens curvature with age". *Exp. Eye Res.*, 19(2), 175–183 (1974).
- T. E. Burriss, P. C. Baker, C. T. Ayer, B. E. Loomas, M. L. Mathis, and T. A. Silvestrini, "Flattening of central corneal curvature with intrastromal corneal rings of increasing thickness: an eye-bank eye study," *J. Cataract Refract. Surg.*, 19(Suppl), 182–187 (1993).

T. E. Burris, "Intrastromal corneal ring technology: results and indications," *Curr. Opin. Ophthalmol.*, 9(4), 9–14 (1998).

C

N. Calvo, S. R. Idelsohn, and E. Onate, "The extended Delaunay tessellation," *Eng. Computat.*, 20, 583-600 (2003).

F. W. Campbell, and A. H. Gregory, "Effect of Size of Pupil on Visual Acuity," *Nature* 187, 1121-1123 (1960).

Campbell C, "Reconstruction of the corneal shape with the MasterVue Corneal Topography System," *Optom. Vis Sci.*, 74(11), 899-905 (1997).

C. E. Campbell, "Nested shell optical model of the lens of the human eye," *J. Opt. Soc. Am. A*, 27(11), 2432–2441 (2010).

D. Cano, S. Barbero, and S. Marcos, "Comparison of real and computer-simulated outcomes of LASIK refractive surgery," *J. Opt. Soc. Am. A*, 21(6), 926–936 (2004).

C. Canovas and P. Artal, "Customized eye models for determining optimized intraocular lenses power," *Biomed. Opt. Express* 2, 1649-1662 (2011).

L. A. Carvalho, "Computer algorithm for simulation of the human optical system and contribution of the cornea to the optical imperfections of the eye," *Revista de Física Aplicada e Instrumentação* 16, 7-17 (2003).

A. de Castro, P. Rosales, and S. Marcos, "Tilt and decentration of intraocular lenses in vivo from Purkinje and Scheimpflug imaging—a validation study," *J. Cataract Refract. Surg.*, 33, 418-429 (2007).

A. de Castro, S. Ortiz, E. Gamba, D. Siedlecki, and S. Marcos, "Three-dimensional reconstruction of the crystalline lens gradient index distribution from OCT imaging," *Opt. Express* 18(21), 21905–21917 (2010).

A. de Castro, S. Barbero, S. Ortiz, and S. Marcos, "Accuracy of the reconstruction of the crystalline lens gradient index with optimization methods from ray tracing and Optical Coherence Tomography data," *Opt. Express* 19(20), 19265–19279 (2011).

A. de Castro, D. Siedlecki, D. Borja, S. Uhlhorn, J. M. Parel, F. Manns, and S. Marcos, "Age-dependent variation of the Gradient Index profile

- in human crystalline lenses,” *J. Mod. Opt.*, 58(19-20), 1781–1787 (2011).
- W. N. Charman, “The eye in focus: accommodation and presbyopia,” *Clin. Exp. Optom.* 91, 207-225 (2008).
- D. Chen and A. K. C. Lam, “Intrasession and intersession repeatability of the Pentacam system on posterior corneal assessment in the normal human eye,” *J. Cataract Refract. Surg.*, 33(3), 448–454 (2007).
- M. F. Chen and Y. P. Chen, “Compensating technique of field-distorting error for the CO₂ laser galvanometric scanning drilling machines,” *Int. J. Mach. Tools Manuf.* 47, 1114-1124 (2007).
- S. R. Chinn, E. A. Swanson, and J.G. Fujimoto, “Optical coherence tomography using a frequency-tunable optical source,” *Opt. Lett.*, 22, 340-342 (1997)
- P. Cho, A. K. C. Lam, J. Mountford, and L. Ng, “The performance of four different corneal topographers on normal human corneas and its impact on ortokeratology lens fitting,” *Optom. Vis. Sci.* 79(3), 175–183 (2002).
- M. A. Choma, K. Hsu, and J. A. Izatt, “Swept source optical coherence tomography using an all-fiber 1300-nm ring laser source,” *J. Biomed. Opt.*, 10:44009 (2005).
- M. Choma, M. Sarunic, C. Yang, and J.A. Izatt, “Sensitivity advantage of swept source and Fourier domain optical coherence tomography,” *Optics Express*, 11, 2183-2189 (2003).
- G. Cleary, D. J. Spalton, and J. Marshall, “Anterior chamber depth measurements in eyes with an accommodating intraocular lens: agreement between partial coherence interferometry and optical coherence tomography,” *J. Cataract Refract. Surg.*, 36, 790-798 (2010).
- R. A. Costa, M. Skaf, L. A. Melo, D. Calucci, J. A. Cardillo, J. C. Castro, D. Huang, and M. Wojtkowski, “Retinal assessment using optical coherence tomography,” *Prog. Retin. Eye Res.*, 25(3), 325–353 (2006).
- J. Colin, B. Cochener, G. Savary, and F. Malet. “Correcting keratoconus with intracorneal rings,” *J. Cataract Refract. Surg.*, 26(8), 1117-22 (2000).
- C. A. Cook and J. F. Koretz, “Methods to obtain quantitative parametric descriptions of the optical surfaces of the human crystalline

lens from Scheimpflug slit-lamp images. I. Image processing methods,” *J. Opt. Soc. Am. A*, 15(6), 1473–1485 (1998).

H. S. M. Coxeter, “Barycentric Coordinates,” in *Introduction to Geometry*, H. S. M. Coxeter, ed. (Wiley, 1969), pp. 216-221.

D

C. Dauwe, D. Touboul, C. J. Roberts, A. M. Mahmoud, J. Kérautret, P. Fournier, F. Malecaze, and J. Colin, “Biomechanical and morphological corneal response to placement of intrastromal corneal ring segments for keratoconus,” *J. Cataract Refract. Surg.*, 35(10), 1761–1767 (2009).

J. Dawczynski, E. Koenigsdoerffer, R. Augsten, and J. Strobel, “Anterior optical coherence tomography: a non-contact technique for anterior chamber evaluation,” *Graefes Arch. Clin. Exp. Ophthalmol.* 245(3), 423–425 (2007).

B. Delaunay, “Sur la sphère vide,” *Izvestia Akademii Nauk SSSR, Otdelenie Matematicheskikh i Estestvennykh Nauk* 7, 793-800 (1934).

J. A. Díaz, N. Blazejewski, J. Fernández-Dorado, J. Arasa, F. Sorroche, and C. Pizarro, “Analysis of the robustness of the lens grin profile in a schematic model eye,” *J Mod Optics*, 58(19-20), 1764–1769 (2011).

J. A. Díaz, C. Pizarro, and J. Arasa, “Single dispersive gradient-index profile for the aging human lens,” *J. Opt. Soc. Am. A*, 25(1), 250–261 (2008).

S. A. Dingeldein, S. D. Klyce, and S. E. Wilson, “Quantitative descriptors of corneal shape derived from computer-assisted analysis of photokeratographs,” *Refract. Corneal Surg.*, 5(6), 372-378 (1989).

R. W. Ditchburn and B. L. Ginsborg, “Involuntary eye movements during fixation,” *J. Physiol.*, 119(1), 1–17 (1953).

M. Doors, L. P. Cruysberg, T. T. Berendschot, J. de Brabander, F. Verbakel, C. A. Webers, and R. M. Nuijts, “Comparison of central corneal thickness and anterior chamber depth measurements using three imaging technologies in normal eyes and after phakic intraocular lens implantation,” *Graefes Arch. Clin. Exp. Ophthalmol.*, 247(8), 1139-46. (2009).

C. Dorransoro, D. Cano, J. Merayo-Llodes, and S. Marcos, “Experiments on PMMA models to predict the impact of corneal

refractive surgery on corneal shape,” *Opt. Express*, 14(13), 6142–6156 (2006).

C. Dorransoro, L. Remon, J. Merayo-Llodes, and S. Marcos, “Experimental evaluation of optimized ablation patterns for laser refractive surgery,” *Opt. Express*, 17(17), 15292–15307 (2009).

W. A. Douthwaite, “Application of linear regression to videokeratoscope data for tilted surfaces,” *Ophthal. Physiol. Opt.* 22, 46-54 (2002).

W. Drexler, O. Findl, R. Menapace, G. Rainer, C. Vass, C.K. Hitzenberger, and A.F. Fercher, “Partial coherence interferometry: a novel approach biometry in cataract surgery,” *Am. J. Ophthalmol* 126(4), 524-534 (1998).

M. Dubbelman, and R.G. van der Heijde, “The shape of the aging human lens: curvature, equivalent refractive index and the lens paradox,” *Vision Res*, 41(14), 1867–1877 (2001a).

M. Dubbelman, R.G.L. van der Heijde, and H.A. Weeber, “The thickness of the aging human lens obtained from corrected Scheimpflug images,” *Optom. Vis. Sci.*, 78(6), 411–416 (2001b).

M. Dubbelman, H. A. Weeber, R. G. Van der Heijde, and H. J. Volker-Dieben, “Radius and asphericity of the posterior corneal surface determined by corrected Scheimpflug photography,” *Acta Ophthalmol. Scand.*, 80, 379-383. (2002).

M. Dubbelman, R. G. L. Van der Heijde, H. A. Weeber, and G. F. J. M. Vrensen, “Changes in the internal structure of the human crystalline lens with age and accommodation,” *Vision Res*, 43(22), 2363–2375 (2003).

M. Dubbelman, R. G. L. Van der Heijde, and H. A. Weeber, “Change in shape of the aging human crystalline lens with accommodation,” *Vision Res*, 45(1), 117–132. (2005a).

M. Dubbelman, R.G.L. van der Heijde, H.A. Weeber Comment on “Scheimpflug and high-resolution magnetic resonance imaging of the anterior segment: a comparative study,” *J. Opt. Soc. Am. A*, 22(6), 1216–1218; discussion 1219– 20 (2005b).

M. Dubbelman, V.A. Sicam, G.L. van der Heijde, “The shape of the anterior and posterior surface of the aging human cornea,” *Vision Res*, 46, 993-1001 (2006).

M. C. M. Dunne, J. M. Royston, and D. A. Barnes, "Normal variations of the posterior corneal surface," *Acta Ophthalmol.*, 70, 255–261 (1992).

M. C. Dunne, L. N. Davies, and J. S. Wolffsohn, "Accuracy of cornea and lens biometry using anterior segment optical coherence tomography," *J. Biomed. Opt.*, 12(6), 064023 (2007).

E

C. Edmund, "Posterior corneal curvature and its influence on corneal dioptric power," *Acta Ophthalmol* 72, 715–720 (1994).

R. A. Egorchenkov and Y. A. Kravtsov, "Complex ray-tracing algorithms with application to optical problems," *J. Opt. Soc. Am. A*, 18, 650-656 (2001).

F

H. Farid and E. P. Simoncelli, "Differentiation of discrete multidimensional signals," *IEEE Trans. Image Process.*, 13(4), 496–508 (2004).

A. F. Fercher, K. Megedoht, and W. Werner, "Eye-length measurement by interferometry with partially coherent light," *Opt. Lett.*, vol 13 pp 1867-1869. (1988).

A. F. Fercher, C. K. Hitzenberger, W. Drexler, G. Kamp, and H. Sattmann, "In vivo optical coherence tomograph," *Am. J. Ophthalmol.*, 116(1), 113-114 (1993).

A. F. Fercher, C. K. Hitzenberger, G. Kamp, and S. Y. Elzaiat, "Measurement of Intraocular Distances by Backscattering Spectral Interferometry," *Optics Communications*, 117, 43-48 (1995).

A. F. Fercher, W. Drexler, C. K. Hitzenberger, and T. Lasser, "Optical coherence tomography--principles and applications," *Rep. Prog. Phys.*, 66, 239-303 (2003).

L. A. F. Fernandes and M. M. Oliveira, "Real-time line detection through an improved Hough transform voting scheme," *Pattern Recogn.*, 41, 299-314 (2008).

B. R. Frieden, "Probabilty, statisitical, optics and data testing," Springer Verlag. (1985).

G

- L. F. Garner, and M. K. Yap, "Changes in ocular dimensions and refraction with accommodation," *Ophthalmic Physiol. Opt.*, 17(1), 12–17 (1997a).
- L. F. Garner, "Calculation of the radii of curvature of the crystalline lens surfaces," *Ophthalmic Physiol. Opt.*, 17(1), 75–80 (1997b).
- P. L. George and H. Borouchaki, "Delaunay Triangulation and Meshing," (Editions Hermes, 1998).
- A. Glasser and M. C. Campbell, "Presbyopia and the optical changes in the human crystalline lens with age," *Vision Res.*, 38(2), 209–229 (1998).
- A. Glasser and M. C. Campbell, "Biometric, optical and physical changes in the isolated human crystalline lens with age in relation to presbyopia," *Vision Res.*, 39(11), 1991–2015 (1999a).
- A. Glasser and P. L. Kaufman, "The mechanism of accommodation in primates," *Ophthalmology*, 106(5), 863–872 (1999b).
- D. Gold and L. Richard, "Clinical Eye Atlas," *Oxford Atlases in Ophthalmology* pp. 396-397 (2010).
- J. A. Goldsmith, Y. Li, M. R. Chalita, V. Westphal, C. A. Patil, A. M. Rollins, J. A. Izatt, and D. Huang, "Anterior chamber width measurement by high-speed optical coherence tomography," *Ophthalmology*, 112(2), 238-244. (2005).
- A. V. Goncharov and C. Dainty, "Wide-field schematic eye models with gradient-index lens," *J. Opt. Soc. Am. A*, 24(8), 2157–2174 (2007).
- M. Gora, K. Karnowski, M. Szkulmowski, B. J. Kaluzny, R. Huber, A. Kowalczyk, and M. Wojtkowski, "Ultra high-speed swept source OCT imaging of the anterior segment of human eye at 200 kHz with adjustable imaging range," *Opt. Express* 17, 14880-14894 (2009).
- D. A. Goss, H. G. Van Veen, B. B. Rainey, and B. Feng, "Ocular components measured by keratometry, phakometry, and ultrasonography in emmetropic and myopic optometry students," *Optom. Vis. Sci.*, 74(7), 489–495 (1997).
- B. Grajciar, M. Pircher, C. K. Hitzenberger, O. Findl, and A. F. Fercher, "High sensitive measurement of the human axial eye length in

vivo with Fourier domain low coherence interferometry,” *Opt. Express*, 16, 2405-2414 (2008).

I. Grulkowski, M. Gora, I. Szkulmowski, I. Gorczynska, D. Szlag, S. Marcos, A. Kowalczyk, and M. Wojtkowski, “Anterior segment imaging with spectral OCT system using a high-speed CMOS camera,” *Opt. Express*, 17, 4842-4858 (2009).

I. Grulkowski, J. J. Liu, B. Potsaid, V. Jayaraman, C.D. Lu, J. Jiang, A.E. Cable, J.S. Duker, and J.G. Fujimoto, “Retinal, anterior segment and full eye imaging using ultrahigh speed swept source OCT with vertical-cavity surface emitting lasers,” *Biomed. Opt. Express* 3(11), 2733-2751 (2012).

L. Guibas, D. Knuth, and M. Sharir, “Randomized incremental construction of Delaunay and Voronoi diagrams,” *Algorithmica*, 7, 381-413 (1992).

M. Guillon, P. M. Lydon, and C. Wilson, “Corneal topography: a clinical model,” *Ophthalmic. Physiol. Opt.*, 6, 47-56 (1986).

A. Guirao and P. Artal, “Corneal wave aberration from videokeratography: accuracy and limitations of the procedure,” *J. Opt. Soc. Am. A*, 17, 955-965 (2000).

A. Guirao, M. Redondo, and P. Artal, “Optical aberrations of the human cornea as a function of age,” *J. Opt. Soc. Am. A*, 17, 1697-1702 (2000).

M. Gora, K. Karnowski, M. J. Szkulmowski, B. J. Kaluzny, R. Huber, A. Kowalczyk, and M. Wojtkowski, "Ultra high-speed swept source OCT imaging of the anterior segment of human eye at 200 kHz with adjustable imaging range," *Opt. Express*, 17, 14880-14894 (2009).

A. Gullstrand, “Appendices to Part I,” in *Helmholtz's Treatise on Physiological Optics* (Optical Society of America, Rochester, NY, 1924), pp. 350-358.

H

W. Haigis, B. Lege, N. Miller, and B. Schneider, “Comparison of immersion ultrasound biometry and partial coherence interferometry for intraocular lens calculation according to Haigis,” *Graefes Arch. Clin. Exp. Ophthalmol.* 238(9), 765-773 (2000).

H. Hashemi and S. Mehravaran, "Central corneal thickness measurement with Pentacam, Orbscan II, and ultrasound devices before and after laser refractive surgery for myopia," *J. Cataract Refract. Surg.*, 33(10), 1701-1707 (2007).

R. C. Haskell, D. Liao, A. E. Pivonka, T. L. Bell, B. R. Haberle, B. M. Hoeling, and D. C. Petersen, "Role of beat noise in limiting the sensitivity of optical coherence tomography," *J. Opt. Soc. Am. A*, 23(11), 2747-2755 (2006).

G. Häusler, and M. W. Lindner, "Coherence radar and spectral radar—new tools for dermatological diagnosis," *J. Biomed. Opt.*, 3, 21-31. (1998).

J. C. He, J. Gwiazda, F. Thorn, and R. Held, "Wave-front aberrations in the anterior corneal surface and the whole eye," *J. Opt. Soc. Am. A*, 20, 1155-1163 (2003).

M. R. Hee, J. A. Izatt, E. A. Swanson, D. Huang, J. S. Schuman, C. P. Lin, C. A. Puliafito, and J. G. Fujimoto, "Optical coherence tomography of the human retina," *Arch Ophthalmol.*, 113(3), 325-32 (1995).

M. R. Hee, C. A. Puliafito, C. Wong, J. S. Duker, E. Reichel, J. S. Schuman, E. A. Swanson, and J. G. Fujimoto, "Optical coherence tomography of macular holes," *Ophthalmology*, 102(5), 748-56 (1995).

M. R. Hee, C. R. Baumal, C. A. Puliafito, J. S. Duker, E. Reichel, J. R. Wilkins, J. G. Coker, J. S. Schuman, E. A. Swanson, and J. G. Fujimoto, "Optical coherence tomography of age-related macular degeneration and choroidal neovascularization," *Ophthalmology*, 103(8), 1260-70 (1996).

M. R. Hee, C. A. Puliafito, J. S. Duker, E. Reichel, J. G. Coker, J. R. Wilkins, J. S. Schuman, E. A. Swanson, and J. G. Fujimoto, "Topography of diabetic macular edema with optical coherence tomography," *Ophthalmology*, 105(2), 360-70 (1998).

H. Helmholtz, "Ueber die accommodation des auges," *Arch. Ophthal* 1, 1-74 (1855).

H. Helmholtz, "Treatise on Physiological Optics. The Optical Society of America (translated from Third German Edition by J. P. C. Southall)," (1924).

R. T. Hennessy, T. Iida, K. Shiina, and H.W. Leibowitz, "The effect of pupil size on accommodation", *Vision Res.*, 16(6), 587-589 (1976).

M. Herzberger, "Automatic ray tracing," *J. Opt. Soc. Am.* 47, 736-739 (1957).

E. A. Hermans, P. J. Pouwels, M. Dubbelman, J. P. Kuijter, R. G. van der Heijde, and R. M. Heethaar, "Constant volume of the human lens and decrease in surface area of the capsular bag during accommodation: an MRI and Scheimpflug study," *Invest. Ophthalmol. Vis. Sci.* 50(1), 281-289 (2009).

J. T. Holladay, "Standardizing constants for ultrasonic biometry, keratometry, and intraocular lens power calculations," *J. Cataract Refract. Surg.*, 23, 1356-1370 (1997).

H. C. Howland, J. Buettner, and R. A. Applegate, "Computation of the shapes of normal corneas and their monochromatic aberrations from videokeratometric measurements," in *Vision Science and Its Applications*, Vol. 2 of Technical Digest Series (Optical Society of America, 1994), pp. 54-57.

C. K. Hitzenberger, W. Drexler, and A. F. Fercher, "Measurement of corneal thickness by laser Doppler interferometry," *Invest. Ophthalmol. Vis. Sci.*, 33(1), 98-103 (1992).

D. Huang, J. Wang, C. P. Lin, C. A. Puliafito, J. G. Fujimoto, "Micron-resolution ranging of cornea anterior chamber by optical reflectometry," *Lasers in Surgery and Medicine*, 11, 419-425 (1991a).

D. Huang, E.A. Swanson, C.P. Lin, J.S. Schuman, W.G. Stinson, W. Chang, M.R. Hee, and T. Flotte, "Optical coherence tomography," *Science* 254,1178-1181 (1991b)

█

D. R. Iskander, M. J. Collins, and B. Davis, "Optimal modeling of corneal surfaces with Zernike polynomials," *IEEE Trans. Biomed. Eng.* 48, 87-95 (2001).

A. Ishibazawa, S. Igarashi, K. Hanada, T. Nagaoka, S. Ishiko, H. Ito, and A. Yoshida, "Central corneal thickness measurements with Fourier-domain optical coherence tomography versus ultrasonic pachymetry and rotating Scheimpflug camera," *Cornea*, 30(6), 615-619 (2011).

J. A. Izatt, M. R. Hee, E. A. Swanson, "Micrometer scale resolution imaging of the anterior eye in vivo with optical coherence tomography," *Arch Ophthalmol.*, 112(12), 1584-1589 (1994).

M. Izdebski, "Ray and wave tracing in uniaxial crystals perturbed by an external field," *Appl. Opt.* 47, 2729-2738 (2008).

J

G. J. Jaffe and J. Caprioli, "Optical coherence tomography to detect and manage retinal disease and glaucoma," *Am. J. Ophthalmol.* 137(1), 156–169 (2004).

F. A. Jakobiec, *Ocular anatomy, embryology, and teratology* (Harper & Row, Philadelphia, 1982).

M. A. Javadi, B. F. Motlagh, M. R. Jafarinasab, Z. Rabbanikhah, A. Anissian, H. Souri, and S. Yazdani, "Outcomes of penetrating keratoplasty in keratoconus," *Cornea* 24(8), 941–946 (2005).

C. E. Jones, D. A. Atchison, R. Meder, and J. M. Pope, "Refractive index distribution and optical properties of the isolated human lens measured using magnetic resonance imaging (MRI)," *Vision Res.* 45(18), 2352–2366 (2005).

K

G. Kamburoglu, A. Ertan, and O. Saraçbasi, "Measurement of depth of Intacs implanted via femtosecond laser using Pentacam," *J. Refract. Surg.*, 25(4), 377–382 (2009).

D. S. Kang, Y. J. Kim, and B. S. Shin, "Efficient large-scale terrain rendering method for real-world game simulation," in *Technologies for E-Learning and Digital Entertainment: First International Conference, Edutainment 2006* (Springer, 2006), pp. 597-605 (2006).

K. Karnowski, B. J. Kaluzny, M. Szkulmowski, M. Gora, and M. Wojtkowski, "Corneal topography with high-speed swept source OCT in clinical examination," *Biomed. Opt. Express*, 2, 2709-2720 (2011).

S. Kasthurirangan, E. L. Markwell, D. A. Atchison, J. M. Pope, "MRI study of the changes in crystalline lens shape with accommodation and in aging in humans," *J. Vis.* 11, pii, 19. doi, 10.1167/11.3.19 (2011).

H. E. Kauffman et al. "The Cornea". Butterworth-Heinemann. Chapter 1 (1998).

- J. B. Keller and H. B. Keller, "Determination of reflected and transmitted fields by geometrical optics," *J. Opt. Soc. Am.* 40(1), 48–52 (1950).
- K. Kawana, K. Miyata, T. Tokunaga, T. Kiuchi, T. Hiraoka, and T. Oshika, "Central corneal thickness measurements using Orbscan II scanning slit topography, noncontact specular microscopy, and ultrasonic pachymetry in eyes with keratoconus," *Cornea*, 24(8), 967–971 (2005).
- J. E. Kelly, T. Mihashi, and H. C. Howland, "Compensation of corneal horizontal/vertical astigmatism, lateral coma, and spherical aberration by internal optics of the eye," *J. Vis.*, 4(4), 2 (2004).
- R. N. Khurana, Y. Li, M. Tang, M. M. Lai MM, Huang D, "High-speed optical coherence tomography of corneal opacities," *Ophthalmology*, 114,1278-85 (2007).
- P. H. Kiely, G. Smith, and G. Carney, "The mean shape of the human cornea," *Opt. Acta* 29, 1027–1040 (1982).
- E. Kim, K. Ehrmann, S. Uhlhorn, D. Borja, and J. M. Parel, "Automated analysis of OCT images of the crystalline lens," *Proc. SPIE* 7163, 716313 (2009).
- E. Kim, K. Ehrmann, S. Uhlhorn, D. Borja, E. Arrieta-Quintero, and J. M. Parel, "Semiautomated analysis of optical coherence tomography crystalline lens images under simulated accommodation," *J. Biomed. Opt.* 16(5), 056003 (2011).
- H. Y. Kim, D. L. Budenz, P. S. Lee, W. J. Feuer, and K. Barton, "Comparison of central corneal thickness using anterior segment optical coherence tomography vs ultrasound pachymetry," *Am. J. Ophthalmol.*, 145(2), 228-232. (2008).
- S. D. Klyce and S. E. Wilson, "Methods of analysis of corneal topography," *Refract. Corneal Surg.*, 5(6), 368–371 (1989).
- A. H. Knoll, S. Russel, L.W. Carrol "New photokeratoscope utilizing a hemispherical object surface". *J Opt Soc Am* 1957, 47, 221-2 (1957).
- A. H. Knoll, "Corneal contours in the general population as revealed by the photokerastoscope," *Am. J. Optom.*, 38, 389-97 (1961)
- J. Kohout, J. I. Kolingerová, and J. Žára, "Parallel Delaunay triangulation in E2 and E3 for computers with shared memory," *Parallel Comput.*, 31, 491-522 (2005).

J. F. Koretz, G.H. Handelman, and N.P. Brown “Analysis of human crystalline lens curvature as a function of accommodative state and age”. *Vision Res*, 24(10):1141–1151 (1984).

J. F. Koretz, C. A. Cook, and J. R. Kuszak, “The zones of discontinuity in the human lens, development and distribution with age,” *Vision Res.*, 34, 2955-2962 (1994).

J. F. Koretz, C. A. Cook, and P. L. Kaufman, “Aging of the human lens: changes in lens shape at zero-diopter accommodation,” *J. Opt. Soc. Am. A*, 18(2), 265– 272 (2001).

J. E. Koretz, S. A. Strenk, L. M. Strenk, and J. L. Semmlow, “Scheimpflug and high-resolution magnetic resonance imaging of the anterior segment, a comparative study,” *J. Opt. Soc. Am A Opt. Image Sci. Vis.* 21(3), 346-354 (2004).

D. A. Kumar, A. Agarwal, G. Prakash, S. Jacob, Y. Saravanan and A. Agarwal, “Evaluation of intraocular lens tilt with anterior segment optical coherence tomography,” *Am. J Ophthalmol.*, 151(3), 406-412 (2011).

S. M. Kymes, J. J. Walline, K. Zadnik, J. Sterling, M. O. Gordon, and Collaborative Longitudinal Evaluation of Keratoconus Study Group, “Changes in the quality-of-life of people with keratoconus,” *Am. J. Ophthalmol.* 145(4), 611–617.e1 (2008).

L

B. Lackner, G. Schmidinger, S. Pieh, M.A. Funovics, and C. Skorpik, “Repeatability and reproducibility of central corneal thickness measurement with Pentacam, Orbscan, and ultrasound,” *Optom. Vis. Sci.*, 82(10), 892-9 (2005).

M. M. Lai, M. Tang, E. M. M. Andrade, Y. Li, R. N. Khurana, J. C. Song, and D. Huang, “Assessing intrastromal corneal ring segment depth in keratoconic eyes using optical coherence tomography,” *J. Cataract Refract. Surg.*, 32(11), 1860- 1865 (2006).

M. M. Lai, M. Tang, E. M. Andrade, Y. Li, R. N. Khurana, J. C. Song, and D. Huang, “Optical coherence tomography to assess intrastromal corneal ring segment depth in keratoconic eyes,” *J. Cataract Refract. Surg.* 32(11), 1860–1865 (2006).

R. Lavanya, L. Teo, D. S. Friedman, H. T. Aung, M. Baskaran, H. Gao, T. Alfred, S. K. Seah, K. Kashiwagi, P. J. Foster, and T. Aung,

- “Comparison of anterior chamber depth measurements using the IOLMaster, scanning peripheral anterior chamber depth analyser, and anterior segment optical coherence tomography,” *Br. J. Ophthalmol.*, 91(8), 1023–1026 (2007).
- R. Leitgeb, C. K. Hitzenberger, and A. F. Fercher, “Performance of Fourier domain vs. time domain optical coherence tomography,” *Opt. Express*, 11(8), 889–894 (2003).
- Y. Li, “Laser beam scanning by rotary mirrors. II. Conicsection scan patterns,” *Appl. Opt.* 34, 6417-6430 (1995).
- Y. Li and J. Katz, “Asymmetric distribution of the scanned field of a rotating reflective polygon,” *Appl. Opt.* 36, 342-352(1997).
- Y. Li, R. Shekhar, D. Huang, “Corneal pachymetry mapping with high-speed optical coherence tomography,” *Ophthalmology*, 113(5), 792-799 (2006).
- Y. Li, M.V. Netto, R. Shekhar, R. R. Krueger, D. Huang, “A longitudinal study of LASIK flap and stromal thickness with high-speed optical coherence tomography,” *Ophthalmology*, 114, 1124-1132 (2007).
- E. Y. Li, S. Mohamed, C. K. Leung, S. K. Rao, A. C. Cheng, C. Y. Cheung, and D. S. Lam, “Agreement among 3 methods to measure corneal thickness: ultrasound pachymetry, Orbscan II, and Visante anterior segment optical coherence tomography,” *Ophthalmology*, 114(10), 1842–1847 (2007).
- Y. Li, “Beam deflection and scanning by two-mirror and two-axis systems of different architectures: a unified approach,” *Appl. Opt.* 47, 5976-5985 (2008).
- Y. Li, D. M. Meisler, M. Tang, A. T. H. Lu, V. Thakrar, B. J. Reiser, and D. Huang, “Keratoconus diagnosis with optical coherence tomography pachymetry mapping,” *Ophthalmology*, 115(12), 2159–2166 (2008).
- Y. Li, M. Tang, X. Zhang, C.H. Salaroli, J.L. Ramos, and D. Huang, “Pachymetric mapping with Fourier-domain optical coherence tomography,” *J. Cataract Refract. Surg.*, 36(5), 826-831 (2009).
- Q. T. Liang and X. D. Zheng, “Ray-tracing calculations for uniaxial optical components with curved surfaces,” *Appl. Opt.* 30, 4521-4525 (1991).

- J. Liang, B. Grimm, S. Goelz, and J. F. Bille, "Objective measurement of wave aberrations of the human eye with the use of a Hartmann-Shack wave-front sensor," *J. Opt. Soc. Am. A*, 11, 1949–1957 (1994).
- H. Lim, Y. Jiang, Y. Wang, Y.-C. Huang, Z. Chen, and F. W. Wise, "Ultrahigh-resolution optical coherence tomography with a fiber laser source at 1 μm ," *Opt. Lett.*, 30(10), 1171–1173 (2005).
- H. Liou and N. A. Brennan, "Anatomically accurate, finite model eye for optical modelling," *J. Opt. Soc. Am. A*, 14(8), 1684–1695 (1997).
- G. R. Liu, "Mesh Free Methods: Moving Beyond the Finite Element Method" (CRC Press, 2002).
- L. Llorente, S. Marcos, C. Dorronsoro, and S. A. Burns, "Effect of sampling on real ocular aberration measurements," *J. Opt. Soc. Am. A*, 24, 2783–2796 (2007).
- R. F. Lowe and B. A. Clark, "Posterior corneal curvature," *Br. J. Ophthalmol.*, 57, 464–470 (1973).
- C. Lu, M. Tsai, Y. Wang, C. Lee, Y. Kiang, and C. C. Yang, "High-resolution swept-source optical coherence tomography with the frequency-sweeping the broadened spectrum of a fs Cr:forsterite laser," in Conference on Lasers and Electro-Optics/Quantum Electronics and Laser Science Conference and Photonic Applications Systems Technologies (Optical Society of America, 2007), paper JTUA44.

M

- B. M. Maceo, F. Manns, D. Borja, D. Nankivil, S. Uhlhorn, E. Arrieta, A. Ho, R. C. Augusteyn, and J. M. Parel, "Contribution of the crystalline lens gradient refractive index to the accommodation amplitude in non-human primates: in vitro studies," *J. Vis.*, 11(13), 23 (2011).
- N. Maeda, S. D. Klyce, M. K. Smolek, and H. W. Thompson, "Automated keratoconus screening with corneal topography analysis," *Invest. Ophthalmol. Vis. Sci.*, 35(6), 2749–2757 (1994).
- L. J. Maguire and W. M. Bourne, "Corneal topography of early keratoconus," *Am. J. Ophthalmol.*, 108(2), 107–112 (1989).
- D. Malacara, *Optical Shop Testing* (Wiley, 1978).

- N. Mamalis, C. W. Anderson, K. R. Kreisler, M. K. Lundergan, and R. J. Olson, "Changing trends in the indications for penetrating keratoplasty," *Arch. Ophthalmol.*, 110(10), 1409–1411 (1992).
- F. Manns, V. Fernandez, S. Zipper, S. Sandadi, M. Hamaoui, A. Ho, and J. M. Parel, "Radius of curvature and asphericity of the anterior and posterior surface of human cadaver crystalline lenses," *Exp. Eye Res.*, 78(1), 39–51 (2004).
- F. Manns, A. Ho, D. Borja, and J.M. Parel, "Comparison of uniform and gradient paraxial models of the crystalline lens," *Invest Ophthalmol Vis Sci*, 51: E–Abstract 789 (2010).
- E. W. Marchand, "Rapid ray tracing in radial gradients," *Appl. Opt.* 27, 465-467 (1988).
- S. Marcos, P. rosales, L. Llorente, I. Jimenez-Alfaro, "Change in corneal aberrations after cataract surgery with 2 types of aspherical intraocular lenses," *J. Cataract Refract. Surg.* 33(2), 217-226 (2007).
- S. Marcos, P. Rosales, L. Llorente, and I. Jiménez-Alfaro, "Change in corneal aberrations after cataract surgery with two types of aspherical intraocular lenses," *J. Cataract Refract. Surg.*, 33(2), 217–226 (2007).
- S. Marcos, P. Rosales, L. Llorente, S. Barbero, and I. Jiménez-Alfaro, "Balance of corneal horizontal coma by internal optics in eyes with intraocular artificial lenses: evidence of a passive mechanism," *Vision Res.*, 48(1), 70–79 (2008).
- G. F. G. Marshall, "Scanning devices and systems," in *Applied Optics and Optical Engineering*, R. Kingslake and B. J. Thompson, eds. (Academic, 1980), Vol. 6, pp. 203-262.
- J. Matsuda J, Hieda O, Kinoshita S, "Comparison of central corneal thickness measurements by Orbscan II and Pentacam after corneal refractive surgery," *Jpn J Ophthalmol.*, 52(4), 245-249 (2008).
- D. J. Meister and S. W. Fisher, "Progress in the spectacle correction of presbyopia. Part 2: Modern progressive lens technologies," *Clin. Exp. Optom.* 91, 251-264 (2008).
- N. Menassa, C. Kaufmann, M. Goggin, O. M. Job, L. M. Bachmann, and M. A. Thiel, "Comparison and reproducibility of corneal thickness and curvature readings obtained by the Galilei and the Orbscan II analysis systems," *J. Cataract Refract. Surg.*, 34(10), 1742-1747 (2008).
- J.C. Merriam, L. Zheng, J.E. Merriam, M. Zaidler, and B. Lindström "The effect of incisions for cataract on corneal curvature."

Ophthalmology, 110(9), 1807-13 (2003).

B. A. Moffat, D. A. Atchison, and J. M. Pope, "Explanation of the lens paradox," *Optom Vis Sci*, 79(3), 148–150 (2002b).

T. Möller and J. F. Hughes, "Efficiently building a matrix to rotate one vector to another," *J Graphics Tools*4(4), 1–4 (1999).

J. I. Montagu, "Galvanometric and resonant scanners," in *Handbook of Optical and Laser Scanning*, G. F. Marshall, ed. (Marcel Dekker, 2004), pp. 417-476.

U. Morgner, F. X. Kärtner, S. H. Cho, Y. Chen, H. A. Haus, J. G. Fujimoto, E. P. Ippen, V. Scheuer, G. Angelow, and T. Tschudi, "Sub-two-cycle pulses from a Kerr-lens mode-locked Ti:sapphire laser," *Opt. Lett.* 24, 411-413 (1999).

D. O. Mutti, K. Zadnik, and A. J. Adams, "A video technique for phakometry of the human crystalline lens," *Invest. Ophthalmol. Vis. Sci.*, 33(5), 1771–1782 (1992).

E. Moreno-Barriuso, S. Marcos, R. Navarro, and S. A. Burns, "Comparing laser ray tracing, spatially resolved refractometer and Hartmann–Shack sensor to measure the ocular wavefront aberration," *Optom. Vis. Sci.*, 78, 152– 156 (2001).

D. T. Moore, "Ray tracing in tilted, decentered, displaced gradient-index optical systems," *J. Opt. Soc. Am.*, 66, 789-795 (1976).

S. Muscat, N. McKay, S. Parks, E. Kemp, and D. Keating, "Repeatability and reproducibility of corneal thickness measurements by optical coherence tomography," *Invest. Ophthalmol. Vis. Sci.*, 43(6), 1791–1795 (2002).

N

T. Nakagawa, N. Maeda, R. Kosaki, Y. Hori, T. Inoue, M. Saika, T. Mihashi, T. Fujikado, and Y. Tano, "Higher-order aberrations due to the posterior corneal surface in patients with keratoconus," *Invest. Ophthalmol. Vis. Sci.*, 50(6), 2660–2665 (2009).

R. Navarro, L. González, and J. L. Hernández-Matamoros, "On the prediction of optical aberrations by personalized eye models," *Optom. Vis. Sci.* 83, 371-381 (2006).

R. Navarro, F. Palos, and L. M. González, "Adaptive model of the gradient index of the human lens. II. Optics of the accommodating aging lens," *J. Opt. Soc. Am. A* 24(9), 2911–2920 (2007).

L. T. Nordan, "Keratoconus: diagnosis and treatment," *Int. Ophthalmol. Clin.*, 37(1), 51–63 (1997).

S. Norrby, "The Dubbelman eye model analysed by ray tracing through aspheric surfaces," *Ophthalmic Physiol. Opt.*, 25, 153–161 (2005).

S. Norrby, "Sources of error in intraocular lens power calculation," *J. Cataract Refract. Surg.*, 34(3), 368–376 (2008).

O

T. Olsen, K. Thim, and L. Corydon "Theoretical versus SRK I and SRK II calculation of intraocular lens power," *J. Cataract Refract. Surg.*, 16, 217–225 (1990).

T. Olsen, "Prediction of the effective postoperative (intraocular lens) anterior chamber depth," *J. Cataract Refract. Surg.* 32(3), 419–424 (2006).

T. Olsen "Calculation of intraocular lens power: a review" *Acta Ophthalmol Scand*, 85, 472–485 (2007).

S. Ortiz, D. Siedlecki, L. Remon, and S. Marcos, "Three-dimensional ray tracing on Delaunay-based reconstructed surfaces," *Appl. Opt.* 48(20), 3886–3893 (2009).

S. Ortiz, D. Siedlecki, L. Remon, and S. Marcos, "Three-dimensional optical distortion correction for quantitative anterior segment OCT," *Invest. Ophthalmol. Vis. Sci.* 50, 5796(2009), abstract.

S. Ortiz, D. Siedlecki, L. Remon, and S. Marcos, "Optical Coherence Tomography for quantitative surface topography," *Appl. Opt.* 48(35), 6708–6715 (2009).

S. Ortiz, D. Siedlecki, I. Grulkowski, L. Remon, D. Pascual, M. Wojtkowski, and S. Marcos, "Optical distortion correction in optical coherence tomography for quantitative ocular anterior segment by three-dimensional imaging," *Opt. Express* 18(3), 2782–2796 (2010).

S. Ortiz, D. Siedlecki, P. Pérez-Merino, N. Chia, A. de Castro, M. Szkulmowski, M. Wojtkowski, and S. Marcos, "Corneal topography from spectral optical coherence tomography (sOCT)," *Biomed. Opt. Express* 2(12), 3232–3247 (2011).

S. Ortiz, P. Pérez-Merino, N. Alejandro, E. Gamba, I. Jimenez-Alfaro, and S. Marcos, "Quantitative OCT-based corneal topography in keratoconus with intracorneal ring segments," *Biomed. Opt. Express* 3(5), 814–824 (2012a).

S. Ortiz, P. Pérez-Merino, E. Gamba, A. de Castro, and Susana Marcos, "In vivo human crystalline lens topography," *Biomed. Opt. Express* 3, 2471-2488 (2012).

G. R. Osche, "Optical Detection Theory for Laser Applications," John Wiley and sons. (2002).

N. Otsu, "A threshold selection method from gray-level histogram," *IEEE Trans. Syst. Man Cybern.* 66, 9–62 (1979).

P

B.H. Park, M.C. Pierce, B. Cense, S.H. Yun, G.J. Mujat, B.E. Tearney, B.E. Bouma, and J.F. de Boer "Real-time fiber-based multi-functional spectral-domain coherence tomography at 1.3 μm ". *Opt. Express*, 13, 3931-3344 (2005).

S. Patel, J. Marshall, and F. W. Fitzke, "Shape and radius of posterior corneal surface," *Refract. Corneal Surg.*, 9, 173–181 (1993).

S. Patel, J. Marshall and F.W. Fitzke "Refractive index of the human corneal epithelium and stroma.." *J. Refract. Surg.*, 11(2), 100-105 (1995).

C. J. Pavlin, M. D. Sherar, and F. S. Foster, "Subsurface ultrasound microscopic imaging of the intact eye," *Ophthalmology*, 97,244–50 (1990).

A. Pérez-Escudero, C. Dorronsoro, L. Sawides, L. Remón, J. Merayo-Llves, and S. Marcos, "Minor Influence of Myopic Laser in Situ Keratomileusis on the Posterior Corneal Surface," *Invest. Ophthalmol. Vis. Sci.*, 50(9), 4146–4154 (2009).

D. P. Piñero, J. L. Alio, M. A. Teus, R. I. Barraquer, and A. Uceda-Montañés, "Modeling the intracorneal ring segment effect in keratoconus using refractive, keratometric, and corneal aberrometric data," *Invest. Ophthalmol. Vis. Sci.*, 51(11), 5583–5591 (2010).

P. Phillips, J. Pérez-Emmanuelli, H.D. Rosskothén, and C. J. Koester, "Measurement of intraocular lens decentration and tilt in vivo," *J. Cataract Refract. Surg.*, 14(2), 129–135 (1988).

L. Plesea and A. G. Podoleanu, "Direct corneal elevation measurements using multiple delay en face optical coherence tomography," *J. Biomed. Opt.*, 13(5), 054054 (2008).

A. G. Podoleanu, G. M. Dobre, and D. A. Jackson, "En-face coherence imaging using galvanometer scanner modulation," *Opt. Lett.* 23, 147-149 (1998).

A. G. Podoleanu, "Unbalanced versus Balanced Operation in an Optical Coherence Tomography System," *Appl. Opt.* 39(1), 173–182 (2000).

A. G. Podoleanu, I. Charalambous, L. Plesea, A. Dogariu, R. Rosen, "Correction of distortions in optical coherence tomography imaging of the eye," *Phys. Med. Biol.*, 49, 1277–1294 (2004).

O. Pomerantzeff, H. Fish, J. Govignon, and C.L. Schepens, "Wide angle optical model of the human eye," *Ann Ophthalmol*, 3(8), 815–819 (1971).

B. Potsaid, B. Baumann, D. Huang, S. Barry, A. E. Cable, J. S. Schuman, J. S. Duker, and J. G. Fujimoto, "Ultrahigh speed 1050nm swept source/Fourier domain OCT retinal and anterior segment imaging at 100,000 to 400,000 axial scans per second," *Opt. Express*, 18(19), 20029–20048 (2010).

B. Povazay, K. Bizheva, A.H. Unterhuber, B. Hermann, H. Sattmann, A.F. Fercher, W. Drexler, and A. Apolonski, "Submicrometer axial resolution optical coherence tomography," *Opt. Lett.*, 27,1800 (2002).

P. R. Preussner, J Wahl, H. Lahdo, B. Dick, and O. Findl, "Ray tracing for intraocular lens calculation," *J. Cataract Refract. Surg.*, 28,1412–1419 (2002).

J. I. Prydal and F. W.Campbell, "Study of precorneal tear film thickness and structure by interferometry and confocal microscopy," *Inv. Opth. Vis. Sci.*, 33(6), 1096-2005 (1992a).

J. I. Prydal, P. Artal, H. Woon, and F. W.Campbell, "Study of human precorneal tear film thickness and structure using laser interferometry.", *Inv. Opth. Vis. Sci.*, 33(6), 2006-2011 (1992b).

Q

B. R. McQueen, C. E. Martinez, and S. D. Klyce, "Corneal topography in cataract surgery," *Curr. Opin. Ophthalmol.*, 6, 22-28 (1997).

R

- Y. S. Rabinowitz and P. J. McDonnell, "Computer-assisted corneal topography in keratoconus," *Refract. Corneal Surg.*, 5(6), 400–408 (1989).
- Y. S. Rabinowitz, "Tangential vs sagittal videokeratographs in the "early" detection of keratoconus," *Am. J. Ophthalmol.*, 122(6), 887-889 (1996).
- Y. S. Rabinowitz, "Keratoconus," *Surv. Ophthalmol.*, 42(4), 297–319 (1998).
- S. Radhakrishnan, A. M. Rollins, and J. E. Roth, et al. "Real-time optical coherence tomography for the anterior segment at 1310nm". *Arch. Ophthalmol.*, 119(8), 1179-85 (2001).
- S. Radhakrishnan, J. Goldsmith, D. Huang, V. Westphal, D.K. Dueker, A.M. Rollins, J.A. Izatt, and S.D. Smith, "Comparison of optical coherence tomography and ultrasound biomicroscopy for detection of narrow anterior chamber angles," *Archive of Ophthalmology*, 123, 1053-1059 (2005a).
- S. Radhakrishnan, D. Huang, S.D. Smith, "Optical coherence tomography imaging of the anterior chamber angle," *Ophthalmology Clinics of North America*, 18(3), 375-381 (2005b)
- S. Radhakrishnan, Y. Li, D. Huang, "Chapter 10, Quantitative measurement of the anterior chamber angle with optical coherence tomography" pp. 109-116 in *Anterior Segment Optical Coherence Tomography*, R. F. Steinert, D Huang eds. (Slack Incorporated, Thorofare, USA 2008).
- R. Ramawasmi, "Optical networks. A practical perspective," (2002).
- S. A. Read, M. J. Collins, D. R. Iskander, and B. A. Davis, "Corneal topography with Scheimpflug imaging and videokeratography: comparative study of normal eyes," *J. Cataract Refract. Surg.*35(6), 1072–1081 (2009).
- H. L. Rao, A. U. Kumar, A. Kumar, S. Chary, S. Senthil, P. K. Vaddavalli, and C. S. Garudadri, "Evaluation of central corneal thickness measurement with RTVue spectral domain optical coherence tomography in normal subjects," *Cornea*30(2), 121–126 (2011).

- D. Z. Reinstein, S. Srivannaboon, and S. P. Holland, "Epithelial and stromal changes induced by intacs examined by three-dimensional very high-frequency digital ultrasound," *J. Refract. Surg.* 17(3), 310–318 (2001).
- J. Rogowska and M. E. Brezinski, "Image processing techniques for noise removal, enhancement and segmentation of cartilage OCT images," *Phys. Med. Biol.* 47(4), 641–655 (2002).
- C. Roberts, "Corneal topography: a review of terms and concepts," *J. Cataract Refract. Surg.* 22(5), 624–629 (1996).
- A. Roorda and A. Glasser, "Wave aberrations of the isolated crystalline lens," *J. Vis.* 4(4), 1 (2004).
- N. Rosa, M. Lanza, M. Borrelli, B. Polito, M.L. Filosa, and M. De Bernardo "Comparison of central corneal thickness measured with Orbscan and Pentacam". *J Refract Surg.* Nov;23(9):895-899 (2007).
- C. H. Rosas Salaroli, Y. Li, and D. Huang "High-resolution optical coherence tomography visualization of LASIK flap displacement", *J Cataract Refract Surg.* 35,1640-1642 (2009).
- P. Rosales and S. Marcos, "Phakometry and lens tilt and decentration using a custom-developed Purkinje imaging apparatus, validation and measurements," *J. Opt. Soc. Am. A* 23, 509-520 (2006a)
- P. Rosales, M. Dubbelman, S. Marcos, and R. van der Heijde, "Crystalline lens radii of curvature from Purkinje and Scheimpflug Imaging," *J. Vision* 6(10), 1057-1067 (2006b).
- P. Rosales and S. Marcos, "Customized computer models of eyes with intraocular lenses," *Opt. Express* 15, 2204-2218 (2007).
- P. Rosales, M. Wendt, S. Marcos, and A. Glasser, "Changes in crystalline lens radii of curvature and lens tilt and decentration during dynamic accommodation in rhesus monkeys," *J. Vis.* 8(1), 1-12 (2008).
- P. Rosales and S. Marcos, "Pentacam Scheimpflug quantitative imaging of the crystalline lens and intraocular lens," *J. Refract. Surg.*, 25, 421-428 (2009).
- A. M. Rosen, D. B. Denham, V. Fernandez, D. Borja, A. Ho, F. Manns, J. M. Parel, and R. C. Augusteyn, "In vitro dimensions and curvatures of human lenses," *Vision Res.*, 46(6-7), 1002–1009 (2006).
- R. B. Rosen, M. Hathaway, J. Rogers, J. Pedro, P. Garcia, P. Laissue, G. M. Dobre, and A. G. Podoleanu, "Multidimensional en-face OCT imaging of the retina," *Opt. Express* 17, 4112-4133 (2009).

J. M. Royston, M. C. M. Dunne, and D. A. Barnes, "Measurement of the posterior corneal radius using slit lamp and Purkinje image techniques," *Ophthalmic. Physiol. Opt.*, 10, 385–388 (1990).

M. Ruggeri, O. Kocaoglu, S. Uhlhorn, D. Borja, R. Urs, T. H. Chou, V. Porciatti, J. M. Parel, and F. Manns, "Small animal ocular biometry using optical coherence tomography," *Proc. SPIE7550*, 755016, 755016-6 (2010).

S

Y. Sakamoto, K. Sasaki, Y. Nakamura, and N. Watanabe, "Reproducibility of data obtained by a newly developed anterior eye segment analysis system, EAS-1000," *Ophthalmic Res.*, 24(Suppl 1), 10–20 (1992).

U. de Sanctis, A. Missolungi, B. Mutani, L. Richiardi, and F. M. Grignolo, "Reproducibility and repeatability of central corneal thickness measurement in keratoconus using the rotating Scheimpflug camera and ultrasound pachymetry," *Am. J. Ophthalmol.*, 144(5), 712–718.e1 (2007).

D. R. Sanders and M. C. Kraff, "Improvement of intraocular lens power calculation using empirical data," *J. Am. Intraocul. Implant. Soc.*, 6, 263–267 (1980).

D. R. Sanders, J. Retzlaff, and M. C. Kraff, "Comparison of the SRK II formula and other second-generation formulas," *J. Cataract Refract. Surg.*, 14: 136–141 (1988).

D. R. Sanders, J.A. Retzlaff, M. C. Kraff, H.V. Gimbel, and M.G. Raanan, "Comparison of the SRK/T formula and other theoretical and regression formulas," *J. Cataract Refract. Surg.*, 16, 341–346 (1990).

J. Santodomingo-Rubido, E. A. H. Mallen, B. Gilmartin, and J. S. Wolffsohn, "A new non-contact optical device for ocular biometry," *Brit. J. Ophthalmol.*, 86, 458-462 (2002).

G. Savini, E. Goto, M. Carbonelli, P. Barboni, and D. Huang, "Agreement between Stratus and Visante optical coherence tomography systems in tear meniscus measurements," *Cornea*, 28, 148-151 (2009).

J. Schwiegerling, J. E. Greivenkamp, and J. M. Miller, "Representation of videokeratoscopic height data with Zernike polynomials," *J. Opt. Soc. Am. A*, 12, 2105-2113 (1995).

- J. M. Schmitt, "Optical coherence tomography (OCT): a review," *IEEE J. Sel. Top. Quantum Electron.* 5, 1205-1215 (1999).
- J. S. Schuman, M. R. Hee, A. V. Arya, T. Pedut-Kloizman, C. A. Puliafito, J. G. Fujimoto, and E. A. Swanson, "Optical coherence tomography, a new tool for glaucoma diagnosis," *Curr. Opin. Ophthalmol.*, 6(2), 89-95 (1995).
- H. Shankar, D. Taranath, C. T. Santhirathelagan, and K. Pesudovs, "Anterior segment biometry with the Pentacam: comprehensive assessment of repeatability of automated measurements," *J. Cataract Refract. Surg.* 34(1), 103–113 (2008a).
- H. Shankar, D. Taranath, C. T. Santhirathelagan, and K. Pesudovs, "Repeatability of corneal first-surface wavefront aberrations measured with Pentacam corneal topography," *J. Cataract Refract. Surg.*, 34(5), 727–734 (2008b).
- A. Sharma, D. V. Kumar, and A. K. Ghatak, "Tracing rays through graded-index media: a new method," *Appl. Opt.* 21, 984-987 (1982).
- A. Sharma and A. K. Ghatak, "Ray tracing in gradient-index lenses: computation of ray-surface intersection," *Appl. Opt.* 25, 3409-3412 (1986).
- M. Shen, M. R. Wang, Y. Yuan, F. Chen, C. L. Karp, S. H. Yoo, and J. Wang, "SD-OCT with prolonged scan depth for imaging the anterior segment of the eye," *Ophthalmic Surg. Lasers Imaging*, 41(6Suppl), S65–S69 (2010).
- V. A. D. P. Sicam, J. Coppens, T. J. T. P. van den Berg, and R. G. L. van der Heijde, "Corneal surface reconstruction algorithm that uses Zernike polynomial representation," *J. Opt. Soc. Am. A*, 21, 1300-1306 (2004).
- D. Siedlecki, A. de Castro, E. Gamba, S. Ortiz, D. Borja, S. Uhlhorn, F. Manns, S. Marcos, and J. M. Parel, "Distortion correction of OCT images of the crystalline lens: gradient index approach," *Optom. Vis. Sci.*, 89(5), E709–E718 (2012).
- D. Siganos, P. Ferrara, K. Chatzinikolas, N. Bessis, and G. Papastergiou, "Ferrara intrastromal corneal rings for the correction of keratoconus," *J. Cataract Refract. Surg.*, 28(11), 1947–1951 (2002).
- R. H. Silverman, "High-resolution ultrasound imaging of the eye - a review," *Clin. Exp. Ophthalmol.*, 37(1), 54–67 (2009).

- T. Simpson and D. Fonn, "Optical Coherence Tomography of the Anterior Segment," *Ocul. Surf.*, 6(3), 117–127 (2008).
- M. V. Sivak, K. Kobayashi, J. A. Izatt, A. M. Rollins, R. Ungrunyawee, A. Chak, R. C. K. Wong, G. A. Isenberg, and J. Willis. "High-resolution endoscopic imaging of the GI tract using optical coherence tomography," *Gastrointest. Endosc.*, 51, 474-479, (2000).
- G. Smith, B. K. Pierscionek, and D. A. Atchison, "The optical modelling of the human lens," *Ophthalmic Physiol. Opt.*, 11(4), 359–369 (1991).
- G. Smith, "Paraxial ray tracing in gradient-index (GRIN) media, problems of convergence," *J. Opt. Soc. Am. A*, 9, 331–333 (1992).
- G. Smith, G. and L.F. Garner, "Determination of the radius of curvature of the anterior lens surface from the Purkinje images," *Ophthalmic Physiol. Opt.*, 16(2):135– 143 (1996).
- G. Smith, "The optical properties of the crystalline lens and their significance," *Clin. Exp. Optom.* 86(1), 3–18 (2003).
- M. K. Smolek and S. D. Klyce, "Is keratoconus a true ectasia? An evaluation of corneal surface area," *Arch. Ophthalmol.*, 118, 1179-1186 (2000).
- A. Sorsby, B. Benjamin, J. B. Davey, M. Sheridan, and J. M. Tanner, "Emmetropia and Its Aberrations. A Study in the Correlation of the Optical Components of the Eye," Medical Research Council Special Report Series No. 293 (Her Majesty's Stationary Office, London, 1957).
- A. Sorsby, B. Benjamin, M. Sheridan, J. Stone, and G. A. Leary, "Refraction and its components during the growth of the eye from the age of three," *Memo. Med. Res. Counc.*, 301(Special):1–67 (1961).
- G. H. Spencer and M. V. R. K. Murty, "General ray-tracing procedure," *J. Opt. Soc. Am.*, 52, 672-678 (1962).
- M. J. Stafford, "The histology and biology of the lens," (Bausch & Lomb, 2001).
- O. N. Stavroudis, "Ray-tracing formulas for uniaxial crystals," *J. Opt. Soc. Am.* 52, 187-191 (1962).
- R. F. Steinert and D Huang, "eds. Anterior Segment Optical Coherence Tomography," (Slack Incorporated, Thorofare, USA 2008) (2008).

S. Stenström, "Investigation of the variation and the correlation of the optical elements of human eyes," *Am. J. Optom.*, 25, 340–350 (1948).

G. Strang and G. Fix, "An Analysis of the Finite Element Method," (Prentice-Hall, 1973) (1973).

E. A. Swanson, J. A. Izatt, M. R. Hee, D. Huang, C. P. Lin, J. S. Schuman, C. A. Puliafito, and J. G. Fujimoto, "In-vivo retinal imaging by optical coherence tomography," *Opt. Lett.*, 18, 1864-1866. (1993).

T. Swartz, L. Marten, and M. Wang, "Measuring the cornea: the latest developments in corneal topography," *Curr. Opin. Ophthalmol.*, 18, 325-333 (2007).

T

J. Taberero, A. Benito, V. Nourrit, and P. Artal, "Instrument for measuring the misalignments of ocular surfaces," *Opt. Express*, 14(22), 10945–10956 (2006a).

J. Taberero, P. Piers, A. Benito, M. Redondo and P. Artal, "Predicting the optical performance of eyes implanted with IOLs to correct spherical aberration," *Invest. Ophthalmol. Vis. Sci.*, 47(10), 4651-8 (2006b).

K. Takada, I. Yokohama, K. Chida, and J. Noda, "New measurement system for fault location in optical waveguide devices based on an interferometric technique," *Appl. Opt.*, 26, 1603-1606 (1987).

I. Takada, "Noise in Optical Low-Coherence Reflectometry," *IEEE J. Quantum Electron.*, 34(7), 1098–1108 (1998).

W. Tang, M. J. Collins, L. Carney, and B. Davis, "The accuracy and precision performance of four videokeratoscopes in measuring test surfaces," *Optom. Vis. Sci.*, 77(9), 483–491 (2000).

M. Tang, Y. Li, M. Avila, and D. Huang, "Measurement of total corneal power before and after LASIK with high-speed optical coherence tomography," *J. Cataract Refract. Surg.*, 32(11), 1843-1850 (2006).

M. Tang, Y. Li, and D. Huang, "An intraocular lens power calculation formula based on optical coherence tomography, a pilot study," *J Refract Surg.*, 26(6), 430-437 (2010).

P. Targowski, T. Bajraszewski, I. Gorczynska, M. Gora, A. Szkulmowska, M. Szkulmowski, M. Wojtkowski, J. J. Kaluzny, B. J.

Kaluzny, and A. Kowalczyk, "Spectral optical coherence tomography for nondestructive examinations," *Opt. Appl.*, 36, 609–619 (2006).

X. Tian, G. Lai, and T. Yatagai, "Characterization of asymmetric optical waveguides by ray tracing," *J. Opt. Soc. Am. A*, 6, 1538-1543 (1989).

A. Tomidokoro, T. Oshika, S. Amano, S. Higaki, N. Maeda, and K. Miyata, "Changes in anterior and posterior corneal curvatures in keratoconus," *Ophthalmology*, 107(7), 1328–1332 (2000).

C. Touma and C. Gotsman, "Triangle mesh compression," in *Proceedings of Graphics Interface '98* 26-34 (Canadian Information Processing Society, 1998) (1998).

L. Tsang, "Scattering of electromagnetic waves," John Wiley and sons. (2000).

L. Tsang, J. A. Kong, K.-H. Ding, and C. O. Ao, "Random rough surface simulations," in *Scattering of Electromagnetic Waves: Numerical Simulations*, L. Tsang, J. A. Kong, K. -H. Ding, and C. O. Ao, eds. (Wiley, 2001), pp. 124-132 (2001).

J. Turuwhenua, "Corneal surface reconstruction algorithm using Zernike polynomial representation: improvements," *J. Opt. Soc. Am. A*, 24, 1551-1561 (2007).

U

S. R. Uhlhorn, D. Borja, F. Manns, and J. M. Parel, "Refractive index measurement of the isolated crystalline lens using optical coherence tomography," *Vision Res.*, 48(27), 2732–2738 (2008).

A. Unterhuber, B. Považay, B. Hermann, H. Sattmann, W. Drexler, V. Yakovlev, G. Tempea, C. Schubert, E. M. Anger, P. K. Ahnelt, M. Stur, J. E. Morgan, A. Cowey, G. Jung, T. Le, and A. Stingl, "Compact, low-cost Ti:Al₂O₃ laser for in vivo ultrahigh-resolution optical coherence tomography," *Opt. Lett.*, 28(11), 905–907 (2003).

V

R. Vanselow, "About Delaunay triangulations and discrete maximum principles for the linear conforming FEM applied to the Poisson Equation," *Appl. Math.*, 46, 13-28 (2001).

H. G. V. Veen and D. A. Goss, "Simplified system of Purkinje image photography for phakometry," *Am. J. Optom. Physiol. Opt.*, 65(11), 905–908 (1908).

A. S. Vilupuru and A. Glasser, "Dynamic accommodative changes in rhesus monkey eyes assessed with A-scan ultrasound biometry," *Optom. Vis. Sci.*, 80(5), 383–394 (2003).

W

X. Wang, C. Zhang, L. Zhang, L. Xue, and J. Tian, "Simultaneous refractive index and thickness measurements of bio tissue by optical coherence tomography," *J. Biomed. Opt.*, 7(4), 628–632 (2002).

G. O. Waring, "Making sense of keratospeak II: Proposed conventional terminology for corneal topography," *Refract. Corneal Surg.*, 5(6), 362–367 (1989).

J. W. Warnicki, P. G. Rehkopf, D. Y. Curtin, S. A. Burns, R. C. Arffa, and J. C. Stuart, "Corneal topography using computer analyzed rasterstereographic images," *Appl. Opt.*, 27(6), 1135–1140 (1988).

J. E. Weddell, J. A. Alvarado, and M. J. Hogan, *Histology of the human eye* (W.B. Saunders and Co, 1971) (1971).

H. Wendland, "Scattered Data Approximation," (Cambridge U. Press, 2004) (2004).

V. Westphall, A. M. Rollins, S. Radhakrishnan, and J. A. Izatt, "Correction of geometric and refractive image distortions in optical coherence tomography applying Fermat's principle," *Optics Express*, 10(9), 397–404 (2002).

J. S. Witkowski and A. Grobelny, "Ray tracing method in a 3D analysis of fiber-optic elements," *Opt. Appl.* 38, 281-294(2008).

M. Wojtkowski, T. Bajraszewski, P. Targowski, A. Kowalczyk. "Real-time in vivo imaging by high-speed spectral optical coherence tomography". *Opt. Lett.*, 28(19), 1745-1747 (2003).

G. Wollensak, E. Spoerl, and T. Seiler, "Riboflavin/ultraviolet-a-induced collagen crosslinking for the treatment of keratoconus," *Am. J. Ophthalmol.*, 135(5), 620–627 (2003).

J. W. Wulfeck, "Infrared photography of the so-called third Purkinje image," *J. Opt. Soc. Am.*, 45(11), 928–930 (1995).

X

J. Xie, S. Huang, Z. Duan, Y. Shi, and S. Wen, "Correction of the image distortion for laser galvanometric scanning system," *Opt. Laser Technol.*, 37, 305-311 (2005).

Y. Xu, J. Singh, C. S. Premachandran, A. Khairyanto, K. W. S. Chen, N. Chen, C. J. R. Sheppard, and M. Olivo, "Design and development of a 3-D scanning MEMS OCT probe using a novel SiOB package assembly," *J. Micromech. Microeng.* 18, 125005 (2008).

Y

R. Yadav, K. Ahmad, and G. Yoon, "Scanning system design for large scan depth anterior segment optical coherence tomography," *Opt. Lett.*, 35(11), 1774–1776 (2010).

Y. Yang, K. Thompson, and S. A. Burns, "Pupil location under mesopic, photopic, and pharmacologically dilated conditions," *Invest. Ophthalmol. Vis. Sci.*, 43(7), 2508–2512 (2002).

R. C. Youngquist, S. Carr, and D. E. N. Davies "Optical coherence domain reflectometry, A new optical evaluation technique", *Opt. Letters*, 12, 158-160 (1987).

S. H. Yun, B. E. Tearney, J. F. De Boer, N. Iftimia, and B. E. Bouma, "High-speed optical frequency-domain imaging," *Opt. Express*, 11, 2953-2963 (2003).

Z

Zemax Optical Design Program User's Manual (Zemax Development Corporation, 2007).

Q. Zhang, W. Jin, and Q. Wang, "Repetability, reproducibility, and agreement of central anterior chamber depth measurements in pseudophakic and phakic eyes: optical coherence tomography versus ultrasound biomicroscopy," *J. Cataract Refract. Surg.*, 36, 941-946 (2010).

BIBLIOGRAPHY

- M. Zhao, A. N Kuo, and J. A. Izatt, "3D refraction correction and extraction of clinical parameters from spectral domain optical coherence tomography of the cornea," *Opt. Express*, 18, 8923-8936 (2010).
- T. Zhou, P. Wright, J. Crawford, G. Mckinnon, and Y. Zhang, "MEMS 3-D optical mirror/scanner," in *Proceedings of the 2003 International Conference on MEMS, NANO and Smart Systems (IEEE Computer Society, 2003)*, pp. 222-226 (2003).
- A. M. Zysk, F. T. Nguyen, A. L. Oldenburg, D. L. Marks, and S. A. Boppart, "Optical coherence tomography: a review of clinical development from bench to bedside," *J. Biomed. Opt.*, 12(5), 051403 (2007).
- M. Zhu, M. J. Collins, and D. Robert Iskander, "Microfluctuations of wavefront aberrations of the eye," *Ophthalmic Physiol. Opt.*, 24(6), 562-571 (2004).

Publications during this research

SCIENTIFIC PAPERS ASSOCIATED WITH THIS THESIS

1. S. Ortiz, D. Siedlecki, L. Remon, and S. Marcos, “Three-dimensional ray tracing on Delaunay-based reconstructed surfaces,” *Appl. Opt.* **48**, 3886-3893 (2009).
2. S. Ortiz, D. Siedlecki, L. Remon, S. Marcos, “Optical coherence tomography for quantitative surface topography,” *Applied Optics* **48**, 6708-6715 (2009).
3. S. Ortiz, D. Siedlecki, Grulkowski I, L. Remon, Pascual D, Wojtkowski M, S. Marcos, “Optical distortion correction in optical coherence tomography for quantitative ocular anterior segment by three-dimensional imaging,” *Opt Express* **18**, 2782-2796 (2010).
4. S. Ortiz, D. Siedlecki, P. Pérez-Merino, N. Chia, A. de Castro, M. Szkulmowski, M. Wojtkowski, and S. Marcos, “Corneal topography from spectral optical coherence tomography (sOCT),” *Biomed. Opt. Express* **2**(12), 3232– 3247 (2011).
5. S. Ortiz, P. Pérez-Merino, N. Alejandro, E. Gamba, I. Jimenez-Alfaro, and S. Marcos. “Quantitative OCT-based corneal topography in keratoconus with intracorneal ring segments,” *Biomed. Opt. Express* **3**(5), 814-824 (2012).
6. S. Ortiz, P. Pérez-Merino, E. Gamba, Alberto de Castro, and S. Marcos. “In vivo human crystalline lens topography,” to *Biomed. Opt. Express* **3**(10), 2471-2488 (2012).
7. S. Ortiz, P. Pérez-Merino, S. Duran, M. Velasco-Ocana, Alberto de Castro, I. Jimenez-Alfaro and S. Marcos. “Full OCT anterior segment biometry: an application in cataract surgery,” submitted to *Biomed. Opt. Express*.

BOOK CHAPTERS

M. Wojtkowski, S. Marcos, S. Ortiz, I. Grulkowski “Application of Fourier Domain OCT imaging technology to the anterior segment of the human eye”. Optical coherence Tomography: Technology and Applications. Chapter 8.

PATENTS

S. Ortiz, S. Marcos, D. Siedlecki y C. Dorronsoro “Procedimiento de calibración y corrección de la distorsión de barrido de un sistema de Tomografía de coherencia óptica” PCT/ES2012/070185 (P201130685) - N/Ref.: 1.2012.0111/MAD.

OTHER PUBLICATIONS

- A. de Castro, S. Ortiz, E. Gamba, D. Siedlecki and S. Marcos, “Three- dimensional reconstruction of the crystalline lens gradient index distribution from OCT imaging”. Opt Express, 18(21): 21905-17, 2010.
- A. de Castro, S. Barbero, S. Ortiz and S. Marcos, “Accuracy of the reconstruction of the crystalline lens gradient index with optimization methods from Ray Tracing and Optical Coherence Tomography data”, Opt Express, 19(20): 19265-79, 2011.
- D. Siedlecki, A. de Castro, E. Gamba, S. Ortiz, D. Borja, S. Uhlhorn, F. Manns, J.M. Parel and S. Marcos, “Distortion correction of OCT images of the crystalline lens: GRIN approach”, Optometry Vision Sci, 89(5): 709-18, 2012.
- J. Birkenfeld, A. de Castro, S. Ortiz, D. Pascual and S. Marcos. “Relative contribution of surface shape and gradient refractive index to spherical aberration and astigmatism in porcine crystalline lenses”, submitted to Vision Research

INTERNATIONAL CONGRESS CONTRIBUTIONS

Personally presented

S.Ortiz, S.Barbero, and S. Marcos. "Computer simulations of optical coherence tomography A-Scans: What can we learn about refractive distribution?" Association for Research in Vision and Ophthalmology's Annual Meeting, poster presentation. IOVS 45: E-Abstract 2781, 2004.

S.Ortiz, S.Barbero, and S. Marcos. "Three-dimensional Optical Distortion Correction for Quantitative Anterior Segment OCT" Association for Research in Vision and Ophthalmology's Annual Meeting, poster presentation. IOVS 45: E-Abstract 2781, 2009.

S.Ortiz, P.Pérez-Merino, E.Gambra, S.Kling, A.deCastro, D.Pascual, I.Grulkowski, M.Gora, M. Wojtkowski and S. Marcos, "Quantitative three-dimensional anterior segment Imaging optical coherence tomography: developments and applications". 5th European Meeting on Visual and Physiological Optics (EMVPO), oral presentation. Stockholm, Sweden, 2010.

S. Ortiz, D. Siedlecki, P. Perez-Merino, S. Marcos. "Anterior Segment Optical coherence tomography (OCT): From nice Images to accurate topography". Association for Research in Vision and Ophthalmology's Annual Meeting, Oral presentation. IOVS 51: E-Abstract 3022, 2011.

S. Ortiz, P. Perez-Merino, E. Gambra, and S. Marcos "Image analysis and quantification in anterior segment OCT: techniques and applications" Biomedical optics (BIOMED). Optical Coherence Tomography in Ophthalmology (BTu2B). 2012.

Presented by collaborators

S. Kling, P. Perez-Merino, S. Ortiz, D. Pascual and S. Marcos "Corneal Biomechanical Response to Intraocular Pressure Changes From Scheimpflug and Anterior Segment OCT" Association for Research in Vision and Ophthalmology's Annual Meeting, poster presentation: 51: E-Abstract 4628. 2010.

E. Gamba, S. Ortiz, P. Pérez, M. Gora, M. Wojtkowski, and Susana Marcos. "Quantitative 3-D-imaging of the in vivo crystalline lens during accommodation". Association for Research in Vision and Ophthalmology's Annual Meeting, oral presentation. IOVS :51: E-Abstract

D. Siedlecki, A. de Castro, S. Ortiz, D. Borja, S. Uhlhorn, F. Manns and S. Marcos, "Estimation of the contribution of the gradient index structure to the posterior surface optical distortion in excised human crystalline lens imaged by optical coherence tomography". 5th European Meeting on Visual and Physiological Optics (EMVPO), oral presentation. Stockholm, Sweden, 2010.

P. Pérez-Merino, S. Ortiz, N. Alejandro, A. deCastro, I. Jiménez-Alfaro and S. Marcos, "Full OCT corneal topography and aberrations in kerato- conic patients and their change after intrastromal corneal ring segments (ICRS) implantation". Association for Research in Vision and Ophthalmology's Annual Meeting, poster presentation. IOVS 52: E-Abstract 4181. Fort Lauderdale, FL, USA, 2011.

J. Birkenfeld, A. de Castro, S. Ortiz, P. Pérez-Merino, E. Gamba and S. Marcos, "Three-dimensional reconstruction of the isolated human crystalline lens gradient index distribution". Association for Research in Vision and Ophthalmology's Annual Meeting, oral presentation. IOVS 52: E-Abstract 3404. Fort Lauderdale, FL, USA, 2011.

S. Marcos, A. de Castro, E. Gamba, J. Birkenfeld, S. Ortiz, P. Pérez-Merino and C. Dorronsoro, "Ocular imaging and crystalline lens optical properties". Frontiers in Optics, invited oral presentation. San José, CA, USA, 2011.

P. Pérez-Merino, S. Ortiz, N. Alejandro, A. de Castro, I. Jiménez-Alfaro and S. Marcos, "Assesing corneal geometrical and optical changes on ICRS-treated corneas with quantitative OCT". Eurokeratoconus II, poster presentation. Bordeaux, France, 2011.

J. Birkenfeld, A. de Castro, S. Ortiz, P. Pérez-Merino, E. Gamba, D. Pascual and S. Marcos, "Role of lens surface and gradient index for spherical aberration in mammal lenses". IONS-11 (11th meeting of the International OSA Network of Students), oral presentation. Paris, France. 2011.

P. Pérez-Merino, S. Ortiz, N. Alejandro, A. de Castro, I. Jiménez-Alfaro, S. Marcos, "OCT-based topography corneal aberrations and ray tracing total aberrations in keratoconus before and after intracorneal ring treatment." Association for Research in Vision and

Ophthalmology's Annual Meeting, poster presentation. Fort Lauderdale, FL, USA, 2012.

J.Birkenfeld, A.deCastro, S.Ortiz, P.Pérez-Merino, E.Gambra, D.Pascual and S. Marcos, "Relative contribution of the crystalline lens surface shape and gradient index distribution to spherical aberration". Association for Research in Vision and Ophthalmology's Annual Meeting, oral presentation. Fort Lauderdale, FL, USA, 2012.

PUBLICATIONS IN PROCEEDINGS

S. Marcos, A. de Castro, E. Gamba, J. Birkenfeld, S. Ortiz, P.Pérez-Merino and C. Dorronsoro, "Ocular imaging and crystalline lens optical properties". Frontiers in Optics, OSA Technical Digest (CD), Optical Society of America, 2011.

S. Ortiz, P. Perez-Merino, E. Gamba, and S. Marcos "Image analysis and quantification in anterior segment OCT: techniques and applications" Biomedical optics (BIOMED). OSA Technical Digest, Optical Society of America. 2012.

NATIONAL CONGRESS CONTRIBUTIONS

Personally presented

S. Ortiz, Y. Navarro, P. Rosales, J. Quesada, A. Llanos, M. Tuduri y F. Márquez, "Laboratorio de Laser Remote Sensing". 9ª Reunión de óptica, Orense, Poster, (2009).

S. Ortiz, D. Siedlecki, L. Remón and S. Marcos "Optical distortion correction for optical coherence tomography devices." 9ª Reunión de óptica, Orense, Oral (2009).

S. Ortiz and S. Marcos "A new method for three-dimensional ray tracing on a Delaunay representation of surfaces" Encuentro Español de diseñadores ópticos (2011).

S. Ortiz, P. Pérez-Merino, J. Birkenfeld, N. Alexandre and Susana Marcos "Análisis y cuantificación de imágenes 3D de OCT del segmento anterior del ojo: Técnicas y aplicaciones" 10ª Reunión de óptica, Zaragoza, Oral (2012).

Presented by Collaborators

Yolanda Navarro, Sergio Ortiz, Antíoco Llanos, Julio Quesada, Patricia Rosales, Maria Tuduri y Fernando Márquez . “Diseño y calibración de un sistema de imagen hiper-espectral basado en un filtro sintonizable de cristal líquido”. 9ª Reunión de óptica, Orense, Poster presentation. 2009.

Yolanda Navarro, Sergio Ortiz, Antíoco Llanos, Julio Quesada, Patricia Rosales, Maria Tuduri y Fernando Márquez, “Medida de MTF y respuesta temporal del fósforo de tubos intensificadores de imagen”. 9ª Reunión de óptica, Orense, Poster. 2009

AWARDS

2009 Premio Cosingo a la mejor ponencia de joven investigador en los campos de la bio-óptica color, vision e imagen. IX Reunión Nacional de óptica.

2011. ARVO International Travel Grant Award. ARVO Ft. Lauderdale. Florida

Agradecimientos

Hace poco tiempo comentaba que el camino de la ciencia es un camino de descubrimiento, no solo de la ciencia si no de uno mismo. En mi opinión la ciencia es una mezcla de ilusión, dedicación, constancia y tan solo un poco de inspiración.

En mi caso todo empezó hace mucho, mucho tiempo con mis padres enseñandome los valores de la disciplina, de la constancia y el esfuerzo. Recuerdo siempre a mi madre con su amor por la lectura y el conocimiento, enseñarme a leer, a sumar y a ser un inconformista haciendome superarme cada día, a no estar conforme con los buenos resultados y sobre todo a no sentir envidia. Mi padre enseñandome como trabajar con las manos, el amor por el trabajo y las cosas bien hechas y su eterno buen humor y optimismo. A los dos gracias por habermelo dado todo y por ayudarme a ser la persona que soy.

Gracias muy especiales a “Fibi” porque en ti se encarnan valores importantes de nuestra familia. Fortaleza de carácter, honradez, amor por el trabajo, los animales y por las cosas bien hechas.

No puedo, ni quiero olvidarme de unas personas muy importantes para mí como fueron mis yayos. Pedro Ortiz del que he heredado parte de mis rasgos físicos. Dorotea Laínez de la que he heredado, sobre todo, mi comprensión del comportamiento de los animales. Antonio Egea mi entrañable abuelo que me enseñó a soñar y me cautivo con sus historias, a él dedique mi licenciatura. Y como no, a Inocencia Mustienes, quizás una de las personas más inteligentes, junto a mi madre, que he conocido a ellas les debo mi capacidad de abstracción. Lastima yayos que no hayáis podido verlo, aunque siempre estaréis conmigo. Sin ser como fuisteis, esto, no hubiera sido posible.

Recuerdo el instituto cuando conocí a dos de los profesores que harían de mi amor a las ciencias mi profesión, María Benítez y Pedro Buera. María Benítez profesora de biología con la que ganamos un accesit de jóvenes investigadores en 1991. Una persona que siempre confió en mí. Pedro Buera un gran profesor capaz de enseñar las matemáticas a un gran nivel y de “abrirme la cabeza” a este mundo abstracto. A ellos millones de gracias, en la etapa más dura, hasta ahora, de mi vida.

La suerte o el destino hizo que estudiara físicas. Lo que mas recuerdo es a José Manuel Marco un recién licenciado en aquellos entonces, porque sirvió de inspiración y por él que estudié óptica. En los duros años de estudio apareció uno de los que a día de hoy sigue siendo un maestro y un amigo David Buisan. Su buen hacer, conmigo en una

AGRADECIMIENTOS

época incontrolable, con demasiada ira y frustración acumuladas, logró canalizarme y que entrará en un ciclo constructivo que todavía hoy perdura. Después de estos años duros conseguí licenciarme y entrar en el departamento de Óptica de la Universidad de Zaragoza. Gracias a todos ellos, pero en especial a Paco Villuendas y Javier Pelayo, por su gran acogida y por enseñarme a hacer “cacharros”.

Un año después Carlos Dorronsoro me contrato para el CIDA, donde pasé muchos años, buenos y malos. Él me convenció para hacer algo por la ciencia y me presento a Susana Marcos, quien es hoy por hoy mi mentora y mi jefa. Gracias Carlos sin ti y sin Susana esta tesis no hubiera sido posible. Antes de empezar a agradecer a la gente del “lab” donde está tesis culmina. Entre el CIDA y el CSIC aprendí que la física es una amante muy exigente que exige grandes sacrificios personales. Me gustaría tener unos recuerdos para la gente del CIDA, ya que allí forje gran parte de mi extraña personalidad como científico y ese laboratorio fue en gran parte mi criatura, ya que requería de un conocimiento amplísimo de óptica, de electrónica y de programación. Allí realice el mayor número de bancos y equipos que he hecho nunca. Por ello a todos los miembros del CIDA con los que tuve el placer de coincidir, gracias. Sin embargo, no me puedo olvidar de tres personas muy especiales; Fernando Márquez que confió en mi en tiempos turbulentos y del que aprendí muchas cosas, María Tudurí mi jefa en Bajas Luminancias y que con su alegría y sus “locuras” hacía del trabajo algo si cabe más entretenido, y Francisco Tierraseca compañero de fatigas, confidente y amigo. A ellos tres, muchas gracias.

Cuando Susana me acogió en el “lab” allí ya estaban Carlos, Dani Cano, Sergio Barbero, Patricia Rosales, Elena García y Lourdes Llorente. A todos ellos gracias por su gran acogida y por los momentos compartidos. Después, se unieron muchos más entre todos ellos me gustaría destacar a los miembros del OCT Team: Laura Remón, Enrique Gamba, Noelia Chia, Cristina Teijeiro, Sonia Duran, Miriam Velasco, y en especial a Alberto de Castro y Judith Birkenfeld con quienes compartí laboratorio y buenos momentos. Gracias a Daniel Pascual, por su comprensión y paciencia con mis locuras. Sabes que siempre eres de los primeros en comentarte una “ida de la pinza o una frikada”. Por supuesto gracias a todos los demás miembros del lab: Lucie Sawides, Sabine Kling, María Viñas, Aiswaryah Radhakrishnan, Pablo de Gracia, Dani Cortes, Nandor Bekesi, Enrique Bustos y Jorge Lamela.

Mención aparte, para mi, merecen Damian Siedlecki y Pablo Pérez. A Damian tengo que agradecer que aparte de ser un colega en física y la

AGRADECIMIENTOS

persona con quien más fácil me ha resultado trabajar, con sus desafíos mentales y su forma de ver las cosas, es también uno de mis mejores amigos y es una de las personas que más me ha apoyado y confiado en mí. Por todo ello gracias Damian, aunque estemos lejos siempre encontramos momentos para charlar, comentar nuevas ideas y colaborar en el trabajo y en la vida. ¡¡Gracias amigo mío, que nuestra amistad dure siempre!! De Pablo Pérez no sé ni por donde empezar, jamás me he encontrado una persona más afable, más dispuesta a colaborar y tan flexible mentalmente. Juntos, hemos sufrido y nos hemos divertido a raudales. Más que un compañero Pablo te considero mi amigo y mi colega. Espero que el tiempo y la distancia no lo estropeen.

Fuera del trabajo y en el plano personal no me puedo olvidar de Manu Benedí con más de 25 años de amistad, de Carlitos Martínez por tantas juergas y tantos kilómetros recorridos, y mucho menos de Julio Quicios maestro y amigo, que para mí, es parte de mi familia en Madrid. No me gustaría parecer un ingrato, así que también quiero agradecer a todos aquellos con los que compartí parte del camino de la vida y cuyos caminos un día se separaron del que yo recorro.

Y por supuesto a quien más tengo que agradecer es a “mi morena” que me aguanta todo los días y que es mi compañera y mi amiga, que soporta mis locuras, me cuida y me anima como solo ella sabe. Gracias Vanessa, gracias amor.

¡¡Ah!!, casi se me olvida con tanta emotividad... Gracias a los grupos de Heavy Metal por tantos años juntos, sin vosotros nunca habría sido posible esta tesis. En especial a... “Fear of the dark” mi canción fetiche, así que os dejo el final:



Final figure. A picture showing my amulet song. In White, the name of the song and the final verses, while the monster is Eddie getting out of a tree. Creepy, eh?

